# Computer Simulation of $SF_6$ Arcs in a Hybrid Circuit Breaker


THE UNIVERSITY *of* LIVERPOOL

**Thesis submitted in accordance with the requirements of the University of Liverpool for the Degree of Doctor in Philosophy by**

**Ki-Yeoung Kweon**

**August 2004**

**Department of Electrical Engineering and Electronics**
**The University of Liverpool**

# Abstract

## *'Computer Simulation of $SF_6$ Arcs in a Hybrid Circuit Breaker'*

K. Y. Kweon

Hybrid circuit breaker is a new generation of high voltage switching device. This circuit breaker takes advantage of the auto-expansion principle in combination with effective arc control by an externally imposed magnetic field to achieve optimum switching performance. A number of physical processes, such as radiation, turbulence, Ohmic heating, nozzle ablation and arc rotation, are involved in the arcing process of the device. Its performance depends on the close coupling of these physical processes.

Significant progress has been made, both experimentally and theoretically, in our understanding of the basic physical processes occurring in a circuit-breaker arc since the late sixties of the last century. Sufficiently accurate mathematical models describing these processes are now available. The close coupling among these fundamental processes, the interaction of the arc with its surroundings, the simulation of the moving parts of a breaker, and the rapid variation of the discharge conditions present a formidable task for establishing a robust algorithm necessary for the realistic computer simulation of the operation of a modern high voltage (HV) circuit breaker.

Computer simulation of the arcing process in air blast, puffer and auto-expansion circuit breakers has been reported in the literature [9, 10, 11]. However, so far there has been no computer simulation for hybrid circuit breaker, which takes into account the afore-mentioned physical processes together with the moving parts. A special feature of the arc in this type of circuit breaker is that during the high current phase, there is strong swirling flow in the azimuthal direction (arc axis in the z direction of a cylindrical polar coordinate system). This swirling flow due to the interaction of the arcing current with the externally imposed magnetic field can have significant influence on the arc behaviour. The aim of this study is therefore to develop a computational model for the hybrid circuit breaker, which includes all important physical processes and the moving contact. Special attention is paid to the effects of the swirling flow on arc behaviour.

To simulate the swirling flow, apart from the conservation equations for mass, axial and radial momentum, and energy, an equation for azimuthal momentum conservation has to be added to the axisymmetric 2D arc model. When the magnetic field is produced by the arcing current flowing in a coil, an equation for magnetic vector potential is used to compute the magnetic field simultaneously with velocity, temperature and electrical field. The eddy currents in the metallic components are taken into account.

In order to gain an understanding of the effects of swirling flow in a hybrid circuit breaker, several steady state cases were studied. Results show that the azimuthal movement of the arc tends to counteract the radial thermal conduction

and radiation transport, thus resulting in a better thermal confinement at the middle section of the arc column. The change in arc shape modifies the Lorentz force, which in turn adjusts the pressure and flow field, and consequently the arc shape. In steady state, the presence of swirling flow only has moderate influence on arc voltage under the conditions studied.

Computer simulation using the arc model was then carried out for the whole arcing process of two types of hybrid circuit breakers. In one type, the magnetic field is produced by the arcing current flowing in an azimuthal coil. Computer simulated results show that the presence of swirling flow has an accumulative effect on the flow, pressure and temperature fields. Complex flow situations are developed during the high current phase in association with contact movement and this significantly affects the shape of the arc column, and hence the arc voltage at a later stage. The most significant influence of the swirling flow is on the pressure build-up in the expansion volume, which is caused by an increased thermal energy flow into the expansion volume. The presence of swirling flow is advantageous to arc extinction at current zero. The thermal recovery performance of the device is predicted in terms of the critical rate of rise of recovery voltage (RRRV) and its dependence on the high current phase analysed.

The other type of breaker utilises a permanent magnet, which has the advantage of maintaining a steady magnetic field even at current zero. Radiation induced ablation of the PTFE nozzle inner surface plays the key role in building up the pressure in the expansion volume of this breaker. Similar to the hybrid circuit breaker with a magnetic coil, attention has also been paid to the mechanisms responsible for the pressurisation of the expansion volume, which is critical to arc extinction at a natural current zero. The increased pressure in the expansion volume is mainly due to the heating of the gas by the hot PTFE/SF6 mixture. The predicted arc voltage and pressure rise in the expansion volume are compared with available test results at typical instants of the arcing period.

The arc model developed is valid for high current arcing where the arc size is comparable to the internal diameter of the hollow contacts. Extreme care must be exercised when the model extends to low current situation. Future work is needed on the calculation of turbulence and radiation transport, since there are no experienced results to help calibrate these subsidiary models when the work in this thesis was carried out.

# Acknowledgements

First of all, I would like to give special appreciation to my supervisor *Professor M T C Fang* for his perceptive advice and thoughtful guidance which has led me to aspire to do research on this work, as well as to the wider sphere of my professional development.

I owe a debt of gratitude to *Dr. Yan* and *Dr. Zhang* for all their help and commitment to the inspirational discussions. I wish to show my sincere appreciation to *Dr K Y Park* and *Mr W P Song* for their invaluable assistance all the time. Admittedly, my deepest gratitude should go to my company *Hyosung Co.* in South Korea for all the support for my study. In addition, I am particularly thankful to the consistent encouragement from my team colleagues in the company and their generous tolerance of my absence over the years.

Last, but not least, I wish to express my grateful thanks to my wife, son and daughter for giving me every support and all their love throughout the time.

# Table of Contents

# Chapter 1
# Introduction and Objectives

## 1.1 Computer modelling of current interruption by $SF_6$ circuit breakers

Since the late nineteen sixties, much progress has been made in our understanding of the physical processes occurring in $SF_6$ circuit beakers [1]. Radiation transport in high pressure arcs confined within a supersonic nozzle can be accounted for sufficiently accurately in terms of an approximate radiation transport model [2, 3]. Thermodynamic and transport data for $SF_6$ are also well established [4]. For the $SF_6$ arcs encountered in gas filled circuit breakers, the discharge conditions, especially the pressure, ensures that the arc in the circuit breaker attains local thermal equilibrium (LTE).

The task of a circuit breaker is to interrupt a normal or a fault current within the power system at a natural current zero. Premature current interruption (known as the current chopping) should be avoided for the safety of the power network. The arc, which is formed between the two contacts inside a breaker, provides an effective means for current interruption. The design of a circuit breaker should ensure to change an arc from its highly conducting state to an insulator within a few microseconds around a natural current zero (commonly known as the current zero period). Thus, the performance of a breaker is closely related to the change of electrical conductivity of the arc during current zero period. Since the electrical conductivity of an arc in LTE is mainly dependent upon its temperature, energy balance of an arc plays a critical role in the determination of arc interruption during current zero period.

Early arc modelling was based on energy balance alone while ignoring the detailed physical processes [5, 6]. In terms of basic physical laws, energy balance is the same as energy conservation. For arcs in gas filled circuit breakers, arc can move at a very high speed due to the induced/imposed pressure gradients and due to the electromagnetic forces produced by the arc current itself or due to the interaction of arcing current with externally imposed magnetic fields. Thus, a proper account of energy balance must be linked to gas motion, which is determined by momentum conservation. The associated gas motion results in mass transport. The thermal state (i.e the temperature and pressure) of an arc can only be determined by a consideration of mass, momentum and energy conservation together with appropriate Maxwell's equations. The latter equations are required for the calculation of the Lorentz force on the arc. The arc conservation equations are almost identical to the Navier-Stokes equations of fluid mechanics. The differences lie in the source terms of momentum and energy equations (see Chapter 3).

Our current understanding of basic physical processes occurring in an arc is such that sufficiently accurate, quantitative descriptions of these processes are available. Robust algorithms for the solution of the coupled, highly non-linear conservation equations have been devised [7]. These algorithms have in fact been implemented in a number of commercial computational fluid (CFD) codes (e.g. [8]). With the rapid advancement of computer technology, the computational costs for the solution of arc conservation equations have been reduced drastically in the past two decades. Realistic modelling of the operation of circuit breakers using a personal computer (PC) with commercially available CFD packages has been reported [9].

In the last twenties years, a new generation of circuit breakers has merged. This new generation of circuit breakers (see Section 1.3.5) relies upon the utilisation of the arc energy during the high current phase to create the conditions at current zero for the quenching of the arc. However, the development of the new generation of breakers has proven very costly, as the effects of changing a

particular design parameter on the breaker's performance are not easily estimated. However, PC based arc modelling and simulation using commercially available CFD packages are able to provide valuable information to breaker designers for the optimisation process. At present, the efforts in developing the computer aided design tools appear to be confined to auto-expansion breakers [9, 10, 11].

It should be emphasised that, at present, computer modelling and simulation cannot replace full power short circuit tests during the development of a breaker. The parameters describing some of the physical processes, such as the rate of ablation of the inner surface of the arc confining vessel, radiation transport in non-axially dominated flow conditions, arc rooting, and the parameters describing arc turbulence, require limited test data to fix their values. However, once theses values are known, computer modelling has proven an effective tool for the optimisation of the breaker design, thus reducing the development costs and the time required to develop a new breaker.

The present investigation is concerned with the establishment of a computer model and the development of CAD and analysis tools for the design and analysis of hybrid circuit breakers. In this chapter, we review the necessary historical background related to arc modelling and the evolution of circuit breaker technology. Finally, the objectives of the present investigation are given.

## 1.2 Review of arc models

### 1.2.1 Early arc models

Historically, the initial focus of attention for current interruption and the magnitude of the recovery voltage on a circuit breaker became apparent in the early 1930s. There are two qualitative theories proposed to account for circuit interruption. The first was given by Slepian [12] in 1928 and became known as the 'race' theory, where interruption was visualised as a race between growing

dielectric strength of the contact gap and the transient recovery voltage of the circuit. The success or failure of interruption depends on the race between the loss of ions/electrons through recombination and other processes, and the rate of rise of the recovery voltage. This theory depends on non-equilibrium effects, which are quite difficult to assess. The mainstream of the effort in arc modelling has moved away from this kind of analysis toward models based on the equilibrium conservation equations. The second qualitative model was the 'wedge' model of Prince [13]. He proposed that convective effects introduced a wedge of cold gas at the upstream stagnation point and that this growing wedge caused circuit interruption. Later in the 1930s, when it became obvious from aerodynamic studies that it was not possible to 'sever' an arc in a gas blast, energy balance theories were formulated for arc extinction, being initiated by Cassie, 1939[5], and Mayr, 1943[6].

Cassie postulated an arc that had a constant current density, so that its area varied directly with current; it also had a constant resistivity and stored energy per unit volume. Cassie assumed an arc channel, in which the power loss was governed by convection only influencing just the arc diameter. This leads to Cassie's equation,

$$R\frac{d}{dt}\left(\frac{1}{R}\right)=\frac{1}{\tau}\left[\left(\frac{E}{E_0}\right)^2-1\right] \tag{1.1}$$

where $R$ is the arc radius, $t$ is time, $\tau$ is the arc time constant, E is the electric field and $E_0$ is the electric field at steady state. This type of arc model in fact described the performance of the arc in an air-blast circuit breaker very well under conditions when the current was large, but it did not really seem applicable to an arc near current zero since the rapid variation of arc temperature cannot be ignored.

Mayr proposed a somewhat improved model, in which the arc was exclusively cooled by thermal conduction, the conductance of the arc varying exponentially with the energy stored in it. This led to Mayr equation,

$$R\frac{d}{dt}\left(\frac{1}{R}\right)=\frac{1}{\tau}\left[\left(\frac{EI}{N_0}\right)-1\right] \tag{1.2}$$

where $N_0$ is the power loss per unit length. The arc was assumed to be cylindrical and axially uniform. $N_0$ was assumed to be constant while the temperature was allowed to vary. This model represents the behaviour of an arc around current zero more realistically than Cassie's model, but in a number of occasions test results showed serious departure from Mayr's model. Both Cassie's and Mayr's models are based on ad hoc assumptions, thus involving parameters which can not easily be related to fundamental physical processes. The application of these two models relies upon test data to provide information on these parameters. However, the mathematical simplicity of these two models makes them still popular among electrical engineers.

In 1948, Browne [14] combined these equations using Cassies's equation for the high current phase and Mayr's equation for the current zero period. This model can, to a certain extent, predict the features of arc interruption. However, it can neither give accurate quantitative prediction of the performance of circuit breakers nor can it elucidate the physical processes occurring inside an arc. Test data are also required to determine the parameters for this model.

In 1946, Elenbaas [15] made the first attempt to describe an arc in terms of the physical processes occurring in the arc. The Elenbaas equation,

$$\frac{1}{r}\frac{\partial}{\partial r}\left(kr\frac{\partial T}{\partial r}\right)+\sigma E^2=0 \tag{1.3}$$

describes a balance between heat conduction and Ohmic heating where r is the radial coordinate, T is the temperature, $\kappa$ the thermal conductivity, $\sigma$ the electrical conductivity and E the electric field.

It is obvious that equations (1.1-1.3) are still over-simplified regarding the processes of energy transport considered. For gas blast arcs, radiation, convection and turbulence should be included.

### 1.2.2 Recent progress in arc modelling

Over the past 30 years, energy-balance theories have been extended and refined in order to incorporate the various physical processes occurring within the arc during the thermal recovery periods. These theories have developed along the following two lines:

Firstly, Black-box models which consider the arc to be a two-pole system and which determine the transfer function using a chosen mathematical form, fitting the remaining free parameters to the measured voltage and current.

Secondly, the Physical arc models that consider the physical processes in detail, with the overall arc behaviour being calculated from the conservation laws with relevant gas and plasma properties, inside energy conservation.

Hermann [16], has provided a useful summary of the development of these models. Most of these models involve to some degree the numerical solution of the arc conservation equations, but there are important differences amongst the different researchers as how to represent the energy transfer process mathematically.

### 1.2.2.1 Black-box arc models

Black box arc models are generally presented as an expression giving the time-varying arc conductance g as a function of circuit parameters like current *i*, arc voltage *v*, time constant τ and power loss *P*. Most black-box models used today are derived from the arc equations published by Cassie, 1939, and Mayr, 1943. These equations were based on physical considerations, as mentioned in section 1.2.1, and assumed constant arc parameters. Over the years, these equations have been combined and modified to produce many black-box models. Most of these rely on first order differential equations that can be transformed into the following general form:

$$\frac{1}{g}\frac{dg}{dt} = \frac{1}{\tau(|i|, g)}\left(\frac{vi}{P(|i|, g)} - 1\right) \tag{1.4}$$

The various black box models differ in the type of dependence of the arc parameter functions P and τ and in the way they are determined. This equation cannot be derived from conservation equation. Most of these models have no real physical justification with the functional dependence of the parameters P and τ often being introduced to achieve a better correlation between tests and calculations. These models must be considered as mathematical descriptions rather than physical descriptions.

Black-box models vary in complexity and detail. A good overview of black-box arc models is given in a CIGRE report [17]. Browne [18, 19], developed a model that combines the two equations using Cassie's equation before current zero and Mayr's equation after current zero. Others have modified the equations by replacing the constant arc parameters P and τ by functions, of the arc parameters, usually the arc conductance [20].

The application of a given black box arc model consists of two stages:

1. Parameter determination.

Experiments provide the waveforms of arc voltage and current during the thermal recovery period. The analysis of these results is specific to the chosen arc equation with approximate assumptions regarding the arc parameters in the equation. The arc equation and the determined arc parameters then define the arc model.

2. Numerical experiments.

For different circuit conditions, the interaction of the circuit and the switching arc is calculated by numerical simulation techniques using the arc model. This allows the determination of important results such as the limiting curves for the circuit breaker. The results can reveal the presence of any critical circuit conditions.

However, all of these "black box" models involve *ad hoc* assumptions which lead to free parameters in the models which cannot be related to the physical processes occurring in the arc. Hence the application of these models requires that test data for the particular interrupter of interest is available in order to fix these parameters. Nonetheless work continues on this type of model due to its simplicity.

### 1.2.2.2 Physical arc models

It has been realised that the arc models of Cassie and Mayr [5, 6] inadequately describe the physical processes occurring in gas circuit breakers, and that in some cases severe departures from these two models occur. Thus, these arc models cannot be used as an analytical design tool.

It appears that for a satisfactory understanding and for the purpose of finding an analytical design tool, one is compelled to resort to the numerical solution of the basic arc conservation equations which became known in the late forties of last century because of intensive research in plasmas associated with the thermo-

nuclear fusion. The arc conservation equations in full differential form are notoriously difficult and costly, in terms of computing time, to solve because of their high non-linearity. Therefore simplifications are often introduced. The basic conservation equations for axisymmetric arcs are of two main forms, the radially integrated form (usually known as the integral method) and the full differential form (known as the differential method). Both of them are widely used at present since each of them has its own advantages.

A. Integral method

Various integral arc models have been exploited by Swanson, Roidt, Topman, Cowley, Fang, Lowke and their colleagues from the late nineteen sixties to the end of nineteen eighties. The main difference between those integral arc models lies in the method for the calculation of radially integrated terms which involve the radial temperature and axial velocity profiles. There have been two different approaches to obtain the information on those radial integrals. One assumes that the shapes of radial profiles of temperature and axial velocity are known functions of radius (Swanson et al. [21-27], Lowke et al. [28-33] and Hermann et al. [34-37]). The other assumes that those shapes can be determined by an arc characteristic quantity (i.e. the correlation parameter, Cowely [38]), which can in turn be calculated from the arc integral equations [38-45]. The major integral arc models are reviewed below by examining their main assumptions, achievements and applicable range.

Swanson, Roidt and Topham recognised the similarity between an arc in axial flow and a boundary layer and this similarity was used to simplify the arc conservation equations into the boundary layer form. Assumptions were then made regarding the radial temperature and velocity profiles of gas, for example in their later papers [24, 25], the shape of the temperature profile is assumed to be a Bessel function, while the arc velocity is assumed to be constant.

Extensive investigations on arcs in gas flow were carried out at Brown Boveri [34, 46]. A special finite difference method has been introduced which avoids

difficulties arising from the strong temperature variations within the region of solution. The main feature of the method is a coordinate transformation which replaces the radial coordinate by the temperature as an independent variable, so that the region of solution is divided into a number of zones separated by isothermal surfaces. A two zone model including turbulent and heat transfer was successfully employed in elucidating the physics of a 2kA DC nitrogen nozzle arc [34]. However, Zhang et al. [3] obtained good agreement between their calculation and experiment of Hermann et al. [34] without considering the effect of turbulence. A similar arc model, which neglected the axial variation of thermodynamic quantities by assuming the pressure gradient to be proportional to the distance, was used to investigate the current zero period [46].

Lowke and Ludwig [32] introduced a channel model in which the arc temperature and axial velocity are uniform across the conducting area. Tuma et al. [28-30, 33] extended it to study the transient behaviour of nozzle arcs.

The most general form of the integral arc conservation equations was derived by Cowley [38] in 1974 and the radial integrals were expressed in the form of arc areas. Later, Chan et al. [41] extended the formulation to include an energy integral equation for the arc conducting core. The other integral models are special cases of this general formulation and differences between the models lie in the closure of the integral equations. The model has achieved considerable success at high currents [42, 47, 48]. Recently the method has been applied to the current zero period by Blundell and Fang [49] and used to investigate the effects of nozzle ablation [10, 39, 40, 45].

B. Differential method

Recently the rapid increase in computing power of PCs at reduced price and the successful development of numerical methods for solving partial differential equations have made the use of the differential method a practical proposition. It

has been successfully used to predict the arc behaviour during the current zero period [3, 50-54]. However, many of the physical mechanisms in switching arcs are too complex to be fully modelled. Approximations and simplifications must therefore be made in the modelling of such phenomena as radiation transport, turbulence and electrode phenomena.

An axisymmetric model was used to study the decay of the hot gas channel after current zero by Ragaller et al. at Brown Boveri [52]. The computational difficulty associated with the steep temperature gradients was overcome by using the isotherm transformation technique [55]. Viscous dissipation and axial heat conduction are neglected in the energy equation. To simplify the problem, the radial momentum equation is reduced to a uniform radial pressure distribution. Thus the cold surrounding flow solely determines the axial pressure distribution. Strong turbulent energy transport needs to be introduced in their model in order to obtain agreement with the measured dielectric recovery characteristics [56]. Turbulence starts to play an important role in the cooling of the residual hot gas at the stagnation point from about 30μs after current zero. Flow downstream of the nozzle throat becomes turbulent before current zero.

Mitchell et al. [53] developed a model, which took no account of turbulence. The model adopted an adaptive mesh in order to solve the special problems of stability and accuracy that arise because of radial gas flow and sharp arc boundary. The calculated net radiation emission coefficients were used to calculate the radiative balance up to arc boundary. It was assumed that all the emitted radiation was absorbed in a single layer of one cell thickness at the arc edge (e.g. a specified temperature between 10,000K and 15,000K). In the case of nitrogen, they obtained good agreement with experiment using the published values for the net radiation emission coefficients of Shayer and Fang [57]. However, in the case of SF6, their calculations using the values given by Libermann and Lowke [4] showed much higher axis temperature than that from experiment. Therefore, the net emission coefficient should be increased by a factor of 4 in this work.

The model developed by Lowke and Lee [54] describes the gas-blast arc in an axisymmetric nozzle by the conservation equations in differential form. A general description of the model and of the method used for its solution is given by Lowke and Lee [54]. Two versions of the model have been developed, one for the steady state case and one for transient situations. The main difference between the two versions lies in the way that the radial velocity is calculated.

Liverpool University has made significant progress in improving the differential method for arc modelling. The model has been successfully applied to the investigation of steady and transient gas blast arcs [3, 10, 47-51]. A 2kA DC nitrogen arc in a supersonic nozzle was modelled. The arc equations simplified by using the boundary layer assumption were then solved with the assumption of laminar flow. Radiation transport was accounted for a semi-empirical model using net emission coefficients in the central region of the arc with a fixed proportion reabsorbed at the arc edge. Good agreement with the experimental results of [36] was achieved. In [58] the same arc model was applied to $SF_6$ nozzle arcs at a relatively low current, for which experimental results exist [60, 61]. A agreement was found to be rather poor. In [59] it was found to be necessary to introduce turbulence enhanced momentum and energy transport. The Prandlt mixing length model was employed, which yields good agreement with the temperature measurements. The reason why turbulence must be added for the case of $SF_6$ but not in the case of $N_2$ is still not understood [62, 63] but there is experimental evidence that $SF_6$ arcs are turbulent [60, 61], at least at low currents.

### 1.2.3 Arc modelling based on commercial CFD (Computational Fluid Dynamics) package

Recently many researchers have carried out a substantial investigation of arcs in puffer circuit breakers using CFD techniques [11, 64, 65, 66]. The first published attempt in this area was that of Rutten [67] who modelled a puffer arc up to 1kA. Trepanier and co-workers used the Euler equations to solve for the flow. Radiation is accounted for in [65] and [66] using net emission coefficients with a re-absorption layer at the arc edge, while in [64] a five-band version of the P1 model is used for the first time. Chevrier and co-workers [68] have investigated arcs in circuit breakers using the Navier-Stokes equations, but not included viscous effects.

The use of commercial CFD packages has proven to be not an easy task. The difficulties encountered are summarised below:

- Generation of grids, which are usually non-uniform and non-orthogonal with moving boundaries. Ideally, these grids should be adaptive.
- The correct specifications of boundary conditions and correct description of arc physics.
- Problems associated with very steep density gradients at the edge of the arc core and highly compressible nature of the flow encountered in a circuit-breaker (flow speeds in the solution domain vary from nearly zero to supersonic).
- The calculation for electromagnetic fields often requires a calculation domain bigger than that of the fluid field.
- Transition from laminar flow to turbulent region and the appropriate turbulence model in the presence of an arc and in the region of low Reynolds number.
- Verification of CFD solutions.

It appears that the majority of commercially available CFD package are based on the finite volume method of Spalding and Patankar [69]. PHOENICS [8] has the longest history. Successful application of commercial CFD packages to circuit

breaker arcs will greatly reduce the cost and effort which need to be spent on the development of purpose-oriented CFD code, including the software for visualisation of the computational results. PHOENICS has been used at the University of Liverpool in the past ten years. Sufficient experience with PHOENICS has been accumulated. The arc results from PHOENICS have been verified by comparison with experimental results or numerical solutions obtained by the software developed at Liverpool [70]. The arc model developed in this thesis will be implemented into PHOENICS to investigate the behaviour of electric arcs in a hybrid circuit breaker.

## 1.3 Review of the evolution of circuit-breaker technology

Circuit breakers are the essential part of a power system. They are needed to de-energise a load or to isolate a fault portion of the system so that the equipment or the line can be repaired or protected from high short circuit current. The operation of circuit breakers is well known. Fundamentally, there is a pair of electrical contacts, one of which is moving and the other usually fixed. The moving contact is actuated by a mechanism. In order to interrupt the circuit, the moving contact is drawn away from the fixed one. During this process an electric arc is formed between the contacts. The electrical conductivity of the arc is high, thus a current path being maintained between the two contacts. Until the arc is extinguished in one-way or another, the current is not interrupted. Thus, the physical process of circuit interruption is one of changing a highly conducting plasma into an insulating gas.

The interrupting capability of circuit breakers increased continuously as the power systems expanded. The means for improving the interrupting capability of circuit breakers have been many and varied. The basic problem has been to control and extinguish the high-power arc which necessarily occurs between the two contacts of a circuit breaker during high-current interruption. Arc quenching media have been used to promote arc extinction. Air, compressed air, oil, sulphur

hexafluoride (SF6) and vacuum environment have been used at various stages of the development of circuit breakers.

Therefore, the history of circuit breakers is consequently closely bound up with that of the breaking techniques and dielectric media used. The present situation can best be explained by reviewing the techniques used throughout the last century.

### 1.3.1 Air circuit breakers

Increased network voltage and power have led to the use of auxiliary arcing contacts, arc blowing and arc elongation by magnetic effect. This technique, used up to 20kV, has no longer been used today due to the large space taken up by the air breakers. Compressed air is used in the production of circuit breakers at extra high voltages. However, since circuit breakers using this technique are complex and costly, it is used today only in high and extra high voltage level in very cold regions, as air has the advantage of retaining its properties at very low temperatures.

### 1.3.2 Oil circuit breakers

Oil, used as the arc quenching and insulation medium, first appeared at the turn of the last century. It made possible the first HV circuit breakers, which achieved a considerable reduction in overall dimensions, thanks to the reduced oil volume technique. These circuit breakers are still used at the MV and HV substations in certain countries, such as Brazil and CIS (former USSR). They are currently being replaced in Europe and the USA by SF6 and vacuum circuit breakers. Their progressive disappearance is due mainly to the dangers inherent in oil (inflammable, explosible), to the civil engineering work required to install them (retention tanks) and to the preventive maintenance involved.

### 1.3.3 SF6 circuit breakers

The discovery in the 1950's of the excellent dielectric and arc quenching properties of $SF_6$ [71] led to a new generation of $SF_6$ blast circuit breaker. $SF_6$ is a very stable, odourless, non-toxic and non-flammable gas. Its dielectric strength is higher than that of oil at an absolute pressure above 3bar and is at least twice that of air owing to its electro-negative property. The adoption of $SF_6$ resulted in a considerable increase in voltage and current ratings without resorting to extreme gas pressures or large number of breaks in series.

The first generation of $SF_6$ circuit breaker required part of the working gas to be stored permanently at a high pressure (typically 16bar) which generates a high speed flow for arc quenching. However, $SF_6$ has a high boiling point, typically 20°C at 24bar. Heating facilities are thus necessary to prevent liquefaction of pressurised $SF_6$ in low temperature environment. A method to overcome this problem is to use the so-called puffer principle: The high speed flow in the nozzle can be generated by compressing the gas in a moving cylinder against a stationary piston during the operation of the circuit breaker. $SF_6$ puffer circuit breakers first appeared in 1964 [72] and have become the most successful technology in current interruption at transmission voltage levels in the last three decades. The interrupting capacity per break has increased from 72kV/25kA in 1970 to 550kV/63kA in 1993 [73]. However, the necessary gas compression in the puffer cylinder requires a very powerful operating mechanism such as the very costly hydraulic system.

### 1.3.4 Vacuum circuit breakers

Vacuum circuit breakers are a special type of switching device. They are self-contained and maintenance free. Arcs generated during the operation are burning in the metallic vapour produced by contact erosion. Vacuum circuit breakers are mainly used in distribution voltage level up to 36kV, although much work has been

done to raise the voltage ratings [74]. Vacuum circuit breakers at 132kV are already in service in some outdoor stations [75].

### 1.3.5 Hybrid circuit interrupter

Hybrid circuit breaker incorporating arc rotation and self-pressurization mechanisms has attracted much attention in recent years because of its advantage over other types of circuit breaker [76, 77]. This type of circuit breaker uses a combination of rotary arc and pressure rise inside the auto-expansion volume in order to achieve some reduction in drive energy and produce simple interrupting devices. The main advantages of this breaker are as follows:

- Low energy mechanism, lighter moving parts, simpler interrupting devices and compact systems
- Long service life and pursuit maintenance free
- Increased reliability and low cost circuit breakers.

A principle of breaking by hybrid breaker is shown in Figure 1.1. When the contacts separate an arc is drawn between them. (The current path is then through the copper contact stem, through a coil which circles the steel tube, through the fixed contact and to the moving contact via the arc.) The current in the coil sets up a magnetic field with radial and axial components. Eddy currents will flow in the metal components of the device, which will affect the magnetic field. During the high current phase, the arc will fill the hollow fixed and moving contacts, and an axisymmetric arc column is formed. The electrical energy dissipated in the arc will cause a pressure rise in the auto-expansion volume. The interaction of the magnetic field produced by the coil and the arc current will produce a swirling flow. As the current drops towards current zero, the overpressure in the auto-expansion volume will cause a gas flow through the hollow contacts to the outlets. This gas flow combined with rotation of the arc, now thin, extinguishes the arc at current zero.

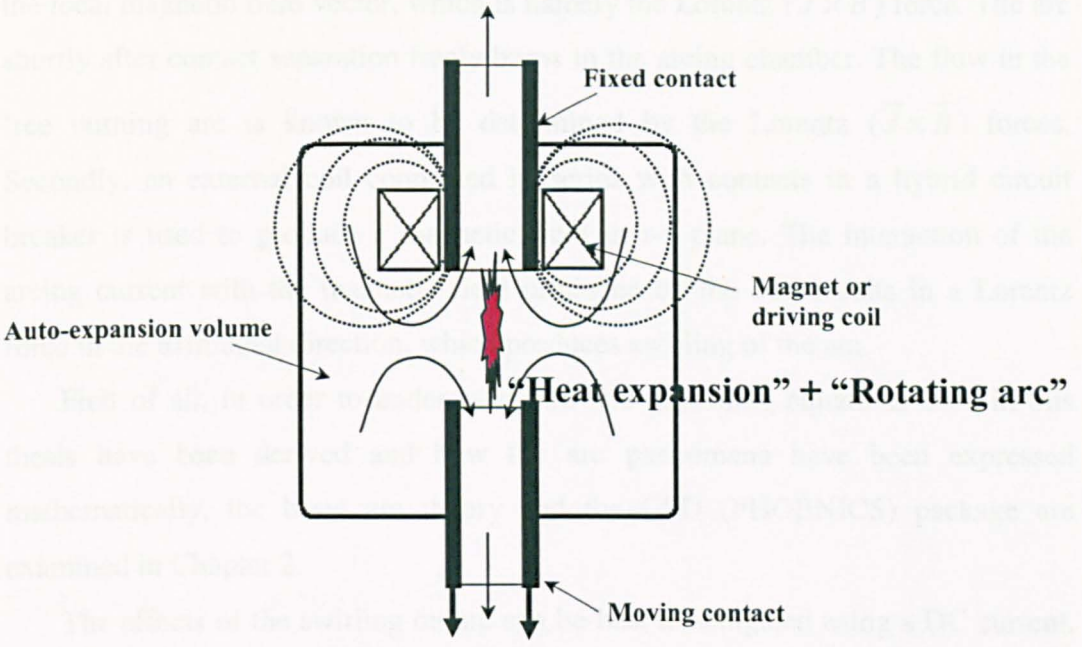


**Figure 1.1** Principle of breaking by hybrid circuit breaker

## 1.4 Aims and organisations of the thesis

The aim of this study is to develop a computational model for the arcing processes in a hybrid circuit breaker. Particular attention is paid to the effects of swirling flow, which is produced due to the interaction of the arcing current with the externally imposed magnetic field.

The work in this thesis will concentrate on the investigation of electric arcs related to hybrid circuit breakers (rotating & self-blast) although the research approach is also applicable for other arcing devices. The arc in the expansion volume burns in the flow established by the arc itself, which differs from a puffer circuit breaker where the nozzle flow is solely imposed by the action of a puffer piston. The flow in a hybrid circuit breaker originates from two sources. Firstly, the interaction between the arcing current and its magnetic field exerts an electromagnetic force which is perpendicular to the local current density vector and

the local magnetic field vector, which is namely the Lorentz ($\vec{J} \times \vec{B}$) force. The arc shortly after contact separation freely burns in the arcing chamber. The flow in the free burning arc is known to be determined by the Lorentz ($\vec{J} \times \vec{B}$) forces. Secondly, an external coil connected in series with contacts in a hybrid circuit breaker is used to produce a magnetic field in r-z plane. The interaction of the arcing current with the magnetic field produced by the coil results in a Lorentz force in the azimuthal direction, which produces swirling of the arc.

First of all, in order to understand how the governing equations used in this thesis have been derived and how the arc phenomena have been expressed mathematically, the basic arc theory and the CFD (PHOENICS) package are examined in Chapter 2.

The effects of the swirling on arc can be best investigated using a DC current. Thus, a 5kA DC arc with and without swirling is computationally investigated in Chapter 3. The arc burns in a duo-flow arcing chamber that has characteristic dimensions similar to those used in industrial circuit breakers

In Chapter 4, we investigate the effects of swirling flow on the behaviour of an $SF_6$ arc in high current phase and the thermal recovery characteristics after current zero. An ac current with a peak of 10kA is simulated.

In Chapter 5, computer simulation of the arc behaviour in the high current phase of a 25.8kV hybrid circuit breaker (permanent magnet-assisted auto-expansion interrupter) has been carried out using a two-dimensional axisymmetric arc model. Attention has been paid to the mechanisms responsible for the pressurisation of the expansion volume, which is critical to arc extinction at a natural current zero. The predicted arc voltage and pressure rise in the expansion volume are compared with available test results at typical instants of the arcing period.

Finally, the work is summarised in Chapter 6, which also includes a proposal for possible future work.

# Chapter 2
# Basic Arc Theory and the CFD (PHOENICS) Package

## 2.1 Electric arcs at high pressure

An electric arc is a plasma whose component species have temperatures typically in excess of 4000K and usually less than 25000K. The arc may be distinguished from other electrical discharges by its ability to conduct relatively high current density (a fraction of an ampere is very small current) whilst being sustained by relatively low electric field strength in the cathode region. The arc usually burns between two electrodes. At low currents, high-pressure arcs have a negative incremental electrical resistance, which can induce instability in an interconnected electrical network and lead to high current arcing of a self-sustaining nature [78].

Electric arcs can be found in power system protection devices, in material processing devices, in light sources, in electromagnetic drive systems and in many industrial applications. The electric arcs may differ substantially from each other with regard to their physical properties.

For most industrial applications, the plasma column of the high-pressure arc is collision dominated so that the particle species in the plasma may attain a common temperature and the plasma properties can be described by continuum theory.

The simplest arc column is that can be found in a long cylindrical tube known as the wall-stabilized arc. When high powers are dissipated in such arcs the thermal loading of the confining wall is sufficient to produce severe ablation, so producing an ablation control situation. When an arc does not have confining wall, the arc burns freely, the free burning arc. Such plasma arc columns are surrounded by a region of relatively hot (ambient to about 4000K) but low electrical conductance gas. The imposition of a flow of gas sustained by an axial pressure gradient leads to a constriction of the arc boundary, the extent of which is determined by the convection flow. Such arcs are known as 'convection stabilised arcs'. Convection stabilised arcs are common in gas blast circuit breakers.

## 2.2 Basic equations of the high-pressure arc column

The high input power which sustains a high-pressure arc produces a high electron density and ensures that, for most operating conditions, all particle species attain a common temperature. For such a particle-collision-dominated arc column, local thermal equilibrium (LTE) is usually a valid assumption. The arc can, therefore, be treated as a single fluid and its thermodynamic and transport properties uniquely determined by two thermodynamic quantities (e.g. temperature and pressure). The equations describing such a plasma are those of equilibrium thermodynamics and conservation equations of a compressible and viscous fluid, which are modified to include the effects of the Lorentz force, radiation transport and electrical power input. These additional effects are described by Maxwell's equations, the generalised Ohm's law for partially ionised gases and the radiation energy transport equation. The radiation energy transport, which is important for high-power arcs, makes arc analysis particularly difficult since it involves the whole volume of the discharge.

The general equations for arcs in LTE can be written in the following form after some simplifications have been made to the electromagnetic terms [79, 80, 86]:

Continuity equation

$$\frac{\partial \rho}{\partial t} + \nabla \cdot \left(\rho \vec{V}\right) = 0 \tag{2.1}$$

Momentum equation

$$\rho \frac{d\vec{V}}{dt} = \rho \vec{g} + \nabla \cdot \Pi_{ij} + \left(\vec{J} \times \vec{B}\right) \tag{2.2}$$

Energy equation

$$\begin{aligned} &\frac{\partial}{\partial t}\left[\rho\left(e + \frac{V^2}{2}\right)\right] + \nabla \cdot \left[\rho\left(e + \frac{V^2}{2}\right)\vec{V}\right] \\ &= \rho \vec{g} \cdot \vec{V} - \nabla \cdot \left(P\vec{V}\right) + \nabla \cdot \left(k \nabla T\right) - q + \vec{J} \cdot \vec{E} + \Phi \end{aligned} \tag{2.3}$$

Equation of state

$$\rho = f(P, T) \tag{2.4}$$

Ohm's law

$$\vec{J} = \sigma\left(\vec{E} + \vec{V} \times \vec{B}\right) \tag{2.5}$$

Ampere's law

$$\nabla \times \left(\frac{\vec{B}}{\mu_0}\right) = \frac{\partial(\varepsilon \vec{E})}{\partial t} + \vec{J} \tag{2.6}$$

Faraday's law

$$\nabla \times \vec{E} = -\frac{\partial \vec{B}}{\partial t} \tag{2.7}$$

and

$$\nabla \cdot \left(\varepsilon \vec{E}\right) = \rho_c \tag{2.8}$$

$$\nabla \cdot \vec{B} = 0 \tag{2.9}$$

The meaning of the symbols used in the above equations is listed below:

$t$ : time

ρ : density

e : internal energy

P : static pressure

k : thermal conductivity

T : temperature

$\vec{V}$ : velocity vector

$\vec{g}$ : acceleration of gravity

$\vec{\Pi}_{ij}$ : stress tensor

$\vec{J}$ : current density

$\vec{B}$ : magnetic flux density

$\vec{E}$ : electric field strength

$q$ : radiation flux vector

Φ : viscous dissipation

$\sigma$ : electrical conductivity

$\mu_0$ : permeability of vacuum

ε : permittivity of the medium

$\rho_c$ : density of space charges

The stress at a point is linearly dependent on the rate of strain of the fluid (i.e. Newtonian fluid). For Newtonian fluid, it is possible to derive [80] a general deformation law which relates the stress tensor to the pressure and velocity component. In compact tensor notation, this relationship becomes

$$\vec{\Pi}_{ij} = -P\delta_{ij} + \mu_1\left(\frac{\partial u_i}{\partial x_j} + \frac{\partial u_j}{\partial x_i}\right) + \delta_{ij}\mu_2\frac{\partial u_k}{\partial x_k} \qquad (i,j,k = 1,2,3) \qquad (2.10)$$

where $\delta_{ij}$ is the Kronecker delta function (i.e. $\delta_{ij}= 1$ if $i = j$ and $\delta_{ij}= 0$ if $i \neq j$); $u_1$, $u_2$ and $u_3$represent the three components of the position vector; $\mu_1$ is the coefficient of viscosity (dynamic viscosity), and$\mu_2$ is the second coefficient of viscosity. The two coefficients of viscosity are related to the coefficient of bulk viscosity $\eta$ by the expression

$$\eta = \frac{2}{3}\mu_1 + \mu_2 \tag{2.11}$$

In general, the coefficient of bulk viscosity can be assumed to be zero (i.e. Stoke's hypothesis). Therefore equation (2.10) can be written as

$$\vec{\Pi}_{ij} = -P\delta_{ij} + \vec{\tau}_{ij} \tag{2.12}$$

where $\vec{\tau}_{ij}$ represents the viscous stress tensor given by

$$\vec{\tau}_{ij} = \mu_{1,2}\left[\left(\frac{\partial u_i}{\partial x_j} + \frac{\partial u_j}{\partial x_i}\right) - \frac{2}{3}\delta_{ij}\frac{\partial u_k}{\partial x_k}\right] \qquad (i, j, k = 1,2,3) \tag{2.13}$$

Then, the viscous dissipation $\Phi$ can be given by

$$\Phi = \vec{\tau}_{ij}\frac{\partial u_i}{\partial x_j} \qquad (i, j = 1,2,3) \tag{2.14}$$

The radiation balance is given by

$$q = \nabla \cdot \vec{F} = \int_0^{\infty}\int_0^{4\pi} I_{\upsilon}\vec{n}d\upsilon d\omega \tag{2.15}$$

where $\vec{n}$ is a unit vector, $\omega$ the solid angle, and $\upsilon$ the frequency. The radiation intensity, $I_{\upsilon}$, is given by

$$\vec{n}\cdot\nabla I_{\upsilon} = \varepsilon_{\upsilon} - I_{\upsilon}k_{\upsilon} \tag{2.16}$$

where $\varepsilon_{\upsilon}$ is the emission coefficient and $k_{\upsilon}$ is the spectral absorptivity at frequency $\upsilon$.

Although a complete solution of those governing equations (2.1) ~ (2.9) is in principle possible, this is still impractical on account of the excessive computing time required, lack of reliable spectroscopic data for radiation transport calculation, and the difficulty of obtaining a clear physical interpretation. In addition, some physical processes occurring in an arc device are difficult to quantify, such as electrode melting, ablation of arc surrounding wall etc.

A number of simplified arc models have, therefore, been evolved, which are based upon the governing equations but related to particular arcing conditions [81].

## 2.3 Method for calculating turbulence

It is well known that arcs in a supersonic nozzle can become turbulent, especially at low currents [81, 82]. Systematic experimental investigations of turbulent arcs are few and are mainly concentrated on arcs in nitrogen [83, 84]. For $SF_6$ arcs the temperature measurements of Lesberg and Pietsch [85] on a turbulent arc were obtained under well-defined experimental conditions for which comparison with theory can be made. Before 1994 there had been virtually no rigours theoretical investigation into the conditions under which an arc in gas flow can become unstable. Niemyer and Ragaller [84] pointed out in 1994 that the vector cross product of axial pressure gradient and radial density gradient is a source of generation of vorticity. This finding was also testified in another research [87].

The electrically conducting core of an arc in a supersonic nozzle can attain very high temperature and velocity of a few thousands meter per second. An arc resembles a high velocity jet. Stability theory of shear layer flow is usually based on the assumption of incompressible fluid. It is well known that when Reynolds number exceeds certain critical value the shear layer flow will become unstable and the fluid subsequently enters into a turbulent state. Arcs in gas flow are very different from a shear layer flow in that compressibility, electrical energy input, and radiation transport also determine the state of the arc.

Turbulent momentum and energy exchange plays a very important part in determining the breaking capacity of $SF_6$ blast circuit breakers. Since direct simulation of turbulence by solving Navier-stokes equations is impossible with available computing power, the statistical behaviour of a turbulent flow is conventionally described by the time-averaged values of the flow and thermodynamic properties. The time mean $\bar{\phi}$ of a turbulent function $\bar{\phi}$ *(x, y, z, t)* is defined by

$$\bar{\phi} = \frac{1}{T}\int_o^T \phi \; dt \tag{2.17}$$

where $T$ is an averaging period taken to be longer than any significant period of the fluctuations themselves. The fluctuation $\phi'$ is defined as the deviation of $\phi$ from its average value

$$\phi' = \phi - \bar{\phi} \tag{2.18}$$

as shown in Figure 2.1. It follows by definition that a fluctuation has zero mean value

$$\overline{\phi'} = \frac{1}{T}\int_o^T \left(\phi - \bar{\phi}\right) \; dt = \bar{\phi} - \bar{\phi} = 0 \tag{2.19}$$

Substituting equation (2.18) in to (2.1), (2.2) and (2.3) results in various time-averaged terms of the correlated fluctuating components. For small density fluctuation, the most important terms are the Reynords stress $-\overline{\rho u_i' u_j'}$ ($i$ and $j$ denote the coordinate) in the momentum equation and the term $-\overline{\rho u_i' e'}$ in the energy equation. It is therefore necessary to introduce additional relations to relate these two terms to the main flow quantities, which is the task of all turbulence models.

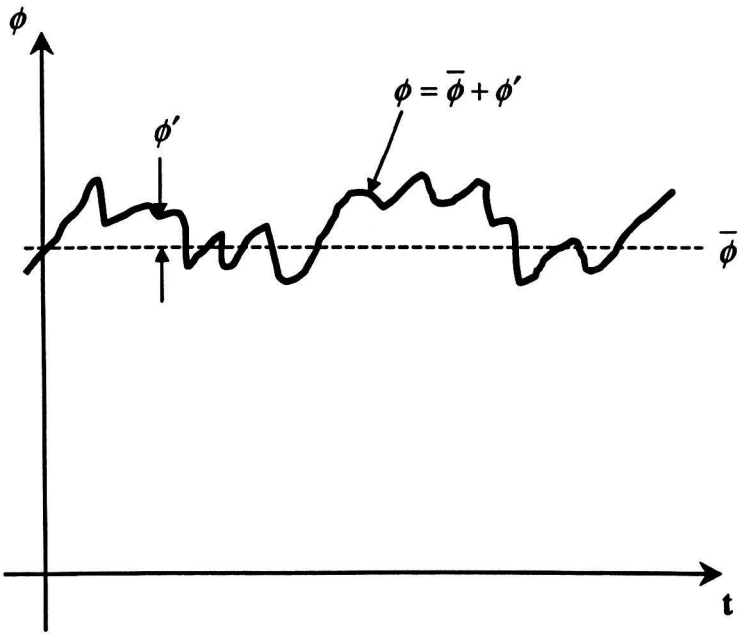


Figure 2.1 Definition of mean and fluctuating turbulent variable

The two most popular turbulence models, namely the Prandtl mixing length model and the K-$\varepsilon$ model, are all based on the assumption of negligible density fluctuation. The concept of eddy viscosity has long been used to model the turbulent viscous effect in analogue to its molecular counterpart. For example, in an axially dominant flow the Reynolds stress and the turbulent energy exchange term can be modelled by

$$-\rho\overline{u_i' u_j'} = \mu_t \frac{\partial u_i}{\partial x_j} \tag{2.20}$$

$$-\rho\overline{u_j' e'} = k_t \frac{\partial T}{\partial x_j} \tag{2.21}$$

where $\mu_t$ is the eddy viscosity which has the same dimension as the molecular dynamic viscosity, and $k_t$ is an equivalent turbulent thermal conductivity which is correlated to the eddy viscosity by the turbulent Prandtl number $P_{rt}$

$$P_{rt} = \frac{\mu_t}{k_t / c_p} \tag{2.22}$$

The eddy viscosity, $\mu_t$, is defined as [7]

$$\mu_t = \rho l_m^{\,2} \left| \frac{\partial u_i}{\partial x_j} \right| \tag{2.23}$$

where $l_m$ is the mixing length for momentum transfer. For a gas-blast nozzle arc, which resembles a rounded jet, $l_m$ is assumed to be

$$l_m = c\delta \tag{2.24}$$

where $\delta$ is the arc's thermal radius defined by

$$\left(\frac{\theta_\delta}{\pi}\right)^{1/2} = \left(\frac{1}{\pi}\int_0^\infty \left(1 - \frac{\rho}{\rho_\infty}\right) 2\pi r \; dr\right)^{1/2} \tag{2.25}$$

$c$ is an adjustable turbulence parameter. Thus, the mixing length turbulence model has two parameters $c$ and $P_{rt}$ to be adjusted according to the experimental results.

In the early work of arc modelling by Swanson and Roidt [21-27], turbulent energy transport was modelled using the Prandtl mixing length theory. However, the behaviour of a turbulent circuit breaker arc was poorly understood. Hermann and Ragaller [46, 52] found that it was necessary to introduce turbulence for $SF_6$ arcs in a duo-nozzle gas-blast circuit breakers. Fang et al. [59] has successfully predicted the critical rate of rise of recovery voltage (RRRV) of $SF_6$ gas-blast arcs with the Prandtl mixing length model. Recently, comparative studies by Kwan [70] and Yan et al. [37] have shown that the $K$-$\varepsilon$ model has no advantage over the Prandtl mixing length model in that one of the five turbulence constants needs to be

adjusted in order to achieve agreement between the predicted and measured radial temperature profiles in a supersonic nozzle [60].

## 2.4 Method for calculating radiation transport

In this section, the three methods of calculating radiation transport (net emission coefficients, partial characteristics and the P1 method) are introduced. Most simulations of arcs have accounted for radiation transport using net emission coefficients, possibly in conjunction with a semi-empirical law for re-absorption at the edge of the arc. Recently, radiation data for two more complex, but potentially more accurate methods – the P1 model and the method of partial characteristics – have become available. With the rapid increase in cheap computing power the use of such models is becoming attractive, if they provide a real improvement in accuracy. These methods for the computation of q have been compared and their merits discussed in terms of the accuracy and the relative computation cost [88]. It is found that all three models give similar radiation distributions with differences as much due to the underlying variation in basic radiation properties as to the methods themselves.

### 2.4.1 Net emission coefficient with re-absorption layer (the NEC method)

The approximate model of Zhang et al. was first used in the modelling of a nitrogen nozzle arc [3]. Subsequently it has been successfully applied to $SF_6$ nozzle arcs [37] and to the modelling of an $SF_6$ auto-expansion circuit breaker [89]. This method assumes a monotonic radial temperature profile. In the region from the axis to the point, $R_e$, at which the temperature is 83% of the axis temperature ($T_a$), q is calculated from the net emission coefficients of [4] as a function of the pressure, temperature and arc radius ($R_a$) defined as the radial position of the 4,000K isotherm. 80% of the radiation flux at $R_e$ is absorbed in the region between $R_e$ and $R_a$. For axial flow dominated $SF_6$ arcs, it has been found that the net emission

coefficient of [4] needs to be multiplied by a factor of 2.5 in order to achieve agreement with experimental results.

### 2.4.2 The method of partial characteristics (the PCM)

This method was devised by Savast'yanenko [90, 91] in 1979 for the calculation of radiation in hot gases where simpler approximations break down. The basic assumption is that in the integration of the equation of radiation transfer the temperature varies linearly between the point of interest and the current point on the integration path. This allows the integration over frequency to be done in advance and the results tabulated.

Radiation intensity, the solution to the radiation transport equation, can be expressed in terms of two special functions [2]. The divergence of radiation flux, $\vec{q}^{\,R}$, can then be written as:

$$\nabla \bullet \vec{q}^{\,R} = \int_0^{4\pi} Som(|X-L|, T_X, T_L)d\Omega - \int_0^{4\pi}\int_X^L \Delta Sim(|X-\xi|, T_X, T_\xi)d\xi d\Omega \tag{2.26}$$

where X is the point of observation, L denotes the plasma edge. Som is given by

$$Som(|X-L|, T_X, T_L) = \int_0^{\infty} B_\nu(X)k_\nu'(X)\exp[-\int_X^L k_\nu'(\eta)d\eta]d\nu \tag{2.27}$$

where $k_\nu'$ is the absorption coefficient including stimulated emission and B(ν) the Planck's function.

$\Delta Sim$ is defined by

$$\Delta Sim(|X-\xi|,T_X,T_\xi)=\int_0^{\infty}(B_\nu(\xi)-B_\nu(X))k_\nu'(X)\times k_\nu'(\xi)\exp\left[-\int_X^{\xi}k_\nu'(\eta)d\eta\right]d\nu \tag{2.28}$$

The approximation introduced by the method of partial characteristics is the assumption of linear temperature distribution between point X and point $\xi$ or L. Thus, *Som* and $\Delta Sim$ can be tabulated and be repeatedly used [2].

### 2.4.3 The 5-band P1 Model

The P1 model has been used in the calculation of radiation transfer since at least 1966 [92]. It has been used for a number of years for the calculation of radiation transfer in industrial CFD simulation particularly in the simulation of combustion systems. In these applications it has assumed that the absorption coefficient is constant, or an effective value is found which is a function of composition and temperature by some averaging technique such as the weighted-sum-of-grey-gases [93]. The approximate solution to the radiation transport equation can be expressed in terms of the zero moment of spectral radiation intensity, G, given by

$$G(\vec{r},\nu)=\int_0^{4\pi}i_\nu(\vec{r},\vec{r}^{\,0})d\Omega \tag{2.29}$$

where $\vec{r}$ and $\vec{r}^{\,0}$ are respectively position and unit vectors. Average absorption coefficients and Planck's function are defined in 5 frequency bands:

$$\overline{K} = (\int_{\nu_1}^{\nu_2} k_\nu^{'}(\nu) B_\nu d\nu) / B,$$
$$B = \int_{\nu_1}^{\nu_2} B_\nu d\nu \tag{2.30}$$

For frequency band $i$ , $G_i$ satisfies

$$\nabla \bullet (\nabla G_i / 3\overline{K}_i) = \overline{K}_i (G_i - 4\pi B_i) \tag{2.31}$$

The net radiation loss is given by

$$\nabla \cdot \vec{q}^R = \sum_{i=1}^{5} \overline{K}_i (4\pi B_i - G_i) \tag{2.32}$$

Marshak boundary condition is usually applied at the solid wall. The average absorption coefficient for the 5-frequency bands was supplied by Gleizes [94].

## 2.5 The finite volume method and the PHOENICS package

### 2.5.1 The finite volume method

The finite volume method is a numerical method for solving partial differential equations that calculates the values of the conserved variables averaged across the volume. Most commercial CFD packages such as Phoenics, CFX and Fluent use the finite volume method. One advantage of the finite volume method over finite difference methods is that it does not require a structured mesh (although a structured mesh can also be used). Furthermore, the finite volume method is preferable to other methods as a result of the fact that boundary conditions can be applied non-invasively. This is true because the values of the conserved variables are located within the volume element, and not at nodes or surfaces. Finite volume

methods are especially powerful on coarse non-uniform grids and in calculations where the mesh moves to track interfaces or shocks.

The numerical algorithm based on this technique can be constructed through the following procedures:

- The geometry (physical boundaries) of the problem is defined.
- The space occupied by the fluid is divided into discrete cells (the mesh).
- Boundary conditions are defined. This involves specifying the fluid behaviour and properties at the boundaries of the problem. For time-varying problems the initial conditions are defined.
- The equations are solved iteratively.
- Analysis or visualisation of the solution.

### 2.5.2 The PHOENICS package

PHOENICS is a general purpose CFD package supplied by CHAM [8]. The governing differential equations are discretized in the finite volume approach and solved by SIMPLE, a solution methodology first developed by Patankar and Spalding [69]. The results given in this thesis are calculated by PHOENICS with appropriate arc models and boundary conditions.

PHOENICS consists mainly of three parts, the pre-processor to specify the problem, the main body to solve the problem and the post-processor to visualize the results. Users can only here access to the Q1 and the GROUND files to generate the suitable grid system and to specify the necessary initial and boundary conditions and the source terms.

The single phase conservation equation solved by PHOENICS can be written as:

$$\frac{\partial(\rho\phi)}{\partial t} + \nabla\cdot\left(\rho\phi\vec{V}\right) - \nabla\cdot\left(\Gamma_\phi\nabla\phi\right) = S_\phi \qquad (2.33)$$

where $\phi$ is the dependent variable to be solved, $\Gamma$ is the diffusion coefficient, and S is the source term. $\phi$ can stand for a variety of different quantities, such as mass

fraction of a chemical species, enthalpy, a velocity component, the turbulence kinetic energy, etc. Accordingly for each of the variables an appropriate meaning will have to be given to the diffusion coefficient, $\Gamma$, and the source term S. Examples of the particular equations are given below.

$\phi = u, v, w$ : *Momentum*

$\Gamma_\phi = \rho(\nu_t + \nu_l) = (\mu_t + \mu_l)$

$S_\phi = -grad(p) + gravity + friction....$

where $\nu = \mu/\rho$ is the kinematic viscosity (turbulent $\nu_t$ and laminar $\nu_l$), ρ the density and μ the viscosity.

$\phi = h$ : *Enthalpy*

$$\Gamma_\phi = \rho\left(\frac{\nu_t}{P_{rt}} + \frac{\nu_l}{P_{rl}}\right) = \frac{(k_t + k_l)}{c_p}$$

$$S_\phi = -\frac{dp}{dt} + heatsources + ....$$

where $P_{rt}$, $P_{rl}$ are the turbulent and laminar Prandtl numbers.

$\phi = 1$ : *Continuity*

$\Gamma_\phi = 0$

$S_\phi = 0 + boundary\ \ sources$

PHOENICS solves a finite volume formulation of these conservation equations. Phoenics uses the method of Patankar and Spalding [69] to solve these equations. This method divides the calculation domain into a number of non-overlapping volumes such that there is one control volume for each grid point. The differential conservation equations are then integrated over each control volume. Piecewise profiles expressing the variation of $\phi$ between the grid points are used to evaluate the required integrals. The result is the discretisation equation containing

the values of $\phi$ for a group of grid points. The conservation of physical quantities (eg. mass, momentum and energy) is exactly satisfied for each control volume.

After integration the finite volume equation has the form:

$$a_P\phi_P = a_N\phi_N + a_S\phi_S + a_E\phi_E + a_W\phi_W + a_H\phi_H + a_L\phi_L + source \quad terms$$

For the grid point P, points E and W (east and west) are its $x$-direction neighbours, N and S (north and south) are the y-direction neighbours, while H and L (high and low for 3-D cases) are the z-direction neighbours.

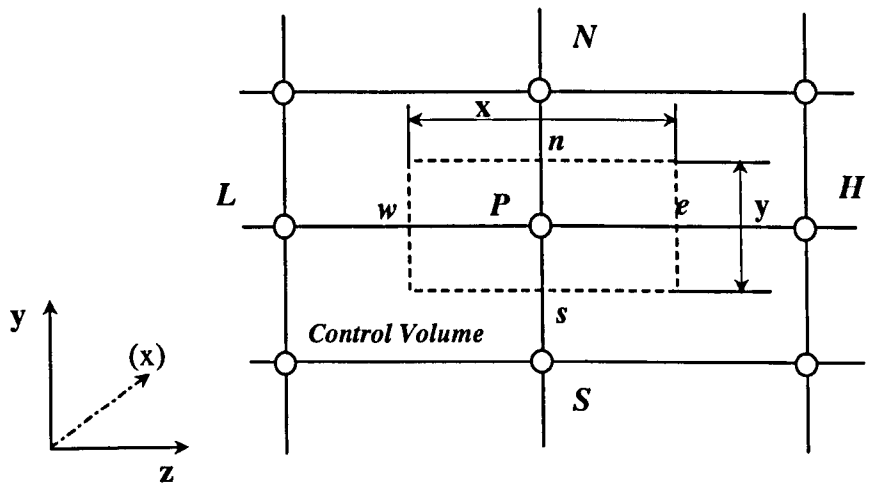


Figure 2.2 Control volume for 2-D cases

## *The Q1 file*

The problem specification is written into a file called the Q1 file which contains all the information needed to simulate a flow. The programming language used is called PIL (PHOENICS Input Language) and is similar in some respects to FORTRAN.

***The GROUND file***

GROUND is a sub-program of EARTH, the program which actually performs the calculations. EARTH will make calls to specific sections in GROUND where it has been instructed to do so in the Q1 file. User specified properties set to GRND indicate that the calculation is performed in the GROUND. For fluid properties the user may need to write the appropriate code to calculate values for the property in all the cells in the PATCH of the current slab if a call to GROUND has been made. The GROUND file can be used for many other purposes as well as for specifying fluid properties and source terms.

***Initial conditions, boundary conditions and source terms***

The differential equations need to be supplemented by boundary conditions before they can be solved. The boundary conditions which define a fluid flow problem usually convey information on how much fluid enters the calculation domain, where it leaves, its incoming temperature, the wall temperature etc. The need for boundary conditions can be demonstrated by integration of the governing equation over the whole volume of the domain of surface $A$:

$$\iiint_V \left[ S - \frac{\partial(\rho\phi)}{\partial t} \right] dV = \iint_A \left[ \rho\vec{v}\phi - \Gamma\nabla\phi \right] dA \qquad (2.34)$$

Therefore the convective and diffusive fluxes must be specified at the domain surface. The PHOENICS default setting takes these fluxes as zero at all boundaries of the calculation domain. For the mass continuity equation the mass flux must be specified as a boundary condition:

$$\frac{\partial}{\partial t}\iiint \rho \; dV + \iint \rho\vec{v} \; dA = 0 \qquad (2.35)$$

The fluid may also have 'internal' boundary conditions or sources which may influence the flow. PHOENICS makes no distinction between boundary conditions and sources.

The finite volume discretisation of the general differential equation yields for each cell, $P$, in the calculation domain the following algebraic equation:

$$a_P\phi_P = \sum(a_i\phi_i) + S_\phi + CT(V - \phi_P) \tag{2.36}$$

where $S_\phi$ is the built-in source and $CT(V\text{-}\phi)$ represents a linearised source term. $C$ is termed the coefficient, $V$ is the value and $T$ is a geometrical multiplier. The units of the source are $[\phi]\cdot kg\cdot s^{-1}$ (where $[\phi]$ is the units of $\phi$) and $T$ is used to convert the source from any given set of units. If the source term is in the energy equation and had units of W/m$^3$ (heat generated per unit volume) then the geometric multiplier, $T$, would be volume.

In PHOENICS boundary conditions and sources are specified in the Q1 file by the commands PATCH and COVAL. PATCH conveys the information of the location of the boundary condition/source term and COVAL gives the Coefficient and VALue of the linearised source. Their syntax is given in documentation for PHOENICS [8].

# Chapter 3
# Swirling Flow and Its Influence on High Current DC Arc

## 3.1 Introduction

Swirl is used extensively in combustion chambers and industrial furnaces as a means of controlling flame size, shape, stability, and combustion intensity [104]. Recently circuit breakers have been added rotary arc breaking mechanism into self-pressurisation mechanism that is developed to save operating power and improve current interruption ability. Based on these considerations, a hybrid circuit breaker has been developed. In this type of circuit breakers, an arc is normally drawn between two hollow contacts during the current interruption period. The arcing process can be characterised by two possible regimes. At low current level, the arc is relatively thin and operates in an unstable mode. The magnetic field produced by the coil current interacts with the arc current and generates a Lorentz force. As a consequence, the arc column is bent and the root of the arc moves over the contact surface in an unpredictable manner. In the second regime, the arc current is sufficiently high so that the radial dimension of the arc column is comparable to the internal diameter of the hollow contacts. In this case, the arc column can be approximated as being axisymmetrical. In contrast to puffer or auto-expansion breakers, the Lorentz force has an azimuthal component, which produces an axisymmetric swirling flow.

The work in this chapter is to study the effects of swirling flow on high current DC arcs. To maintain a steady state arc in the device shown in Figure 3.1, the contact gap length is fixed and gas has to be introduced through the inlet. The strength of swirling is controlled by the current in the coil and that in the arc. Arc behaviour with different strengths of swirling is investigated and is compared with a similar arc for which swirling flow is ignored. Suitable conclusions are then drawn.

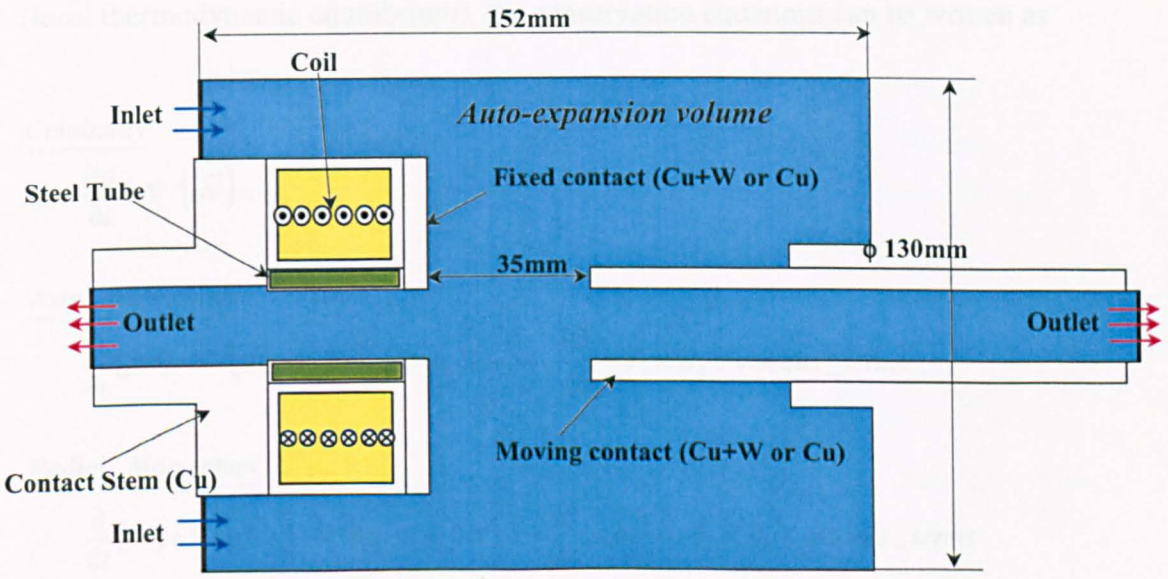


**Figure 3.1** Schematic diagram of a hybrid circuit breaker. The fixed hollow contact is cathode and the "moving contact" (no movement in the present work) is anode.

## 3.2 Swirling Arc Model

### 3.2.1 Governing equations

The governing equations for circuit breaker arcs without swirling flow have been described in [3]. The presence of swirling flow adds a source term to the radial momentum equation and hence alters the pressure field. The Lorentz force in the azimuthal direction is generated by the magnetic field and electric current density in the r-z plane of a cylindrical polar co-ordinate system. Assuming LTE (local thermodynamic equilibrium), the conservation equations can be written as

*Continuity*

$$\frac{\partial \rho}{\partial t} + \nabla \cdot \left(\rho \vec{V}\right) = 0$$

*Axial Momentum*

$$\frac{\partial}{\partial t}(\rho w) + \nabla \cdot \left(\rho \vec{V} w\right) - \nabla \cdot [(\mu_l + \mu_t)\nabla w] = -\frac{\partial P}{\partial z} + J_r \times B_\theta + viscous\_terms$$

*Radial Momentum*

$$\frac{\partial}{\partial t}(\rho v) + \nabla \cdot \left(\rho \vec{V} v\right) - \nabla \cdot [(\mu_l + \mu_t)\nabla v] = -\frac{\partial P}{\partial r} + \rho \frac{u^2}{r} - J_z \times B_\theta + viscous\_terms$$

(3.1)

*Azimuthal Momentum*

$$\frac{\partial}{\partial t}(\rho u) + \nabla \cdot \left(\rho \vec{V} u\right) - \nabla \cdot [(\mu_l + \mu_t)\nabla u] = -\rho \frac{vu}{r} + \left(J_r \times B_z + J_z \times B_r\right) + viscous\_terms$$

*Enthalpy*

$$\frac{\partial}{\partial t}(\rho h) + \nabla \cdot \left(\rho \vec{V} h\right) - \nabla \cdot \left[\frac{(k_l + k_t)}{c_p}\nabla u\right] = \sigma E^2 + q + \frac{dP}{dt} + viscous\_terms$$

*Equation of State*

$$\rho = f(p, h)$$

where ρ, h and p are respectively the density, enthalpy and pressure, $\mu_l$ the molecular viscosity, $\mu_t$ the turbulent eddy viscosity, $k_l$ the molecular thermal conductivity, $k_t$ the turbulent thermal conductivity, $c_p$ the specific heat of $SF_6$ at constant pressure, E the electric field and σ is the electrical conductivity. $\vec{V}$ is the velocity vector. The three momentum equations are written explicitly for the axial velocity, w, the azimuthal velocity, u and the radial velocity, v. For the interrupter shown in Figure 3.1, the flow is found to be turbulent [1]. The equation of the state and the transport properties as a function of enthalpy and pressure are given for $SF_6$ by Frost and Liebermann [105].

### 3.2.2 Electric field calculation

The current density and the electric field are calculated from the current continuity equation, which is expressed in terms of electrical potential

$$\nabla \cdot (\sigma \nabla \phi) = 0 \tag{3.2}$$

where $\phi$ is the electrical potential. Appropriate boundary conditions need to be prescribed for the solution of the above equation.

A schematic diagram of the boundary conditions and material properties used in calculating the electric potential is shown in Figure 3.2. The boundary conditions for this equation are as follows. Axisymmetric condition is set on the axis at r = 0 and we set $\partial\phi/\partial n = 0$, where n is the normal, at all outside non-conducting boundaries apart from the calculation domain of flow field. On the cathode, we set $\phi = 0$. The potential on the anode should be adjusted until the specified current flows between the contacts. However we use the following alternative scheme. The equation for conservation of current (3.2) is solved with the potential at one contact fixed at 0V and the potential on the other at an arbitrary fixed value, say 5V. From the resulting potential field we calculate the electric and total current which would result from a 5V potential difference which we denote as $I_{5V}$. The potential and

electric field with specified instantaneous current can then be found by multiplying those obtained at 5V by $I_s/I_{5V}$ where $I_s$ is the specified current. The electrical conductivity in the SF6 gas is found from tabulated values. For the non-conducting part of the gas, outside of the arc, the electrical conductivity is set to a small value ($10^{-3}\Omega^{-1}m^{-1}$). The electrical conductivity in both electrodes is set to a high value ($10^{5}\Omega^{-1}m^{-1}$).

Current collection at the hollow contacts is through the introduction of transparent contacts [9]. Right in front of the cathode, there is a space charge sheath. Electrons are emitted from the cathode surface and ions from the arc plasma side hit the surface being neutralized on cathode surface. The mechanisms for the formation of cathode spots, which are also dependent on the surface conditions, are not fully understood. For arcs in gas flow, the arc voltage is dominated by the arc column. A simplified approach, a transparent electrode [9], which has been proven successful, will therefore be adopted here. The virtual arc root is replaced by a cathode spot to the flow at a fixed position inside the hollow electrode. The presence of such a transparent electrode ensures the collection of the electric current and axisymmetry. They have no blockage to gas flow. The transparent contact filling the left hollow contact in Figure 3.1 is the cathode. The effective area of the cathode spot is approximated by defining a circular conducting spot at the centre of the transparent contact tip. Its radius is given by

$$R_c = \sqrt{\frac{I}{\pi J_c}} \tag{3.3}$$

where I is the current and $J_c = 10^8$ A/m$^2$ is the current density in the cathode spot [100]. The remaining part of the cathode surface is assumed to be non-conducting. Special care must be taken with calculation of the electric field and current density from the electrostatic potential or incorrect values will result at positions with abrupt changes in electrical conductivity.

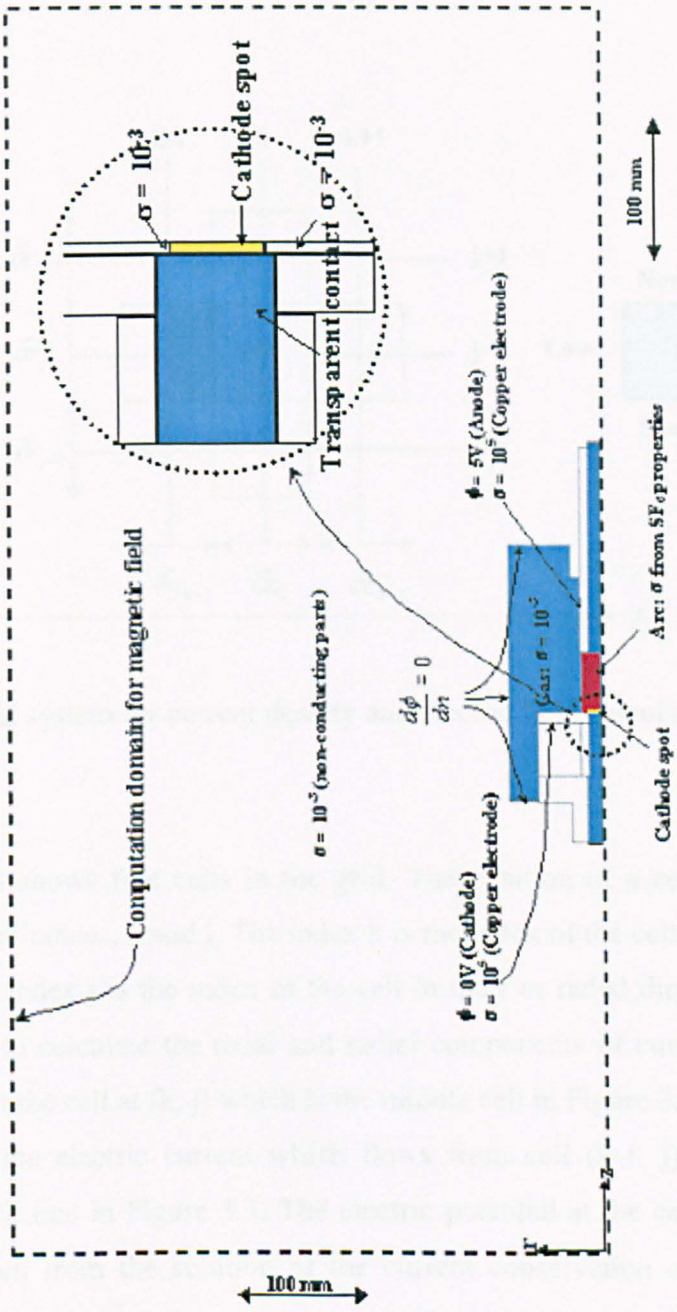


**Figure 3.2** Schematic diagram showing the boundary conditions and the material properties used calculation of the electric potential in a hybrid circuit breaker.

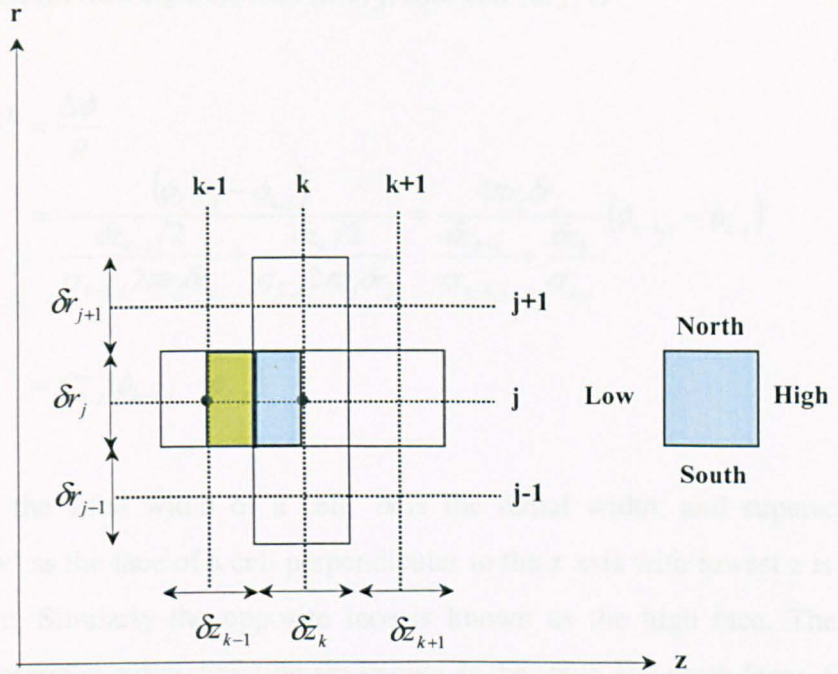


**Figure 3.3** Grid system for current density and electric field calculation.

Figure 3.3 shows five cells in the grid. The position of a cell in the grid is denoted by two indices, k and j. The index k is the index of the cell in the z or axial direction. The index j is the index of the cell in the r or radial direction. We shall consider how to calculate the axial and radial components of current density and electric field in the cell at (k, j) which is the middle cell in Figure 3.3.

Consider the electric current which flows from cell (k-1, j) into cell (k, j) across the thick line in Figure 3.3. The electric potential at the centres of the two cells are known from the solution of the current conservation equation and are denoted by $\phi_{k-1,j}$ and $\phi_{k,j}$. To find the current we consider the two shaded regions in Figure 3.3 to be a pair of series resistors. The resistance of a resistor is given by

$$R = \frac{l}{\sigma A} \tag{3.4}$$

where $A$ is the cross-sectional area of the resistor and $l$ is the length of the resistor. Hence the current flowing from cell (k-1, j) into cell (k, j) is

$$\begin{aligned} I^L &= \frac{\Delta\phi}{R} \\ &= \frac{\left(\phi_{k-1,j}-\phi_{k,j}\right)}{\dfrac{\delta z_{k-1}/2}{\sigma_{k-1,j}2\pi r_j\delta r_j}+\dfrac{\delta z_k/2}{\sigma_{k,j}2\pi r_j\delta r_j}} = \frac{4\pi r_j\delta r_j}{\dfrac{\delta z_{k-1}}{\sigma_{k-1,j}}+\dfrac{\delta z_k}{\sigma_{k,j}}}\left(\phi_{k-1,j}-\phi_{k,j}\right) \\ &= C^L_{k,j}\left(\phi_{k-1,j}-\phi_{k,j}\right) \end{aligned} \tag{3.5}$$

where $\delta z$ is the axial width of a cell, $\delta r$ is the radial width, and superscript L denotes 'low' as the face of a cell perpendicular to the z axis with lowest z is called the low face. Similarly the opposite face is known as the high face. The faces perpendicular to the radial direction are known as the south and north faces. Similar equations for the other three faces of the cell are found,

$$I^H = \frac{4\pi r_j\delta r_j}{\dfrac{\delta z_k}{\sigma_{k,j}}+\dfrac{\delta z_{k+1}}{\sigma_{k+1,j}}}\left(\phi_{k,j}-\phi_{k+1,j}\right) = C^H_{k,j}\left(\phi_{k,j}-\phi_{k+1,j}\right) \tag{3.6}$$

$$I^S = \frac{4\pi\delta z_k}{\dfrac{\delta r_{j-1}}{r_{j-1}\sigma_{k,j-1}}+\dfrac{\delta r_j}{r_j\sigma_{k,j}}}\left(\phi_{k,j-1}-\phi_{k,j}\right) = C^S_{k,j}\left(\phi_{k,j-1}-\phi_{k,j}\right) \tag{3.7}$$

$$I^N = \frac{4\pi\delta z_k}{\dfrac{\delta r_j}{r_j\sigma_{k,j}}+\dfrac{\delta r_{j+1}}{r_{j+1}\sigma_{k,j+1}}}\left(\phi_{k,j}-\phi_{k,j+1}\right) = C^N_{k,j}\left(\phi_{k,j}-\phi_{k,j+1}\right) \tag{3.8}$$

The components of the current density and electric field are calculated from equations (3.4), (3.5), (3.6), (3.7) and (3.8). The z component of current in the cell

is taken as $I = (I^H + I^L)/2$, which $j_z$ is calculated. For the z component of electric field we have $E = \Delta V/\delta z_k$ where $\Delta V = IR$ giving

$$E_z = \frac{I^H + I^L}{4\pi r_j \delta r_j \sigma_{k,j}} \tag{3.9}$$

and similarly for the radial direction

$$E_r = \frac{I^N + I^S}{4\pi r_j \delta z_k \sigma_{k,j}} \tag{3.10}$$

The resulting values of $E_z$ and $E_r$ are used to calculate the Ohmic heating.

### 3.2.3 Magnetic field calculation

The magnetic field in this device will have radial (r-) and axial (z-) components produced by an external coil with current flowing in azimuthal direction and an azimuthal (θ-) component caused by the axisymmetrical arc itself. For an axisymmetric arc, the azimuthal magnetic flux density is given by

$$\oint H \cdot dl = \int J \cdot dS \tag{3.11}$$

where H is the magnetic field strength and J is current density.

The magnetic field produced by the coil and that by the arcing current are shown in Figure 3.4. As the contacts separate, an arc appears between the two contacts. The current I is flowing into the arc that produces $B_\theta$. The influence of the arc on the magnetic field is two folds: the magnetic field produced by the arc current and that due to the eddy current induced within the arc. The magnetic field produced by the eddy current in the arc is negligible in comparison with that produced by the excitation current without the arc because the field variations are

low frequency. Thus, the modification to the magnetic field produced by the arc itself can be calculated by

$$B_\theta = \mu_0 \int_0^r 2\pi\xi J_z d\xi \Big/ 2\pi r \tag{3.12}$$

where $J_z$ is the axial component of current density and $\mu_0$ is the permeability of free space.

The magnetic field produced by the coil is calculated from a vector potential $\vec{A}$, $\vec{B} = \nabla \times \vec{A}$. The current in the coil flows in the azimuthal direction. The vector potential has only an azimuthal component ($A_\theta$). The equations for the calculation of $A_\theta$ can be summarised as

$$\nabla^2 A_\theta = \left\{ \begin{array}{ll} -\nu j_s & in\ the\ coil \\ \nu\sigma \dfrac{\partial A_\theta}{\partial t} & in\ other\ conducting\ parts \\ 0 & in\ non-conducting\ parts \end{array} \right\} \tag{3.13}$$

where $j_s$ is the excitation current density in the coil and $\nu$ the permeability. In other conducting parts the currents are purely induced by the changing magnetic fields (eddy current), while in gas there is no current flowing. The total magnetic field is therefore the superposition of that produced by the coil without the arc and that given by (3.12). Since magnetic field estimates even slower than electrical field, the solution domain for magnetic field is considerably larger than that for the electrical potential. The solution domain for the magnetic is shown in Figure 3.2. Equation (3.12) and (3.13) are simultaneously solved with the arc conservation equations.

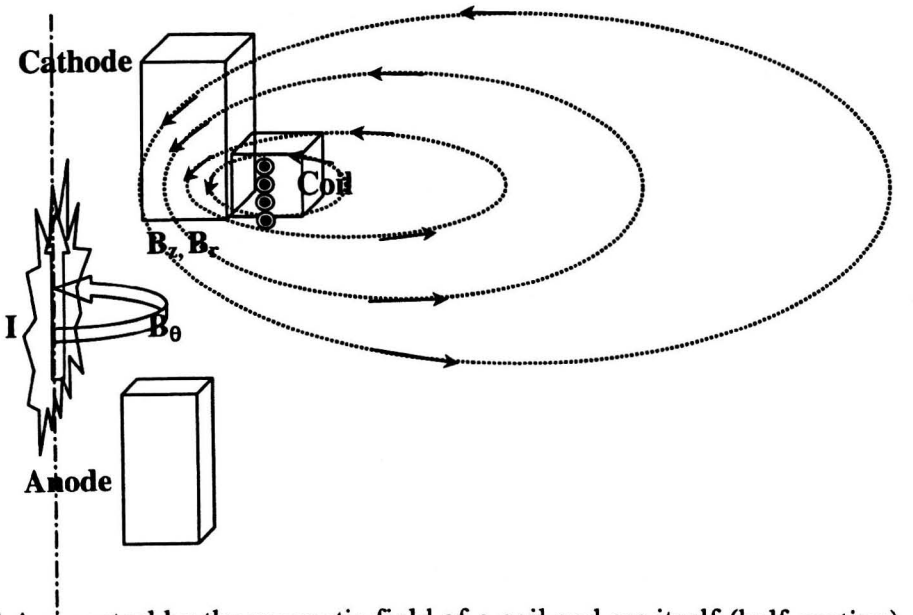


**Figure 3.4** Arc control by the magnetic field of a coil and arc itself (half-section)

### 3.2.4 Radiation and turbulence model

In the energy conservation equation, q represents the net radiation loss (per unit volume and time). The calculation of q involves the solution of radiation transport equation for the whole arc volume (thus three dimensional) in the spectra region relevant to SF6 arc plasma. For a temperature range from 10,000K to 30,000K, the spectra ranging from infrared to vacuum ultra violet are dominated by the a few hundreds lines [2]. The computational cost for such an approach is prohibitively high. Several approximate methods for radiation transport, the partial characteristics [2][88] and P1 [64][88], and the net emission coefficients [3][4], have been proposed. Recently, a comparative study of these three radiation transport models has been carried out [88], which shows that for arcs in strong gas flow, the approximate radiation transport model of Zhang et al. is remarkably successful in predicting the correct temperature. Of the three approximate radiation transport models, the method of Zhang et al. is most economical in terms of computation cost. We therefore adopt the approximate model of Zhang et al. [3] to obtain q. This model assumes a monotonic radial temperature profile. The

maximum temperature is on the axis and is denoted by $T_{max}$. The arc core is defined as the region from the axis to the radial position of the $0.83T_{max}$ isotherm. In the arc core, q is a function of temperature, pressure, and arc radius, which is defined as the radial distance from the axis to 2000K isotherm. q is then calculated for the arc core from the net emission coefficient, ε(T, p, r), as given by Liebermann and Lowke [4]. Radiation from the arc core is partly absorbed in the region between the core edge and 2000K isotherm. This region is also called the re-absorption region. In the calculation for the simulation of the duo-flow hybrid circuit breaker with a peak current of 5kA, it is assumed that on average 80% of the radiation from the arc core is re-absorbed in the re-absorption region.

The portion of the radiation at the edge of the arc core to be reabsorbed is not known precisely. The percentage of the radiation absorbed is therefore computationally investigated in the range from 40% to 80% in Chapter 4.

$SF_6$ arcs in gas flow are almost always turbulent. There has been very little work on the characteristics of arc turbulence. At present the modelling of arc turbulence follows similar lines as those adopted in fluid mechanics. The comparative studies of two most often used turbulence models (the K-ε model and Prandtl mixing length model) by Yan et al. indicate that the Prandtl's mixing length model is sufficiently accurate to describe the turbulent arc plasmas. The calculation of the turbulent viscosity and thermal conductivity in equation (3.1) is therefore based on the Prandtl mixing length.

Following Lilley [101], we assume isotropic turbulence. The turbulent viscosity in the presence of swirling flow is given by

$$\mu_t = \rho l_m^2 \left\{ \left( \frac{\partial w}{\partial r} \right)^2 + \left[ r \frac{\partial}{\partial r} \left( \frac{u}{r} \right) \right]^2 \right\}^{1/2} \tag{3.14}$$

where the mixing length, $l_m$, is chosen as equation (2.24) with $\delta$ being the arc's thermal radius (equation (2.25)) which is defined as the radial distance from the axis to the position of 4,000K isotherm. The choice of 4000K is to ensure that the definition of $\delta$ is sensible when the gas temperature in the expansion volume increases during the high current phase as result of arc heating. $c$ in equation (2.24) is a turbulence parameter, the value of which is to be adjusted according to

experimental results. It must be made clear that thermal recovery of residual plasma mainly depends on turbulent cooling after current zero in a circuit breaker. At least one test result of the critical RRRV is required to calibrate the turbulence model for a particular geometry.

The turbulence enhanced thermal conductivity, $k_t$, is related to the turbulent viscosity through the turbulent Prandtl number in equation (2.22). It has been found that for turbulent arcs the turbulent Prandtl number can be assumed to be unity [59]. Thus, the parameter $c$ in equation (2.24) needs to be adjusted.

### 3.2.5 Boundary conditions

Axisymmetry is imposed on the axis of the interrupter for all variables solved by (3.1), (3.2) and (3.13). For the present arrangement, the stagnation pressure at the inlet is fixed at 3.5 bar and the static pressure at the outlet fixed at 2.0 bar. Heat flux to the walls is set at zero. Energy loss by thermal conduction at electrode surface is not taken into account because of its negligible effects on the arc behaviour. Radiation reaching the confining wall of the interrupter is assumed to be permanently lost.

The electrical potential of one of the hollow contacts is fixed to zero and that of the other is adjusted so that solution to (3.2) gives the specified arc current. The gradient of the electrical potential is set to zero along the outer boundary of the flow field.

The axis condition for the vector potential is $A_\theta = 0$. This can be understood from the fact that $B = \nabla \times A$ must remain finite on the axis. In the current case this equation reduces to

$$B = \nabla \times A = \frac{\partial A_\theta}{\partial r} + \frac{A_\theta}{r} \tag{3.15}$$

and hence $A_\theta$ must vanish on the axis. Chen and Turner [106] set $A_\theta$ to zero on the other boundaries and it is ensured that the boundaries for $A_\theta$ are far enough away from the area of interest so that this condition has negligible effect on the solution.

They do this by comparing numerical results with an analytical formula for a solenoid. They find that the boundary conditions have no influence as long as the radial extent of the domain is greater than five solenoid radii and the axial extent is greater than four solenoid lengths. To allow for the inclusion of materials with a very high value of relative permeability, $\mu_s$ such as steel, internal boundaries are set around the areas containing the material. These conditions can be found from the magnetic interface conditions [107]. The conditions are that at a boundary between two materials the normal component of B is continuous and the tangential component of H is continuous. Using the second of these we find that at an interface

$$\frac{1}{\mu_1}\frac{\partial A}{\partial n}\bigg|_1 = \frac{1}{\mu_2}\frac{\partial A}{\partial n}\bigg|_2 \tag{3.16}$$

so that if $\mu_2$ is very large this reduces to

$$\frac{\partial A}{\partial n}\bigg|_1 = 0. \tag{3.17}$$

This is a zero-flux boundary condition for A.

### 3.3 Results and discussions

Solution to the governing equations is obtained by implementing the arc model into a commercial computational fluid dynamics (CFD) package, PHOENICS [8]. The gap length between the cathode and the anode is 35mm and the internal diameter of hollow contacts is 18mm. Two typical cases were first studied in order to gain knowledge of the effects of swirling flow. The arc current used in both cases is 5kA. The magnetic field induced by the coil is zero in the first case, which means there is no swirling flow. In the second case, the excitation current of the coil is 5kA.

Axial and radial components of magnetic field are produced by the azimuthal current flowing in the coil and also the azimuthal eddy currents which flow in the copper parts and in the arc. These components of the magnetic field are calculated

from the vector potential. It can be seen that the axial field in the area occupied by the arc is significantly larger than the radial component as shown in Figure 3.5.

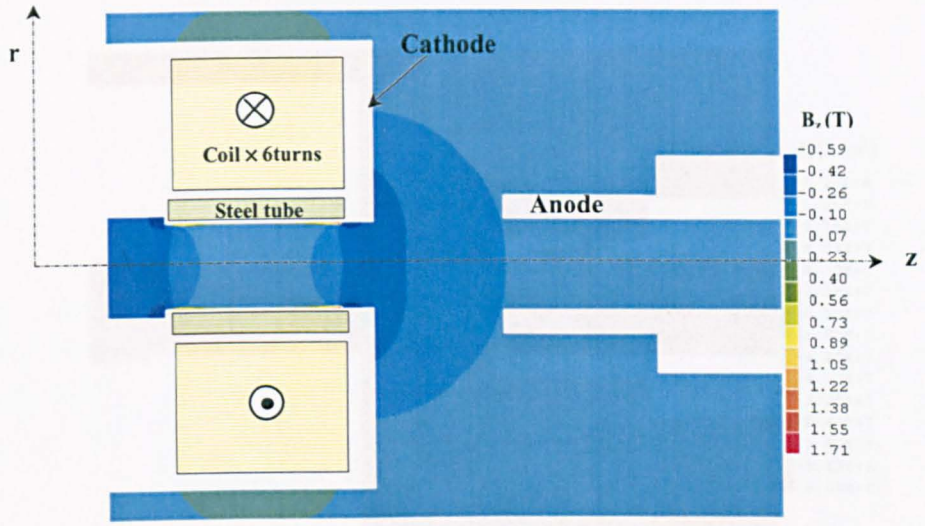


(a)

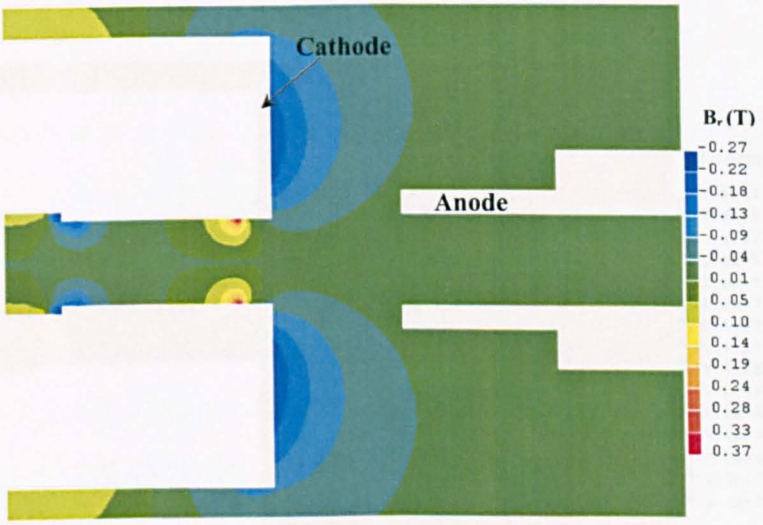


(b)

**Figure 3.5** Magnetic flux (axial magnetic flux $B_z$, radial magnetic flux $B_r$) at the arc current of 5kA. The excitation current of the coil is also 5kA.

Figure 3.6 shows axial and radial components of current density. At the cathode the value of the axial current density takes on the prescribed density of $1\times10^8$ A/m$^2$. The radial component of the current density changes sign near the two electrodes. This is because the arc is slightly fatter in the middle than at the ends,

so that the current spreads at one end, giving a positive radial current density, while converges at the other end giving a negative radial component of current density.

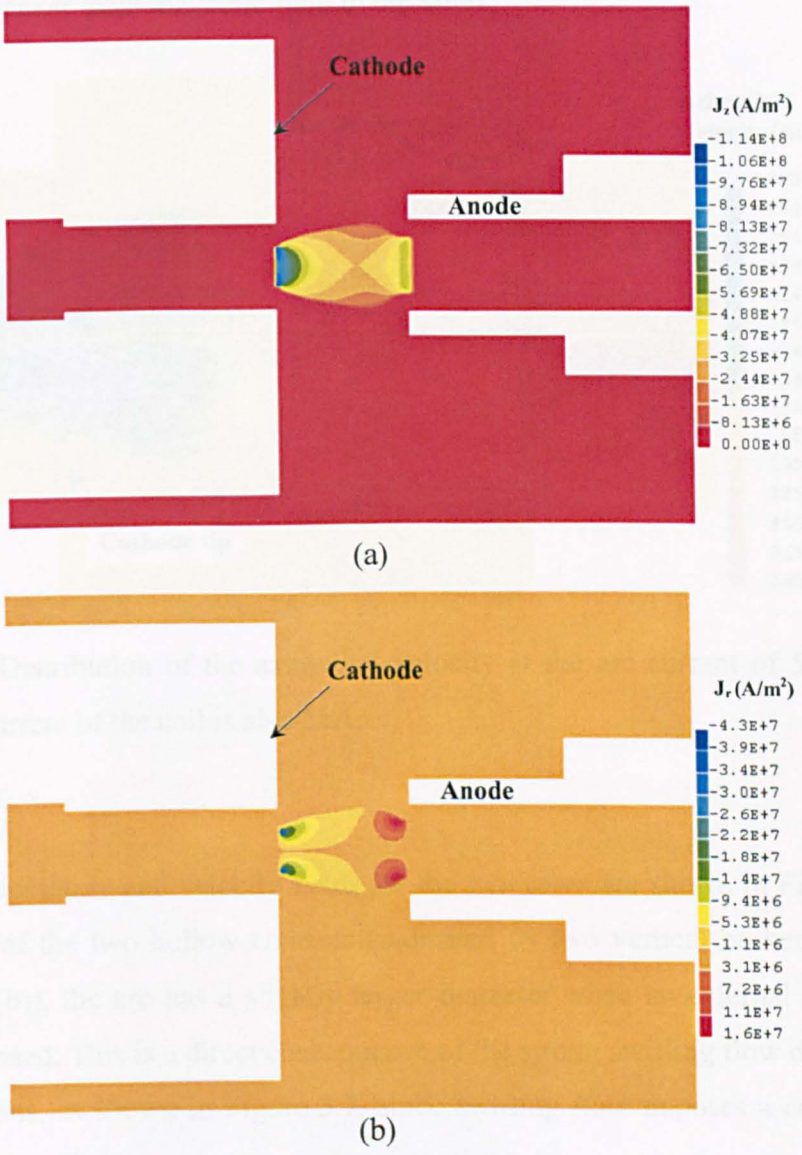


**Figure 3.6** Current density (axial current density $\mathbf{J}_z$, radial current density $\mathbf{J}_r$,) at the arc current of 5kA.

Results in Figure 3.7 show that gas swirls in opposite directions in regions close to the two contacts. This is closely related to the shape of the arc column. With the arrangement used in the present work, azimuthal Lorentz force generated by the radial current density and axial magnetic field is dominant. As shown in

Figure 3.6 (b), the radial current density changes its sign near the contact tips, which results in opposite Lorentz force in the azimuthal direction. Swirling in the region close to the cathode is stronger than that in the region close to the anode because of weaker axial magnetic field in the latter.

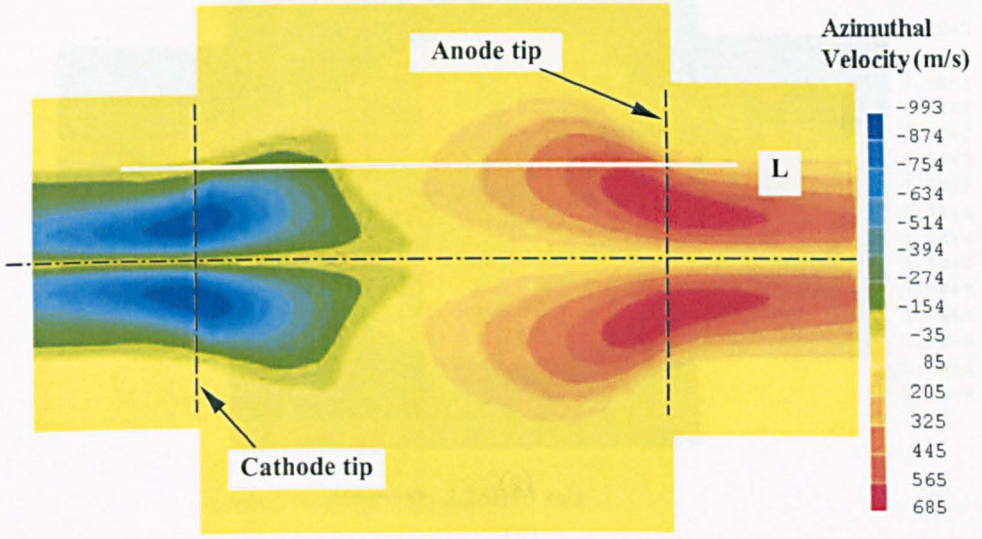


**Figure 3.7** Distribution of the azimuthal velocity at the arc current of 5kA. The excitation current of the coil is also 5kA.

The temperature and velocity fields for the two cases are shown in Figure 3.8. At the tips of the two hollow contacts (indicated by two vertical broken lines in Figure 3.8 (b)), the arc has a slightly larger diameter when an external magnetic field is imposed. This is a direct consequence of the strong swirling flow developed in two regions, as shown in Figure 3.7, since swirling flow imposes a centrifugal force on the arc plasma.

In the absence of swirling flow, magnetic pinch results in a stagnation point on the axis, as shown in Figures 3.8 (a) and 3.9 (solid line). The swirling flow reduces the axis pressure (broken line in Figure 3.9). As a result the stagnation point shifts in the direction of the positive axis as shown in Figure 3.10.

The pressure around the arc column is higher in the case with swirling flow. Under the fixed stagnation pressure condition at the inlet, this implies a reduction in the mass exhausted through the two exits. This reduction in mass flow rate is

expected to be more profound at higher current. The predicted arc voltage at 5kA is 142V in the presence of swirling flow, which is slightly lower than the value of 144V in the absence of swirling flow.

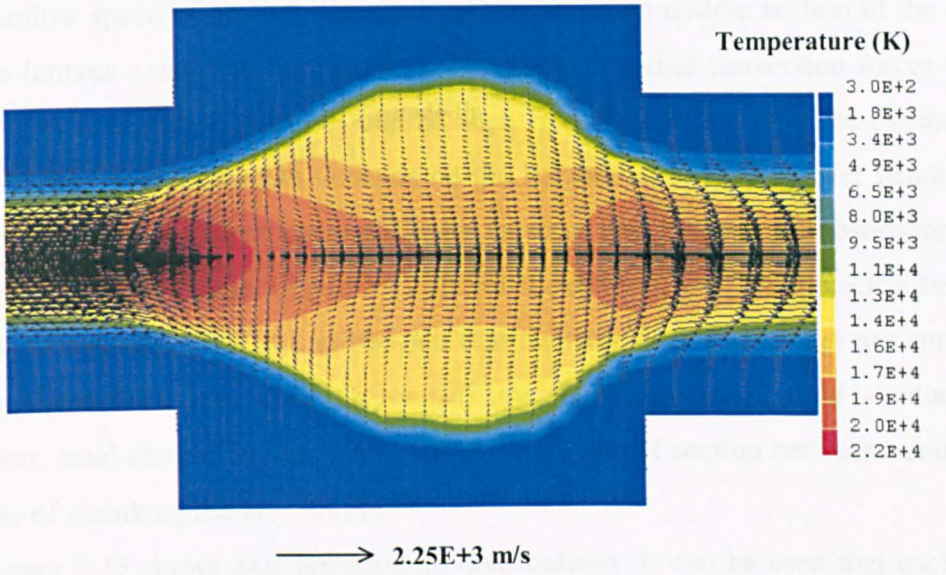


(a)

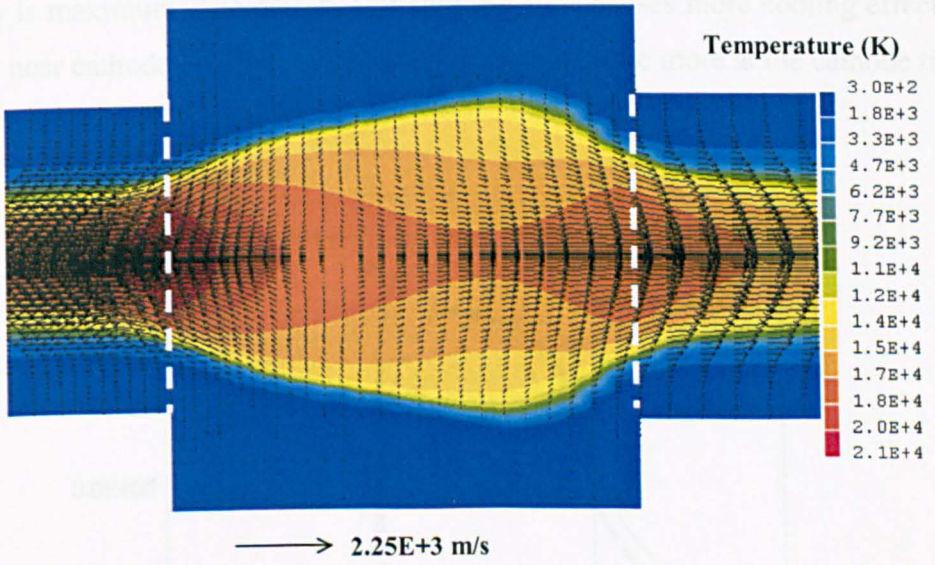


(b)

**Figure 3.8** Temperature distribution of $SF_6$ gas inside the arcing chamber at 5kA. (a) without swirling flow; (b) with swirling flow and the coil current is 5kA.

The modified pressure field with the presence of swirling flow reduces the radial inflow speed into the arc column at the axial locations corresponding to the tips of the two hollow contacts. This is clearly shown in Figure 3.11. However, the radial inflow speed of gas into the arc is enhanced at the middle section of the arc column (curves e and f in Figure 3.11). The stronger radial convection forces the arc column to shrink slightly, as can be seen from Figure 3.8 (b). The extent to which the arc column shrinks depends on the balance of energy transfer resulting from convection, turbulent cooling, Ohmic heating and radiation re-absorption at the arc edge. Furthermore, Figure 3.12 shows the difference of axial electric fields due to the swirling flow. It can be seen that swirling flow causes the arc spread more in the radial direction at both contacts tips, thus axial electric field is reduced. However, axial electric field is increased at the middle of section between contacts because of shrinking the arc column.

Figure 3.13 shows axis temperature distributions. It can be seen that each of the profiles exhibits a maximum temperature near the cathode tip where the current density is maximum. The presence of swirling flow causes more cooling effects to the arc near cathode tip, thereby reducing the temperature more at the cathode tip.

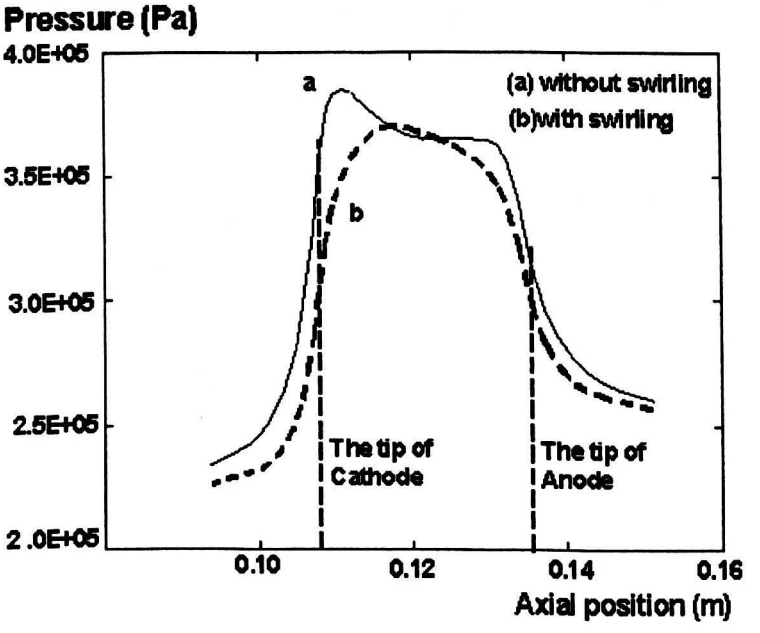


**Figure 3.9** Axis pressure distributions at an arc current of 5kA. The excitation current of the coil is also 5kA for curve b.

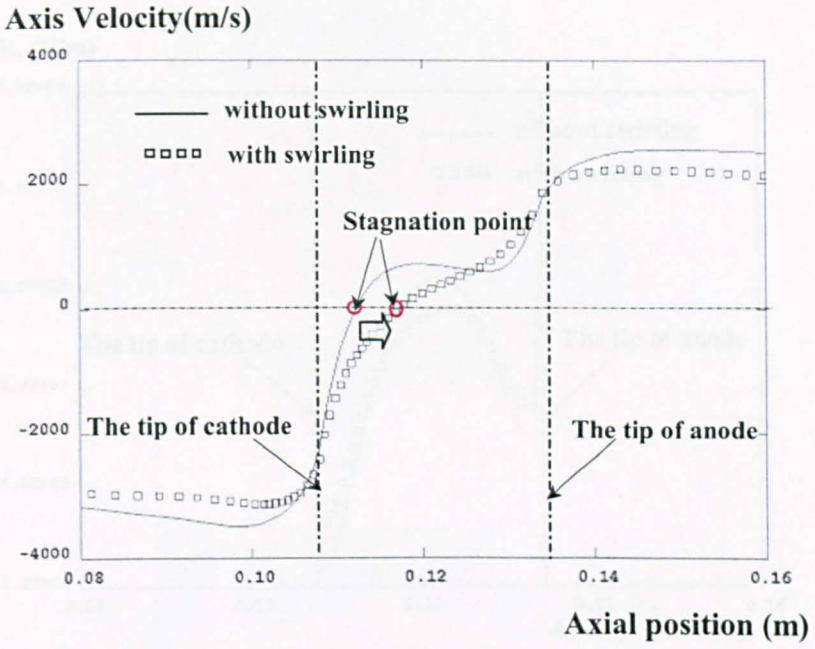


**Figure 3.10** Axis velocity at an arc current of 5kA. The excitation current of the coil is also 5kA for curve b.

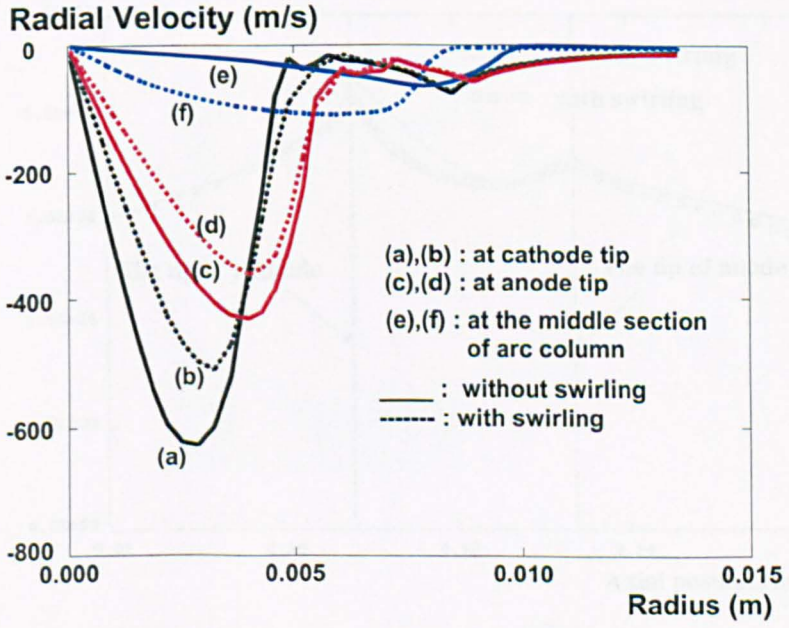


**Figure 3.11** Radial velocity field distributions between contacts at 5kA.

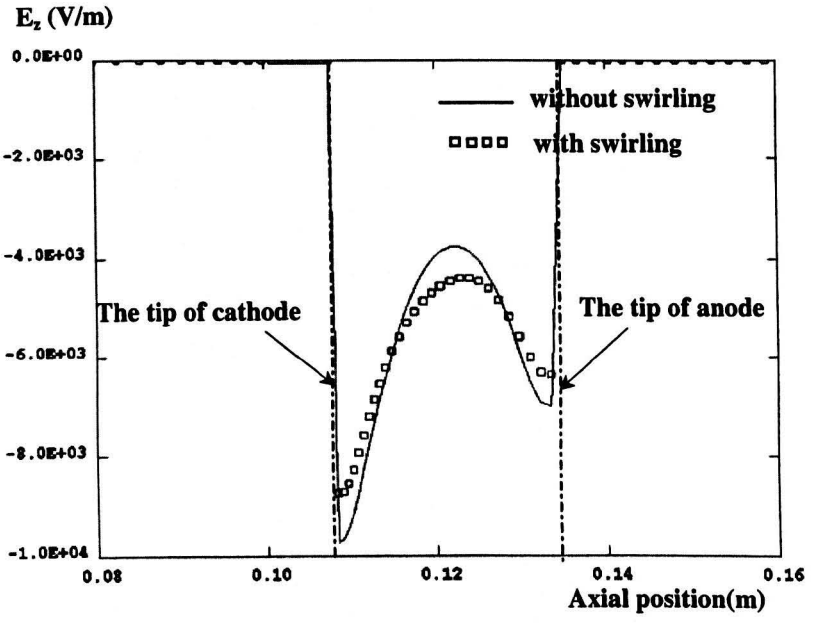


**Figure 3.12** Electric field on the axis at an arc current of 5kA. The excitation current of the coil is also 5kA for curve b.

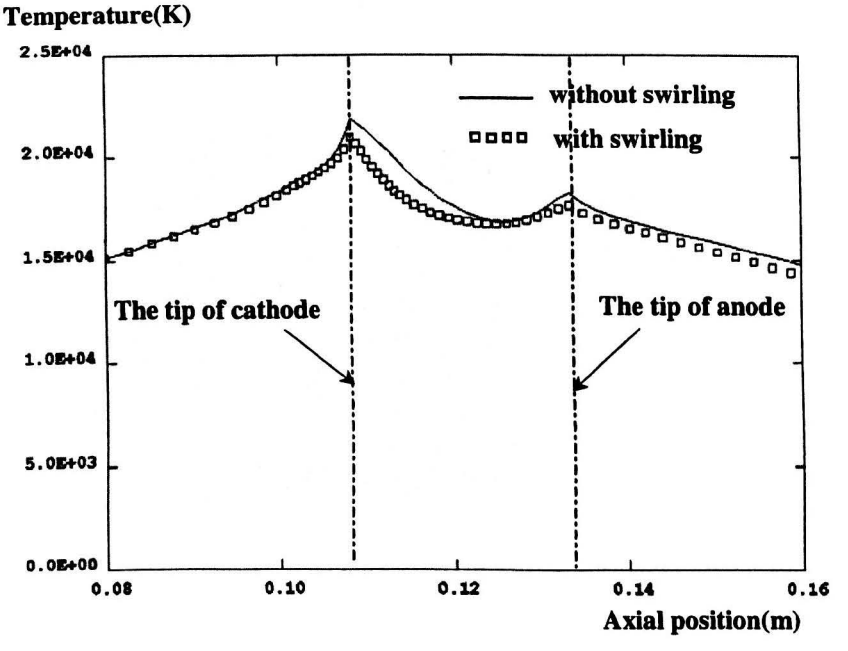


**Figure 3.13** Axis temperature distributions at an arc current of 5kA.

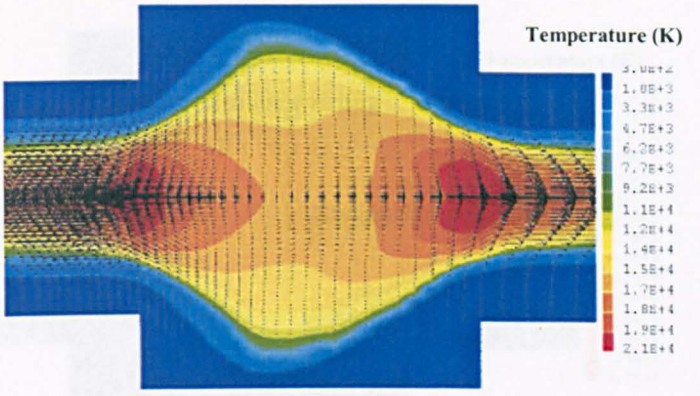


(a) arc current: 5000A / *coil current: 3000A*

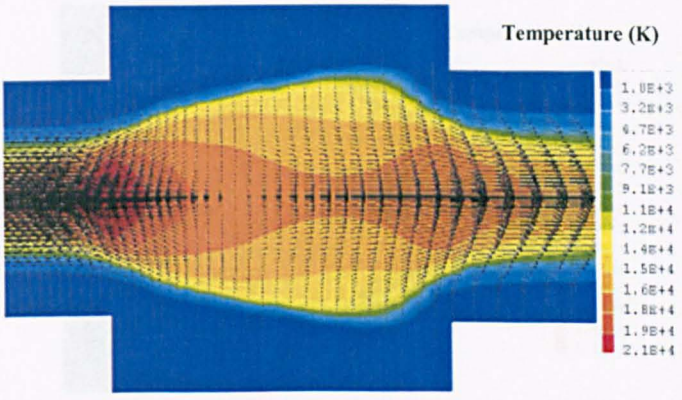


(b) arc current: 5000A / *coil current: 5000A*

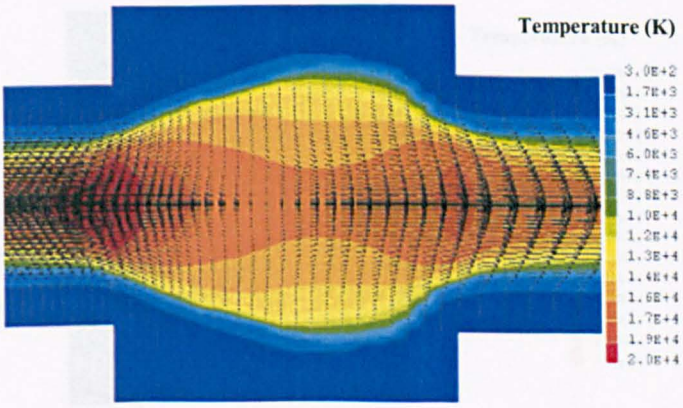


(c) arc current: 5000A / *coil current: 7000A*

**Figure 3.14** Temperature distributions of $SF_6$ gas inside the arcing chamber for three different coil currents.

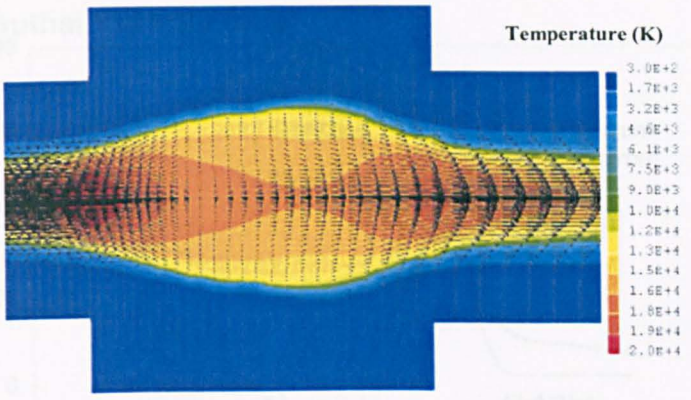


(a) *arc current: 3000A* / coil current: 5000A

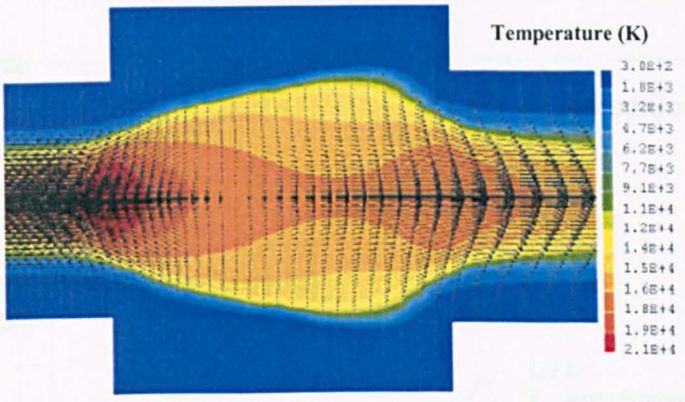


(b) *arc current: 5000A* / coil current: 5000A

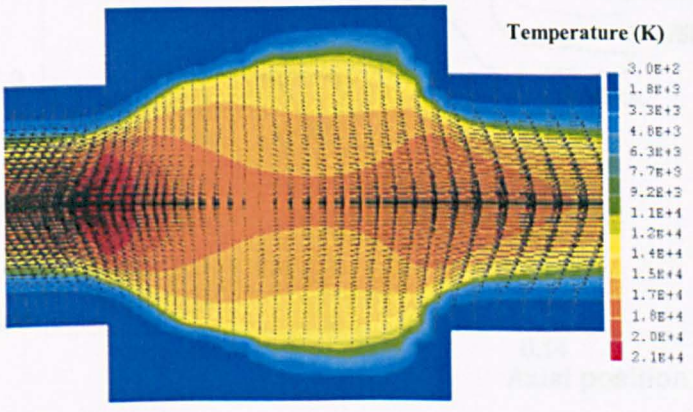


(c) *arc current: 7000A* / coil current: 5000A

**Figure 3.15** Temperature distribution of $SF_6$ gas inside the arcing chamber for three different arc currents.

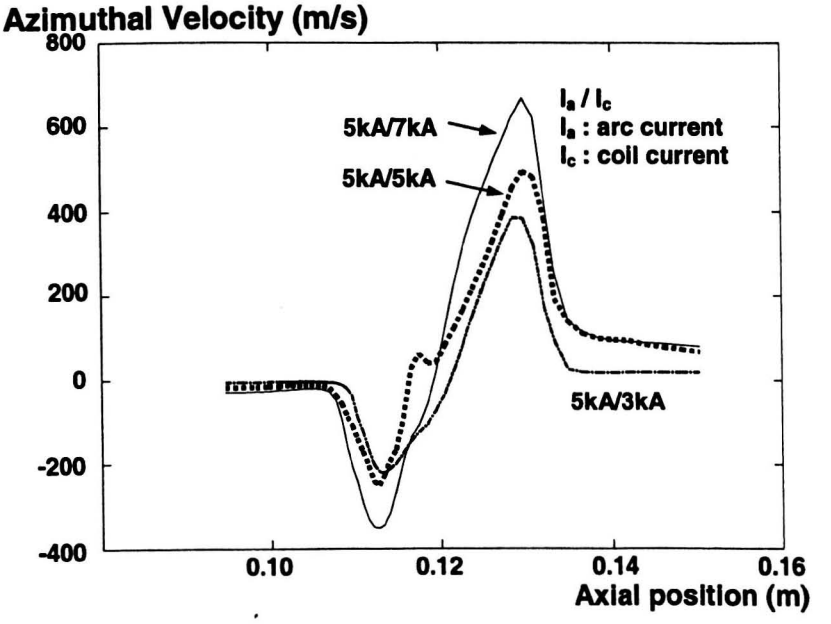


(a)

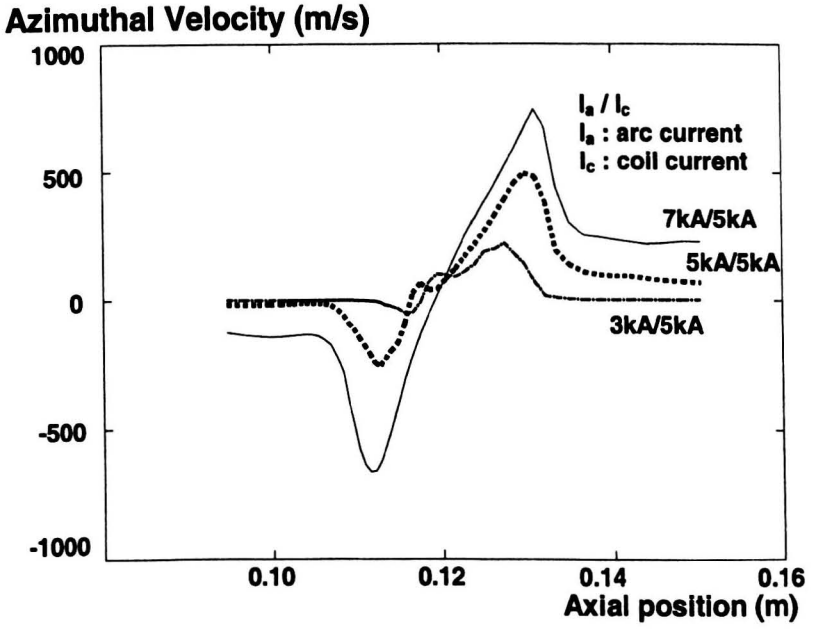


(b)

**Figure 3.16** Distribution of the azimuthal velocity along line L in Figure 3.7 for different coil current (a) and arc current (b).

Figure 3.14 and 3.15 show temperature distributions and velocity vectors according to the strength of swirling, which is controlled by the different coil currents and arcing currents respectively. It is also seen that upon increasing the coil current and arc current the azimuthal velocity is increased as shown in Figure 3.16. This seems consistent with physical reasoning because the magnetic fields ($B_z$, $B_r$) produced by the coil current will be stronger and the current density will be denser. The results in Figure 3.14 and 3.15 indicate the swirling flow tends to spread out the arc at both contacts tips and to constrict the middle section of the arc.

Figure 3.17 shows the predicted current-voltage characteristics. This result indicates that the swirling flow affected more arc behaviour below 5.0kA even though the difference of arc voltage is very little (< 2%) between with and without swirling flow ((a) and (b)).

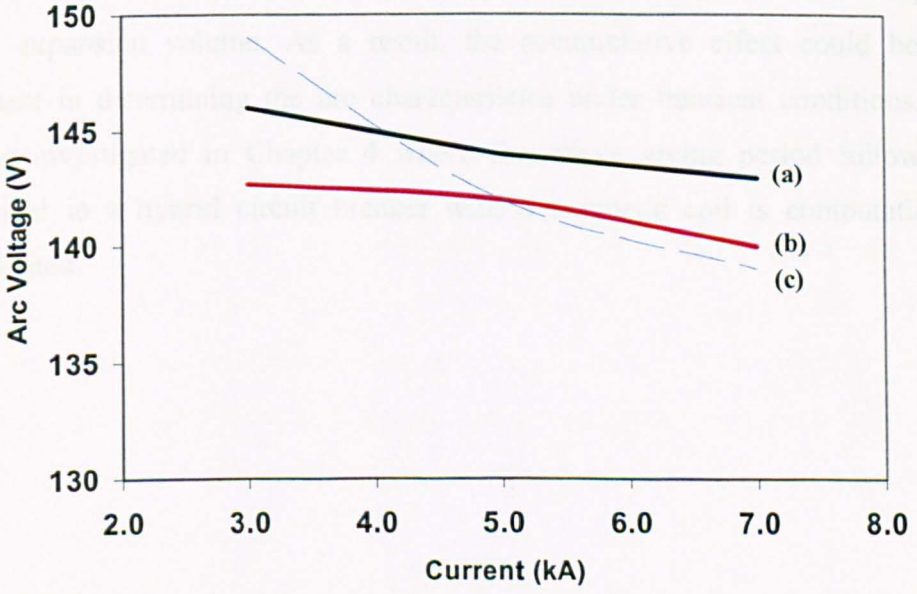


**Figure 3.17** Predicted current-voltage characteristics of hybrid circuit breaker (a) without swirling flow, (b) with swirling flow and (c) with swirling flow and fixed coil current 5kA.

## 3.4 Conclusions

The mechanisms through which the swirling flow affects the arc behaviour is analysed and explained in this Chapter under steady state conditions. The steady state conditions were chosen to eliminate the accumulative effects, which will appear in transient case. Strong swirling flow occurs in regions where radial current density is high. The axis pressure is effectively lowered with the presence of strong swirling flow and the shape of the arc column is changed as a result of modified pressure and flow fields. The arc voltage is only slightly reduced (<2%) in comparison with a similar arc without swirling flow. This shows that the effects of the swirling flow on arc voltage for a given current is moderate under the conditions studied. The gas flows from the expansion volume into the two hollow contacts since an artificial gas inlet is specified in the former. This will not be the case in the operation of a hybrid circuit breaker as no flow from outside is supplied to the expansion volume. As a result, the accumulative effect could be very important in determining the arc characteristics under transient conditions. This will be investigated in Chapter 4 where the whole arcing period following a sinusoidal in a hybrid circuit breaker with a magnetic coil is computationally investigated.

# Chapter 4
# Simulation of $SF_6$ Arcs in a Duo-flow Hybrid Circuit Breaker

## 4.1 Introduction

Computer simulation has been undertaken for a duo-flow hybrid circuit breaker which incorporates the auto-expansion principle with an externally imported magnetic field as shown in Figure 4.1. The device has a fixed contact and a moving contact; both of them are hollow contacts. When the contacts separate, an arc is drawn between them. The current path is then through the copper contact stem, through a coil which circles the steel tube, through the fixed contact and to the moving contact via the arc. The coil has 6 turns and is jointed to the steel tube. The current in the coil will set up a magnetic field with radial and axial components. An azimuthal magnetic field is produced by the arc current during the high current phase, the arc will fill the hole of the fixed and moving contacts, and an axisymmetric arc will result.

An azimuthal velocity component is generated in such a device by the interaction between the arc and the imposed magnetic field. Such a velocity component is unique to this type of breaker. Emphasis is therefore given to the investigation of the effects of the flow in the azimuthal direction (commonly known as the swirling flow). Comparative studies of arc behaviour with and without the swirling flow have been undertaken for a sinusoidal current. The effects of swirling flow in arc shape, flow and pressure fields, and arc voltage are discussed in detail.

The thermal interruption capability is investigated by calculating the critical rate of rise of recovery voltage (RRRV).

The work in this chapter is to investigate the main features characterising the arc which are the arc shape, flow field, pressure change and arc voltage during the high current period with special attention paid to the effects of swirling flow. Post arc current behaviour and the critical rate of rise of recovery voltage (RRRV) after current zero are examined.

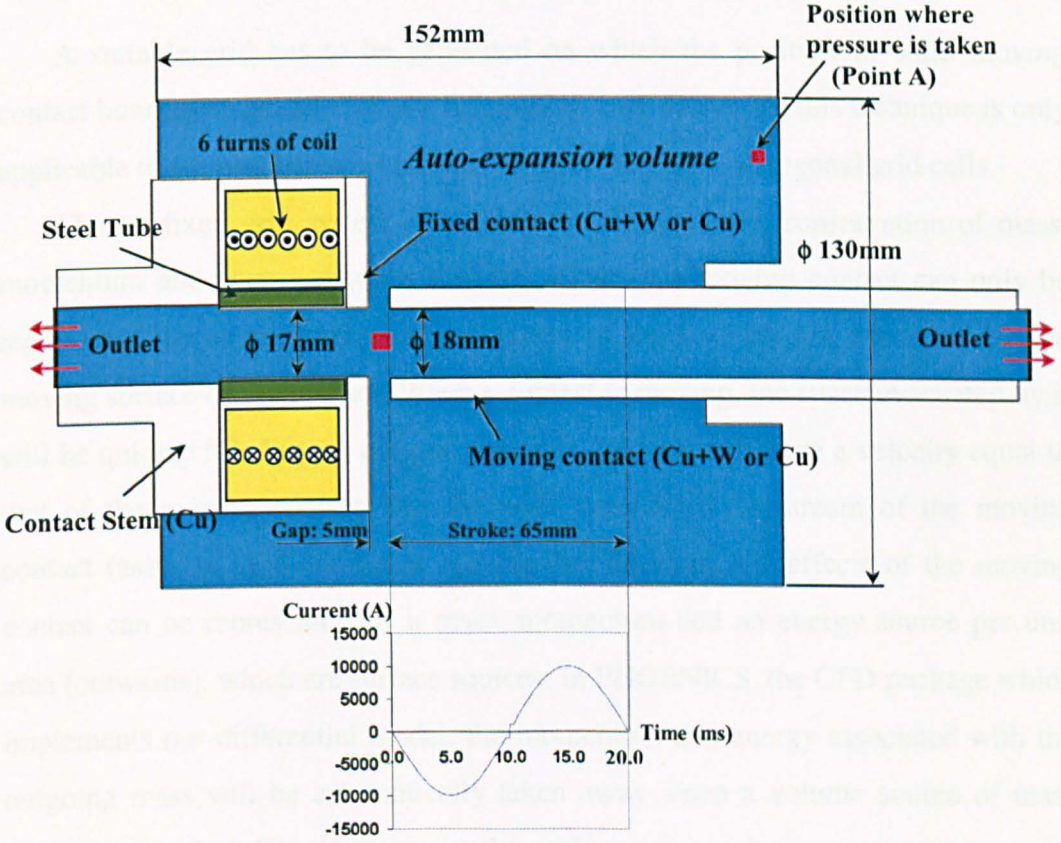


**Figure 4.1** Schematic diagram of a prototype hybrid circuit breaker.

## 4.2 Arc model, boundary conditions and grid system

The arc model used for the simulation is the same as that given in Chapter 3 with the time dependent term included. PHOENICS is used to obtain the solutions with the appropriate boundary conditions. Since one contact is moving at a pre-defined velocity, the boundary conditions at the moving surface (the tip of the moving hollow contact) need to be specified. The discussion in the arc model used in the current zero period is deferred to section 4.3.

A suitable grid has to be generated on which the position of solid moving contact boundaries are altered as a function of time. However, this technique is only applicable to simple shapes which can be represented by orthogonal grid cells.

When a fixed grid system is used in the computation, conservation of mass, momentum and energy requires that the effect of a moving contact can only be represented by source terms in two layers of cells which are separated by the moving surface of the contact. When a contact is moving, the space evacuated by it will be quickly filled up by the gas around it. The gas will have a velocity equal to that of the moving contact. For the cells immediately upstream of the moving contact (assuming the contact is moving downstream), the effects of the moving contact can be represented by a mass, momentum and an energy source per unit area (outwards), which are surface sources. In PHOENICS, the CFD package which implements our differential model, the momentum and energy associated with the outgoing mass will be automatically taken away when a volume source of mass (sink) is specified. We thus convert the surface sources for mass, momentum and energy for the cells upstream of the moving contact into a volume mass source. Mathematically, the volume source of mass is

$$S_m = \frac{w_c \rho}{\Delta z} \tag{4.1}$$

where $w_c$ is the speed of contact, $\rho$ and $\Delta z$ are respectively the density of gas and axial width of the cell immediately upstream of the moving contact. Numerically, when a cell is unblocked in a time interval of $\Delta t$, its density, velocity and enthalpy are copied from the cell upstream of it. The total mass, momentum and energy, which are required to fill the newly unblocked cell, are just equal to those which leave the upstream cell in the time interval of $\Delta t$. Thus, the mass, momentum and energy are conserved in the simulation of moving contact. The skin friction at the contact surface is small and is neglected.

Body fitted coordinate (BFC) grid system is used to model the complex geometry of the expansion volume. Because of the large size of the CFD domain, a compromise has to be made between the total number of cells and computing cost. The general rule is that in the radial direction the grids are densely populated in the arc region and in the axial direction dense grids are used in regions where flow field undergoes rapid change. A total number of 195(axial) by 84(radial) cells are used in the computation. To resolve the steep gradient of arc parameters, 45 cells are densely used in the first 10mm in the radial direction. Further increase in the number of cells produces negligible improvement to the results. A typical BFC grid system for the expansion volume is shown in Figure 4.2.

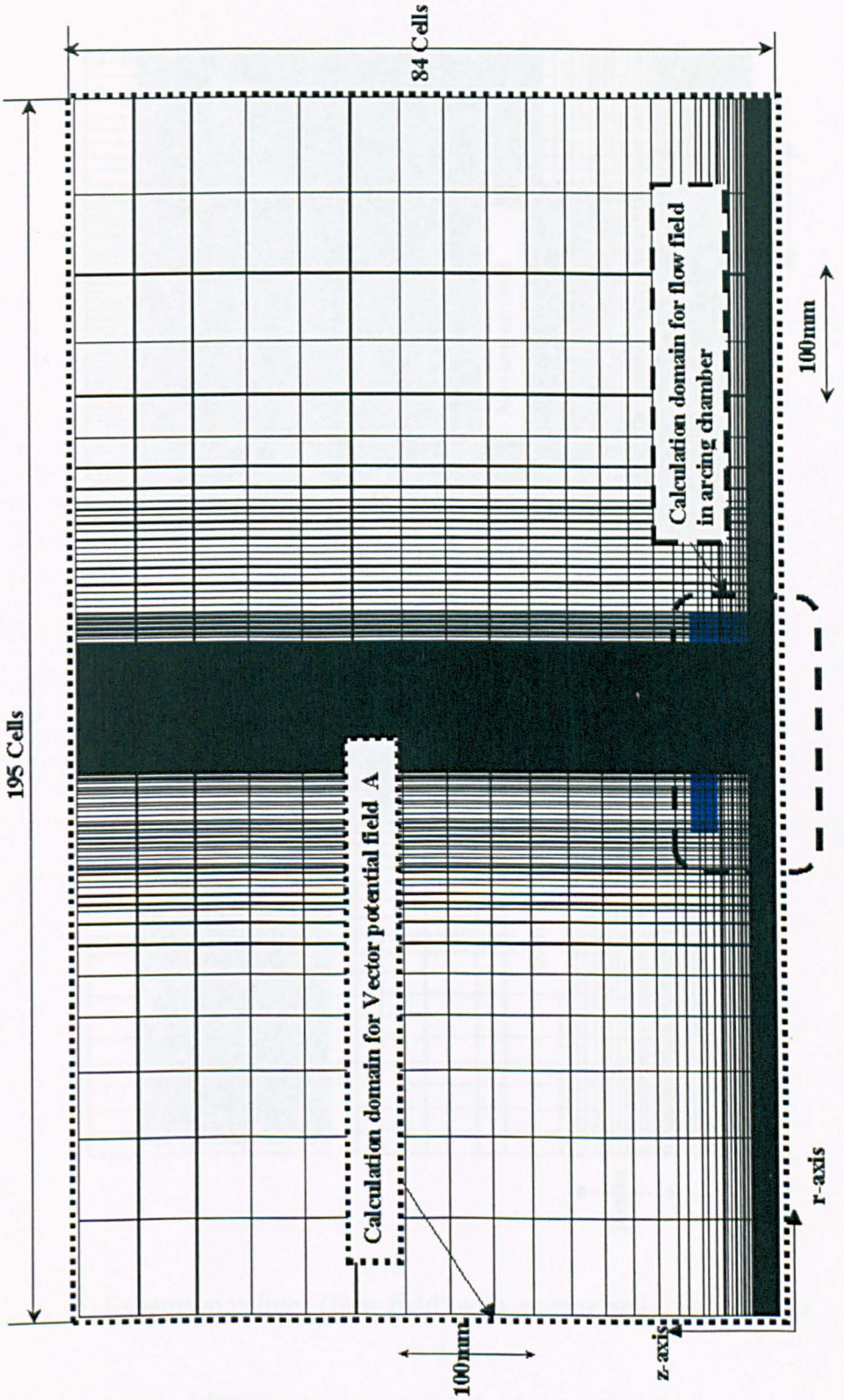


(a) Whole field computation domain

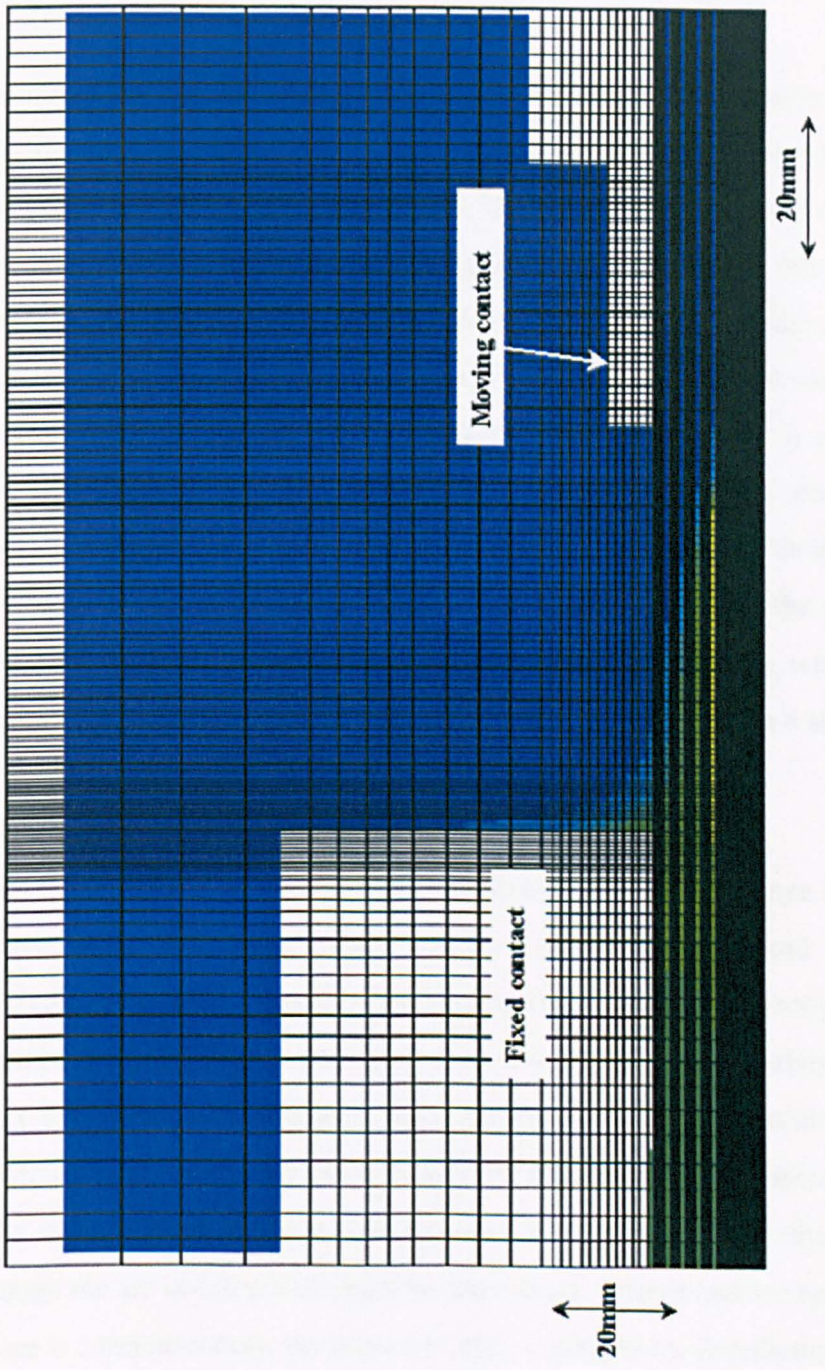


(b) Expansion volume (flow field) with moving and fixed contacts

**Figure 4.2** A typical BFC grid system in a hybrid circuit breaker

## 4.3 Arc modelling during the current zero period

It is common to discuss arc interruption in terms of current zero period. However, for the arc under investigation, there is no clear demarcation between the high current phase and the current zero period. The arc near current zero depends on the whole arcing history. When current decays towards current zero, the arc will not be big enough to completely fill the two holes of the hollow electrodes. The arc may have random movement because of the movement of the arc root as well as arc instability. The shape of the arc can be seriously deformed. Such a complex situation is still beyond present capability of arc modelling. As previously discussed, there is no satisfactory model for arc rooting. We will still assume that for small currents the arc burns along the axis with a length equal to the distance between the two contacts. Since the arc may be in rapid motion within the interrupter, the centrally positioned arc may be a good approximation in a statistical sense.

Thermal interruption or failure depends on the overall energy balance between Ohmic power input and power losses due to turbulence enhanced thermal conduction, radiation and convection. If the interrupter is designed correctly, power losses exceed power input after current zero, thus resulting in the thermal extinction of the arc. To avoid the consideration of the interaction between the circuit breaker and power network, arc modelling assumes that the current is known before current zero and the voltage is known after current zero. For the latter case, the current passing through the arc is calculated from the known arc voltage and arc resistance. Arc resistance is computed from the known electric conductivity distribution within the arc. Since the arc is very thin, the electric field within the arc is almost entirely axial and is independent of radial position [70]. Thus, the electric field is computed by

$$E(z) = I(t) / \int \sigma(z,r) 2\pi r dr = I(t) / g(z). \qquad (4.2)$$

The current can then be calculated from

$$V(t) = I(t) \cdot \int \frac{1}{g(z)} dz . \tag{4.3}$$

## 4.4 Results and discussions

Computational results are given for the breaker shown in Figure 4.1 for a 50Hz sinusoidal current with a 10kA peak. Chapter 3 shows that the swirling flow greatly changes (in comparison with a DC arc with swirling) the cold gas entrainment, which relies upon the radial velocity. As a consequence, the arc with swirling flow has a smaller cross section than that of an arc without swirling. For AC arc discharges, such effects are accumulative. We therefore make a comparative study of the arc behaviour in the breaker of Figure 4.1 with and without swirling flow.

For the convenience of discussions we divide a whole AC period into two periods. For our investigation, if current is below 1200A AC current zero near the second current zero, it is considered within current zero period. For the current zero period the number of cells in the first 2mm in the radial direction from the axis is twice that for the high current period.

### 4.4.1 Arc initiation and cathode spot

The arc calculation must begin with an initial condition of the arc (Figure 4.3). The arc is initiated at a current of -200A across a gap of 5mm between two contacts by introducing a conducting plasma column across the gap. The fixed contact is the cathode. The column has a radius of 2mm, over which the gas temperature linearly decreases from 20,000K at the axis to 300K at the edge. The location of the initial hot column in the expansion volume is shown in Figure 4.4 where the cathode is

indicated. The moving contact starts to move with a speed of 3.0m/s after arc initiation. The exact form of the initial temperature distribution will have no effects on the temperature distribution, but it can affect the convergence at the starting calculation.

Once the arcing process is initiated, Ohmic heat and radiation transfer inside the arc column lead to the rapid build-up of a strong heat source accompanied by the establishment of a flow field. The initial stage of the arcing is shown in Figure 4.5. At the arc centre, the electromagnetic force ($j_z \times B_\theta$, $j_y \times B_\theta$) of arc itself builds up the rapid flow. On the other hand, flow at the arc edge is generated by gas expansion which is caused by radiation re-absorption in this layer. When the arcing current is increased gradually, the hot column has been extended towards the exit of the hollow contact. The temperature within the arc becomes very high, since the energy generated by Ohmic heating cannot be rapidly removed from the arc column by the slow gas flow near the stagnation point. However, the contribution of arcing to the pressure rise in expansion volume in initial arcing period is small.

The temperature field changes rapidly. The radial temperature profile at the mid-plane between the two transparent electrodes is shown in Figure 4.6 (a), for which the current is maintained at –200A. The corresponding net radiation loss is given in Figure 4.6 (b), which is typical for arcs in gas flow [37, 89]

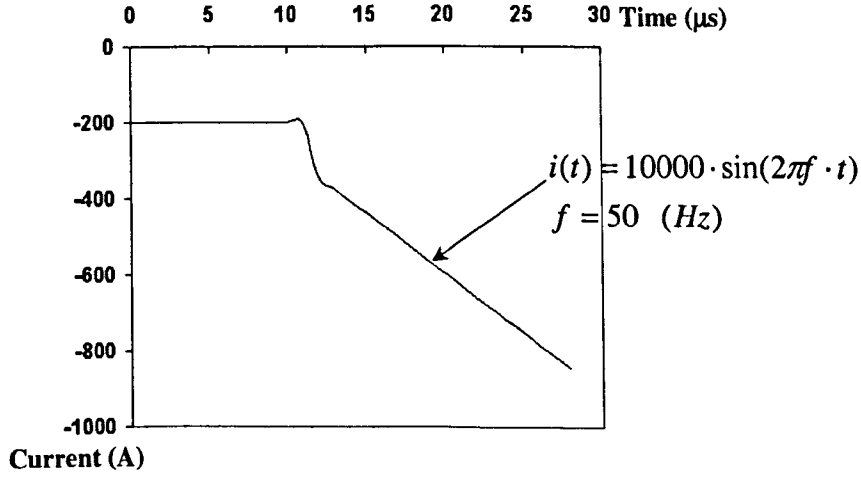


**Figure 4.3** The electric current waveform used for arc initiation. The current remains constant at -200A for the first 10μs.

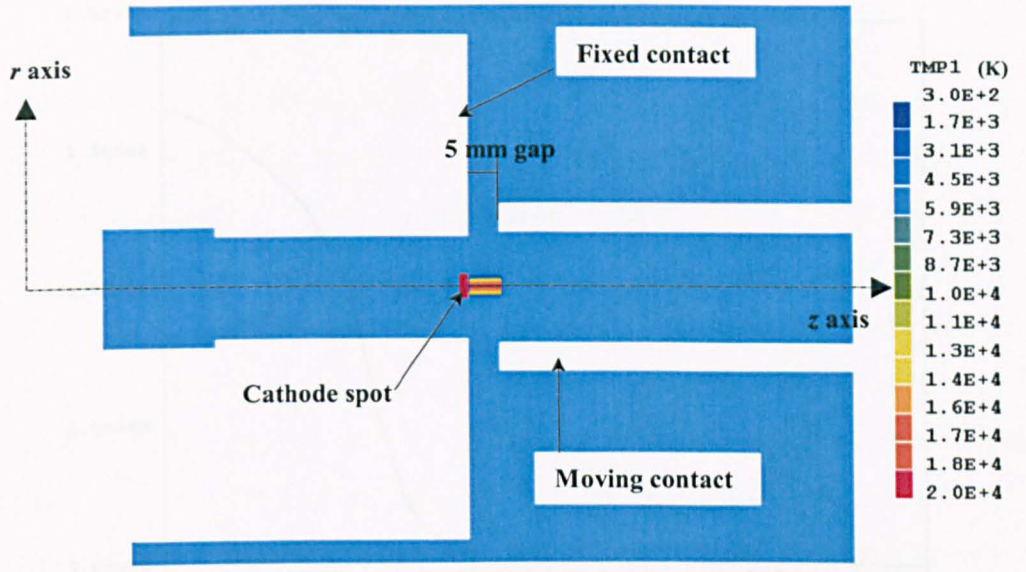


**Figure 4.4** The axially isothermal hot column for arc initiation at -200A in the expansion volume

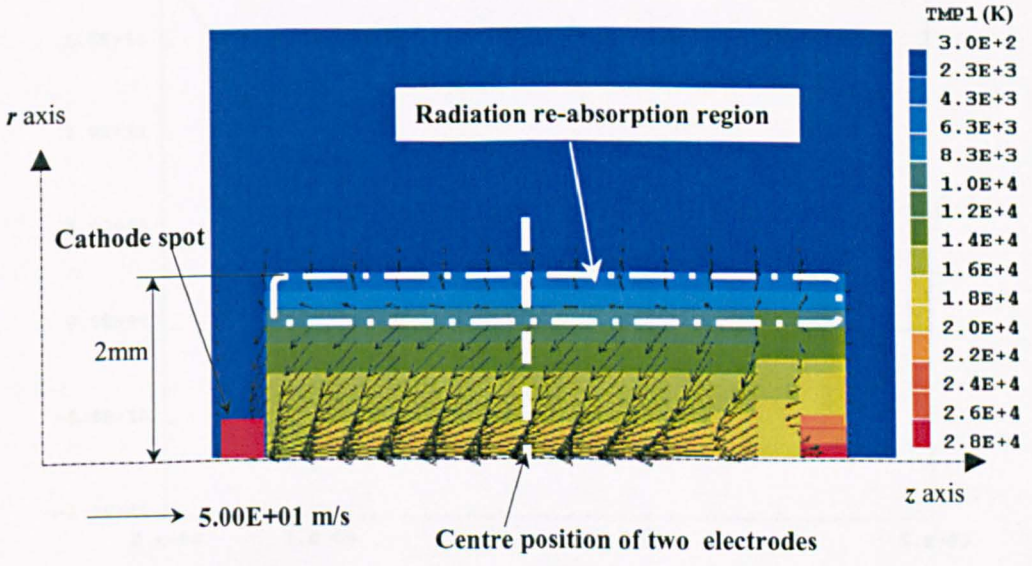


**Figure 4.5** Temperature distribution and velocity vector at an instant of 10μs. Arcing current is -200A.The oval circle indicates the radiation re-absorption region at the arc edge.

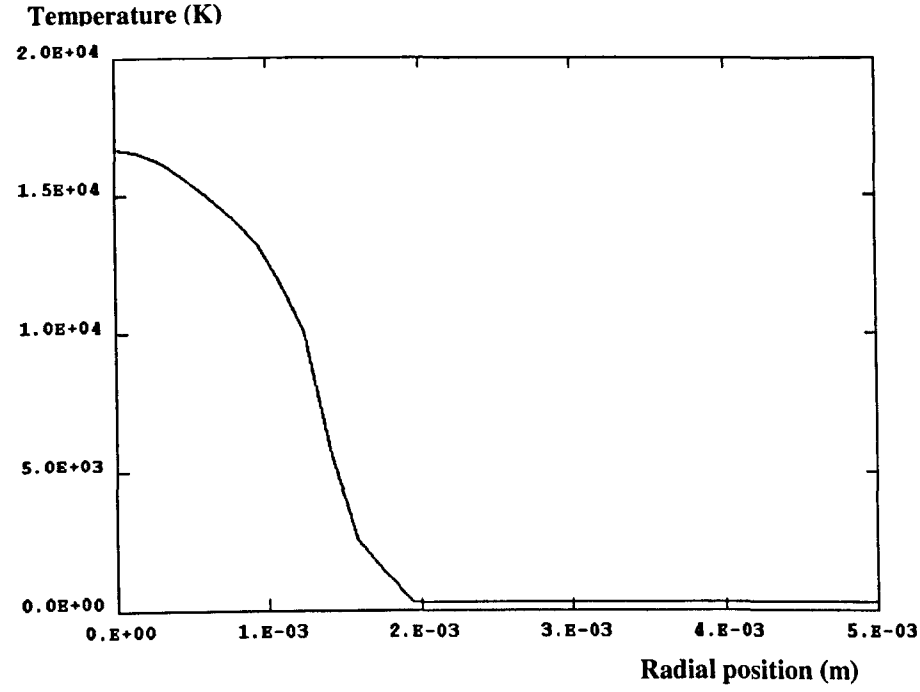


(a)

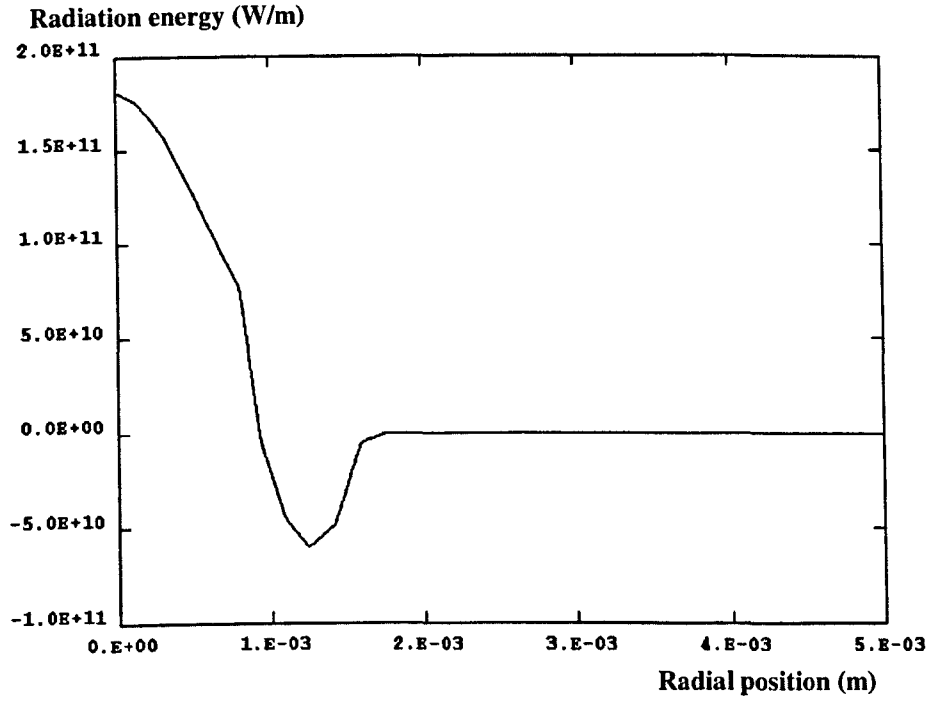


(b)

**Figure 4.6** Temperature distribution (a) and net radiation emission (b) along a radial dashed line in Figure 4.5 between two transparent electrodes at 10μs.

### 4.4.2 General characteristics of the high current phase

For the convenience of discussions, we call the period from the end of arc initiation to 1.2kA before the second current zero as the high current phase. The detailed current wave form is given in Figure 4.9, which shows a sudden change in current from –(1.0) kA to +(1.0) kA near the first current zero. The reason for using such a current variation is that for this type of circuit breaker, arc extinction does not take place at the first current zero. To avoid the re-distribution of the grids, which is necessary for resolving the temperature distribution inside a thin arc at current zero, we use a relative high current to bypass the first current zero. The effects of the changing waveform around the first current zero are forgotten within a few microseconds.

After the arc initiation, the temperature and velocity fields continue to evolve while the arc is lengthened due to the moving contact. Figure 4.7 shows a sequence of the temperature fields within the interrupter for the whole arcing period, where, for comparison, the results of an arc without swirling velocity are also shown. In the first half period of arcing, the high temperature region of the arc starts to block a substantial part of the hole of the fixed contact (the cathode) at a current around above 5kA. As a consequence, the arc near the fixed electrode spreads out radially along the surface of the fixed contact. For the arc with swirling velocity included, radial entrainment into the arc as a whole is stronger than that into the arc without swirling, as discussed in Chapter 3. The radial entrainment for the swirling arc is more uniform than that of the arc without swirling along the arc length as the velocity of an arc element on the arc axis is linearly increased with the distance away from the stagnation point (Figure 4.8). Since the arc temperature is very high and the arc volume is small relative to the volume of the interrupter, the amount of gas exhausted through the two exits of the hollow contacts is too small to affect the pressure within the expansion volume. However, the hot gas flow from the arc region to the expansion volume does result in a pressure rise in the first half of

arcing (Figure 4.9). Detailed discussion on pressure variation in the expansion volume is deferred to section 4.4.4

Similar to the DC case (Chapter 3), the negative radial velocity at the moving contact in the first half period of arcing for an arc without swirling is stronger than that with swirling. Thus, the arc without swirling is thinner than the arc with swirling at the moving contact (Figure 4.7). In the first quarter of the arcing period, the difference in arc voltages between the two arcs (with and without swirling) is small (Figure 4.10) although the detailed distribution of the axial field on the arc axis shows distinct differences (Figure 4.11). A typical distribution of electrical potential is given in Figure 4.12.

The extent of the arc spreading radially out along the surface of the fixed contact is far larger for an arc without swirling in the second quarter of the arcing (Figure 4.7). The arc with swirling on the whole is thinner. The arc voltage for swirling flow arc gradually becomes higher than that of a non-swirling flow arc.

A selection of typical computation results (the axis velocity (Figure 4.8), the axis temperature and axis electric field (Figures 4.11), and the axis pressure (Figure 4.13)) illustrates the changes within the arc following a 50Hz, 10kA peak current. The major difference between the two arcs (with and without swirling flow) lies with the pressure distribution. In comparison with the arc without swirling, the close coupling between the radial and azimuthal momentum conservation results in a very different pressure distribution for the swirling arc. The accumulated effects of the swirling flow are reflected in electrical behaviour, which shows a higher arc voltage, especially after the second current peak (Figure 4.10). For the second half period, the cathode is located at the moving contact. There are also marked differences between arc temperature and electrical field (Figure 4.11). The swirling arc is also considerably thinner (Figure 4.7) at the second current zero where thermal interruption takes place.

Radiation transport depends on the temperature field. The approximate radiation transport model of Zhang et al. [3] has given excellent results for arcs dominated by axial flow [88], for which the radial temperature profile is monotonic.

For the arcs, which do not burn in a shaped nozzle, the radial component of the velocity could be comparable with the axial component. This is the case for the arc under investigation. For example, the arc at 5ms (-10kA) has a complex radial temperature profile (Figure 4.14), which is not monotonic. For such a non-monotonic radial temperature profile, it is not certain if the radiation model of Zhang et al. could yield good results. There are two uncertainties: one is the choice of the arc radius for the calculation of the net radiation emission coefficient and the other is the radiation re-absorption region and the amount of radiation absorbed.

An empirical approach is adopted here to optimise the radiation transport model. We define a radiation re-absorption region from a radial position at which the temperature reaches 83% of (axis or the highest temperature) to a point where the temperature attains 4000K. 4000K is chosen as this gives a reasonable estimate of the arc radius. The choice of the radius at 2000K as in Chapter 3 will result in a too large arc radius, which would greatly reduce the radiation loss. The percentage of absorption of the radiation flux at the starting point of re-absorption region is varied from 40% to 80%. The computed arc voltages with different percentages of absorption are compared with that measured (Figure 4.15). It is rather surprising that the arc voltage is not very sensitive to the percentage of absorption. Careful examination of computational results indicates that radiation transport only accounts for 10 ~ 50% of Ohmic input. Convection and turbulent transport of energy take 50 ~ 90% of the Ohmic input. Thus, the percentage of radiation absorption does not very much the arc voltage. The computed arc voltage is slightly below that measured except in the region close to second current zero (the arc voltage around the first current zero is not properly computed due to the current waveform used in the computation.) Experimental results show that there is an extinction peak near current zero. The discussion on the current zero period is deferred to Section 4.4.5.

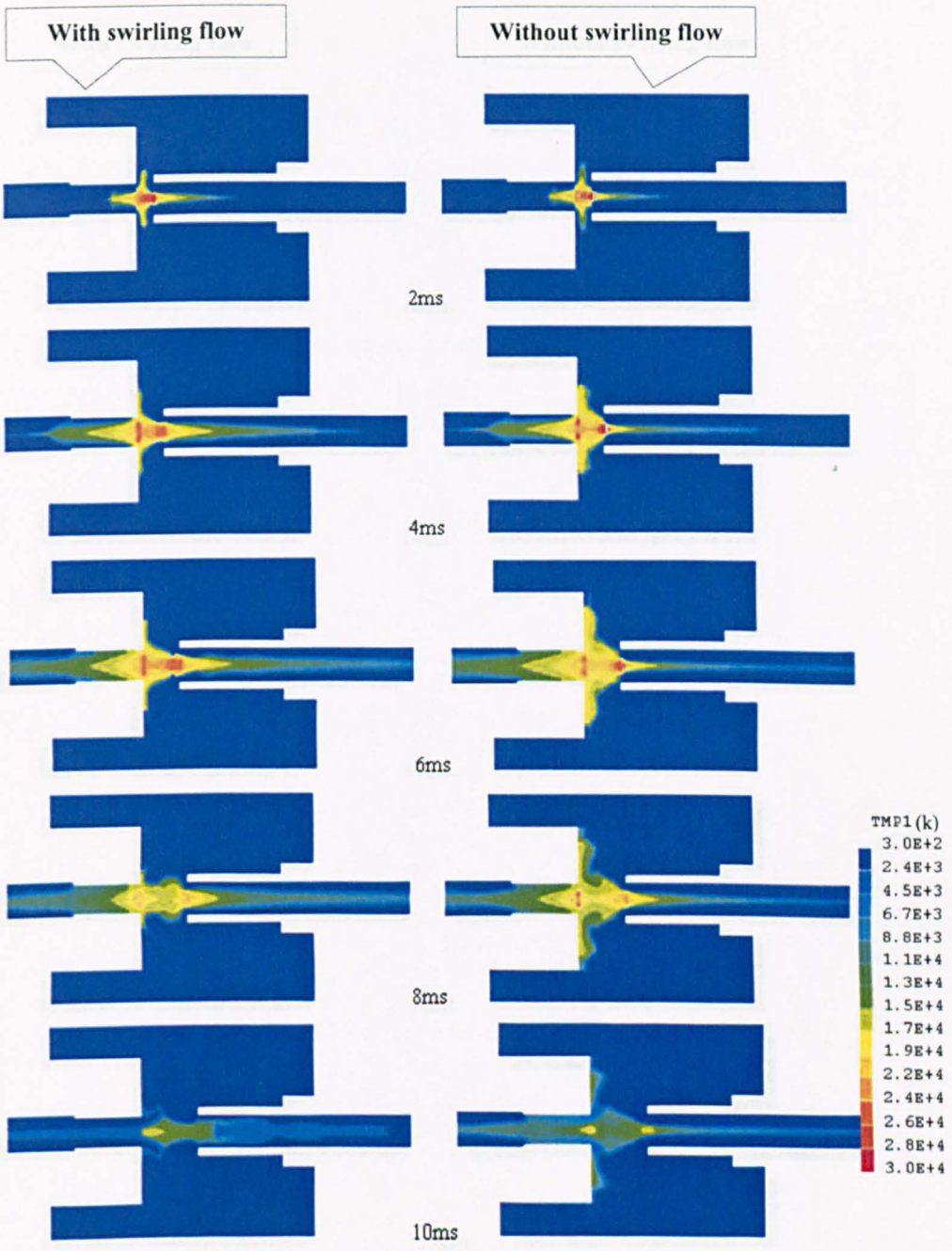


(a) First half cycle

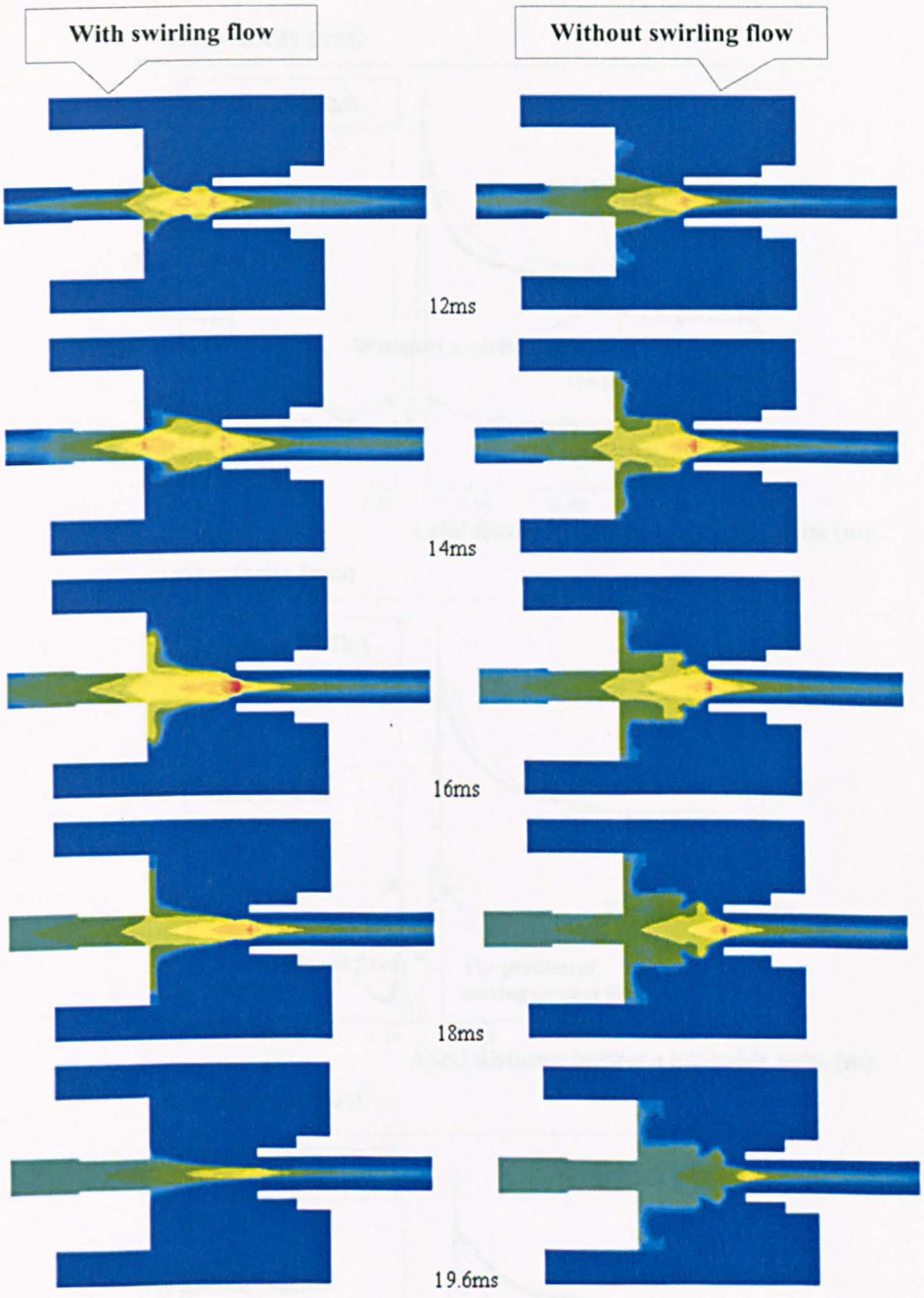


(b) Second half cycle

**Figure 4.7** Temperature distribution in the expansion volume at (a) first half cycle 2ms, 4ms, 6ms, 8ms, 10ms and (b) second half cycle 12ms, 14ms, 16ms, 18ms, 19.6ms. The peak current is 10kA

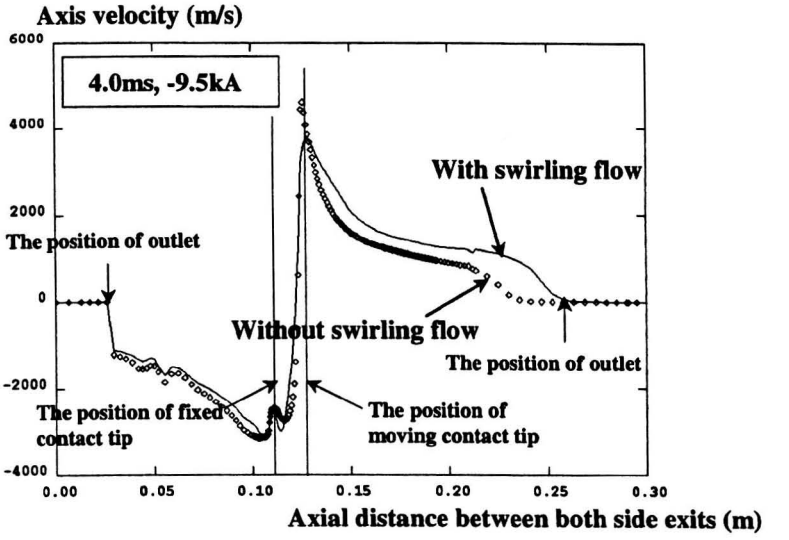


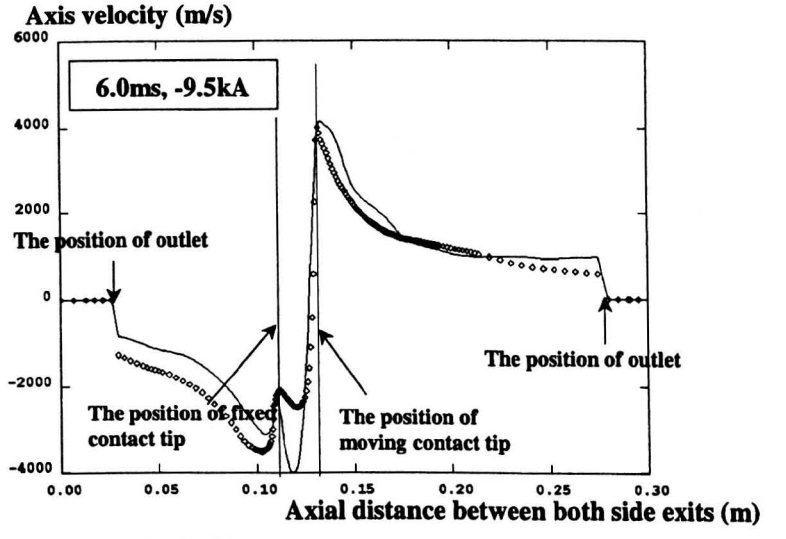


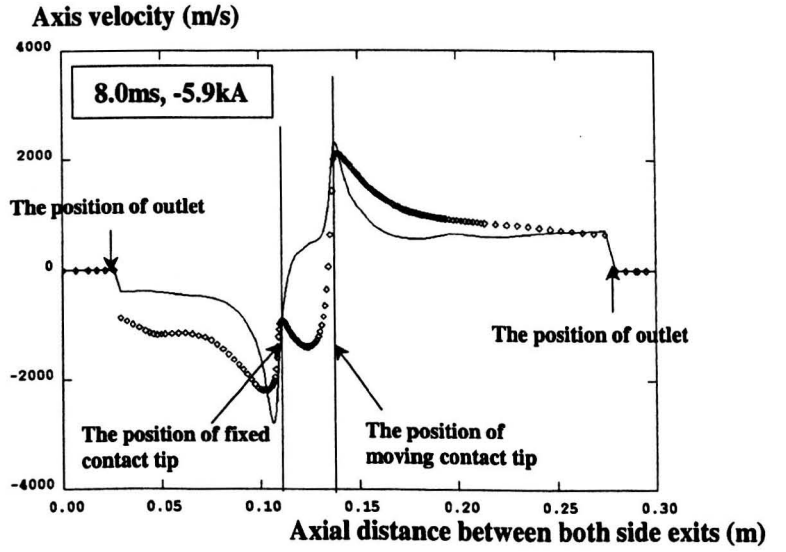


(a) First half cycle

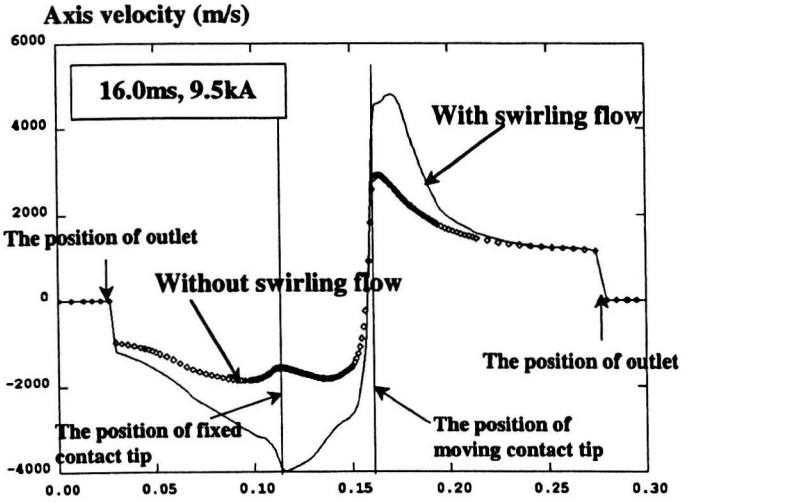


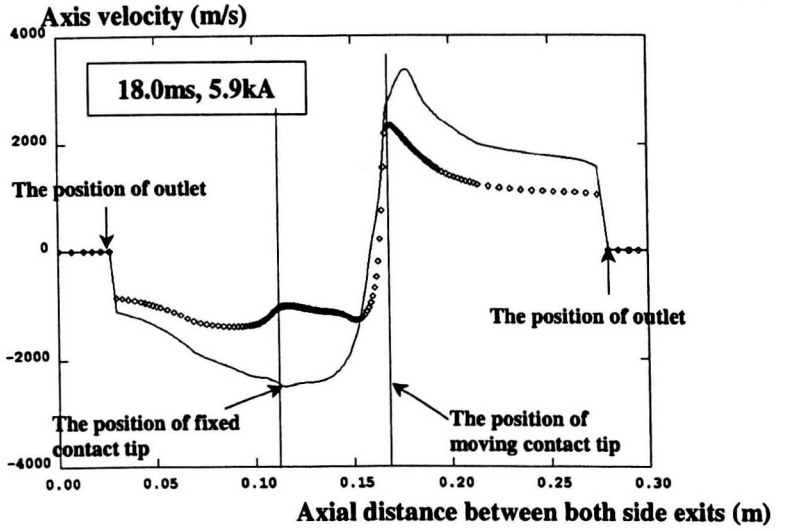


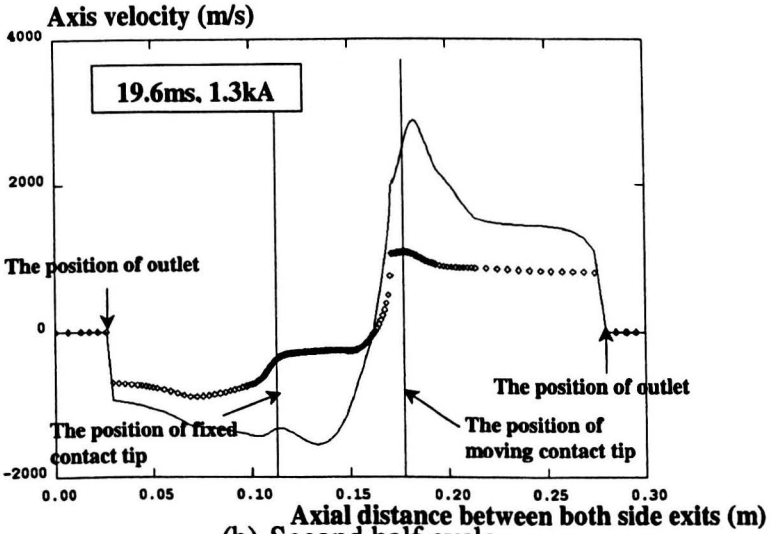


(b) Second half cycle

**Figure 4.8** Axis velocity at distribution at (a) first half cycle 4ms, 6ms, 8ms and (b) second half cycle 14ms, 16ms, 19.6ms. The peak current is 10kA.

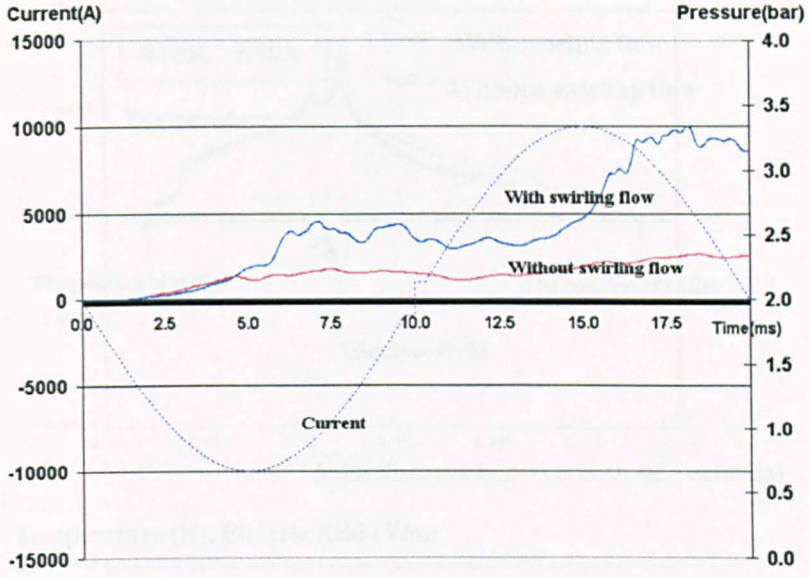


**Figure 4.9** Predicted pressure variation at the position indicated in Figure 4.1 in the expansion volume for cases with and without swirling flow

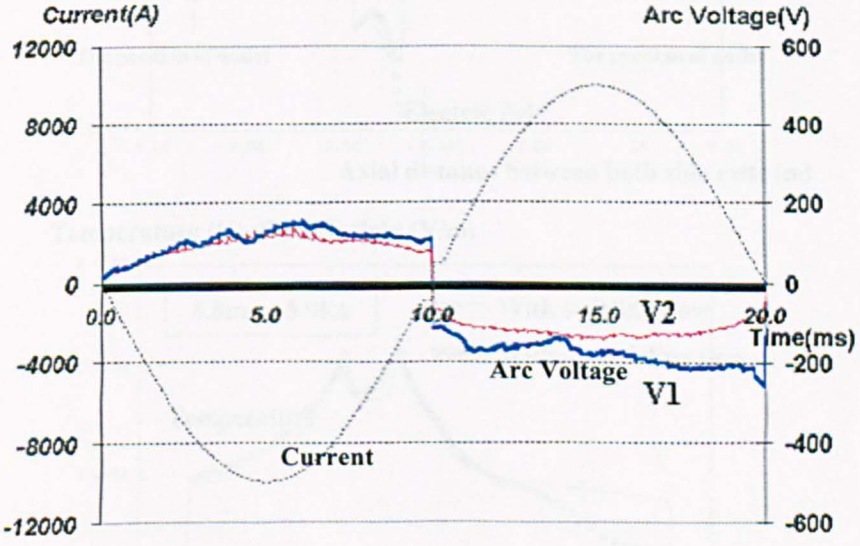


**Figure 4.10** Arc current and predicted arc voltage (V1: with swirling flow, V2: without swirling flow) as a function of time for the duo-flow hybrid circuit breaker.

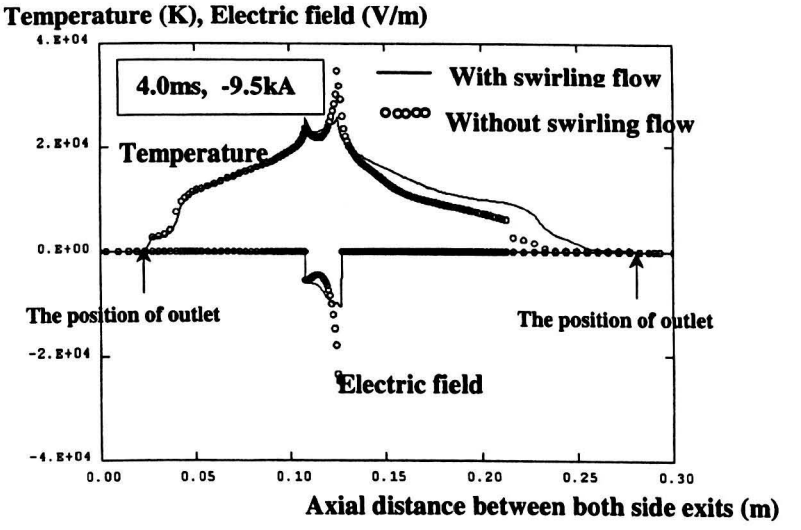


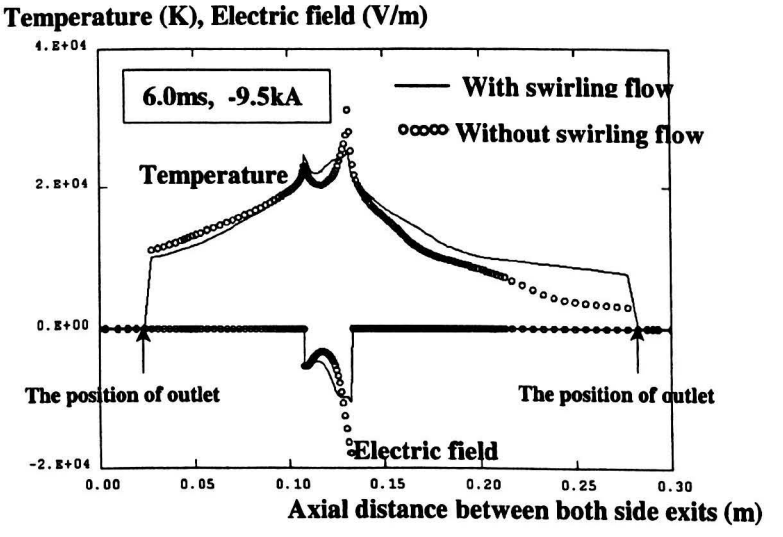


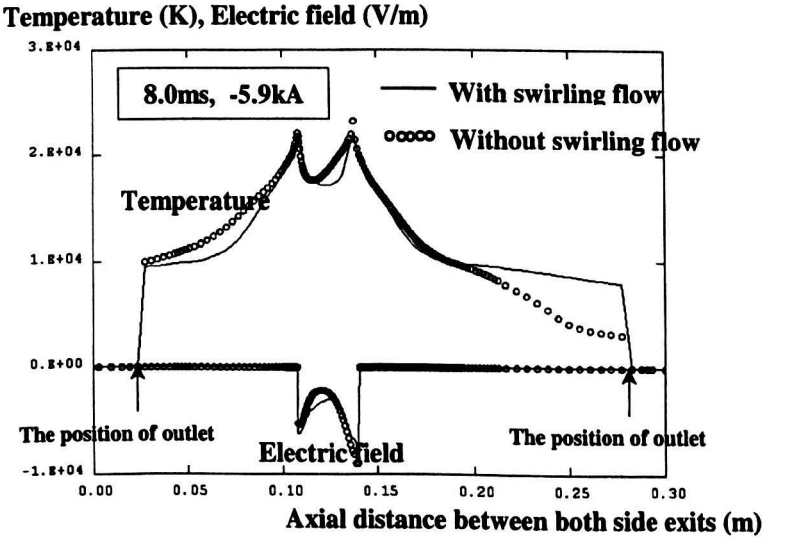


(a) First half cycle

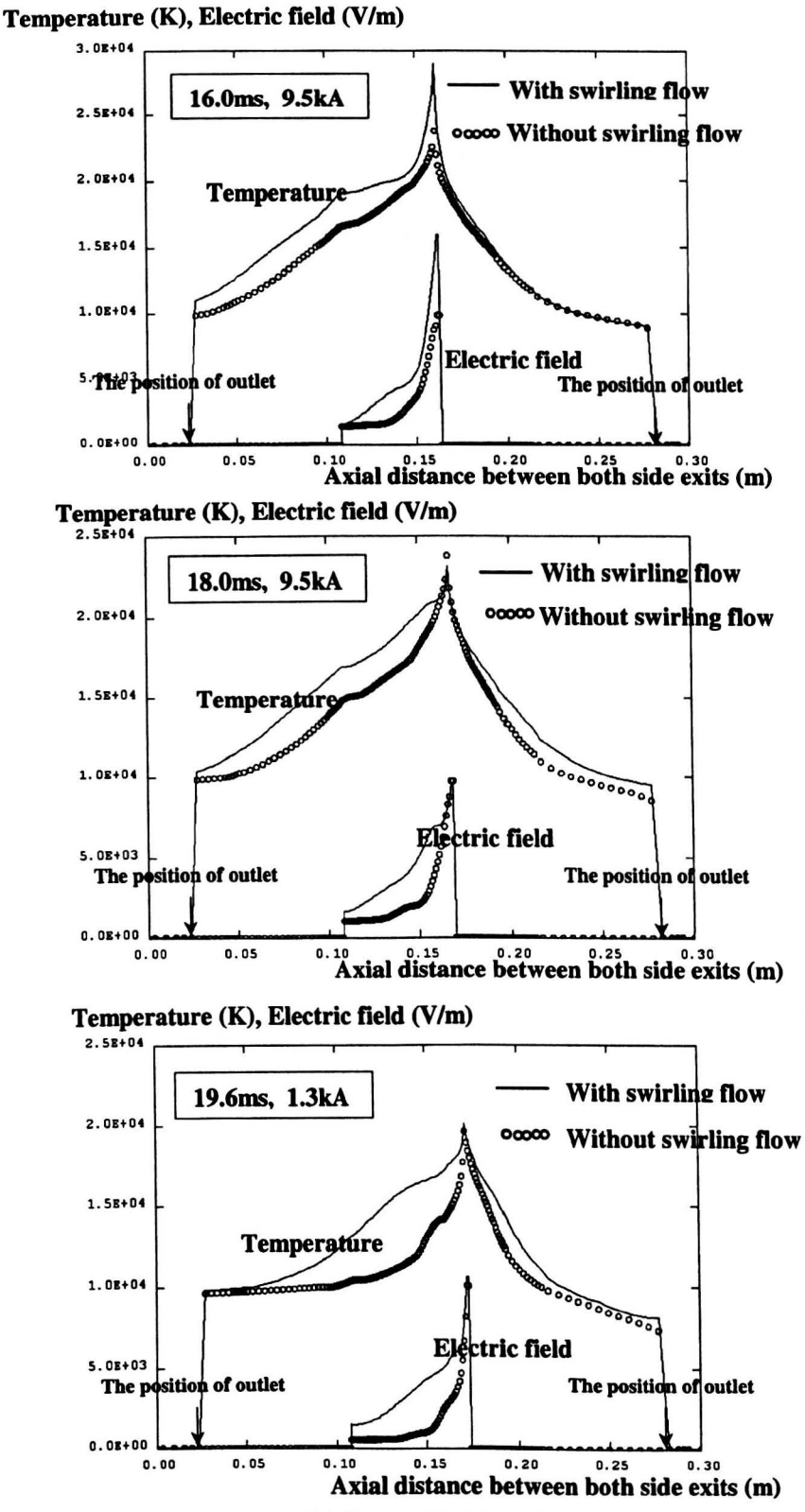


(b) Second half cycle

**Figure 4.11** Temperature and axial electric field on the axis at (a) first half cycle 4ms, 6ms, 8ms and (b) second half cycle 14ms, 16ms, 19.6ms. The peak current is 10kA

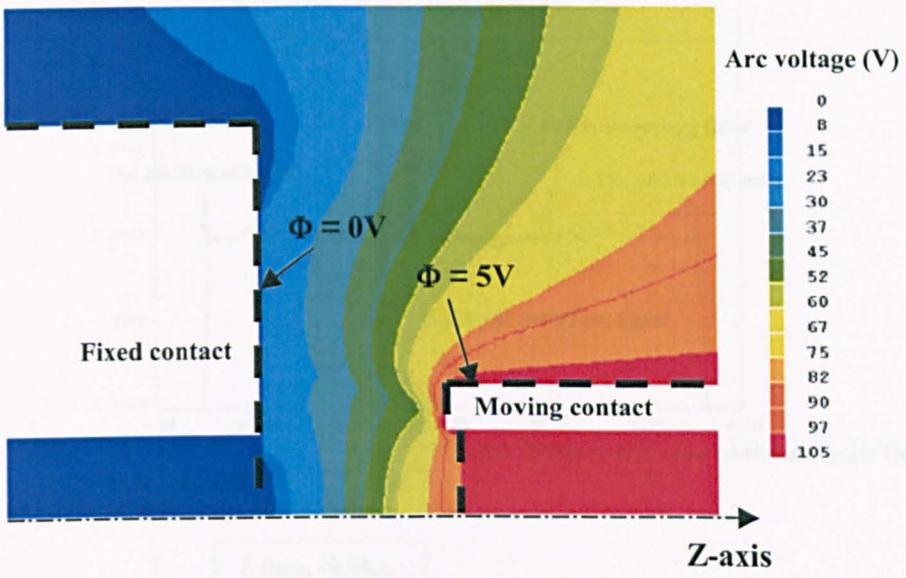


**Figure 4.12** Arc voltage at 5.0ms with arcing current of -10.0kA for with the swirling flow case.

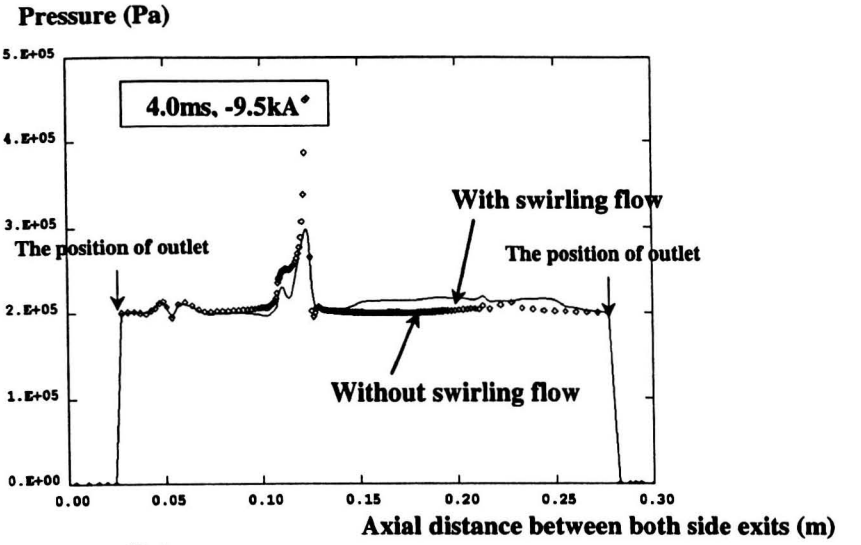


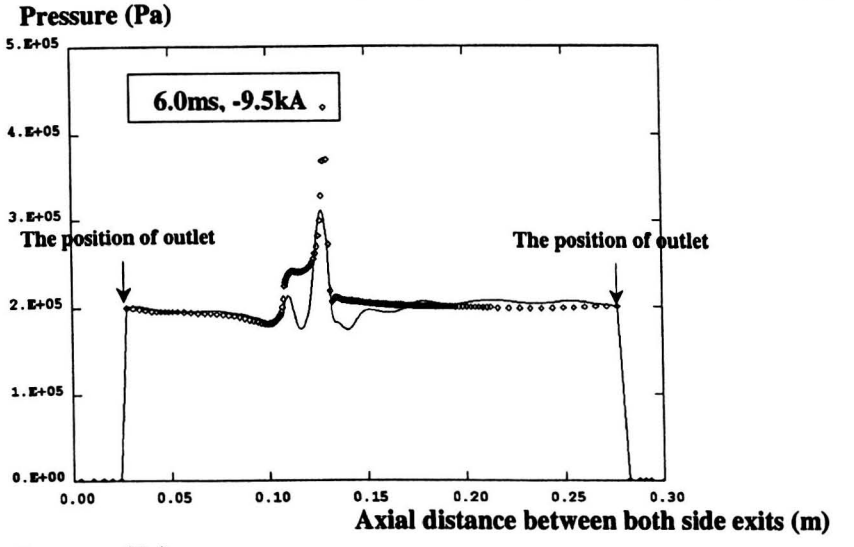


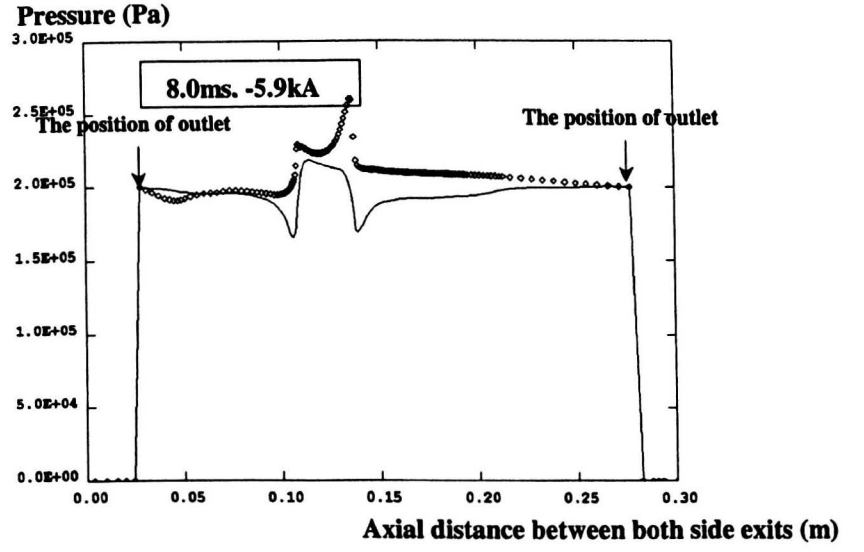


(a) First half cycle

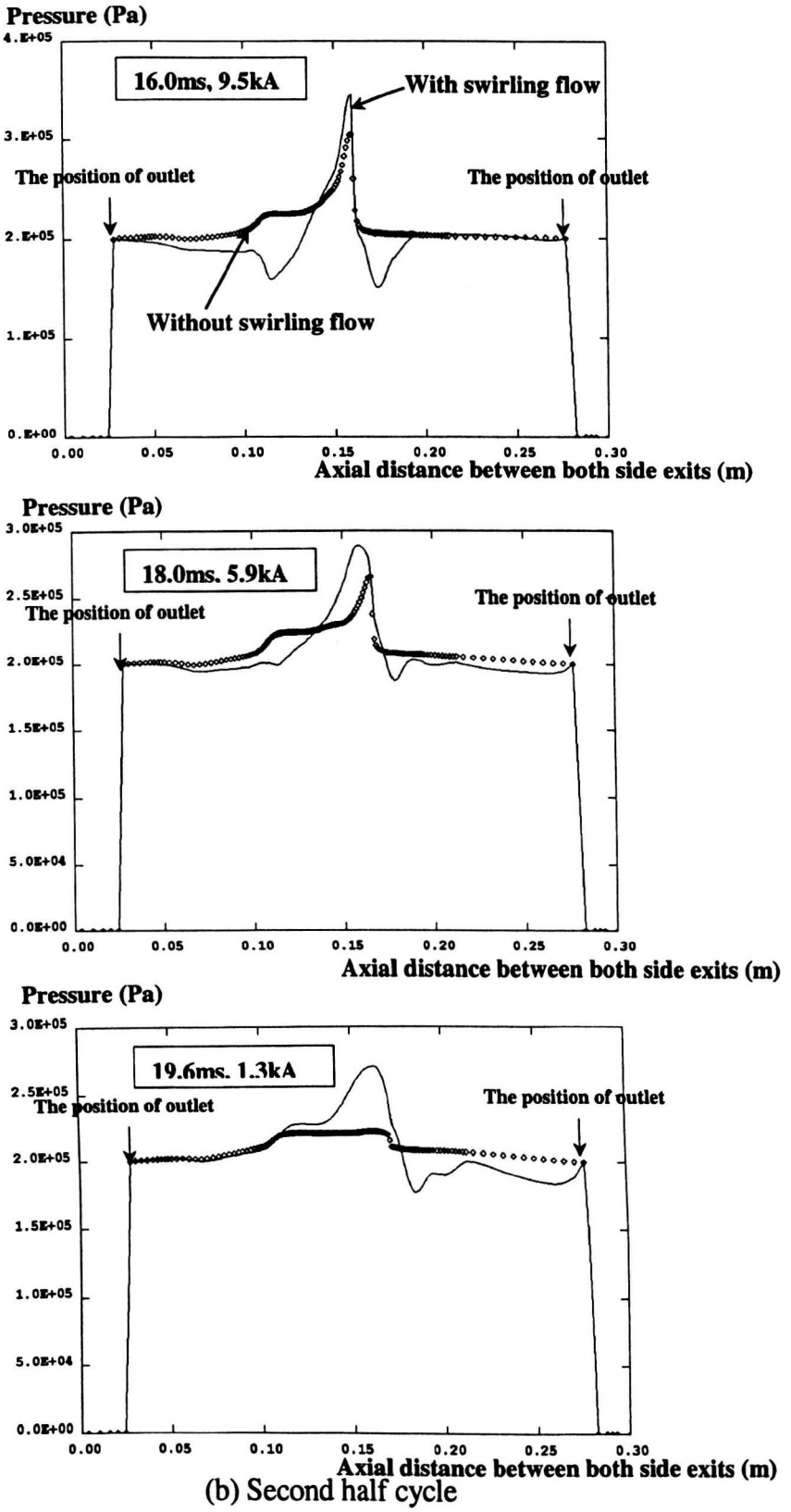


(b) Second half cycle

**Figure 4.13** Pressure distribution on the axis at (a) first half cycle 4ms, 6ms, 8ms and (b) second half cycle 14ms, 16ms, 19.6ms. The peak current is 10kA.

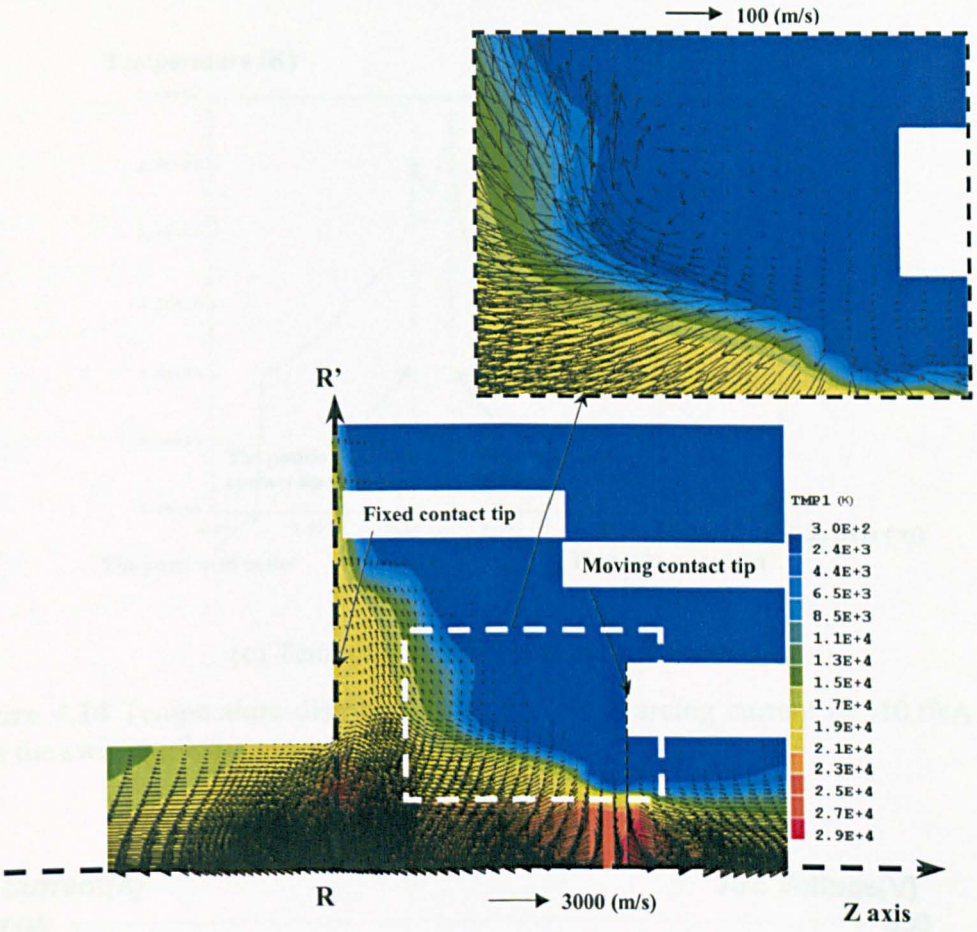


(a) Temperature distribution and velocity vector

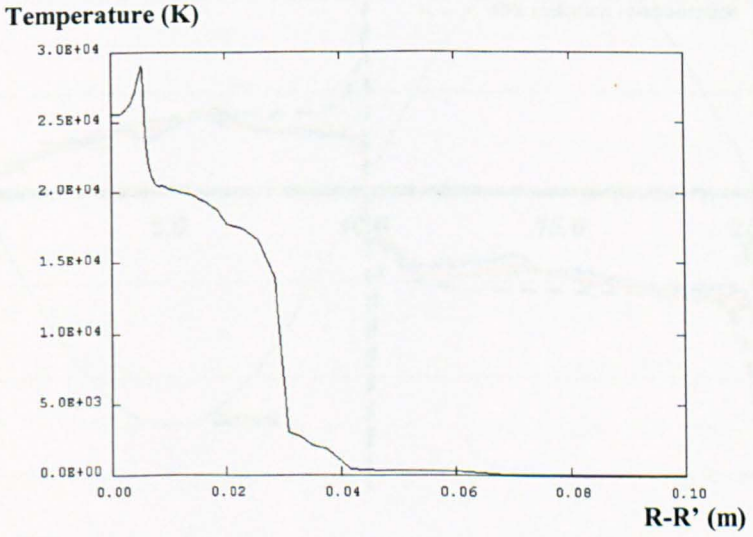


(b) Temperature distribution along a radial RR' dashed line in Figure 4.14 (a)

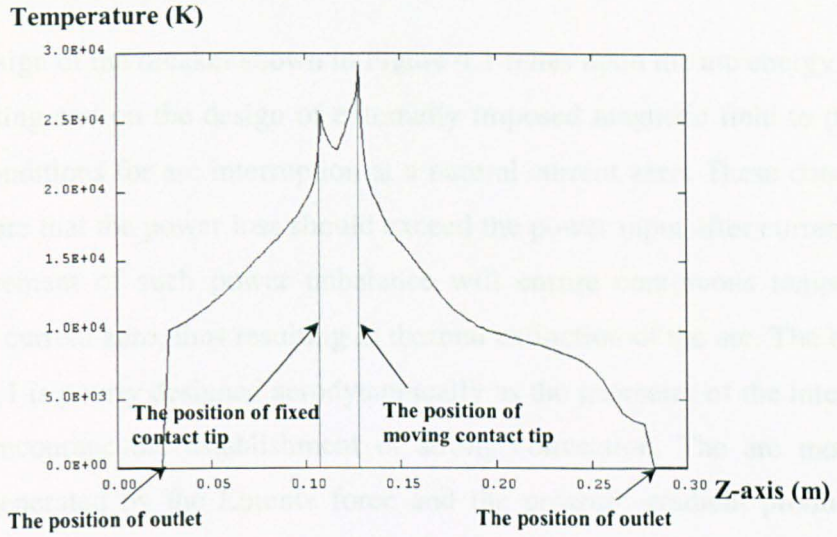


(c) Temperature distribution on the axis

**Figure 4.14** Temperature distributions at 5ms with arcing current of -10.0kA for with the swirling flow case

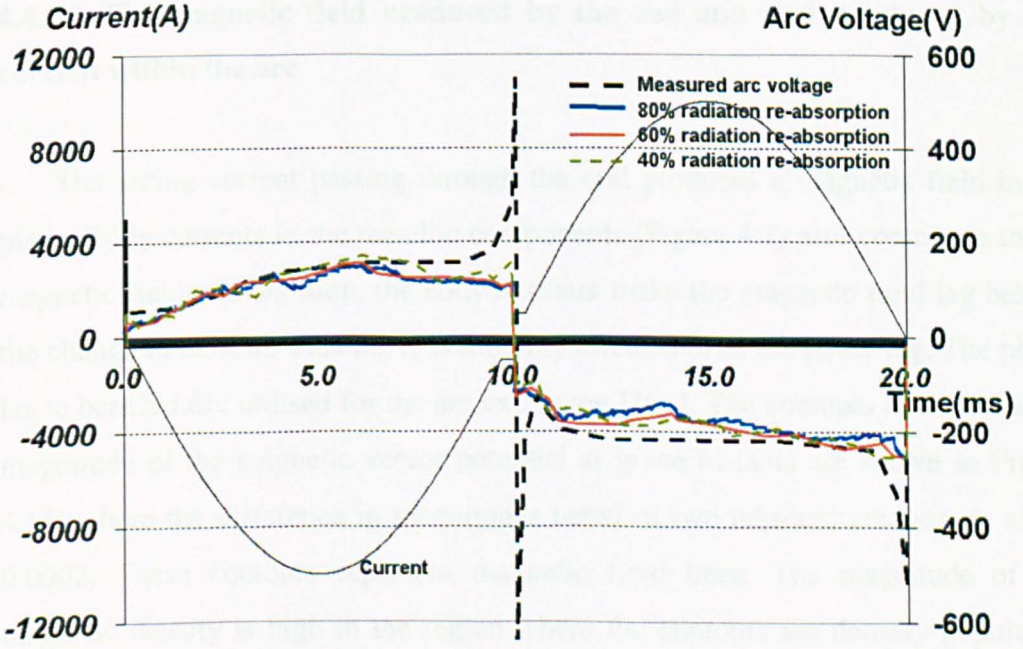


**Figure 4.15** Predicted (with swirling flow) and measured arc voltage as a function of time for the duo-flow hybrid circuit breaker.

### 4.4.3 The role of the Lorentz force and the generation of swirling flow

The design of the breaker shown in Figure 4.1 relies upon the arc energy due to Ohmic heating and on the design of externally imposed magnetic field to provide the right conditions for arc interruption at a natural current zero. These conditions should ensure that the power loss should exceed the power input after current zero. The achievement of such power unbalance will ensure continuous temperature decay after current zero, thus resulting in thermal extinction of the arc. The breaker in Figure 4.1 is poorly designed aerodynamically as the geometry of the interrupter does not encourage the establishment of strong convection. The arc motion is therefore generated by the Lorentz force and the pressure gradient produced by non-uniform heating since the electrical power input is confined within the arc region. In practice, these two causes for the generation of arc motion cannot be separated as they are closely coupled.

#### 4.4.3.1 The magnetic field produced by the coil and that produced by the current within the arc

The arcing current passing through the coil produces a magnetic field in r-z plane. Eddy currents in the metallic components (Figure 4.1) also contribute to the magnetic fields. In addition, the eddy currents make the magnetic field lag behind the change in current. This lag is commonly referred to as the phase lag. The phase lag is beneficially utilised for the arc extinction [102]. The contours of the constant magnitude of the magnetic vector potential at given instants are shown in Figure 4.16, where the difference in magnitudes between two adjacent contours is set at 0.0002. These contours represent magnetic field lines. The magnitude of the magnetic density is high in the region where the contours are densely populated. This is apparent in the region in the vicinity of the steel cylinder. Since the permeability of steel is much greater than those for SF6 and copper, the magnetic field lines enter or leave the surface of the steel part at an angle close to 90 degrees. Within the steel part, the magnetic field lines are nearly parallel to the surface.

Saturation of steel will change the magnetic field around and within the steel part. The configuration of the magnetic field lines shown in Figure 4.16 indicates that the magnetic field has not reached quasi-steady sinusoidal state as the fields at 5ms and 15ms still show differences at the back (away from the arcing region) end of the steel tube. The region of interest is the one between the two contacts where the arc burns.

The magnetic field produced by the coil in the region between two contacts is dominated by axial component. The magnetic flux density components (Br and Bz) derived from the magnetic vector potential are given in Figure 4.17.

The magnetic field produced by the current passing through the axisymmetrical arc is in the azimuthal direction. For the interrupter under investigation the calculation of magnetic field becomes a non-linear problem if the permeability of the steel tube varies substantially with the magnetic flux density. For the peak arcing current of 10kA, the permeability of the steel is essentially constant for the system under investigation. Thus, we use superposition theorem to compute the magnetic field due to the current passing through the arc by assuming that the eddy current inside the arc induced by the changing magnetic field due to coil and that due to the time variation of the current passing the arc are small in comparison with the arcing current itself. This is confirmed by the orders of magnitude estimate of the eddy current produced by the magnetic field of the coil (Figure 4.16) and by the azimuthal field produced by the current passing through the arc. The azimuthal magnetic field can be easily calculated from equation (3.12). Typical results are shown in Figure 4.18.

**The direction of the current in the coil**

⊙ : Coming out of the paper

⊗ : Going into the paper

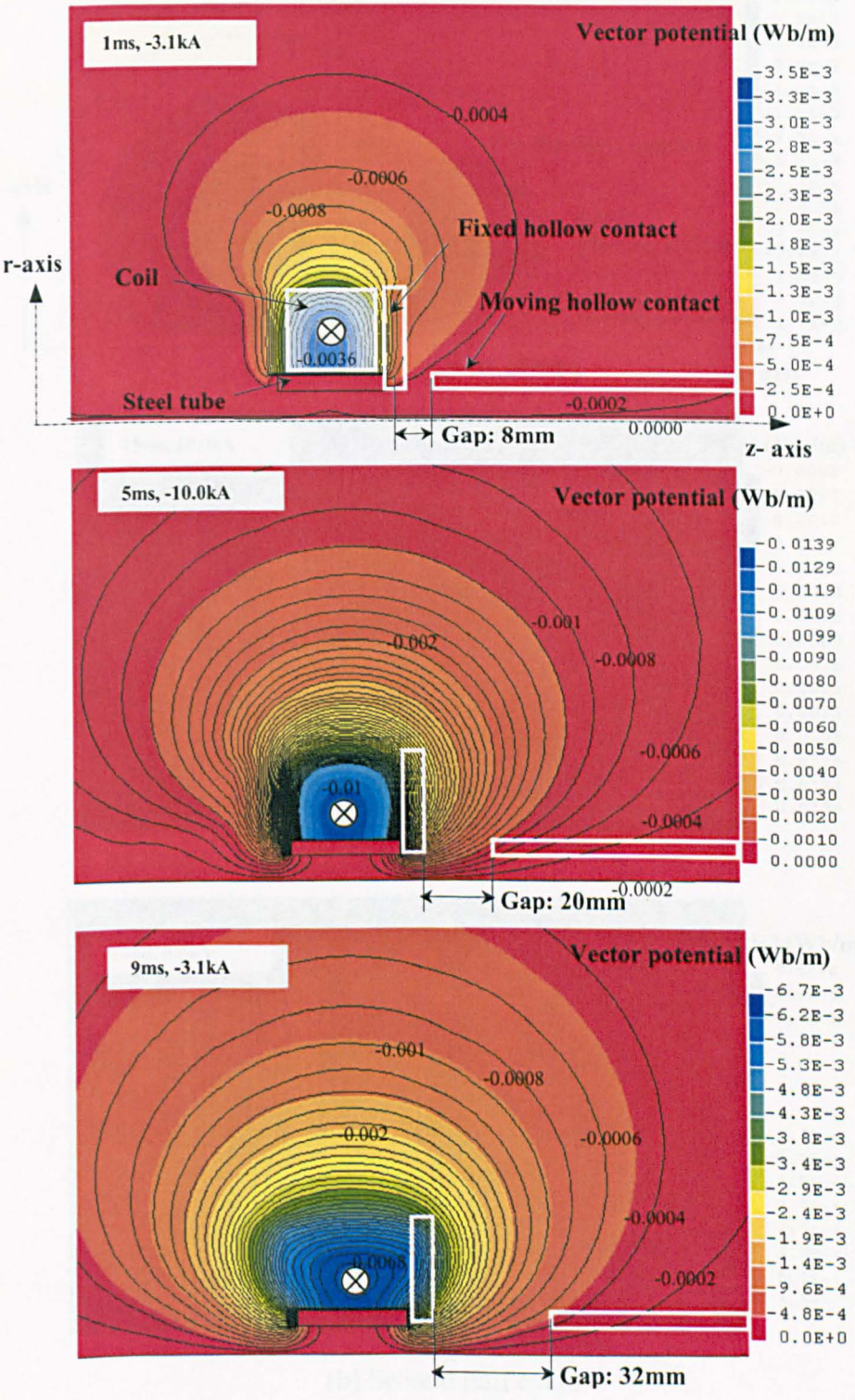


(a) First half cycle

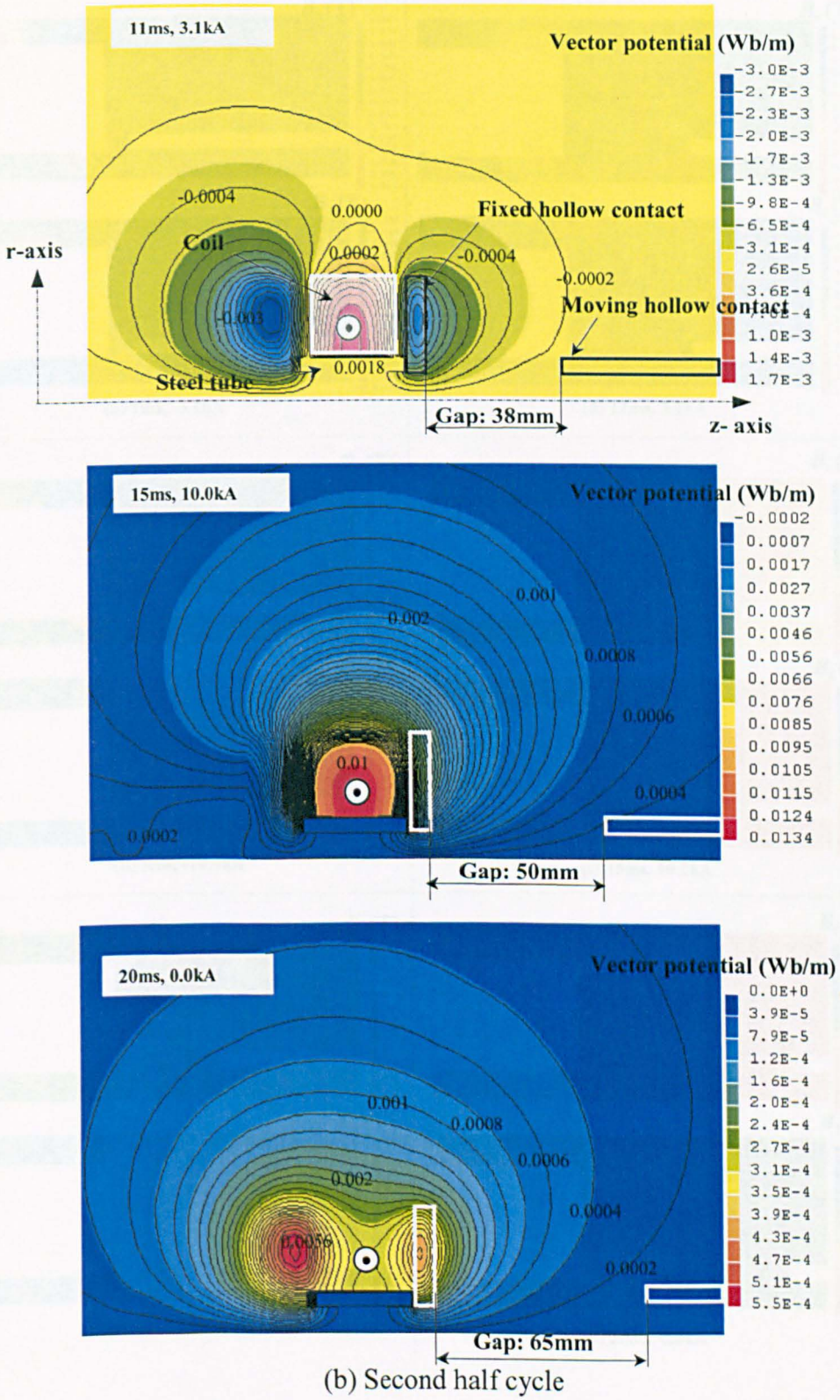


(b) Second half cycle

**Figure 4.16** Vector potential distributions around the coil at 1.0ms, 5.0ms, 9.0ms, 11.0ms, 15.0ms and 20.0ms

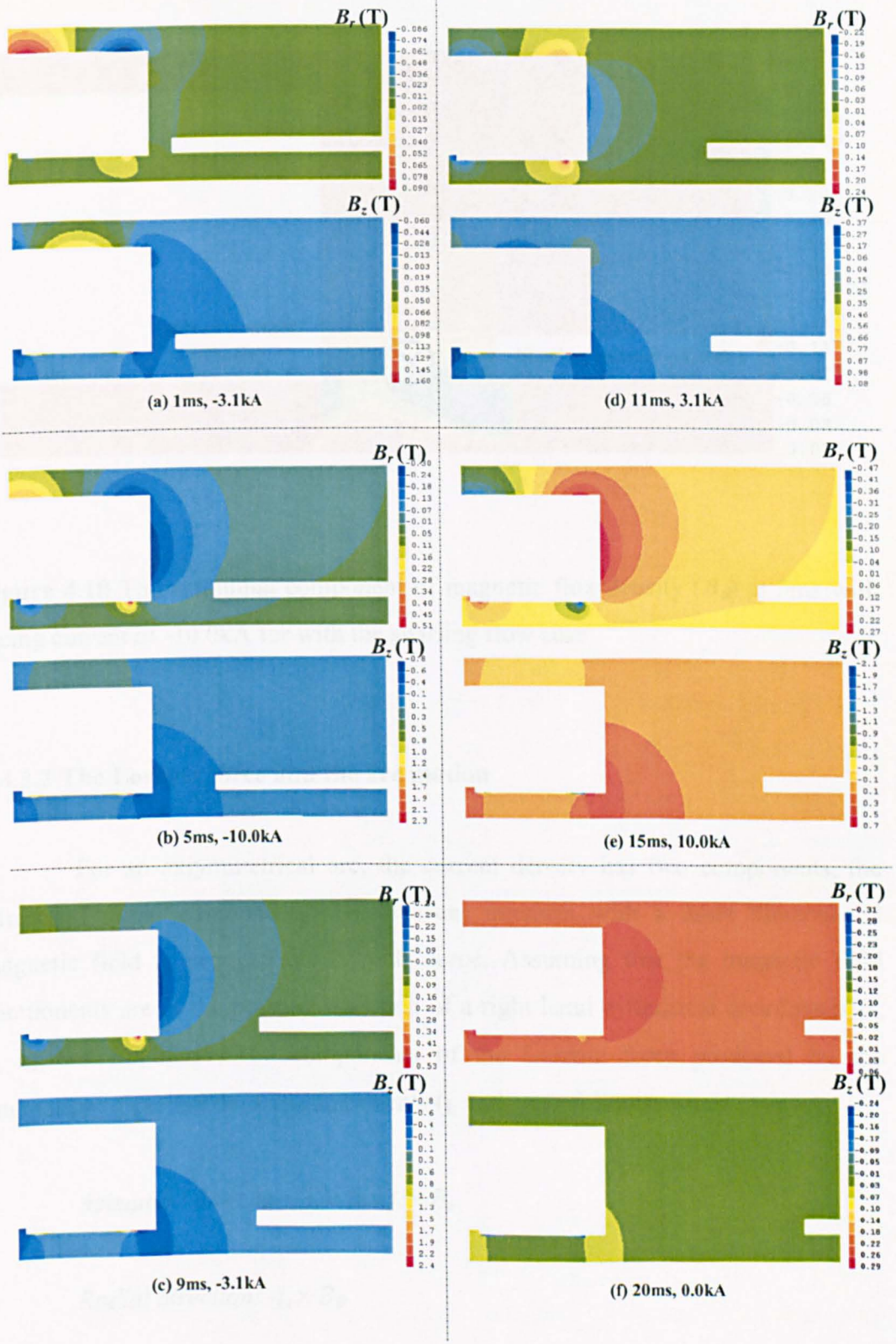


**Figure 4.17** Magnetic flux (radial magnetic flux $B_r$, axial magnetic flux $B_z$) at 1.0ms, 5.0ms, 9.0ms, 11.0ms, 15.0ms and 20.0ms.

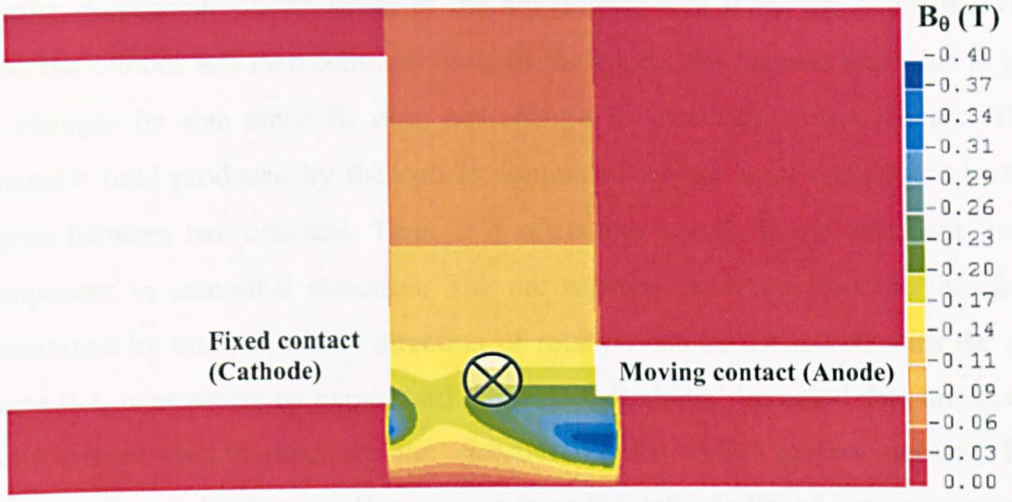


**Figure 4.18** The azimuthal component of magnetic flux density ($B_\theta$) at 5ms with arcing current of -10.0kA for with the swirling flow case

#### 4.4.3.2 The Lorentz force and the arc motion

For an axiymmetrical arc, the current density has two components, the axial and radial components. This current interacts with a three dimensional magnetic field to produce the Lorentz force. Assuming that the magnetic field components are in the positive direction of a right hand cylindrical coordinates (r, θ, z), we can derive the components of the Lorentz force produced by the interaction of current density components ($j_r$ and $j_z$) as follows:

*Azimuthal direction:* $j_z \times B_r - j_r \times B_z$

*Radial direction:* $-j_z \times B_\theta$

*Axial direction:* $j_r \times B_\theta$

For an axisymmetrical arc, the direction of the radial component of the current density, $j_r$, depends on the shape of the arc (Figure 4.7) If the arc expands away from the cathode and then contracts towards the anode, the Lorentz force due to $j_r \times B_z$ changes its sign since $B_z$ does not change its direction within the arc. The magnetic field produced by the coil is dominated by the axial component in the region between two contacts. Thus, it is often that $j_r \times B_z$ is the dominant force component in azimuthal direction. The arc rotation (swirling flow) is therefore determined by this force. The direction of rotation can be associated with the arc shape (i.e. contraction or expansion). However, it should be noted that arc shape alone cannot decide precisely the direction of the radial current density. For example, the arc in Figure 4.19 contracts from the cathode (fixed contact) towards the anode. However, the formation of the cathode spot makes the current lines converge towards the cathode spots. The two components of the azimuthal Lorentz force are in the same direction at point **B** but in opposite direction at point **A** (Figure 4.19). The azimuthal component of Lorentz force changes its direction, thus producing arc swirling in different directions. The azimuthal velocity at a current of –10kA (5ms) is shown in Figure 4.19. Since the gas is at a high temperature (thus very low density), the azimuthal velocity can reach a very high value. The change in direction of the azimuthal Lorentz force produces two arc sections rotating in opposite directions. The azimuthal movement of the arc during the whole arcing period is given in Figure 4.20. Such high azimuthal velocity has strong influence on the distribution of pressure within the arc through its coupling with the radial momentum balance. The change in pressure due to swirling motion in turn influences the axial velocity through axial momentum balance. Thus, the whole pressure field is changed by the azimuthal motion.

The radial component of the Lorentz force is the result of the interaction of the current passing through the arc with its self-generated magnetic field. This force always points towards the arc axis. Maecker (Maecker H, Z. Phys. Vol. 148, 198, 1955) first pointed out that this force produces a higher axis pressure where arc cross section is small and a lower axis pressure where the arc cross section is larger. Thus, a negative pressure gradient is established in the region where the arc

expands, thus resulting in an acceleration of the plasma. This force is also commonly associated with the cause of the so-called magnetic pumping and a simple expression can be derived for the axis pressure by assuming that the inertia associated with the radial motion is negligible. Thus, the radial pressure gradient is balanced by the radial Lorentz force. For the arc under investigation such a simplification is no longer valid for two reasons. One is that the azimuthal movement substantially changes the radial moment balance, which changes the pressure. The other is that the radial velocity can be comparable with the axial velocity and the inertia term in the radial moment equation can no longer be neglected. However, the concept of magnetic pumping is helpful in visualising the axial motion of the arc. Our computer simulated results indicate that the acceleration from small arc cross section to large cross section is still valid although the axis velocity cannot be computed using the magnetic pumping approach.

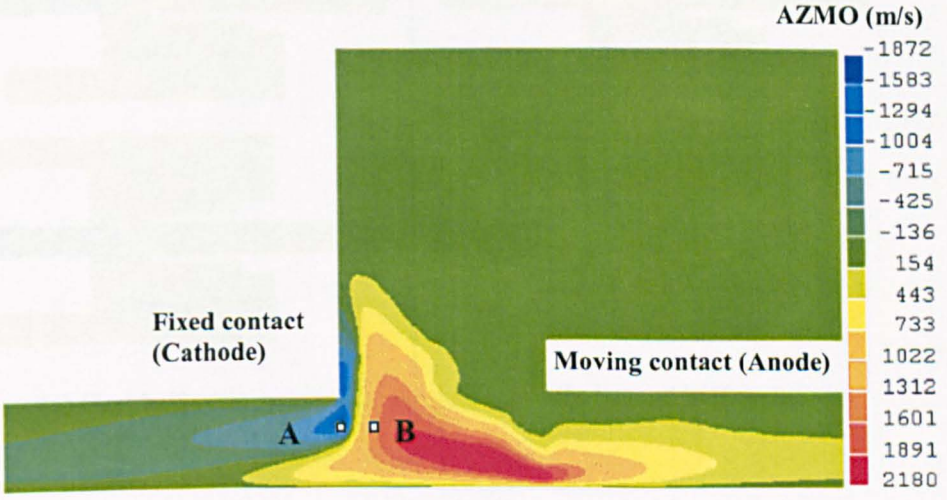


**Figure 4.19** Azimuthal velocity (*AZMO*) distribution between contacts at 5ms with arcing current of -10.0kA for with the swirling flow case


**Figure 4.20** Azimuthal velocity (*AZMO*) distribution between contacts at (a) first half cycle 2ms, 4ms, 6ms, 8ms, 10ms and (b) second half cycle 12ms, 14ms, 16ms, 18ms, 19.6ms. The peak current is 10kA.

### 4.4.4 Flow in the expansion volume, vortices and pressure waves

The temperature and velocity vector in the expansion volume for two cases (with swirling flow and without swirling flow) are shown in Figure 4.21 for eight instants in the high current phase. The position of the moving contact and current waveform can be found in Figure 4.1. Pressure rise in the expansion volume starts to rise at 2.0ms (Figure 4.9) when the arc column blocks both hollow contacts after arc initiation and is relatively small in the first half cycle since the incoming hot gas flow is not enough to supply input power to increase the pressure. However, pressure difference between two cases is large with passing the first peak current (-10kA), because the swirling flow enhances the hot gas flowing to mix with the cold gas in front of fixed contact surface. After 5.0ms, the current is decreasing and the moving hollow contact has been away from the fixed contact. Gas is more flowing out from the expansion volume to both outlets since the pressure inside both the hollow contacts has become lower than that in the expansion volume. When the current enters into its second loop, pressure variation is still small up to 14.0ms due to the energy balance. After this period the pressure rise in the expansion volume for with swirling flow case starts to increase rapidly again (Figure 4.9) with current, because the arc column affected by swirling flow becomes bigger to block both the hollow contacts and introduce the hot gas into the expansion volume. The hot gas in the swirling flow case enters into the expansion volume and is turned around by the wall. The cold patch moves effectively into the arc column when the current approaches its second zero in the swirling flow case. The pressure difference of both cases (with swirling flow and without swirling flow) is larger due to swirling flow effect as mentioned in previous section.

Gas flow interaction in the expansion volume for with swirling flow results in vortices, which are shown in Figure 4.21. The circulation region is formed when the hot gas enhanced by the swirling flow moves into the expansion volume along the surface of fixed contact, and then reaches the wall.

Figure 4.9 indicates that there are more than one peak in the computed pressures during the period from 16ms to 20ms. Detailed analysis of computed velocity and pressure fields around these peaks shows that the pressure variation at

the measurements location is caused by propagation of pressure waves in the expansion volume. The time interval between two adjacent peaks is approximately 1.5ms. Gas temperature in the expansion volume is between 300K to 1000K in the path from the pressure measurement location to the point A (Figure 4.1). Taking an average sonic speed of the gas to be 200m/s, corresponding to 700K, the time for the pressure wave to propagate from the measurement location to the point A is, therefore, 1ms over the length of 152mm. This matches roughly the 1.5ms time interval between two adjacent pressure peaks. Despite the propagation of the pressure wave in this period, hot gas continues to be pumped into the expansion volume due to swirling flow.

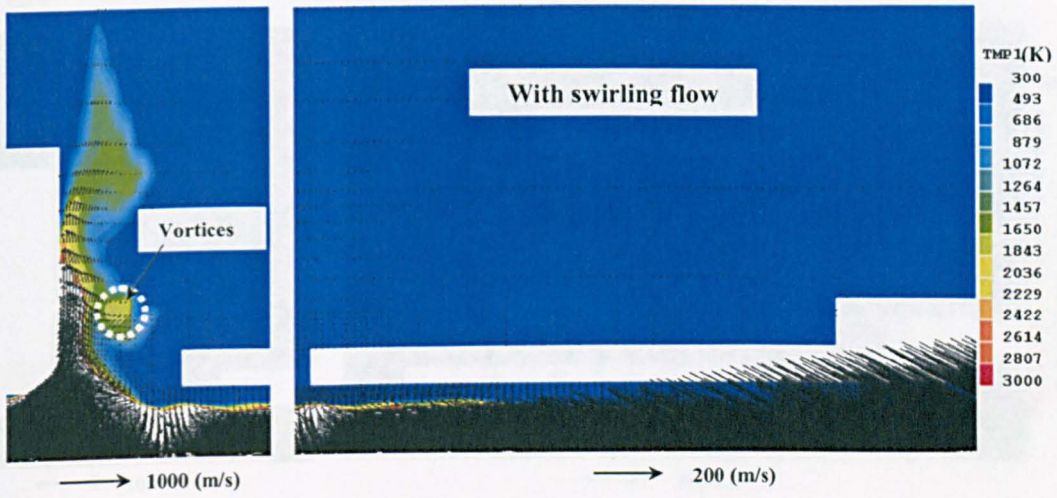
With swirling flow
Vortices
TMP1(K)
300
493
686
879
1072
1264
1457
1650
1843
2036
2229
2422
2614
2807
3000
1000 (m/s)
200 (m/s)

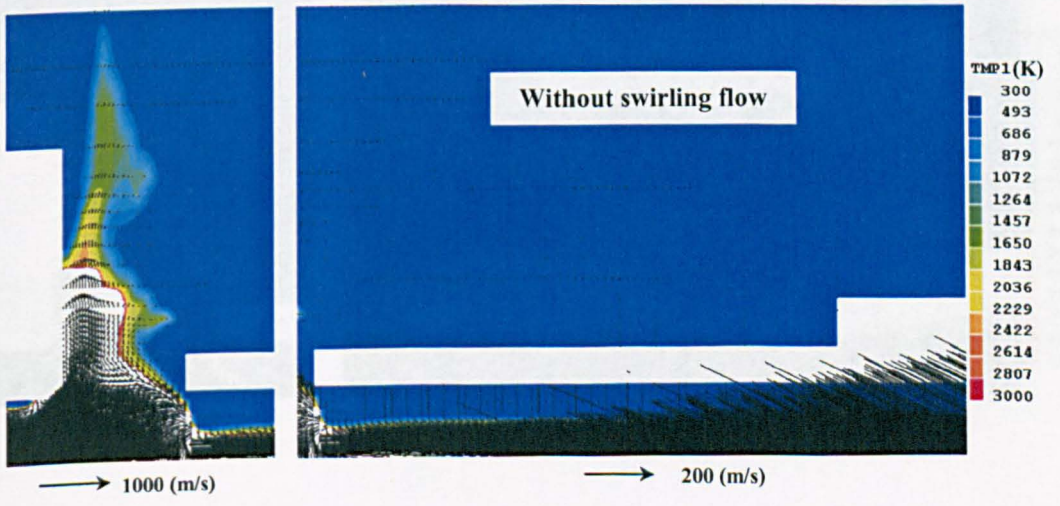
Without swirling flow
TMP1(K)
300
493
686
879
1072
1264
1457
1650
1843
2036
2229
2422
2614
2807
3000
1000 (m/s)
200 (m/s)

**(a) 4.0ms, -9.5kA**

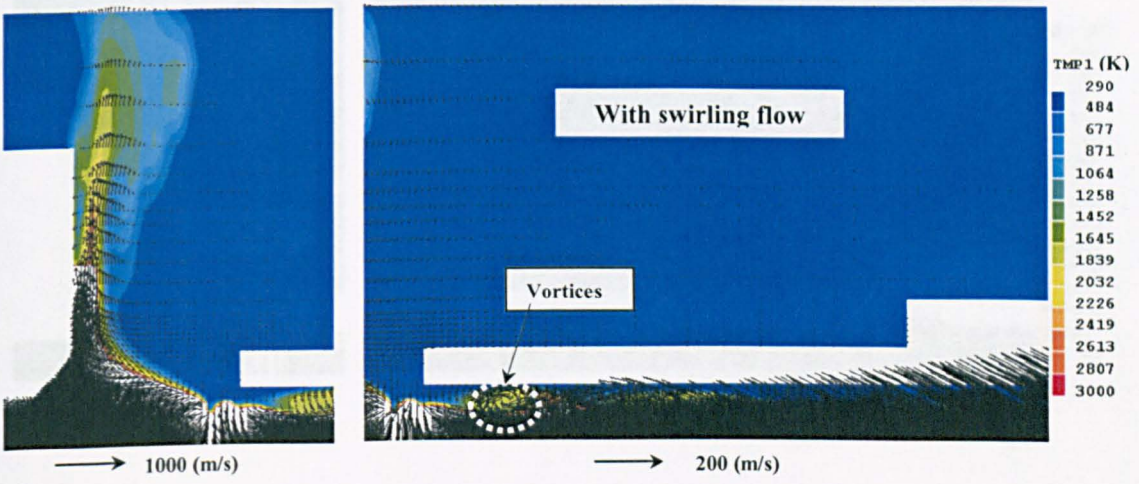
With swirling flow
Vortices
TMP1 (K)
290
484
677
871
1064
1258
1452
1645
1839
2032
2226
2419
2613
2807
3000
1000 (m/s)
200 (m/s)

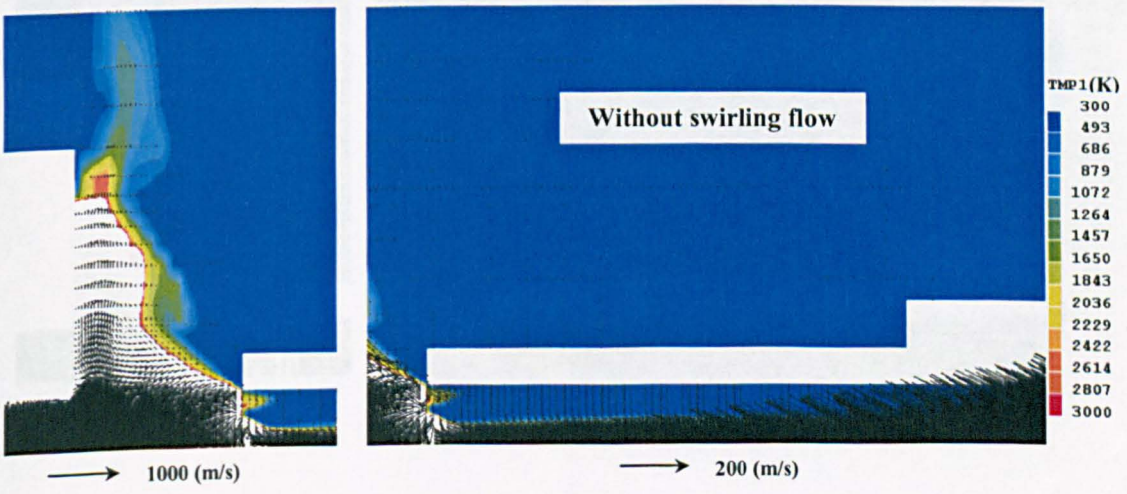
Without swirling flow
TMP1(K)
300
493
686
879
1072
1264
1457
1650
1843
2036
2229
2422
2614
2807
3000
1000 (m/s)
200 (m/s)

**(b) 6.0ms, -9.5kA**

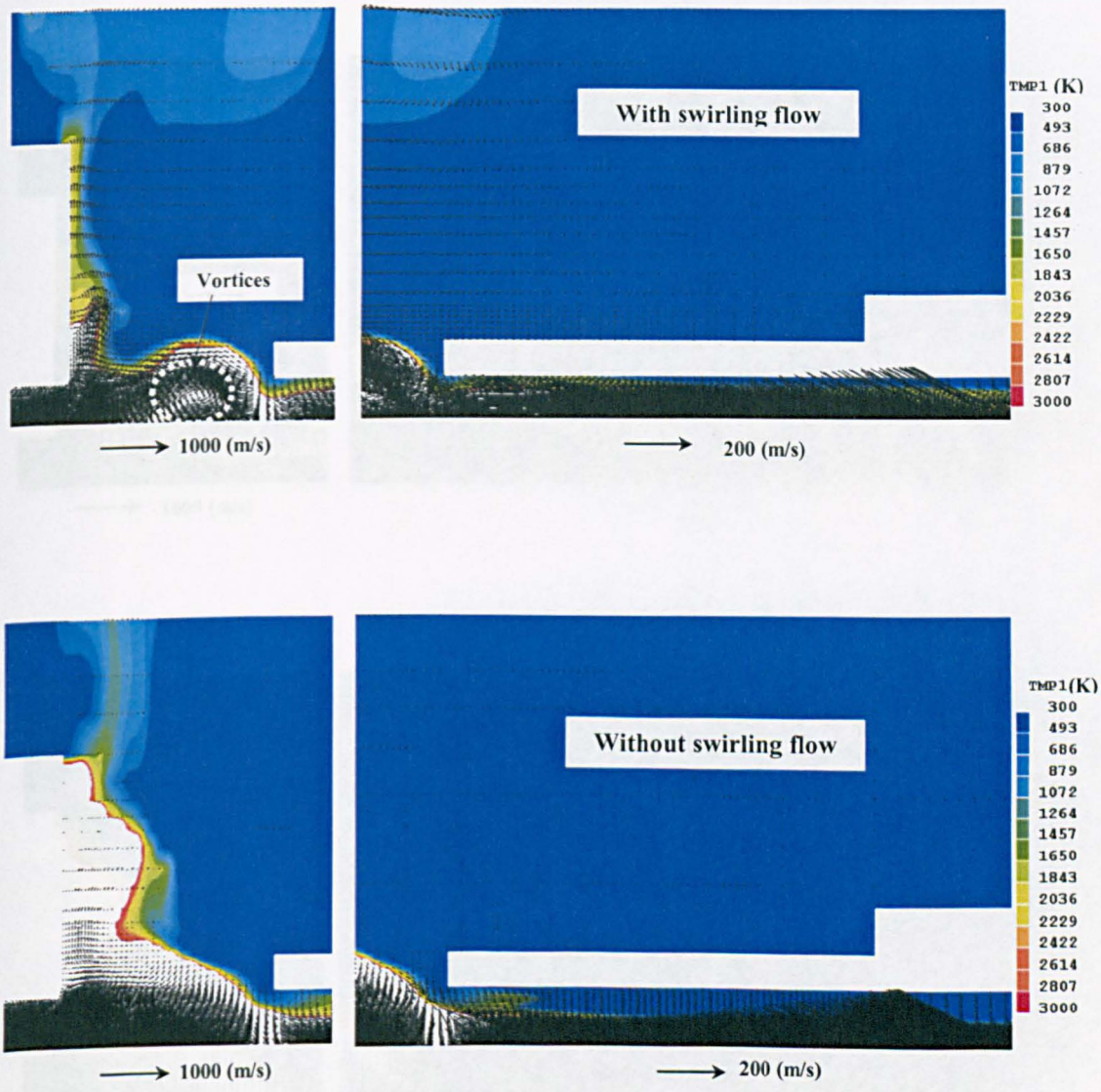
Vortices
With swirling flow
TMP1 (K)
300
493
686
879
1072
1264
1457
1650
1843
2036
2229
2422
2614
2807
3000
1000 (m/s)
200 (m/s)
Without swirling flow
TMP1(K)
300
493
686
879
1072
1264
1457
1650
1843
2036
2229
2422
2614
2807
3000
1000 (m/s)
200 (m/s)

**(c) 8.0ms, -5.9kA**

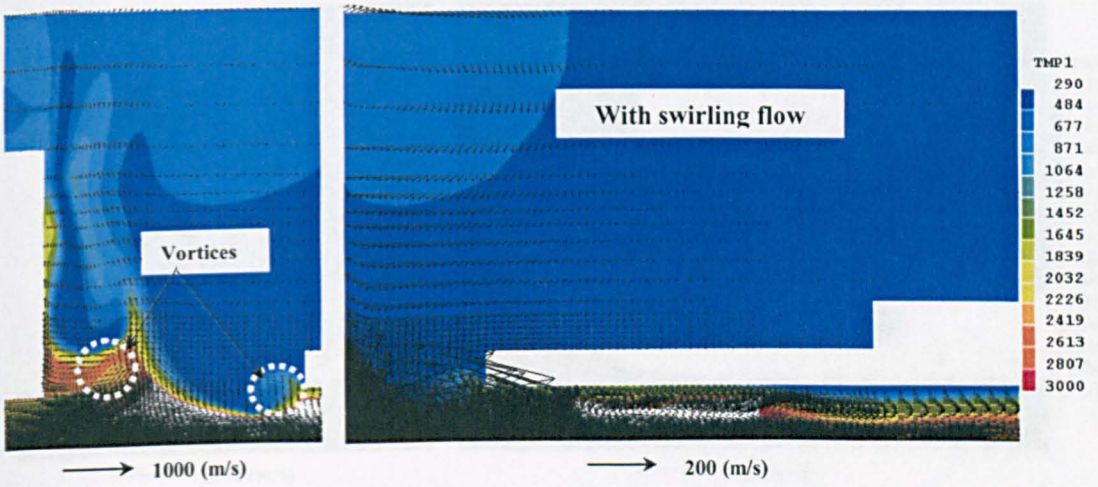
Vortices
With swirling flow
TMP1
290
484
677
871
1064
1258
1452
1645
1839
2032
2226
2419
2613
2807
3000
1000 (m/s)
200 (m/s)

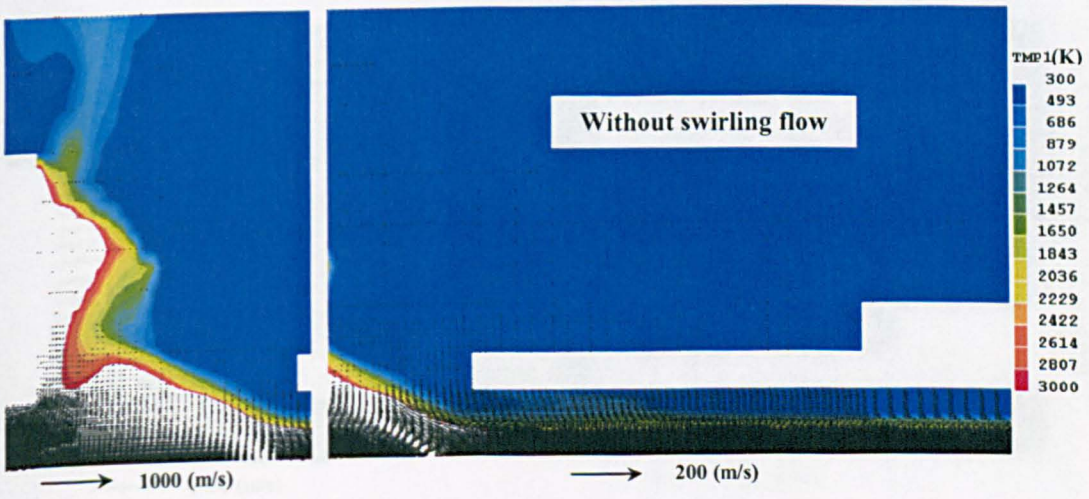
Without swirling flow
TMP1(K)
300
493
686
879
1072
1264
1457
1650
1843
2036
2229
2422
2614
2807
3000
1000 (m/s)
200 (m/s)

**(d) 10.0ms, -9.5kA**

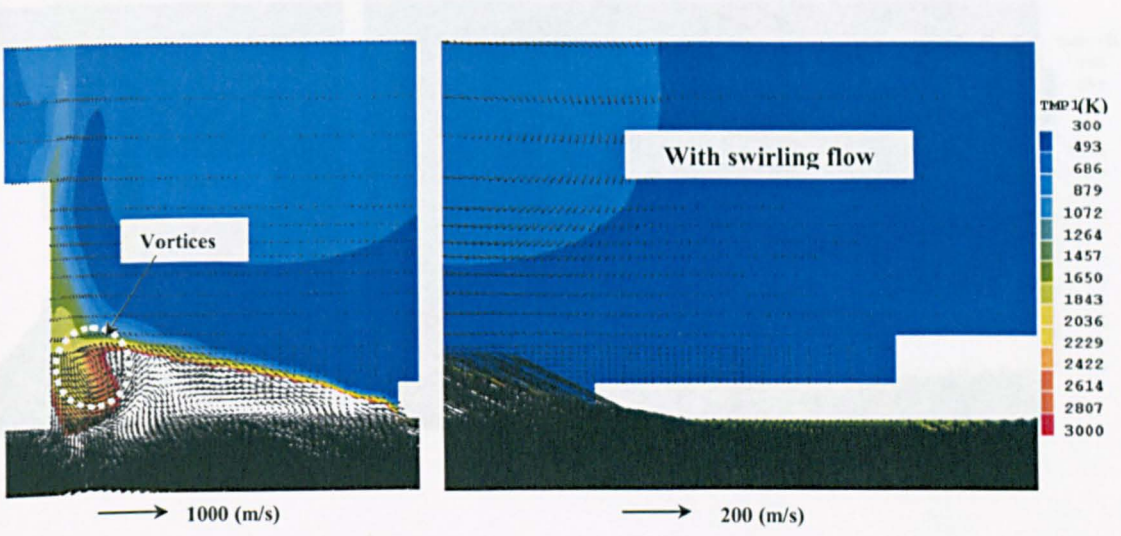
Vortices
With swirling flow
TMP1(K)
300
493
686
879
1072
1264
1457
1650
1843
2036
2229
2422
2614
2807
3000
1000 (m/s)
200 (m/s)

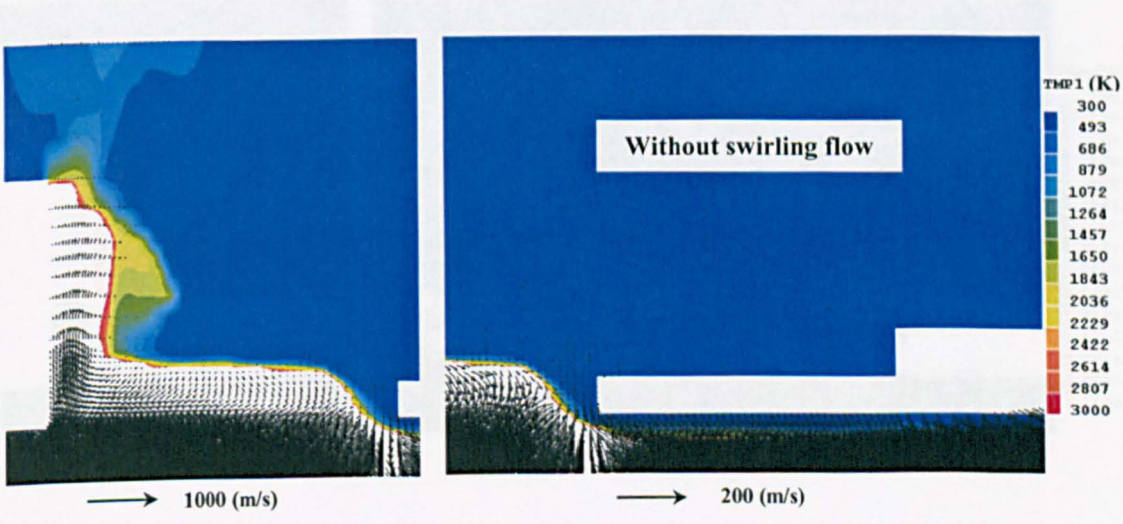
Without swirling flow
TMP1 (K)
300
493
686
879
1072
1264
1457
1650
1843
2036
2229
2422
2614
2807
3000
1000 (m/s)
200 (m/s)

**(e) 14.0ms, 9.5kA**

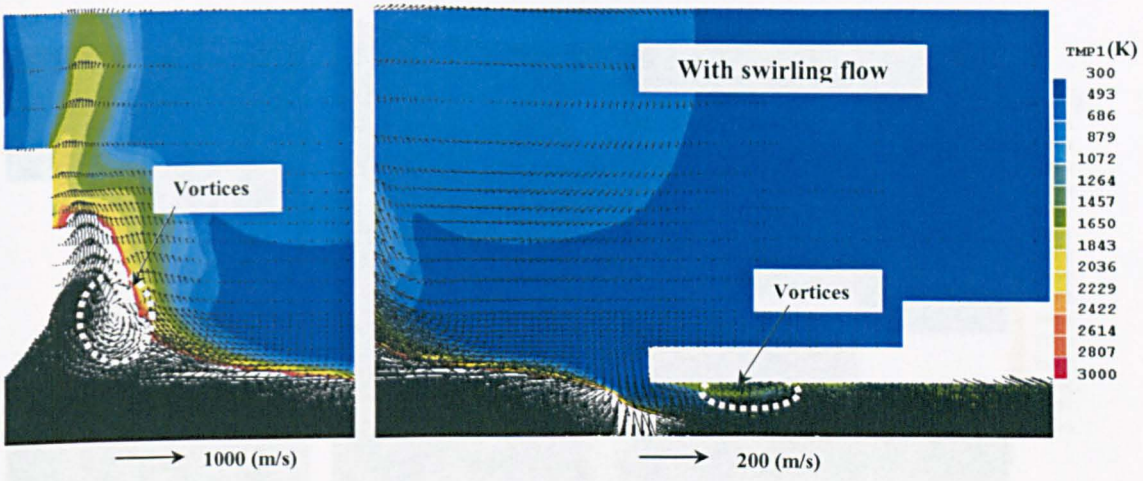
Vortices
With swirling flow
Vortices
TMP1(K)
300
493
686
879
1072
1264
1457
1650
1843
2036
2229
2422
2614
2807
3000
1000 (m/s)
200 (m/s)

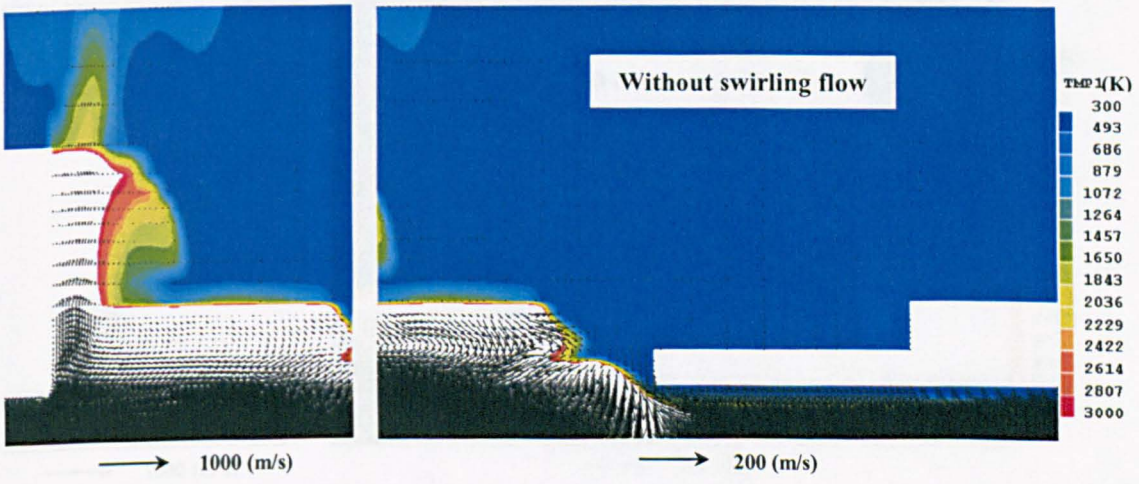
Without swirling flow
TMP1(K)
300
493
686
879
1072
1264
1457
1650
1843
2036
2229
2422
2614
2807
3000
1000 (m/s)
200 (m/s)

**(f) 16.0ms, 9.5kA**

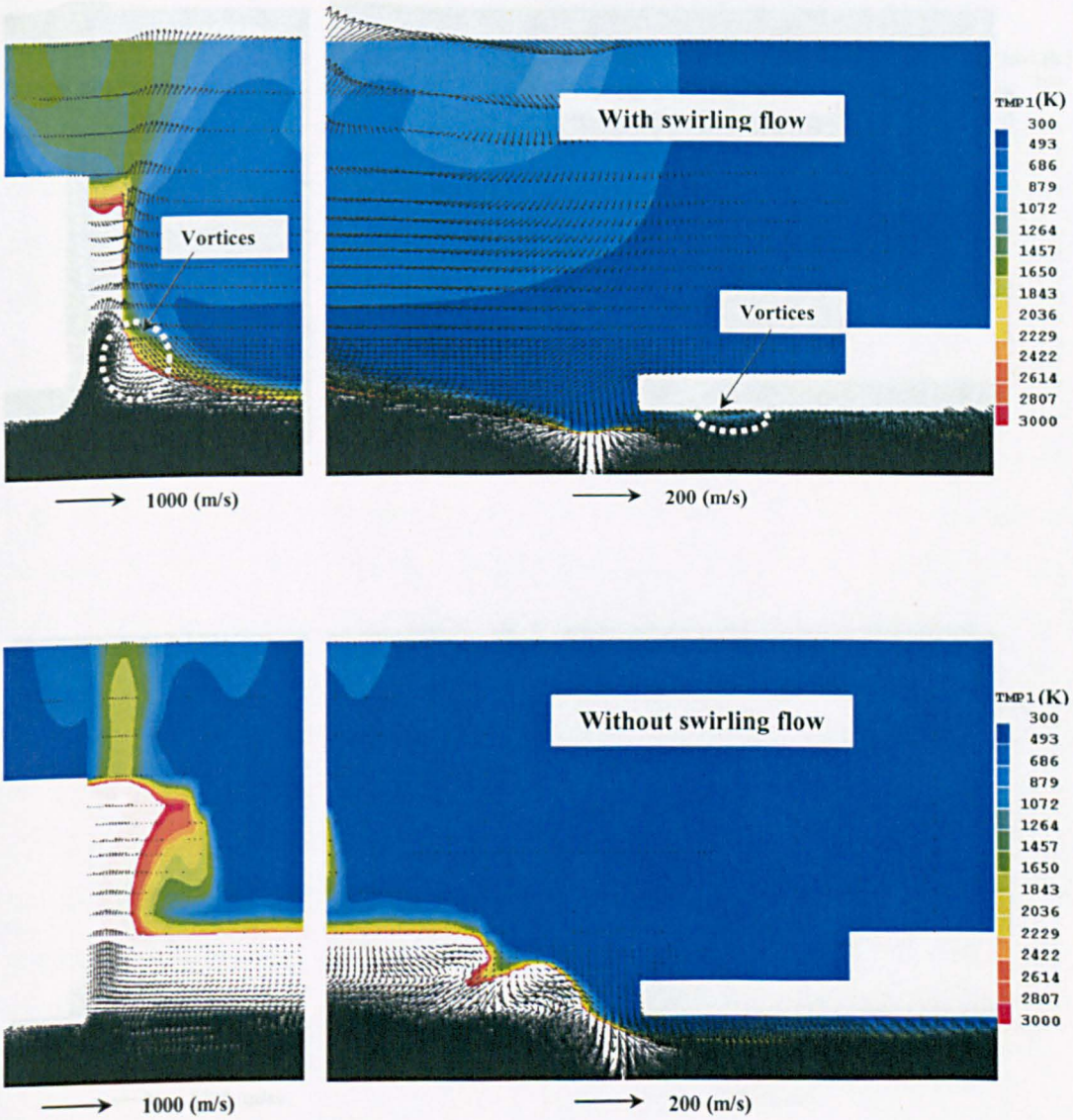
With swirling flow
Vortices
Vortices
TMP1(K)
300
493
686
879
1072
1264
1457
1650
1843
2036
2229
2422
2614
2807
3000
1000 (m/s)
200 (m/s)
Without swirling flow
TMP1(K)
300
493
686
879
1072
1264
1457
1650
1843
2036
2229
2422
2614
2807
3000
1000 (m/s)
200 (m/s)

**(g) 18.0ms, 5.9kA**

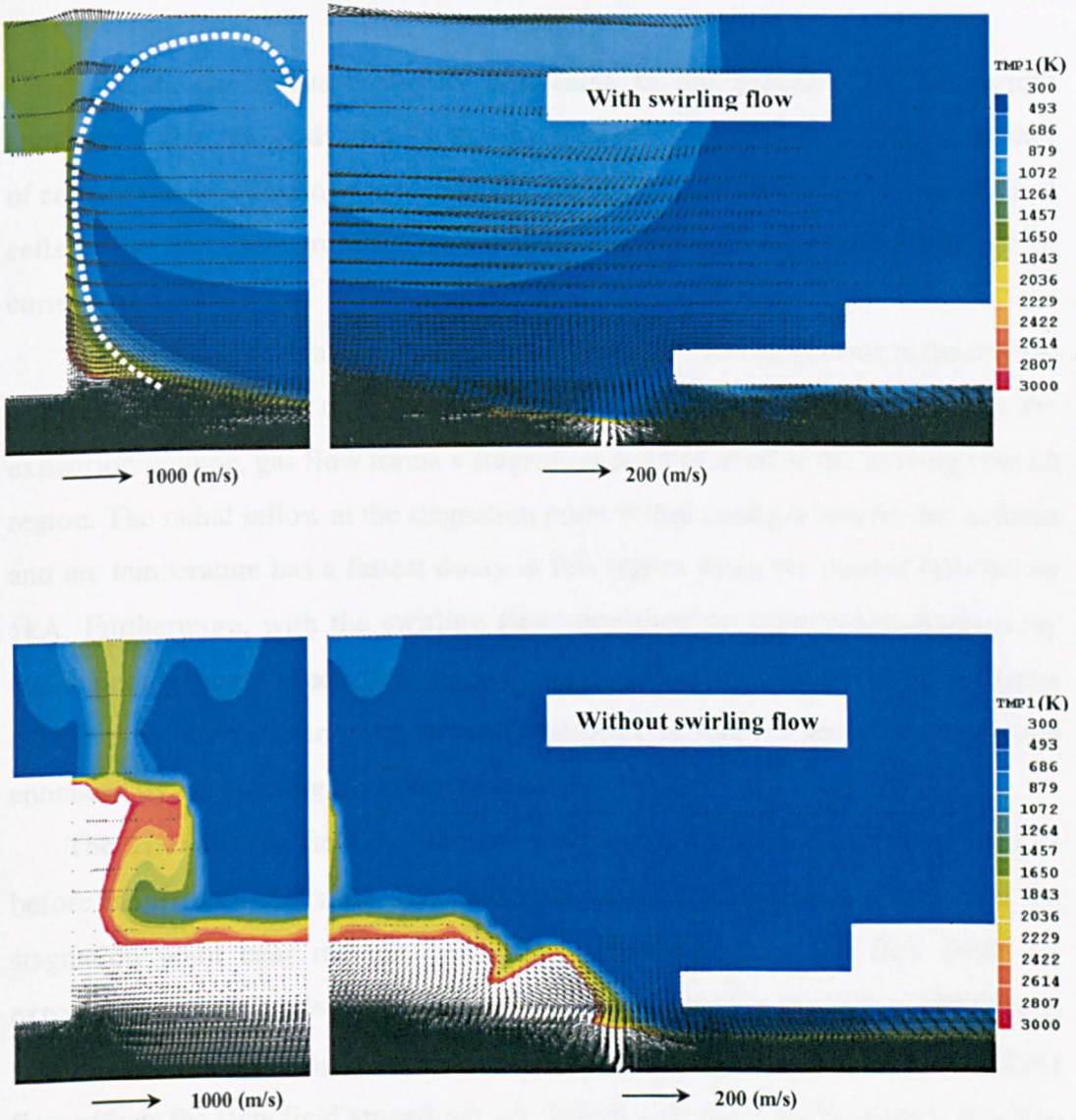


**(h) 19.6ms, 1.3kA**

**Figure 4.21** Temperature and velocity vector in the expansion volume at eight instants in the high current phase. (a), (b), (c), (d) : first half cycle / (e), (f), (g), (h) : second half cycle. The peak current is 10kA. The position of the solid contact and current waveform are shown in Figure 4.1.

### 4.4.5 The current zero period

#### 4.4.5.1 Pre-current zero

Since the arc radius is rapidly decreasing in this period when the current approaches zero, the grids near the axis must be refined to ensure sufficient number of cells in the arc column at low currents. For the present simulation, the number of cells in the first 2mm from the axis is increased from 25 to 45 at 1.13kA before current zero.

The arc has its maximum temperature in front of moving contact in the second half cycle and the arc temperature is 20000K at 19.6ms (Figure 4.11). In the expansion volume, gas flow forms a stagnation point in front of the moving contact region. The radial inflow at the stagnation point brings cold gas into the arc column and arc temperature has a fastest decay in this region when the current falls below 1kA. Furthermore, with the swirling flow case there is more temperature decay inside both hollow contacts than that without swirling flow case as shown in Figure 4.22 due to the difference of the axial velocity in that region which has been enhanced by the swirling flow (Figure 4.8).

The axial electric field on the axis is shown in Figure 4.23 for three instants before the final current zero. The maximum axial electric fields are located at the stagnation point near moving hollow contact where the cross flow from the expansion volume cools the arc and forms a minimum in arc radius (4000K) as shown in Figure 4.24. Figure 4.25 shows that the vortex due to the residual swirling flow affects the flow field around the arc column in front of fixed contact, which in turn has considerable influence on arc radius. Thus, axial electric field with swirling flow is much higher than that without swirling flow in front of fixed contact.

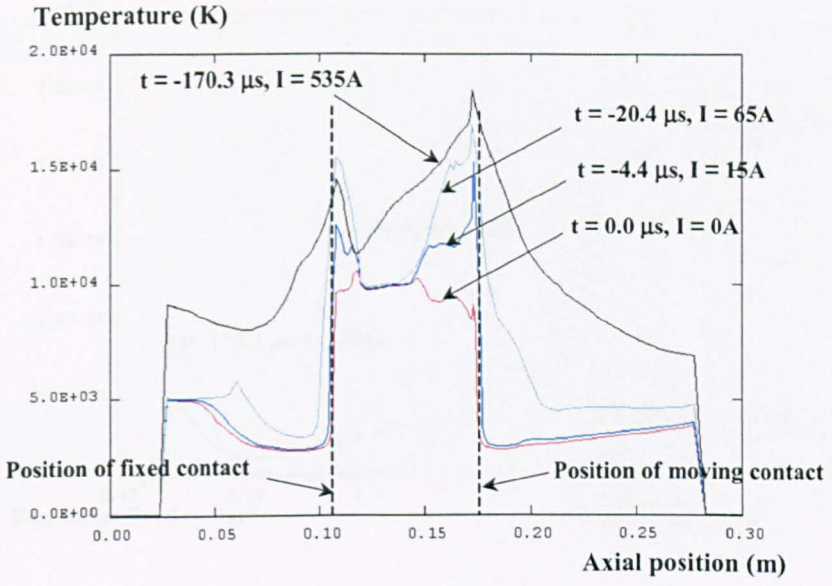


(a) With swirling flow

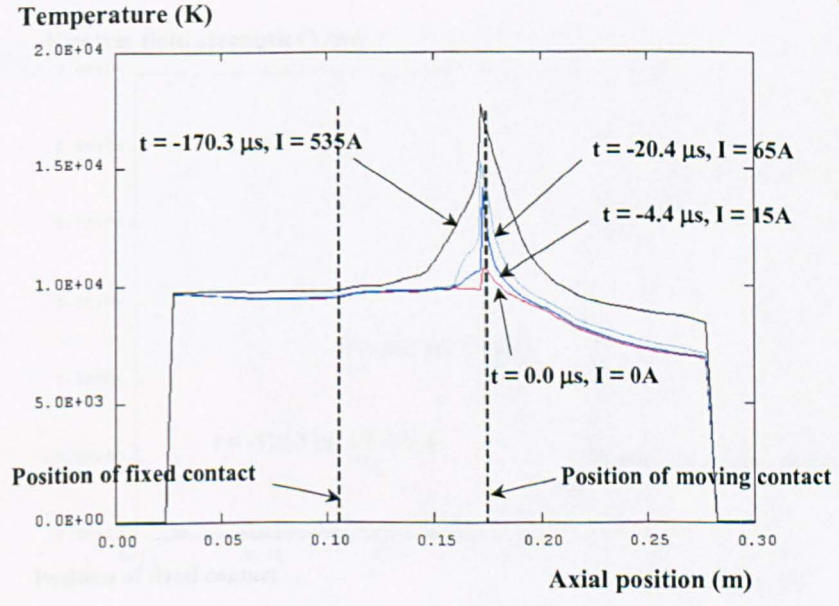


(b) Without swirling flow

**Figure 4.22** Axis temperature before the final current zero. Time shown in this figure is relative to the instant of current zero.

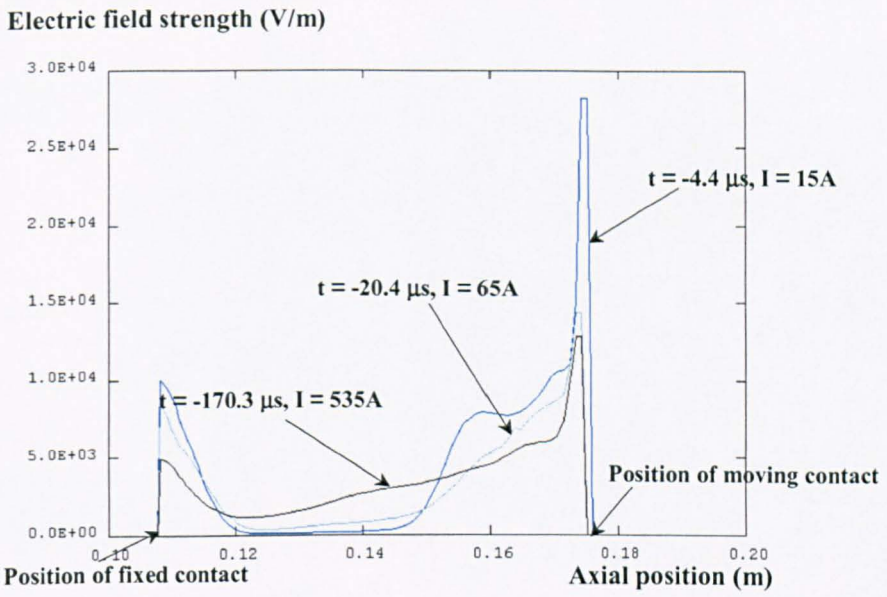


(a) With swirling flow

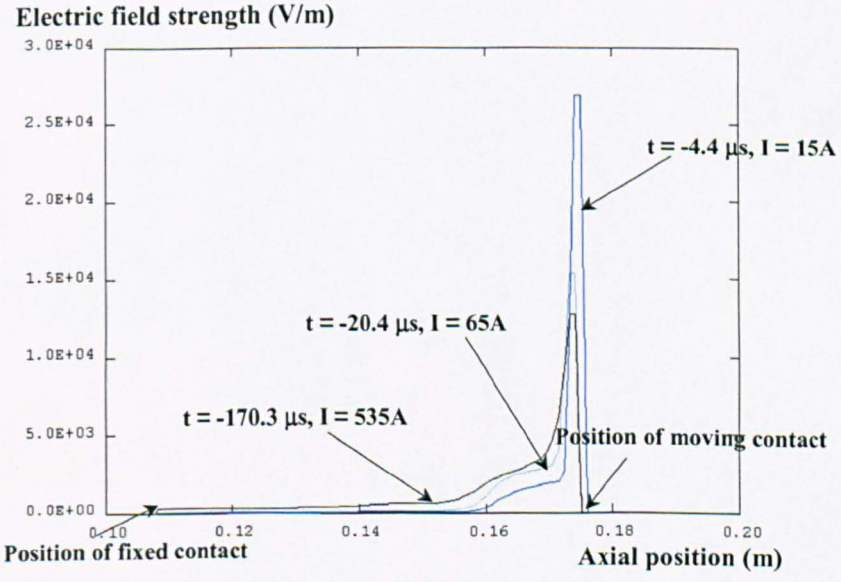


(b) Without swirling flow

**Figure 4.23** Axial electric field before current zero. Time shown in this figure is relative to the instant of current zero.

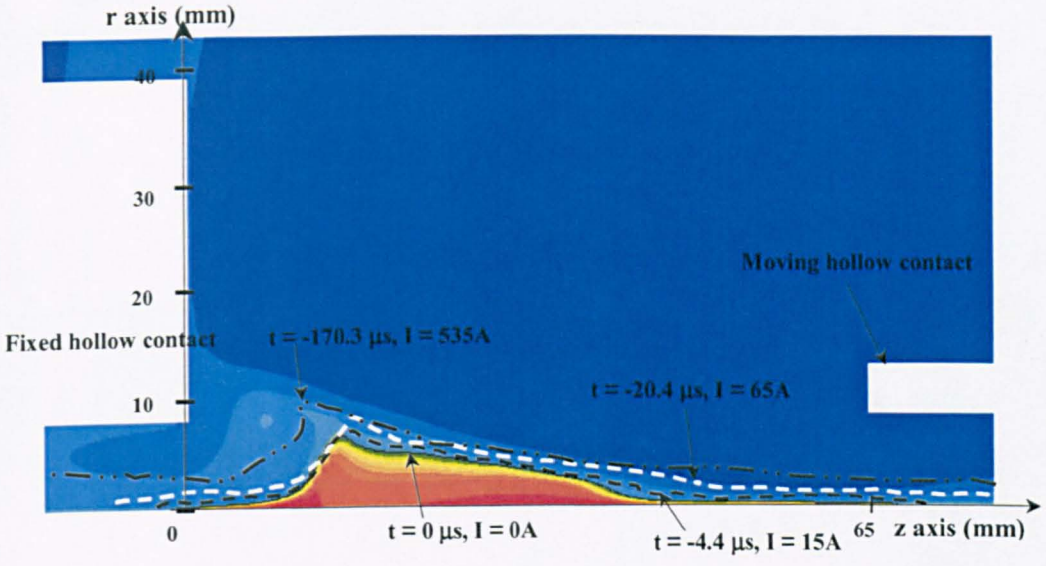


(a) With swirling flow

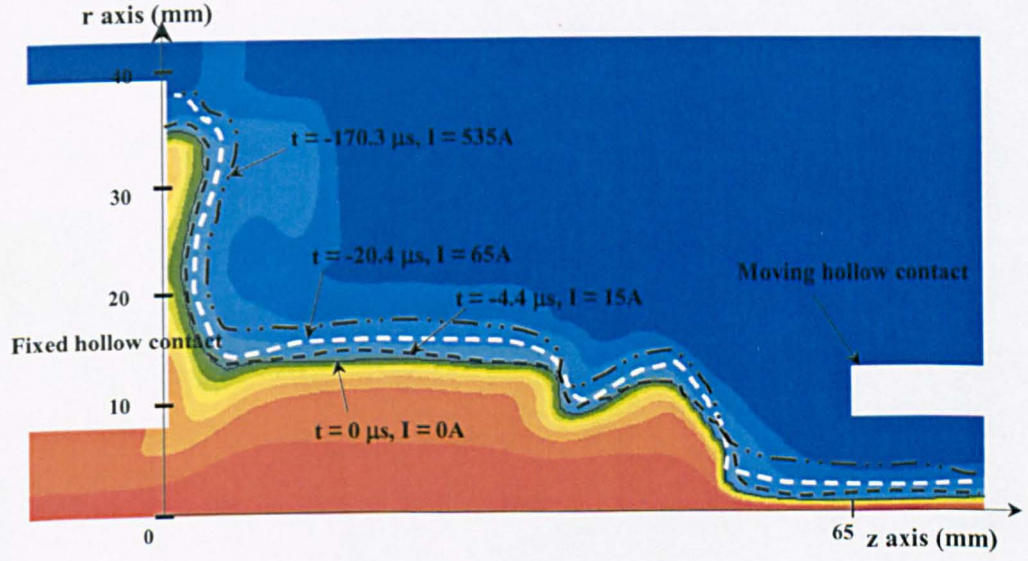


(b) Without swirling flow

**Figure 4.24** Arc radius (4000K) before the final current zero. Time shown in this figure is relative to the instant of current zero.

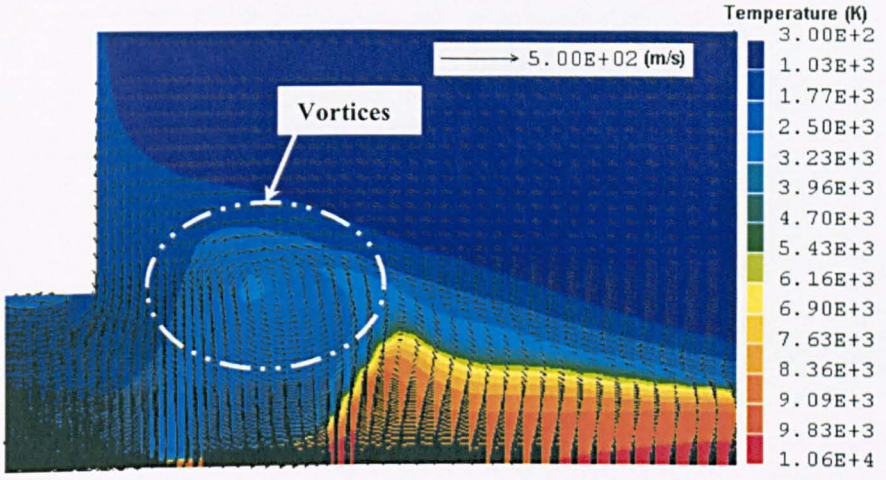


**Figure 4.25** Temperature and velocity vectors at the final current zero for with swirling flow case.

### 4.4.5.2 Thermal recovery process

The thermal interruption capability of the circuit breaker is predicted in terms of the critical RRRV. The time scale for the thermal recovery process is usually a few microseconds after current zero. RRRV, which is defined as the value of dV/dt, is increased in small steps until it reaches a value at which the discharge current starts to increase exponentially, as shown in Figure 4.26. The thermal performance of this hybrid circuit breaker with the swirling flow case predicts a critical RRRV of 1.6kV/μs. In contrast, without the swirling flow the residual plasma is reignited, even though RRRV is very low (0.05kV/μs).

Arc extinction depends largely on turbulent cooling. The turbulence parameter in the Prandtl mixing length model must be calibrated by test results. A value of 0.1 for $c$ in question (2.24) is used to obtain the results in this section, which form a qualitative account of the thermal recovery process in the hybrid circuit breaker.

Figure 4.27 shows the decay of axis temperature for a recovery voltage of 1.6kV/μs at which our model predicts thermal recovery. The residual plasma has a very high rate of temperature decay where strong axis flow takes place in the front of both contacts as shown in Figure 4.28. The fastest decay occurs in the front of fixed hollow contact where the vortex (Figure 4.25) rapidly cools down the plasma. However, the temperature decay is slow at stagnation point between the two contacts and axis temperature in the hollow contact does not decay in the first 2μs after current zero since the cold gas from the expansion volume has yet negligible influence on the axis.

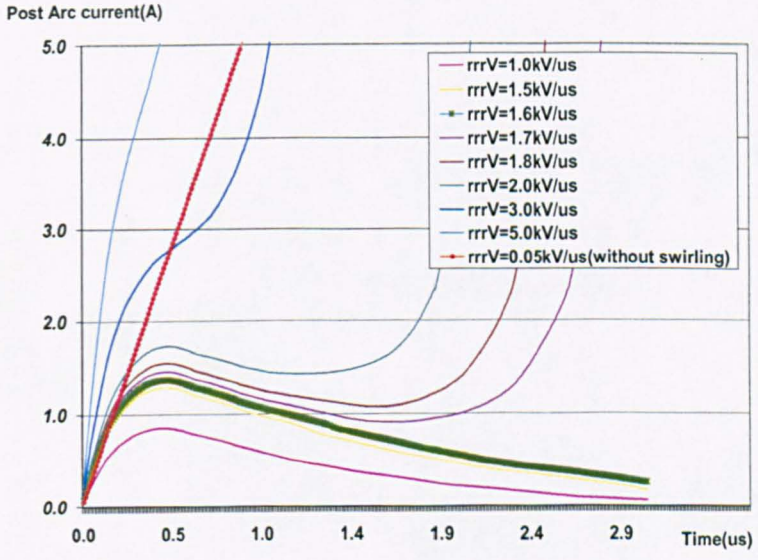


**Figure 4.26** Post arc current with different values of RRRV (dV/dt) for cases with and without swirling flow

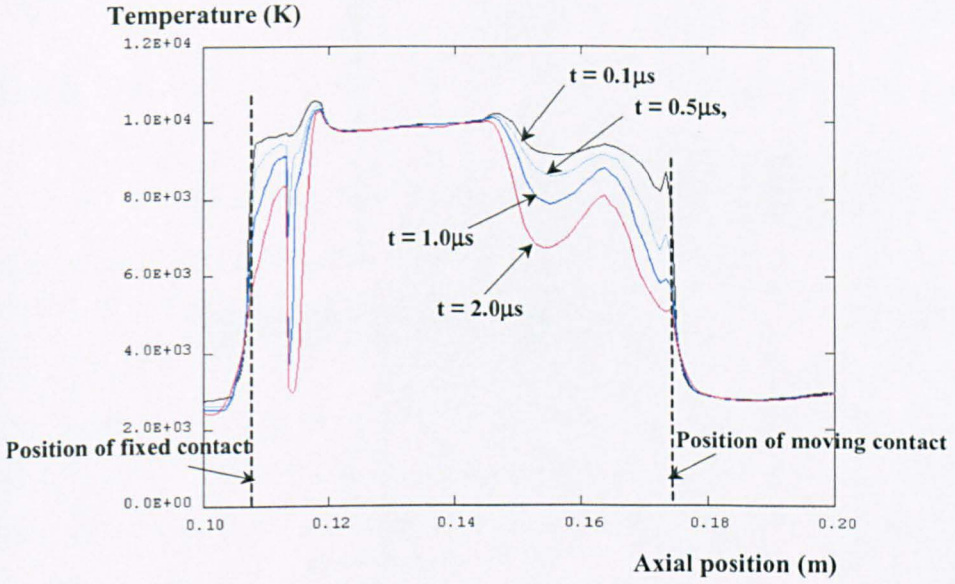


**Figure 4.27** Decay of axis temperature between the tips of the fixed and moving contacts after current zero for dV/dt = 1.6kV/μs. Time shown in this figure is relative to the instant of current zero.

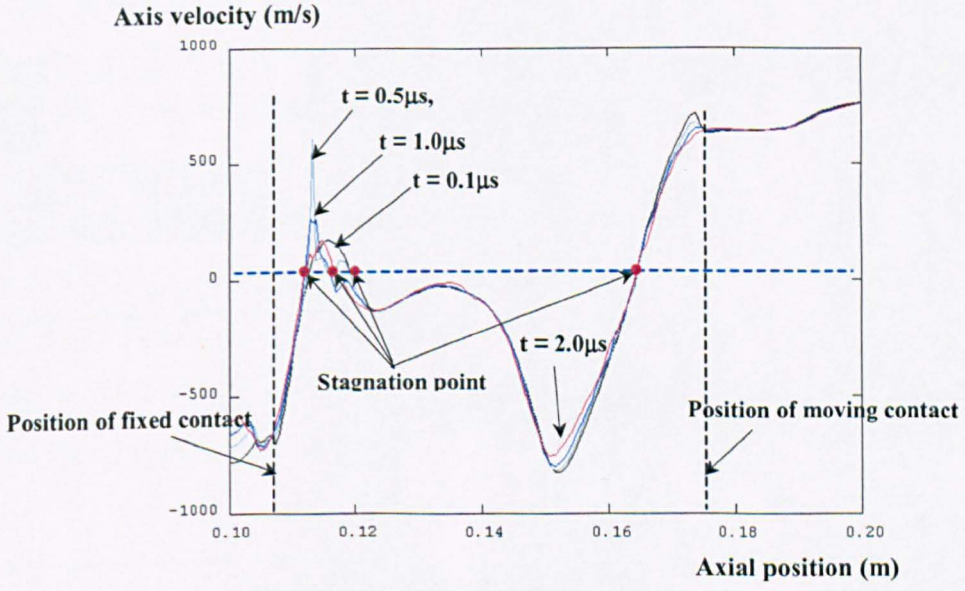


**Figure 4.28** Axis velocity between the tips of the fixed and moving contacts after current zero for dV/dt =1.6kV/μs. Time shown in this figure is relative to the instant of current zero.

## 4.5 Conclusions

The effects of swirling flow on the behaviour of a transient $SF_6$ arc in a hybrid circuit breaker have been investigated for the whole arcing period. The thermal interruption capability is established in terms of the critical rate of rise of recovery voltage. Typical results at various instants are presented and discussed. Results show that the generation of swirling flow by the strong magnetic field interacting with the current density inside the arc column is closely coupled with the shape of the arc column. In association with contact movement, complex flow situations are developed during the high current phase under the accumulative effect of swirling flow and significantly affect the shape of arc column, the arc voltage and more importantly the pressure rise in the expansion volume. By combining magnetic control mode with auto-expansion blowing, circuit breaker performance can be considerably enhanced. Our results indicate that the inclusion of swirling flow in the arc model produces beneficial results for current interruption. The model parameters such as these used in the radiation and turbulence calculation may need further adjustment according to the experimental results.

With a magnetic coil, the magnetic flux in the arcing region changes proportionally with the coil current, which is equal to the arcing current. Thus, the magnetic field is weakened when the magnitude of arcing current is decreased. It would be of interest to study the arc behaviour under a constant externally imposed magnetic field; the arcing process in a hybrid circuit breaker with a permanent magnet will be studied in Chapter 5.

# Chapter 5
# Computer Simulation of a Permanent Magnet Assisted Hybrid Circuit Breaker

## 5.1 Introduction

The use of a permanent magnet has the advantage of maintaining a steady magnetic field. The results given in Chapter 4 indicate that the pressure increase in the expansion volume is only moderate. The investigation of the pressure rise in an auto-expansion breaker (Yan et al. [9]) shows that the radiation induced inner surface ablation of a PTFE nozzle plays a critical role in the determination of the pressure and flow conditions during the current zero period. The breaker under investigation has a PTFE nozzle and a permanent magnet.

The radiation induced ablation consisting of the inner surface of the PTFE nozzle affects the performance of a circuit breaker in two ways. First, the ablated PTFE vapour, adds mass, momentum, and energy to the system and consequently modifies the arcing environment. This changes the arc characteristics, hence the electrical power input. As a result, the arc conditions at current zero, which determine the thermal interruption capacity of the breaker, depend critically on nozzle ablation. Second, nozzle ablation may have a significant influence on the composition of the gas or residual plasma left between the two contacts after the thermal extinction of the arc, thus affecting the dielectric strength [98]. Because of the very different chemical compositions between $SF_6$ and PTFE, the

thermodynamic and transport properties of $SF_6$ and PTFE vapour differ substantially. The mass or volume concentration of PTFE within a mixture has to be known if the effects of nozzle ablation on circuit breaker performance are to be investigated. With the assumptions of LTE (local thermodynamic equilibrium) and local chemical equilibrium PTFE concentration can be calculated by using the mass concentration equation of PTFE [10]. However, the approach of [10] considerably lengthens the computational time. For auto-expansion breakers, it has been shown by Yan et al. [9] that the use of the $SF_6$ thermodynamic and transport properties for $SF_6$-PTFE mixture can predict the pressure rise in the expansion volume, which is in reasonable agreement with experimental results. Thus, the thermodynamic as transport properties of pure $SF_6$ are used for $SF_6$-PTFE mixture in the present investigation.

The axisymmetric model described in Chapter 4 is used to simulate the arcing process of a 25.8kV hybrid circuit breaker. Simulation results are compared with available measurements. PHOENICS [8] is again used to implement the arc model.

## 5.2 Geometry of a 25.8kV hybrid circuit breaker (permanent magnet-assisted auto-expansion interrupter)

The interrupter under investigation is shown in Figure 5.1. A PTFE nozzle is employed and the moving contact is solid, which further assists the building up the pressure within the interrupter. The solid contact of diameter 20mm moves at a speed of 4.0m/s and the maximum distance between the two contacts (the stroke) is 80mm.The nozzle is connected to an exhaust volume. In contrast to the flow arrangement of the breaker investigated in Chapter 4 the gas exhausted from the fixed hollow contact is returned to the expansion volume. The filling pressure of $SF_6$ within the interrupter is 4.0 bar.

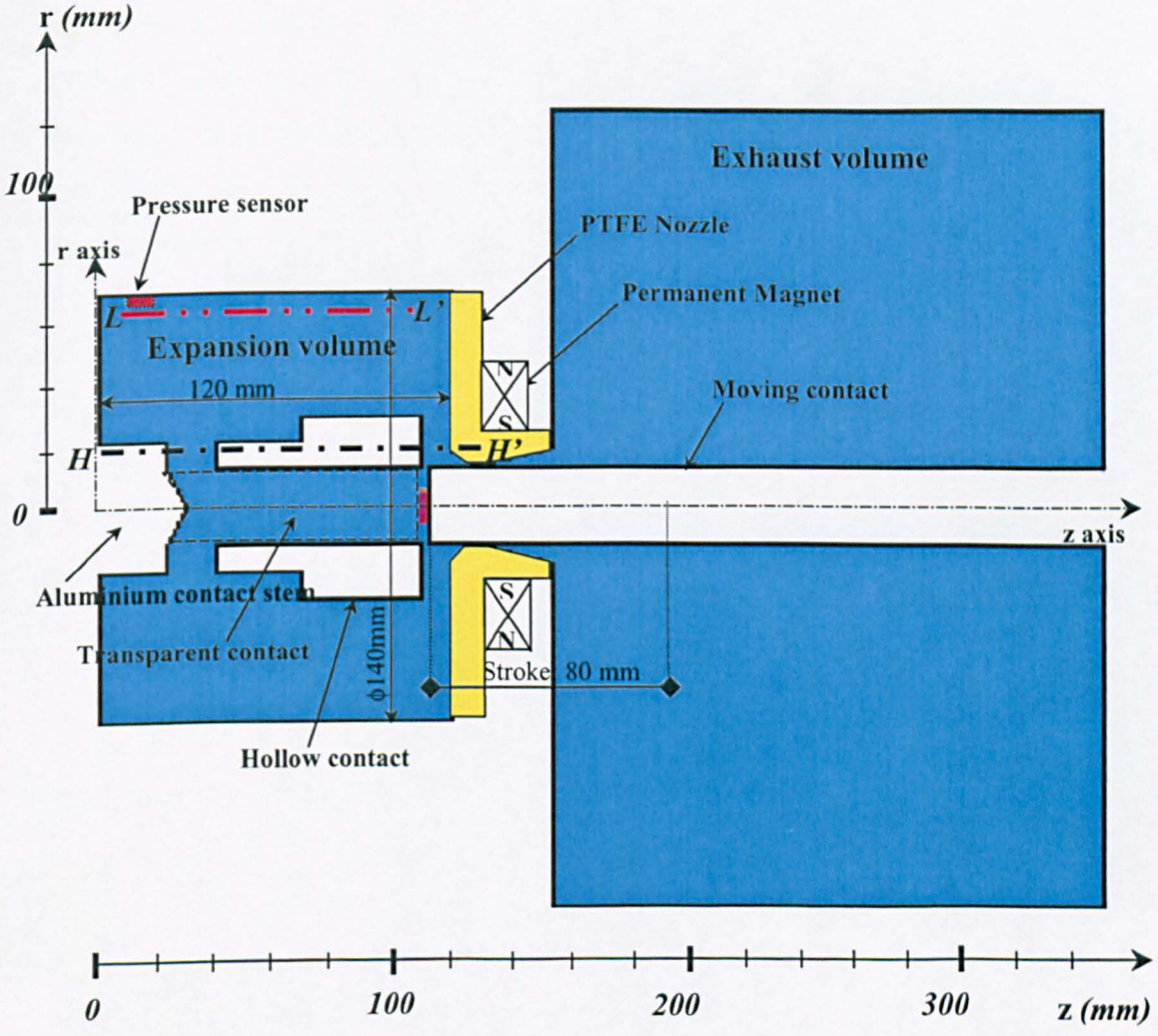


**Figure 5.1** Schematic diagram of a 25.8kV hybrid circuit breaker (permanent magnet-assisted auto-expansion interrupter) under investigation.

## 5.3 The simulation domain and boundary conditions

The computation domain is shown in Figure 5.2, where the flow computation domain is coloured with blue and green. Non-slip conditions for velocity and adiabatic conditions for temperature on the solid surfaces are imposed. The pressure at gas outlet (see Figure 5.2) is fixed at the filling pressure, 4.0 bar. When the full stroke is reached, the moving contact is situated in the exhaust volume. The gas adjacent to the moving contact will be in motion. The size of the exhaust volume is much bigger than that of the expansion volume (the actual diameter of the gas exhaustion volume is twice as bigger as that shown in the schematic diagram of the breaker, Figure 5.2). Therefore, it is expected the gas motion around the moving contact and the exhaust gas from the nozzle hardly affect the large part of the exhaust volume. In order to simulate the gas movement near the moving contact while keeping the computational time reasonable, we place an artificial boundary, AA' (Figure 5.2), where the pressure is set at 4.0 bar.

As mentioned in Chapter 3, the computation domain for electrical potential is larger than that of the fluid. The required boundary conditions for the electrical potential together with the electrical conductivity for the moving and fixed contacts and the low temperature $SF_6$ are given in Figure 5.2. The boundary conditions at the tip of the moving contact are the same as those used in Chapter 4. Radiation induced ablation of the PTFE nozzle surface is considered as a surface source for the mass, momentum and energy equations, the details of which are given later.

Body fitted coordinates are used to model the complex geometry. Altogether there are 169 (axial) and 69 (radial) cells, the distribution of which is shown in Figure 5.3. There are 70 (axial) and 55 (radial) cells in the region between the two contacts (arcing region), 72 (axial) and 15 (radial) cells in the expansion volume and 47 (axial) and 36 (radial) cells in the exhaust volume.

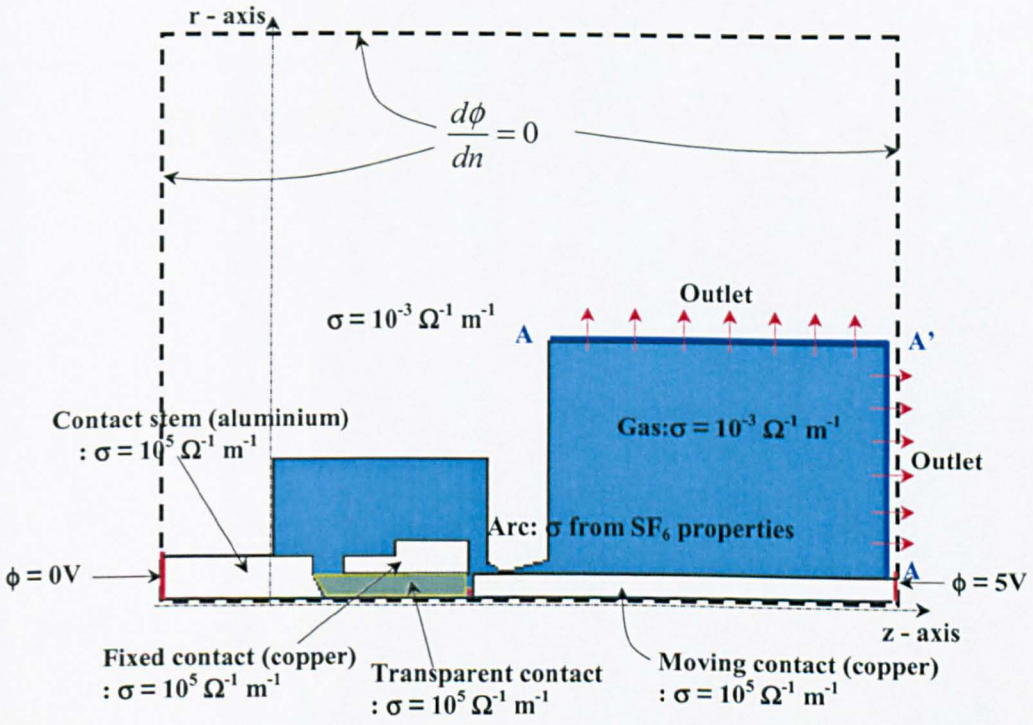


**Figure 5.2** Schematic diagram showing the boundary conditions and the material properties used in the calculation of the electric potential in a 25.8kV hybrid circuit breaker (permanent magnet-assisted auto-expansion interrupter).

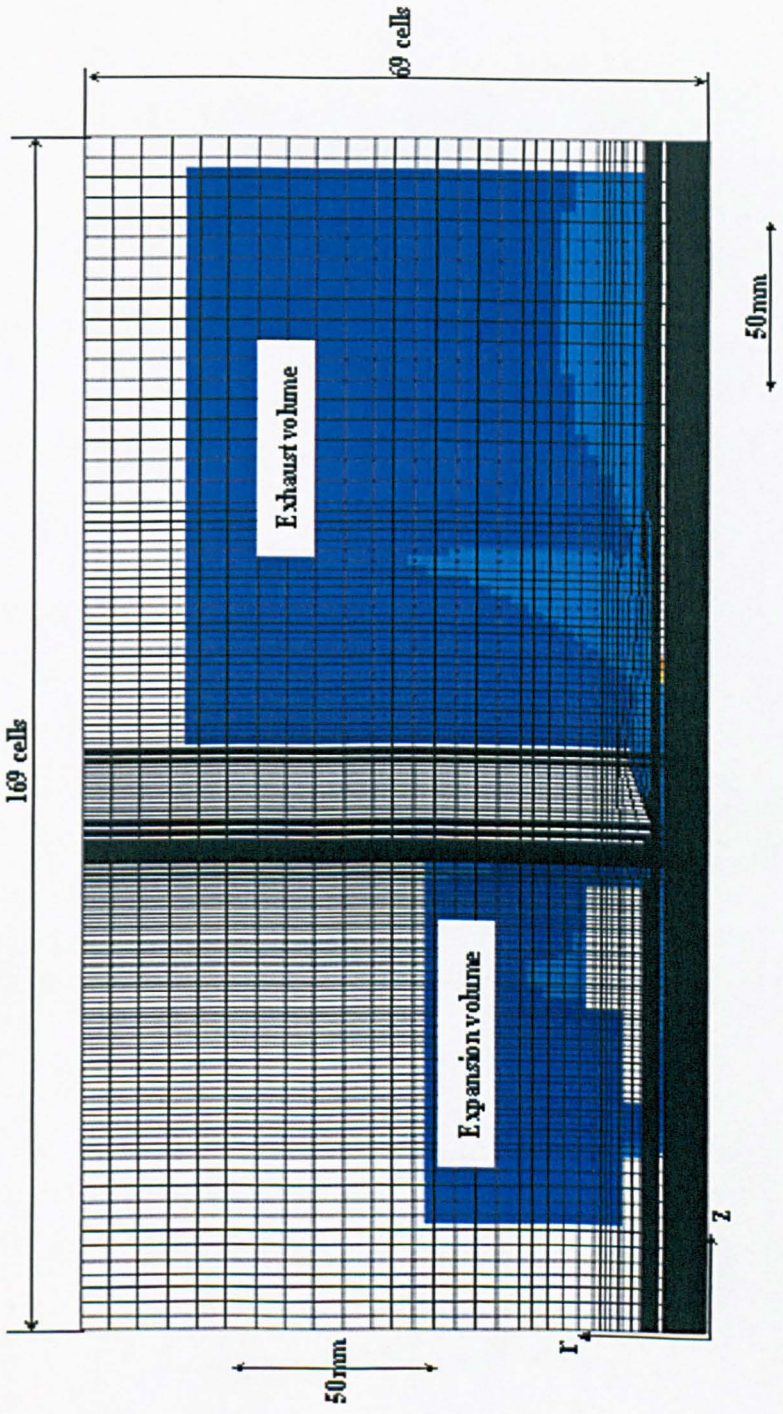


**Figure 5.3** A typical BFC grid system potential in a 25.8kV hybrid circuit breaker (permanent magnet-assisted auto-expansion interrupter).

## 5.4 Subsidiary models

### 5.4.1 The radiation transport and ablation model

Net emission coefficient with a re-absorption layer (the NEC method) used in Chapter 3 is used to here to compute the net radiation loss. For the present work, arc radius is defined as the radial position of 4,000K isotherm as in Chapter 4, 50 ~ 60% of the radiation flux is absorbed in the re-absorption region, and the net emission coefficient of [4] has adjusted to be multiplied by a factor of 4.0 in order to achieve agreement with experimental results.

Radiation flux reaching the inner surface of the PTFE nozzle causes it to ablate. The process of ablation of PTFE is very different from that of solids. For PTFE, the ablation does not take place in the form of phase changes [40]. The ablation of PTFE is due to the break up the large polymer chain. The break-up polymer PTFE in the form of vapour is further heated up by the absorption of radiation from the arc to a temperature of 3400K [99]. Thus, for evaporation dominated ablation process, the rate of ablation is computed by

$$Q = \overline{m} \cdot H_V \tag{5.1}$$

where Q is the radiation flux per unit length reaching the inner surface of the nozzle and $\overline{m}$ the rate of ablation per unit length. Since 60% of the radiation flux from the arc core edge is absorbed, 40% of this flux reaches the inner surface of the nozzle. However, 10% of the radiation flux reaching the inner surface is assumed not to be absorbed [9]. $H_V$ is the energy required to break up the polymer PTFE chain and to raise the PTFE vapour from room temperature to 3400K[99], which is equal to $1.19\times10^7$ J/kg.

### 5.4.2 Calculation of the magnetic fields

The magnetic field produced by the magnet is computed using a separate solver (FLUX2D [103]) and inputed into the arc model through a data file. The effects of the imposed magnetic field on the arc are represented by a Lorentz force term in the momentum equations for axial, radial and azimuthal flow.

The computed magnetic fields together with the magnitude plots are shown in Figure 5.4. The magnetic field lines at north and south poles are not symmetrical for a ring permanent magnet. The inner surface of the permanent magnetic ring is the south pole. Such a structure of the magnet makes the magnetic fields within the ring magnet and the nozzle weak as shown in Figure 5.4. The magnetic field is far from uniform. This in contrast to the magnetic field produced by the coil for which the magnetic field on the arc axis is higher than that in region surrounding the axis. The magnetic field produced by the arcing current is assumed to be in azimuthal direction, which is included in the calculation of the Lorentz force.

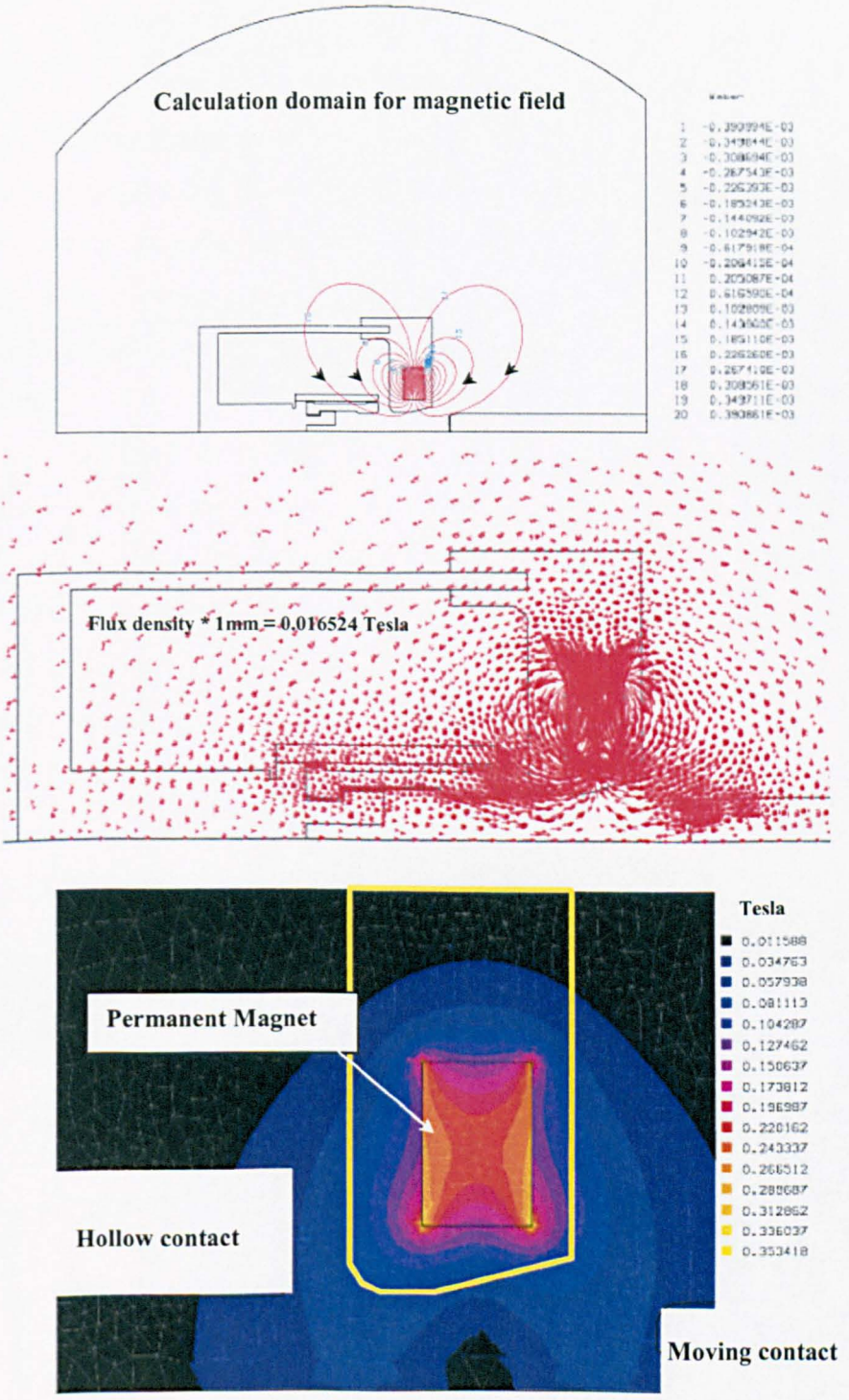


**Figure 5.4** Magnitude of magnetic field produced by the permanent magnet in a 25.8kV hybrid circuit breaker (permanent magnet-assisted auto-expansion interrupter).

## 5.5 Results and discussions

There are very little test results on the interruption of this kind of circuit breaker in the open literature, which can be used for meaningful comparison with computational results. For the interrupter under investigation, the pressure in the expansion volume was measured using a piezoelectric pressure transducer (Kistler model 601A) at a location shown in Figure 5.1. Figure 5.5 shows the measured current, arc voltage and pressure in the expansion chamber with an arc current of 28kA(rms).

Computation has been performed for a 25.8kV magnet-assisted auto-expansion interrupter with the current waveform given in Figure 5.6, where the position of the solid contact as a function of time is also shown. The solid contact moves at a speed of 4.0m/s. A transparent contact is employed in the hollow contact to ensure the current collection.

Arcing process can be divided into typical phases according to the instantaneous current and the position of the moving contact.

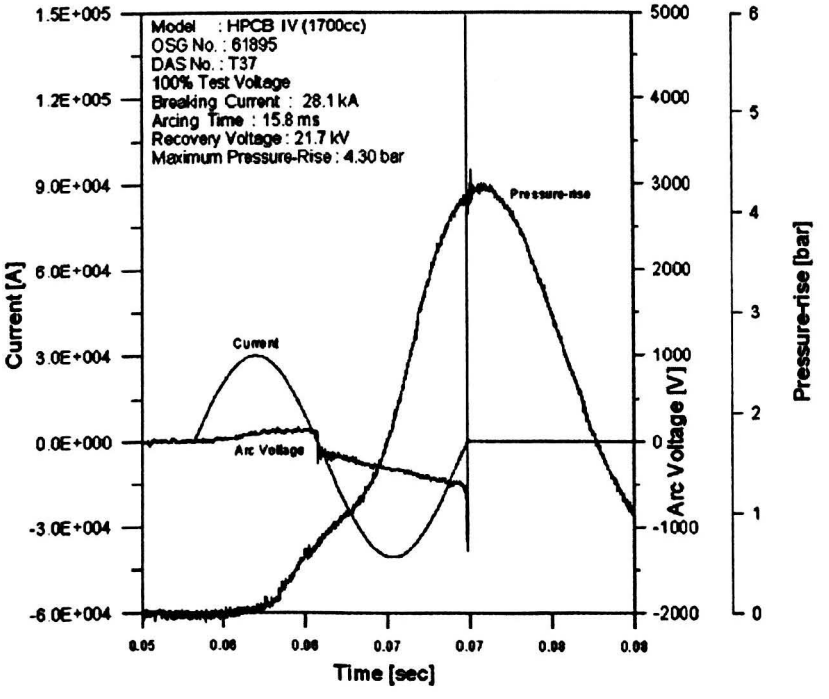


**Figure 5.5** Measured arc voltage and pressure rise for a 25.8kV hybrid circuit breaker (permanent magnet-assisted auto-expansion interrupter).

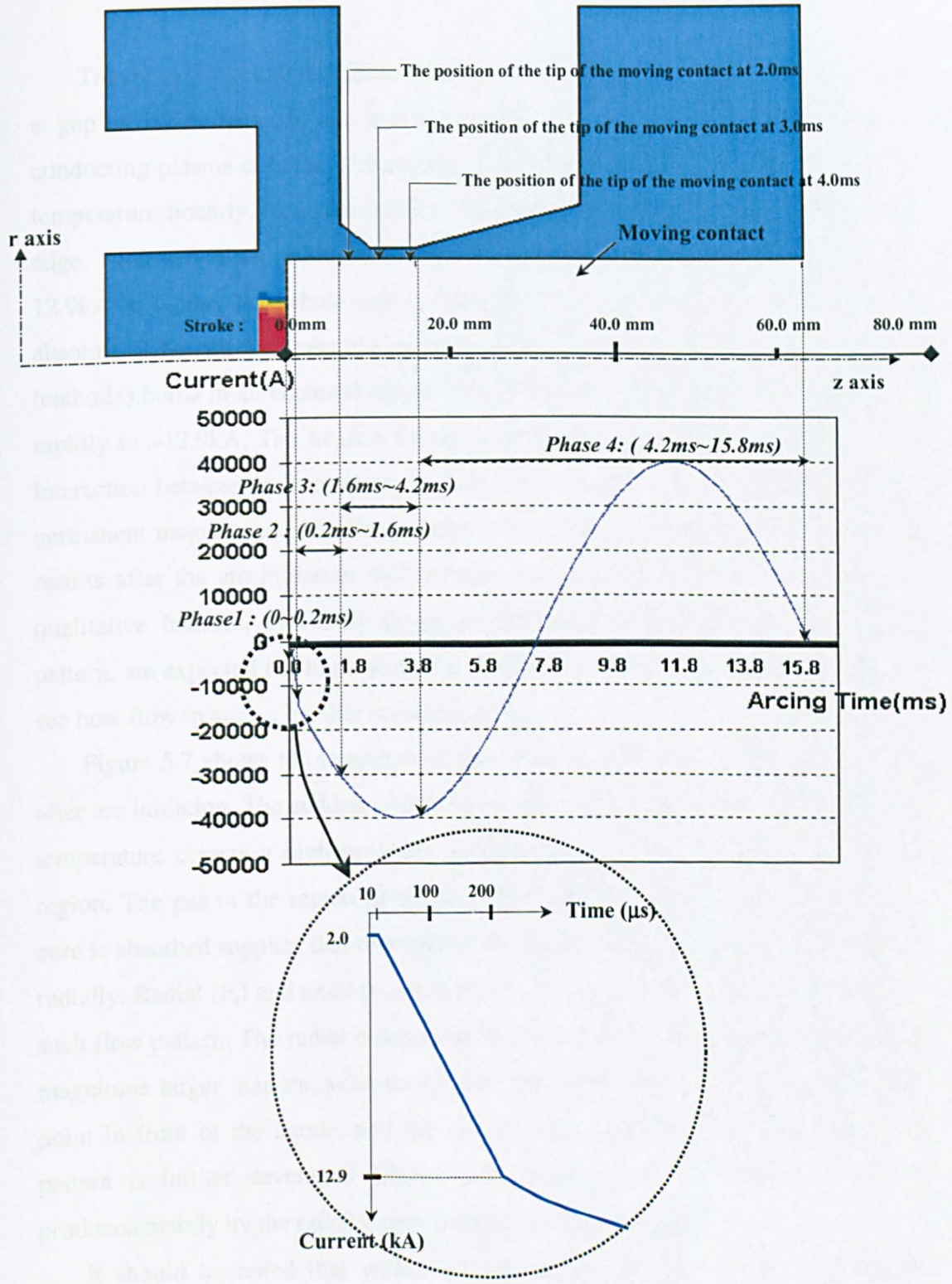


**Figure 5.6** The position of the moving solid contact and the different phases of arcing are indicated.

### *A. Phase 1 : Arc Initiation (0 ~ 0.2ms).*

This phase is from 0 to 0.2ms. The arc is initiated with a current of -2kA across a gap of 5mm between the transparent and solid contacts by introducing a conducting plasma column. The column has a radius of 3mm, over which the gas temperature linearly decreases radially from 20,000 K at the centre to 300K at the edge. After arc initiation, the instantaneous current is ramped up to a current of -12.9kA in 0.2ms. The whole arcing chamber is initially filled with SF6 at 4.0bar absolute. The arc between the solid contact (anode) and transparent contact (cathode) burns in an enclosed space. During this period the current is ramped up rapidly to –12.9kA. The intense Ohmic heating and the Lorentz force due to the interaction between the arc current with its own magnetic field and that due to the permanent magnet make the flow pattern very complex. Although the quantitative results after the arc initiation will depend on the initial conditions assumed, the qualitative features, especially those concerning the establishment of the flow pattern, are expected not to be sensitive to the initial conditions. It is of interests to see how flow in such a breaker is established.

Figure 5.7 shows the temperature and velocity field in r-z plane immediately after arc initiation. The sudden switching on of the Ohmic heating and the high arc temperature creates a high pressure region which drives the gas out of the hot region. The gas in the region of the arc edge where much radiation from the arc core is absorbed supplies that required by the arc core and surplus flows out mainly radially. Radial ($F_r$) and axial ($F_z$) components of Lorentz force are responsible for such flow pattern. The radial component of the Lorentz force is about one order of magnitude larger than the axial component. The radial inflow creates a stagnation point in front of the anode, and the arc expands towards the cathode. The flow pattern is further developed (Figure 5.8). There is evidence of flow rotation produced mainly by the radial component of the current density.

It should be noted that within the arc region the flow in the r-z plane is dominated by the radial movement. Thus, the conventional understanding of the role of the radial component of the Lorentz force (which produces magnetic pinch and an axial pressure gradient) is not applicable here.

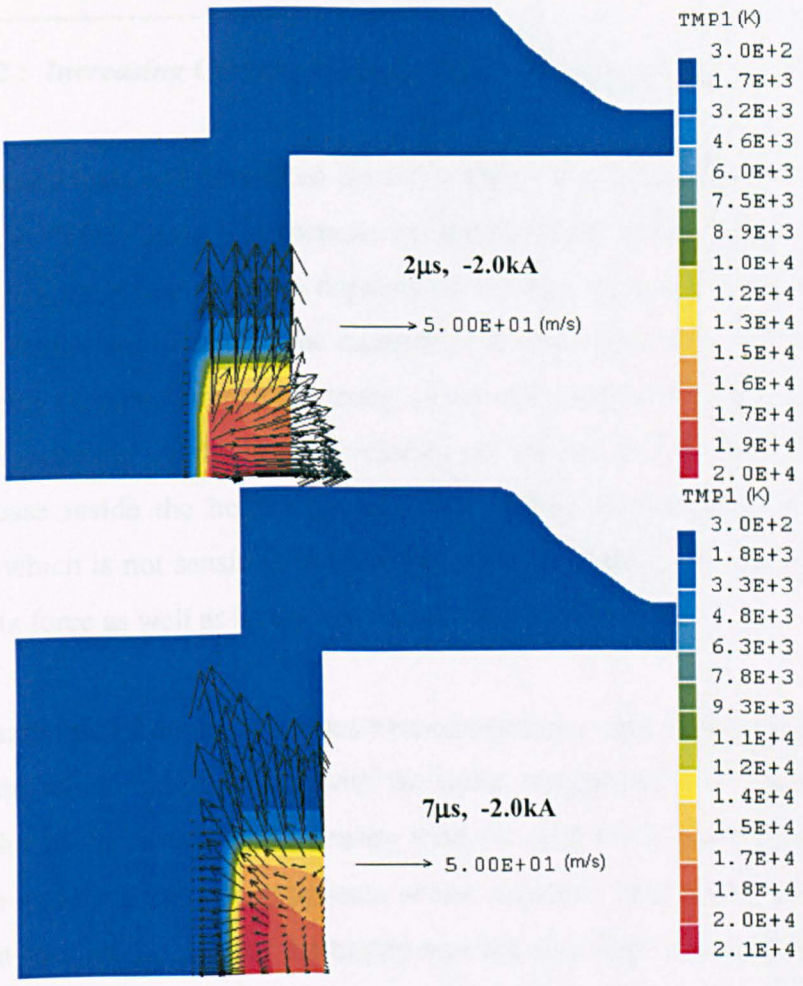


**Figure 5.7** Gas flow generated by the intense Ohmic heating at 2μs and 7μs after the arc initiation. Current = -2kA

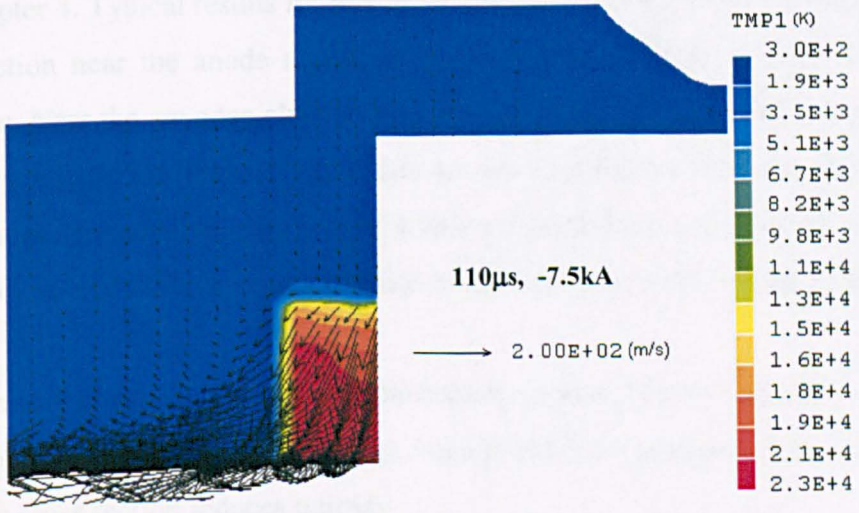


**Figure 5.8** The fast arc expansion and the radiation re-absorption region make the gas in the re-absorption layer supplying that required by the arc due to acceleration. The remaining gas in this layer flows into the cold region.

***B. Phase 2 : Increasing Current Without Nozzle Ablation (0.2ms ~ 1.6ms).***

This phase ends at 1.6ms when the tip of the moving contact is in the entrance plane for the PTFE nozzle. The increase in current results in arc expansion (Figures 5.9 and 5.10), the shape of which depends on the flow pattern. Discussions on the simulated results are limited to the qualitative features as the arc and its flow are still in highly transient state. The strong, clockwise rotational Lorentz force in r-z plane is responsible for the highest velocity off the arc axis (Figure 5.9). This is also the case inside the hollow contact. The highest arc temperature is around 25,000K, which is not sensitive to the instantaneous current. The arc is shaped by the Lorentz force as well as it depends on the previous history.

The azimuthal Lorentz force has two components: that due to the interaction between the axial current density with the radial component of the magnetic field and that due to the radial current density with the axial component of the magnetic field. The axial and radial components of the magnetic field are produced by the permanent magnet. Because of the highly non-uniform distribution of the magnetic field, especially the decay of the magnetic field towards the centre, it is expected that the azimuthal velocity field would be complex and different from that shown in Chapter 4. Typical results for this phase are shown in Figures 5.11 and 5.12. The arc section near the anode rotates in the opposite direction to that close to the cathode. Near the arc edge close to the cathode transparent electrode, the azimuthal velocity attains the highest value due to arc contraction near the cathode. The maximum azimuthal velocity for the whole arc period (i.e not confined to Phase 2) does not exceed 800m/s, which is much lower than that in the breaker in Chapter 4.

The arc plasma penetrates into the hollow contact, which is cooled by radiation and convection. Because of the large inward radial component of the velocity the hot gas cross section reduces quickly.

Within the hollow contact there is no Lorentz force, angular momentum should be preserved if viscous effects can be neglected. Thus, the inward flow, which

reduces the cross section of the high temperature region, tends to increase the azimuthal component of the velocity. In practice, this velocity is attenuated mainly by turbulent diffusion and the increasing gas density as the temperature decreases within the hollow cathode.

The pressure disturbances created by the increasing arcing current propagate through the hole of the hollow contact as well as through the gap between the two contacts (Figure 5.13). It is not easy to link the velocity field with the pressure distribution as the flow is still highly transient. However, at the instant shown in Figure 5.13 there is a region near the flow exit from the hollow cathode the pressure is the lowest. In this region, close to the axis some gas is sucked into the hollow contact from the stagnation point in front of the contact stem (Figure 5.2), which creates another stagnation point on the axis when the flow from the transparent cathode collides with this reverse flow as shown in Figure 5.14, where the axis velocity is plotted.

During this phase, the arc voltage rises slowly, which is in close agreement with the measure voltage (Figure 5.15). The pressure at the measuring point in the expansion volume has hardly changed during this phase (Figure 5.16).

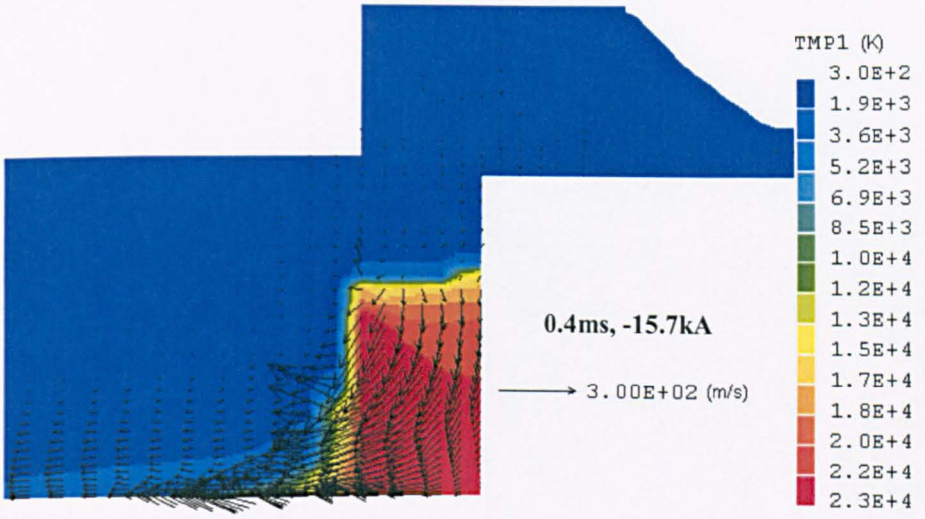


**Figure 5.9** Strong rotational Lorentz force is responsible for the maximum velocity off the axis in certain regions.

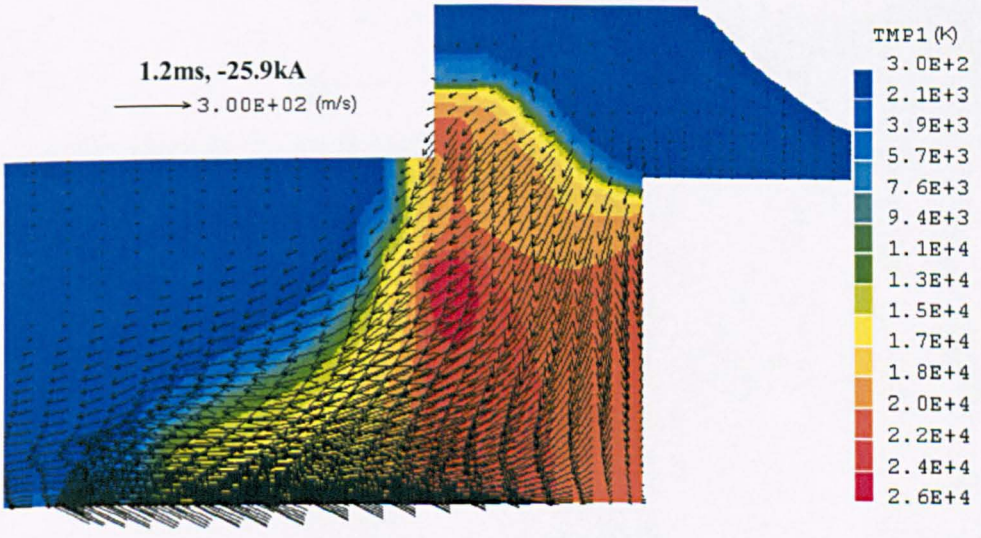


**Figure 5.10** The arc fills the hole of the hollow contact. Basic flow features are similar to previous instants.

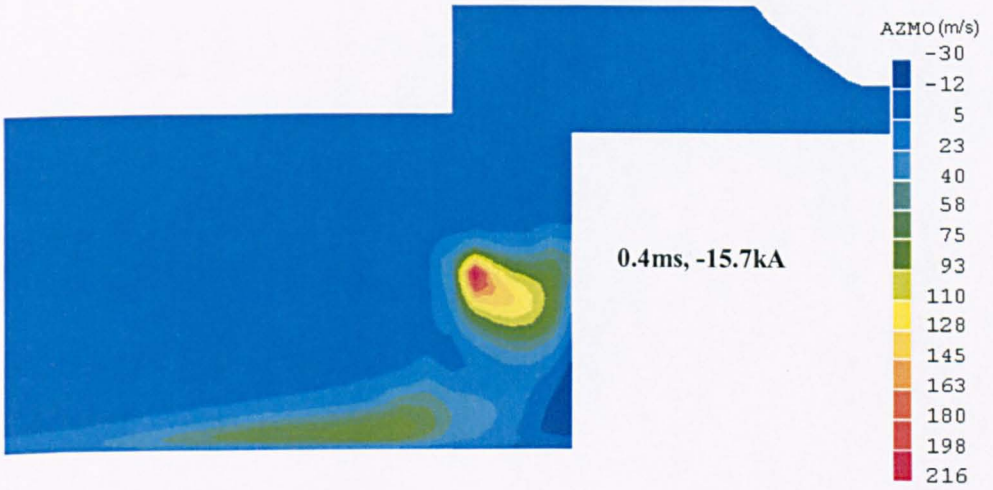


**Figure 5.11** The azimuthal velocity generated by the Lorentz force. The complex pattern is due to the highly non-uniform magnetic field and the arc shape.

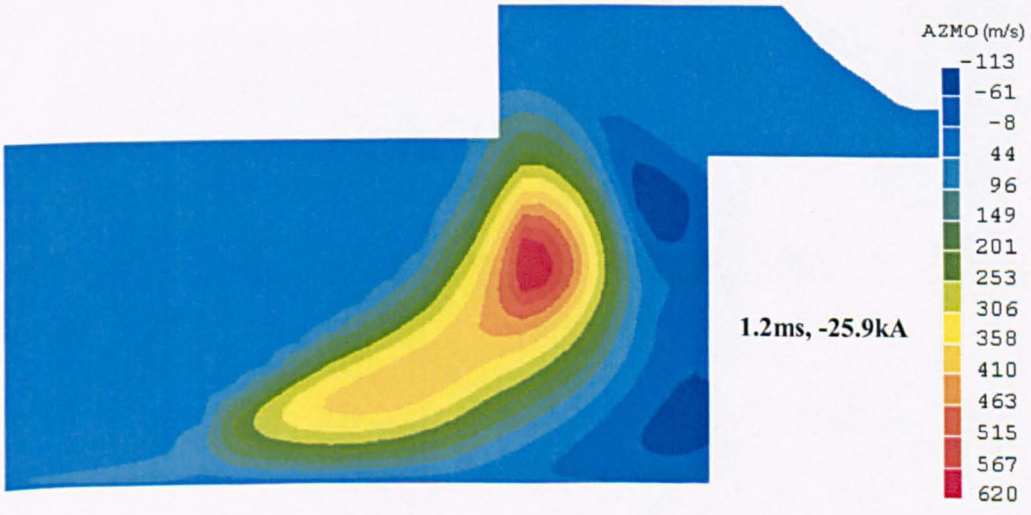


**Figure 5.12** Azimuthal velocity field showing the direction of rotation near the anode is opposite to that near the transparent cathode. The high azimuthal velocity near the edge of the transparent cathode is due to arc contraction.

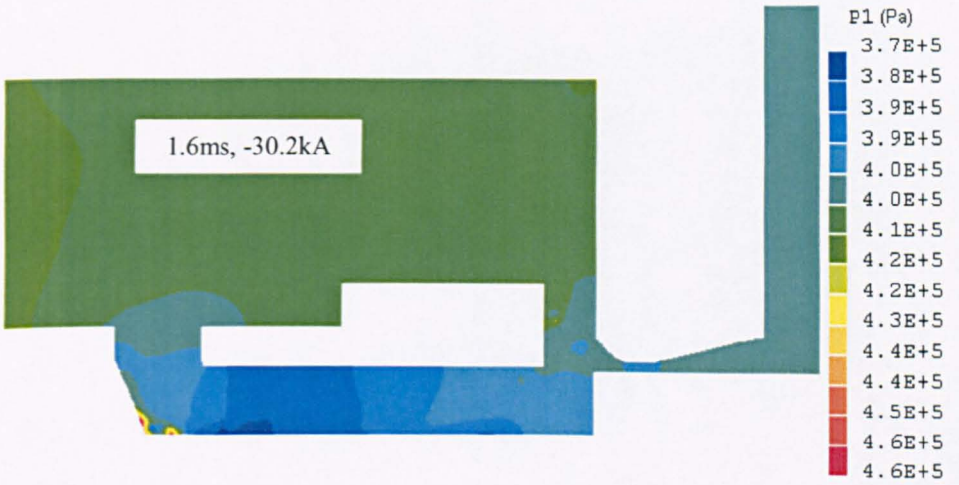


**Figure 5.13** Pressure distribution showing pressure waves originated from arc region

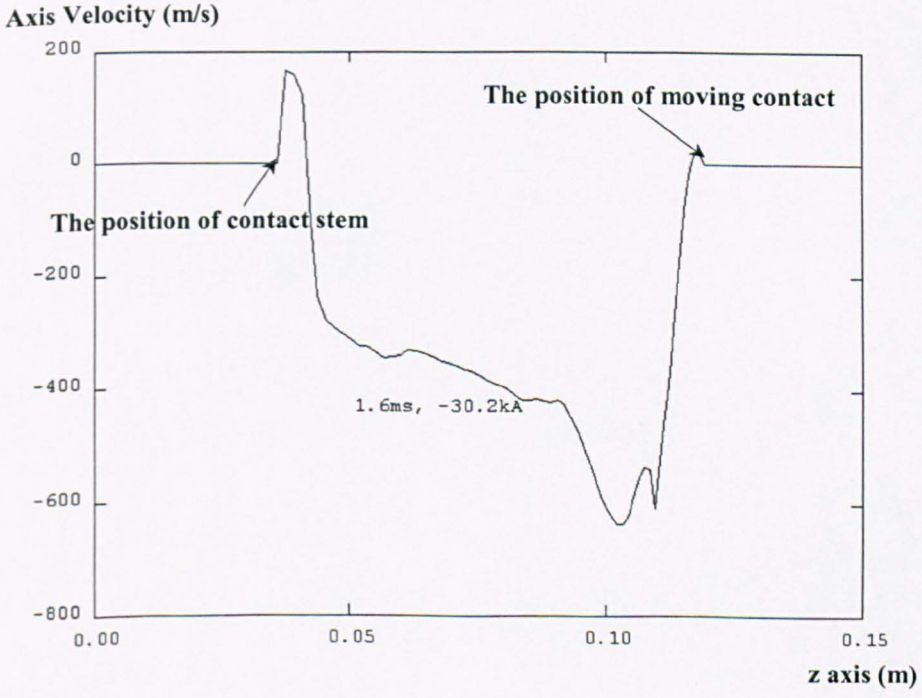


**Figure 5.14** Axis velocity at 1.6ms

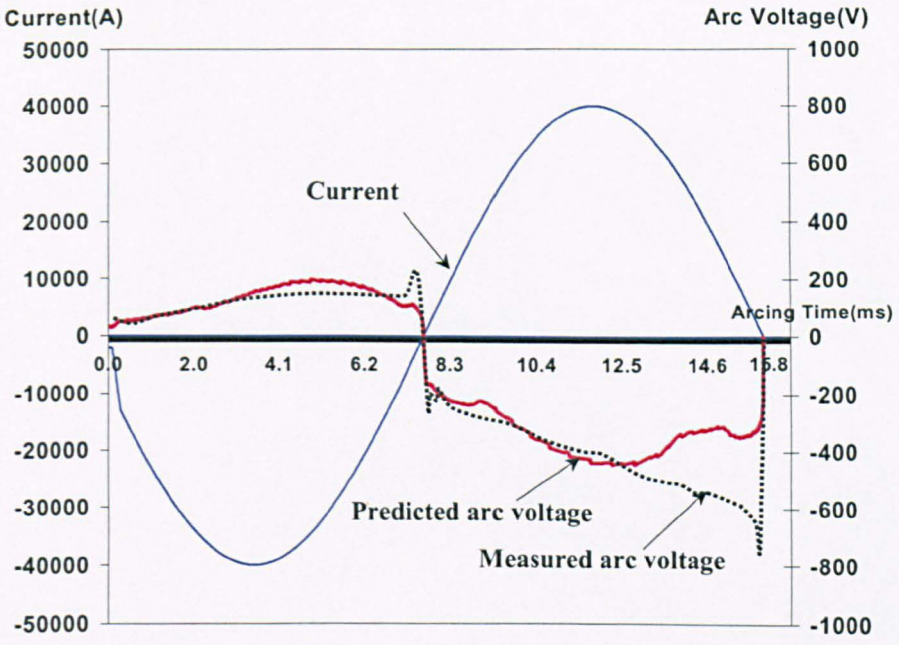


**Figure 5.15** Comparison of predicted and measured arc voltage for the hybrid circuit breaker under investigation

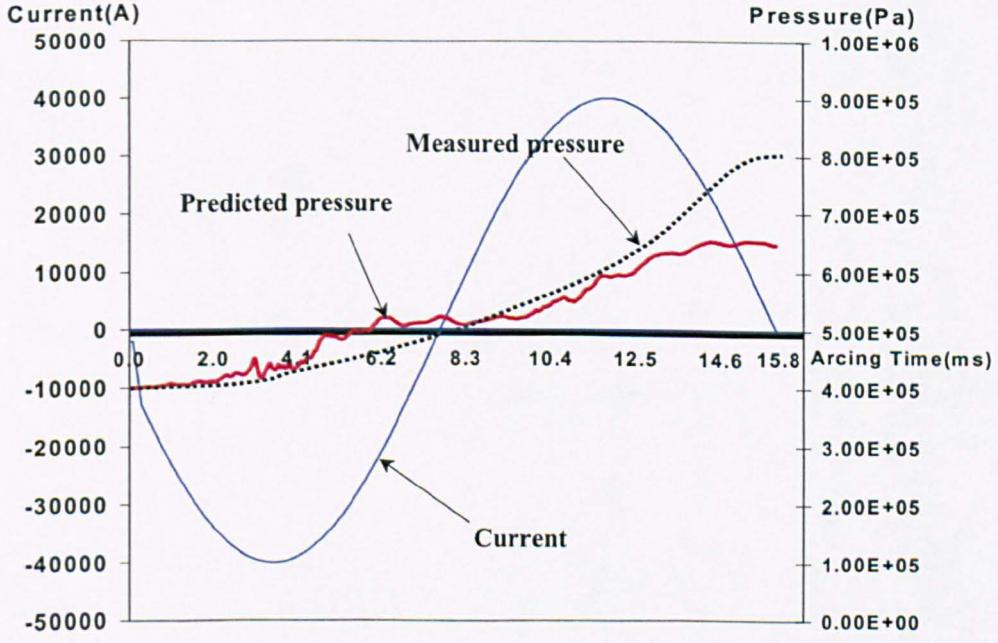


**Figure 5.16** Predicted and measured pressure variation at the position indicated in Figure 5.1.

### *C. Phase 3 : Nozzle ablation in blocked nozzle (1.6ms ~ 4.2ms).*

During this phase the inner surface of the PTFE is exposed to arc radiation although the flow is still blocked by the solid contact. At the end of this phase the tip of the moving contact moves the end plane of the parallel section of the nozzle (Figure 5.2). The gap between the moving contact and the nozzle allows a certain leakage of the gas.

When the tip of the moving contact first started moving into the nozzle, the ablation is not noticeable as the arc diameter is over one centimetre, and the radiation flux incident on the nozzle surface is rather low. In addition, the surface available for ablation is also small. The flow features are qualitatively similar to those at the end of phase 1 (Figure 5.17). The velocity has been increased due to the increasing current. It should be noted that a vortex is developed near the anode and close to the arc axis. The cross section of the high temperature core of the arc changes gently with a minimum in the middle. The temperature and velocity inside the hollow contact are given in Figure 5.18 and the azimuthal velocity in Figure 5.19. The cross section of the hot gas within the hollow contact reduces for the reason given previously. However, at the entrance of the hollow cathode the arc has blocked the hole. The shape of the clockwise rotation and that of the anticlockwise rotation (as viewed from the positive z-axis end towards the r-θ plane) have changed and both penetrate into the hollow cathode.

With the increase in arcing current and the further withdrawal of the moving contact into the nozzle, the effects of the ablation become more pronounced. At 3.0ms and at a current of –39.3kA, the temperature and velocity field in r-z plane are shown in Figure 5.20. The ablated PTFE vapour now acts as a source of supply of the gas fed into the arc, the gas leakage to the exhaust volume as well as that into the expansion volume. The vortex in front of the anode has grown in its size and much hot gas is exhausted through the hollow contact.

After the current passes its first peak, the tip of the moving contact is now near the exit plane of the parallel throat at 4.0ms with a current –39.3kA. The vortex at the anode has disappeared as there is sufficient amount of PTFE to be fed into the arc (Figure 5.21). The flow in r-z plane is now mostly parallel. The qualitative feature for the azimuthal velocity component for 3.0ms and 4.0 ms are similar (Figures 5.22 and 5.23). The distinct feature is that in the bulk of the arc plasma the swirling is in one direction.

In the expansion volume, hot gas patches from the gap between the nozzle and hollow contact and from the exhaust through the hole of the hollow contact can be seen at 4.0ms (Figure 5.24). The pressure in the expansion volume is also increased (Figure 5.25) but the distribution is far from uniform. Although the pattern of the pressure transients are complex, the snap shots of the pressure variation (Figure 5.25) along the straight line of LL' in Figure 5.1 show that the pressure waves travels at a speed of 160m/s, which is approximately equal to the sound speed of SF6 at room temperature.

The axis temperature, electric field and pressure are respectively shown in Figure 5.26, Figure 5.27 and 5.28 for three instants when the moving contact withraws into the nozzle. The three instants correspond respectively to the position of the tip of the moving contact at the upstream middle of the nozzle throat (2.0ms), at the end of the nozzle throat (3.0ms) and close to the downstream end of the nozzle throat (4.0ms).The relative position of the moving contact and current waveform can be found in Figure 5.6. Results indicate that ablation of PTFE by radiation from the arc causes the hot gas to flow into the expansion volume through the fixed hollow contact.

The pressure at the point of the detection in the expansion volume (Figure 5.16) has started increasing and shown the pressure oscillation. Arc voltage has also increased due to stronger convection, increase in pressure and arc lengthening.

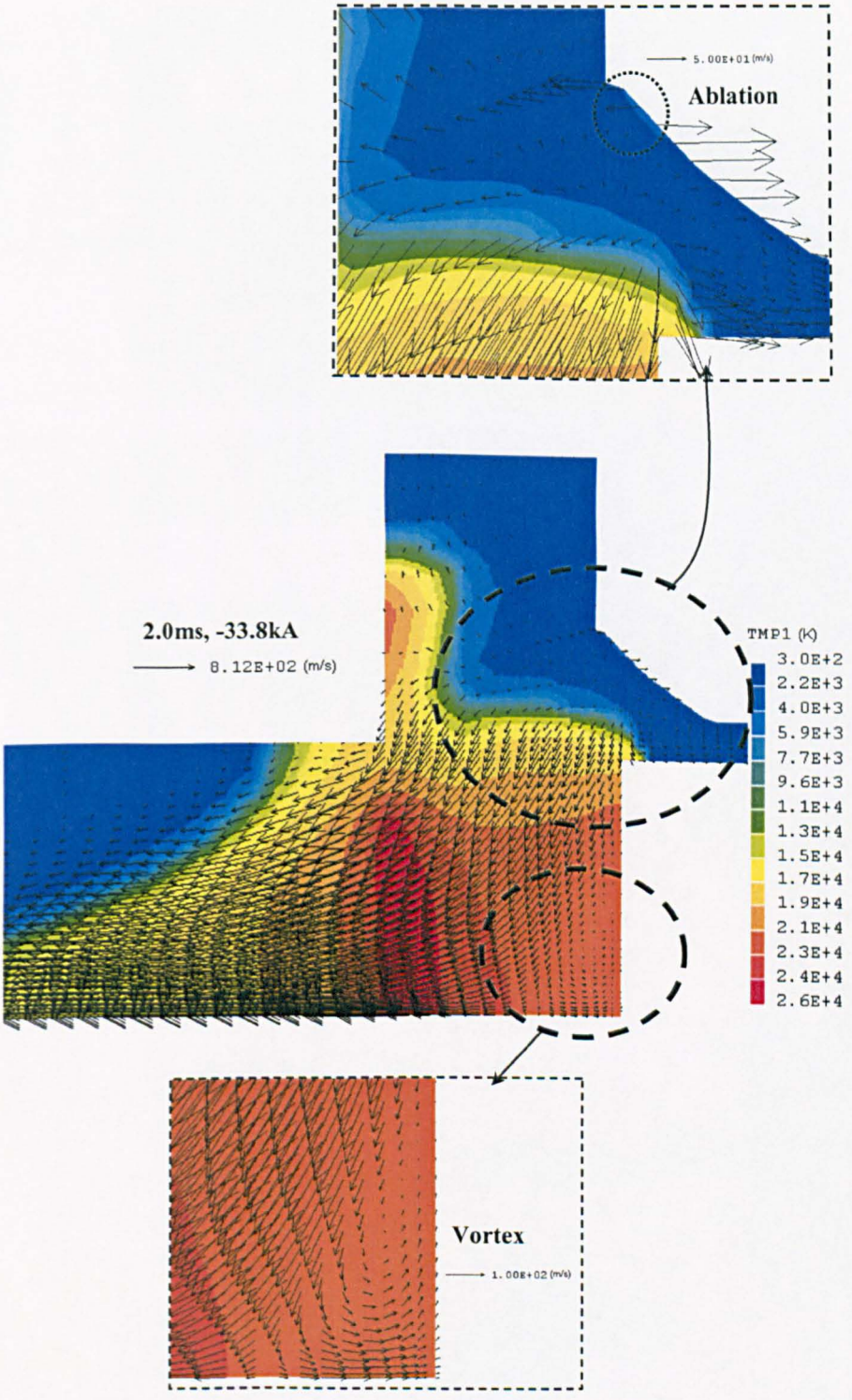


**Figure 5.17** Flow and temperature fields. A vortex is developed near anode.

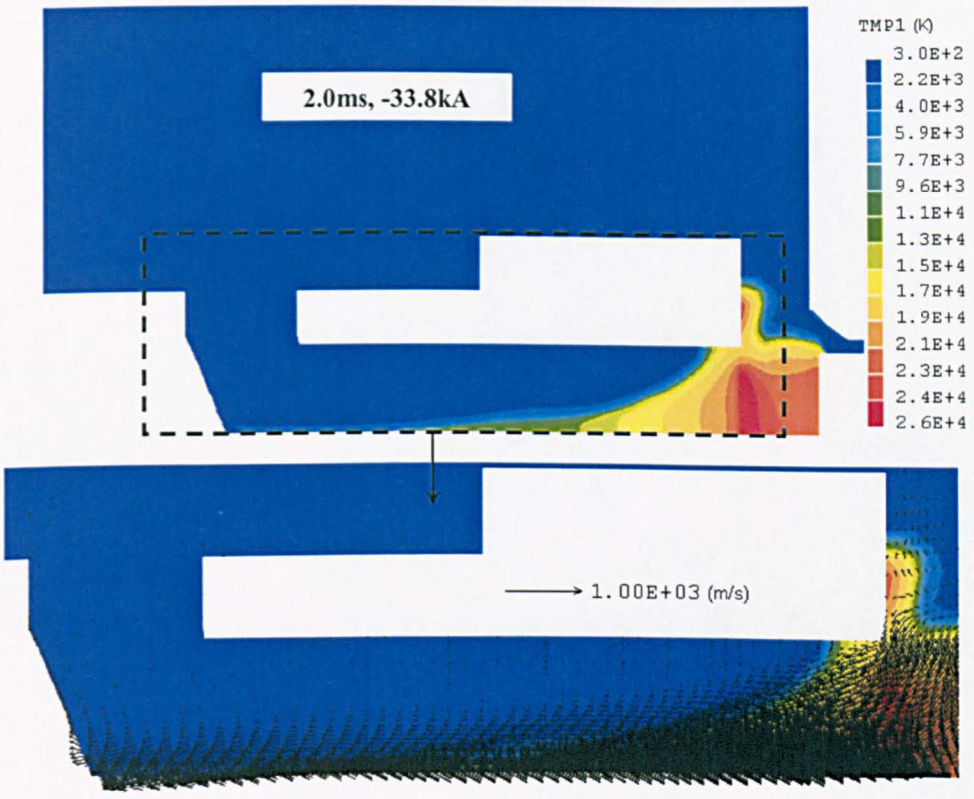


**Figure 5.18** The whole temperature field within the interrupter and the velocity field in r-z plane.

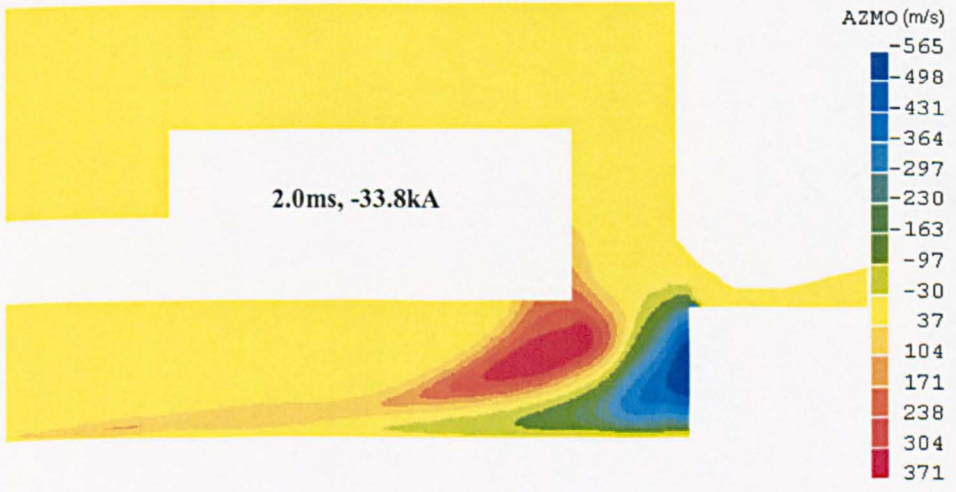


**Figure 5.19** Azimuthal velocity at 2.0ms.

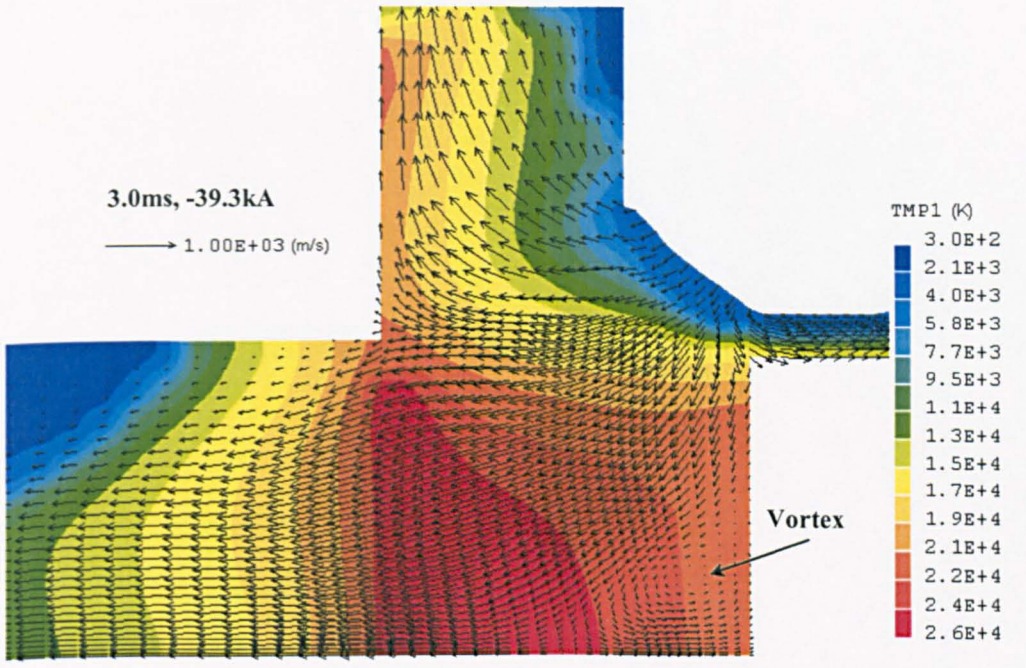


**Figure 5.20** Ablated PTFE vapour feeds into the arc as well as causing a gas flow at an elevated temperature going into the expansion volume.

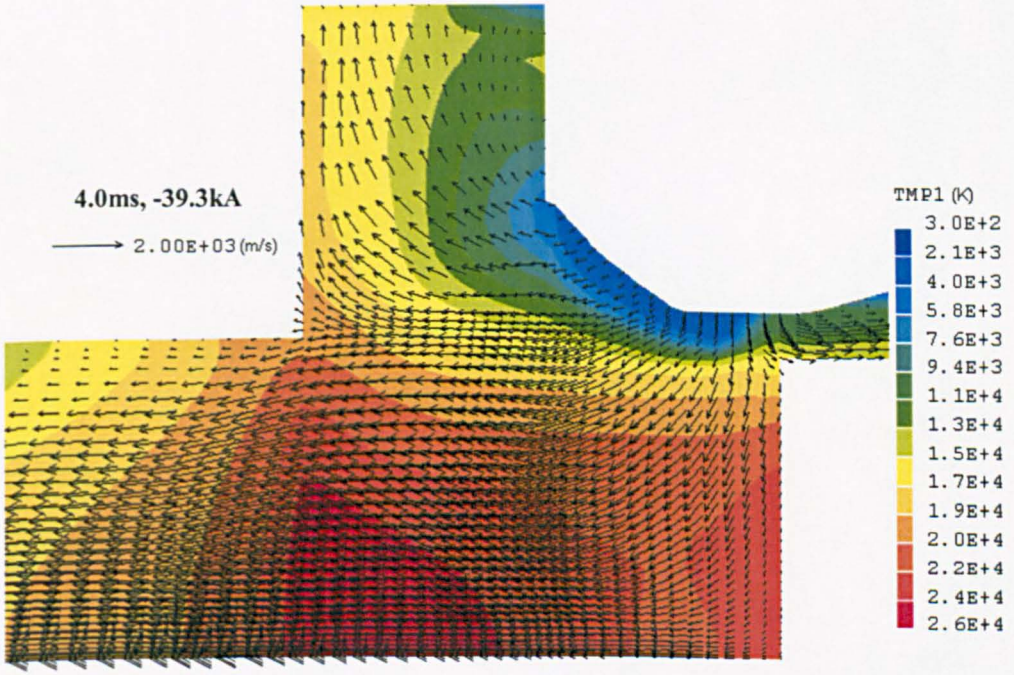


**Figure 5.21** Ablation is further developed. The flow passage in the gap between the hollow contact and the nozzle is now filled as high temperature gas. The arc has fully blocked the hollow contact.

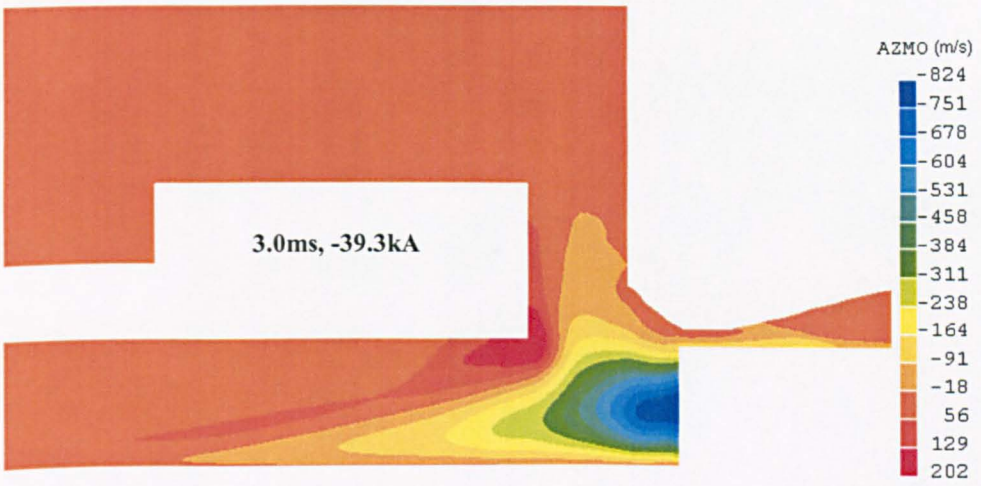


**Figure 5.22** The azimuthal velocity component at 3.0ms. In a large part of the arc the swirling is in one direction.

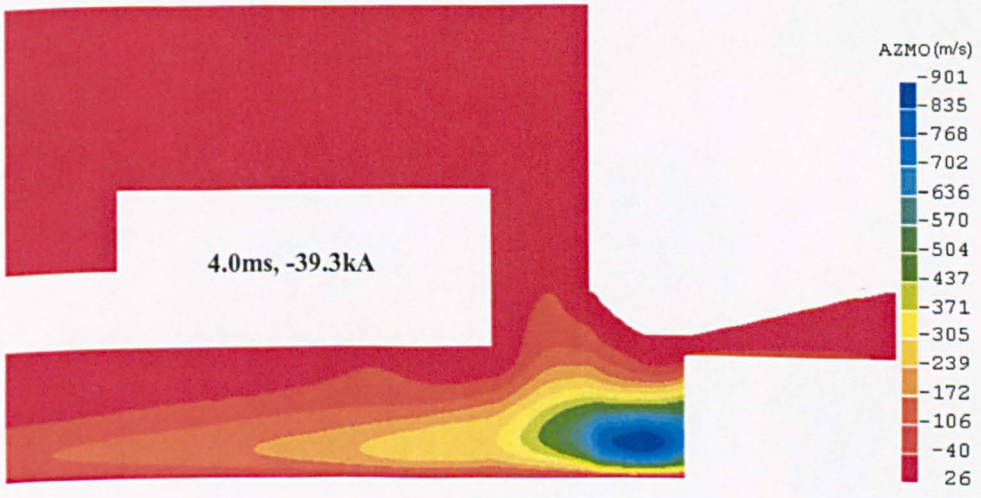


**Figure 5.23** The azimuthal velocity component at 4.0ms.

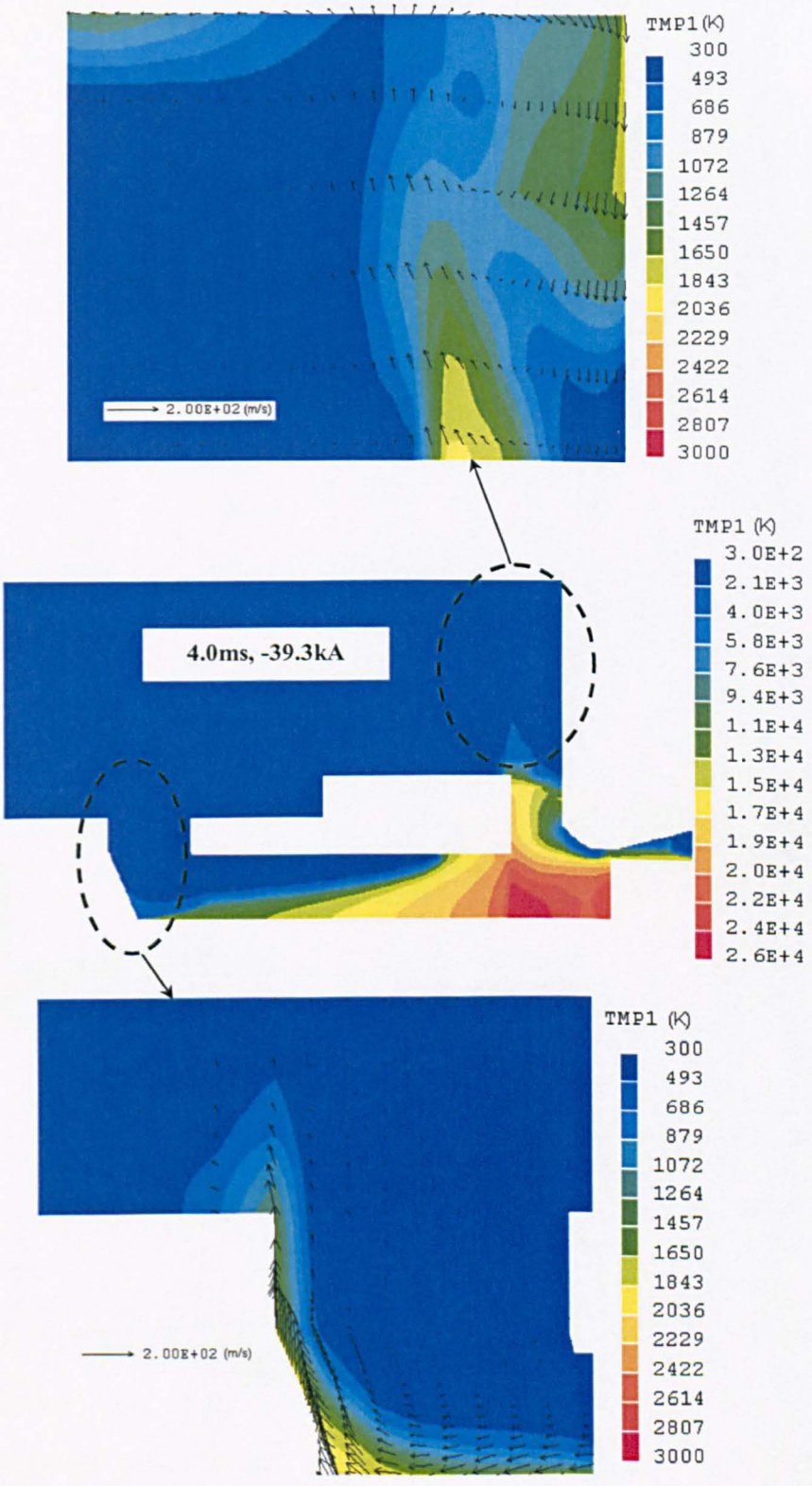


**Figure 5.24** Expansion volume at 4.0ms.

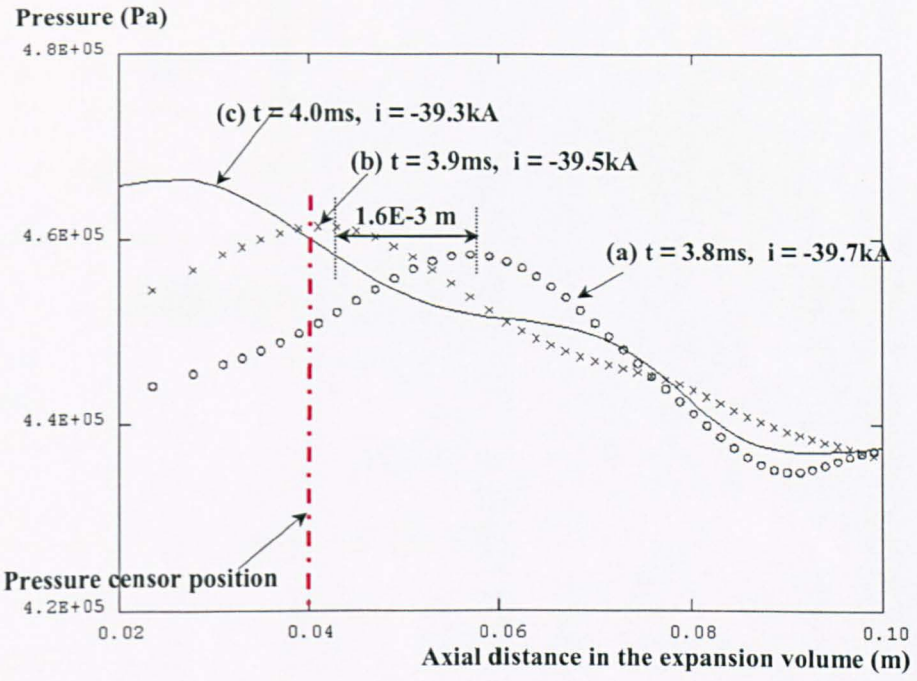


**Figure 5.25** Pressure variation along the red line ( $\overline{LL'}$ ) marked in Figure 5.1 at three instants in phase 3.

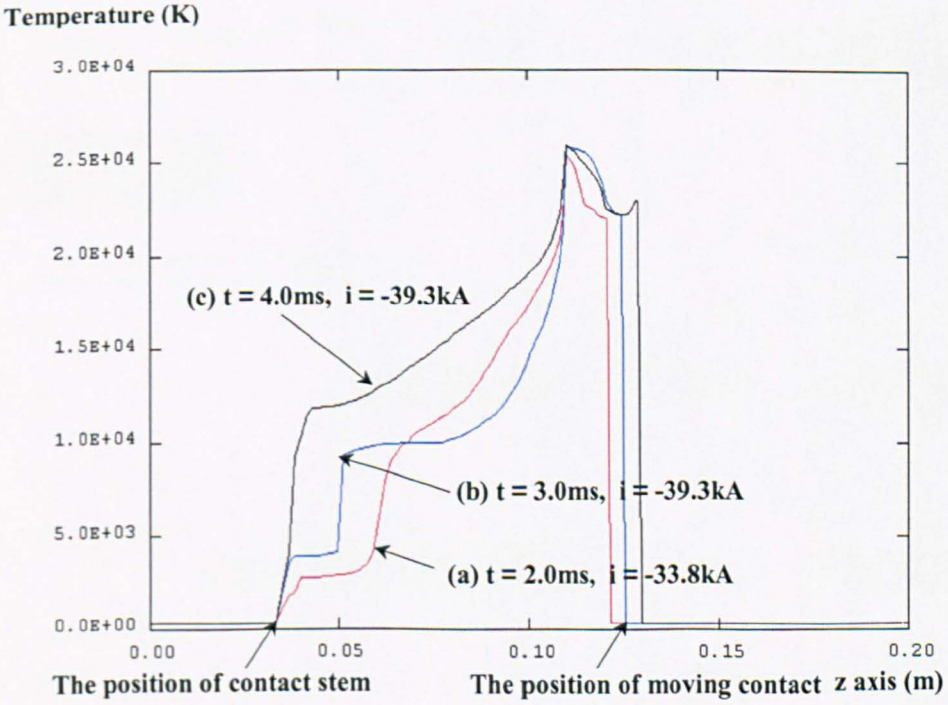


**Figure 5.26** Temperature on the axis at three instants in phase 3. The position of the moving contact and current waveform are indicated in Figure 5.6.

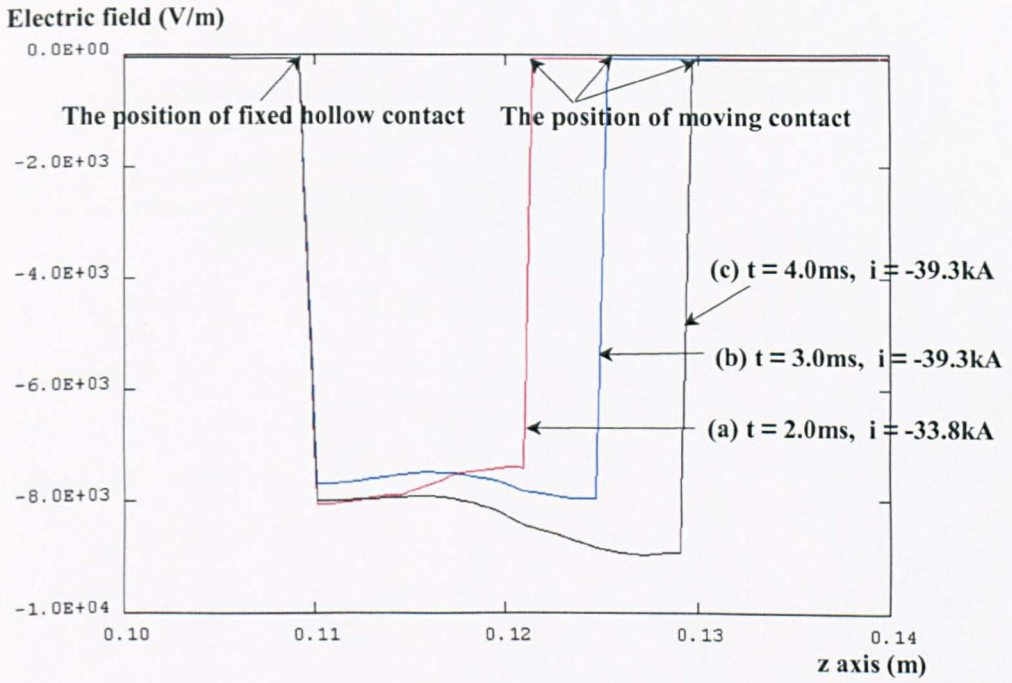


**Figure 5.27** Electric field on the axis at three instants in phase 3. The position of the moving contact and current waveform are indicated in Figure 5.6.

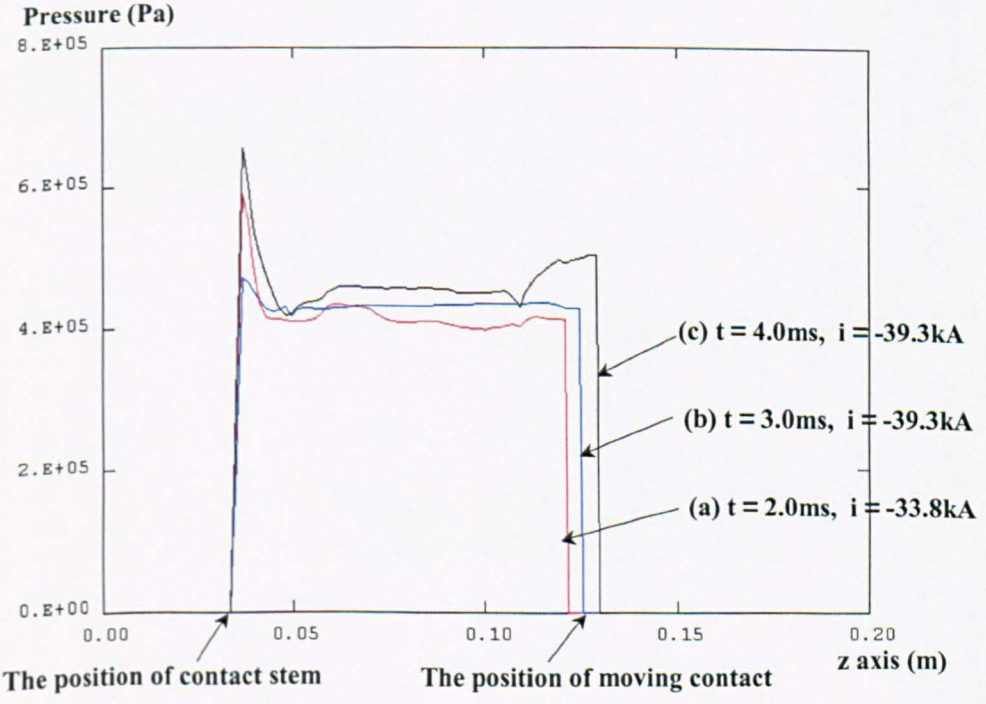


**Figure 5.28** Pressure on the axis at three instants in phase 3. The position of the moving contact and current waveform are indicated in Figure 5.6.

***D. Phase 4 : Moving contact gradually withdrawing from the nozzle (4.2ms ~ 15.8ms).***

For the convenience of the discussion we subdivide this phase into several periods.

*Period 1 (4.2ms to 7.9ms)*

During this period, the current decreases towards the first current zero while the tip of the moving contact is situated at a position of 40mm (Figure 5.6). At an instant of 6.0ms, the accumulated ablation of PTFE is still strong enough to maintain a flow pattern consistent with the highest pressure within the nozzle (Figure 5.29). There is a vortex near the anode. The whole temperature field and the pressure filed at the same instant are given respectively in Figures 5.30 and 5.31. The hot gas still goes into the expansion volume through the passage between the hollow contact and the nozzle, and through the exhaust from the hollow contact. The pressure in the expansion volume is still lower than the pressure in the nozzle.

The continued reduction in the rate of ablation due to current decreasing towards the first current zero reduces the pressure within the nozlle. By the time the current is reduced to –7.9kA at 7.0ms the flow in the whole interrupt is reversed (Figure 5.32). The gas in the hole of the hollow contact has a temperature over 10,000K (Figure 5.33). This hot gas was accumulated due to previous arcing but the flow inside it is now reversed. There is a distinct rapid rise in temperature when the hot gas from the hole passes through the transparent cathode. This is perhaps rather artificial as Ohmic heating is suddenly switched on after the gas passing the transparent electrode. The pressure within the interrupter for this instant is given in Figure 5.34.

*Period 2 (7.9ms to 15.8ms)*

During this phase of arcing, the current direction is reversed and the moving contact is the cathode. Ablation of the nozzle is gradually increased due to the

increasing current. However, at 8.0ms with a current of 5.1kA (Figure 5.35) the flow is still in reverse direction (i.e. from nozzle entrance to the exit of the divergent section). With the increasing of nozzle ablation and the build up of the pressure in the nozzle, a stagnation point, where the pressure is the highest, is again established within the nozzle as shown in Figure 5.36. The pressure within the expansion volume is increased by the high temperature gas pumped in from the nozzle side. The situation near the peak current is illustrated in Figure 5.37.

The current is again reduced after the peak and the flow in the nozzle is reversed, for example, at 14.0ms (Figure 5.38). The arc temperature and flow field in r-z plane near current zero (at 15.8ms, 2.9kA) are given in Figure 5.39. Figures 5.40 and 5.41 show temperature distribution in the whole interrupter at these two instants. The temperature surrounding the arc (Figure 5.41) is at 2000K, which is rather high.

Figure 5.42 shows the pressure distribution inside the interrupter at three instants. The distribution is consistent with the flow in the nozzle. Near current zero, there is substantial pressure drop in the nozzle.

Typical results of the azimuthal velocity are given in Figure 5.43. The azimuthal Lorentz force tends to generate very high swirling velocity. The direction of rotation changes according to the sign of the local gradients of arc cross-section although the magnetic field is not changed. Part of the azimuthal component of the Lorentz force is due to the radial current density interacting with the axial component of the magnetic field. The azimuthal Lorentz force is dominated by the radial current density. Thus, the arc rotates in opposite direction after passing the maximum arc cross section.

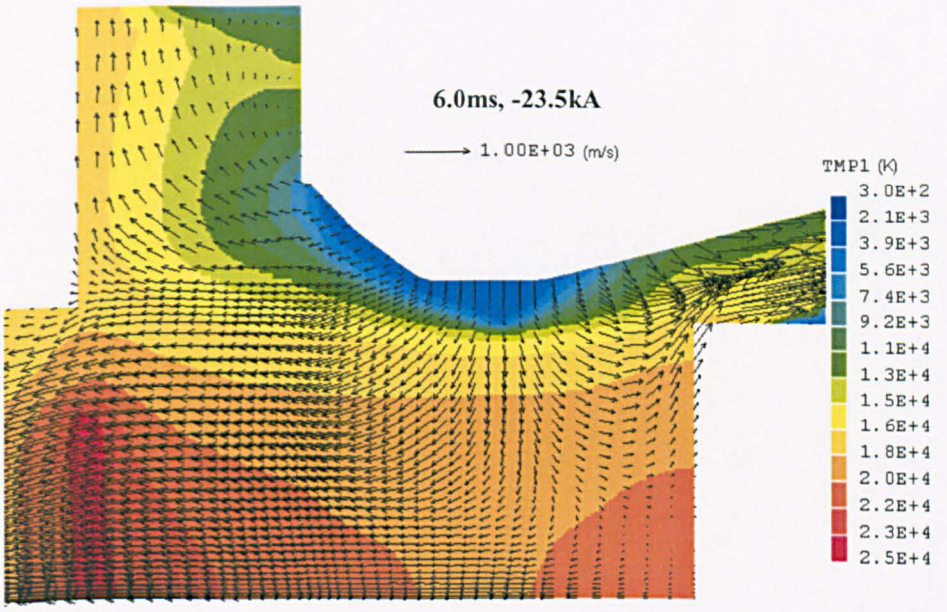


**Figure 5.29** Temperature and velocity fields at 6.0ms. Stagnation point is located in the middle of the throat region. Gas is exhausted from both sides of the stagnation point.

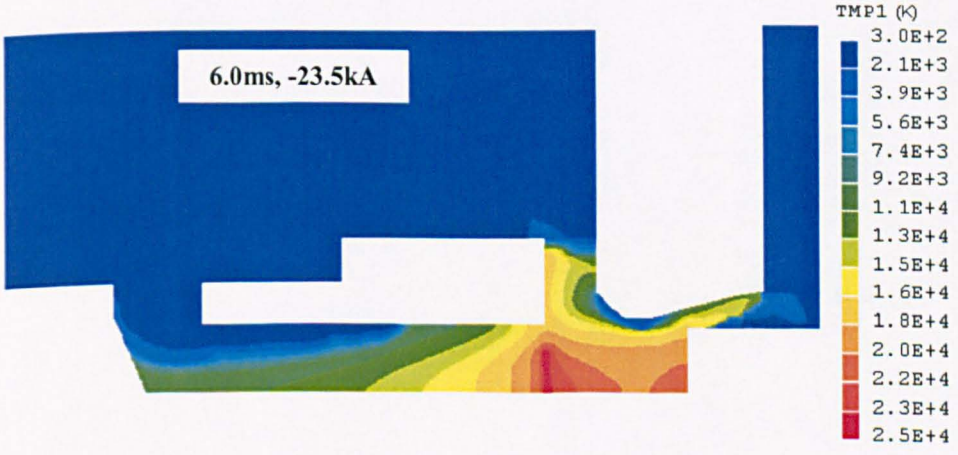


**Figure 5.30** Temperature distribution within the interrupter. Hot gas is extended right to the contact stem.

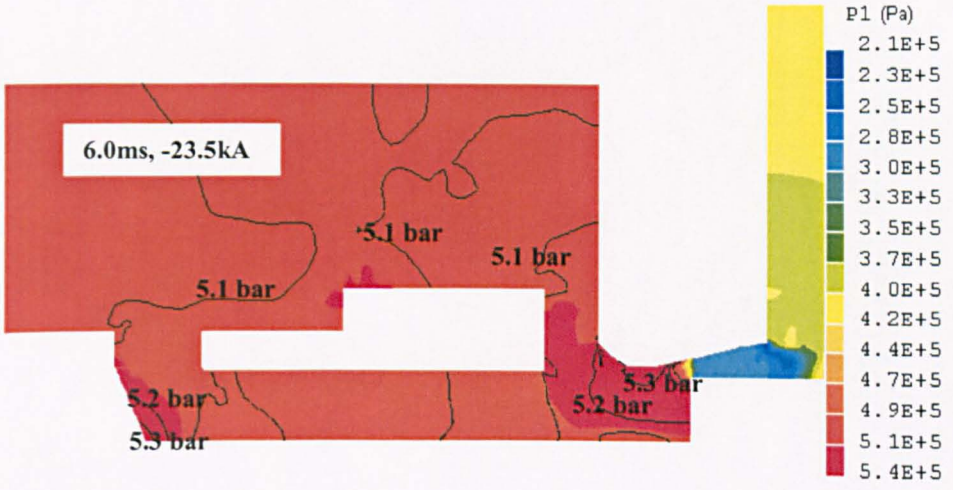


**Figure 5.31** Pressure field showing that the exhaust pressure is still lower than that in the nozzle

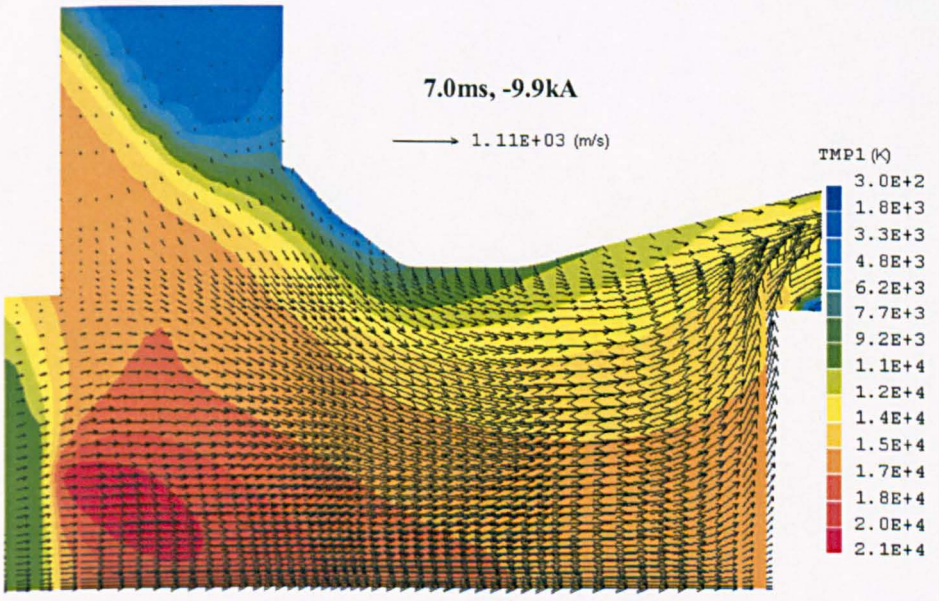


**Figure 5.32** The temperature and velocity fields at 7.0ms. The flow is reversed due to the reduction of nozzle ablation.


**Figure 5.33** The temperature distribution in the interrupter at 7.0ms.

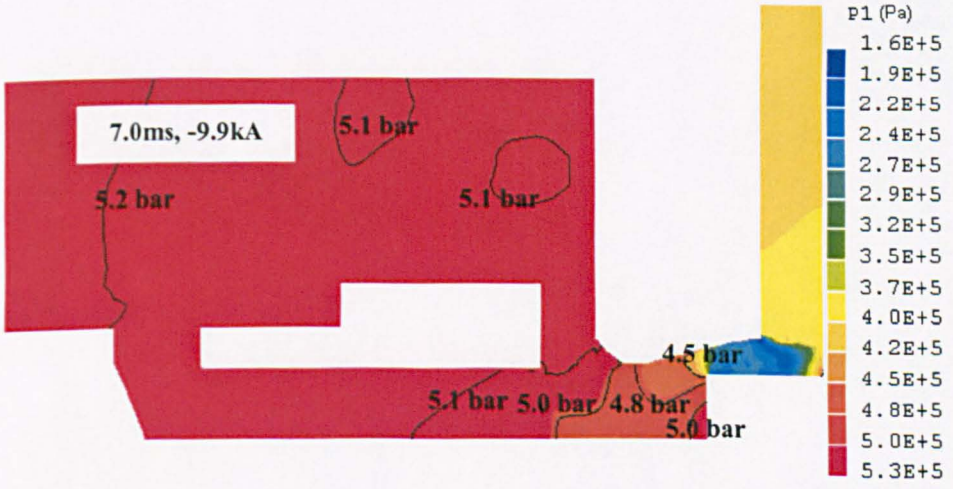


**Figure 5.34** Pressure distribution in the interrupter at 7.0ms.

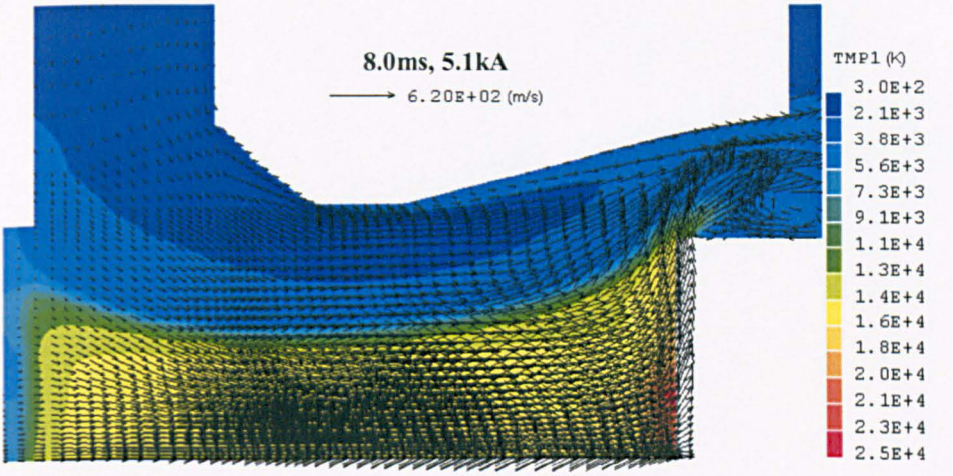


**Figure 5.35** Temperature and velocity at 8.0ms. The gas in the arc region is mainly supplied through the hollow contact while the gas surrounding the arc by the flow passage between the nozzle and hollow contact.

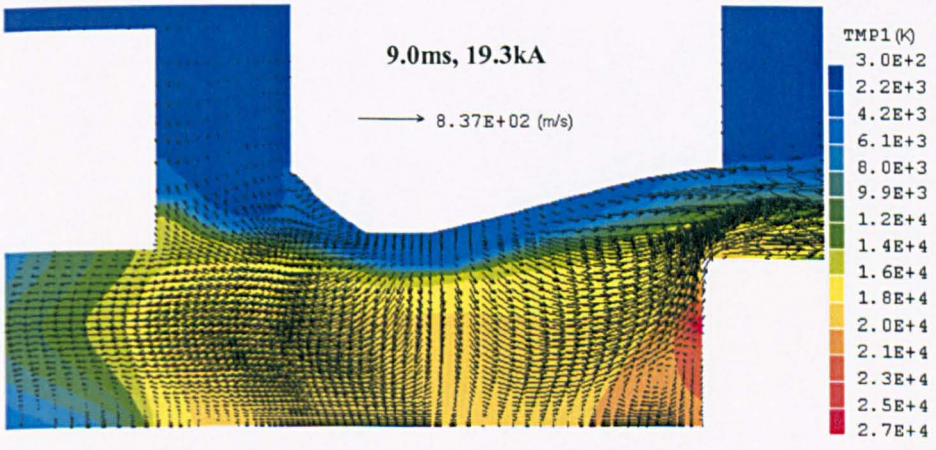


**Figure 5.36** Temperature and velocity fields at 9.0ms. The highest pressure in the interrupter is now located in the nozzle. PTFE vapour is exhausted in both directions, one to the expansion volume is used to increase the pressure there.

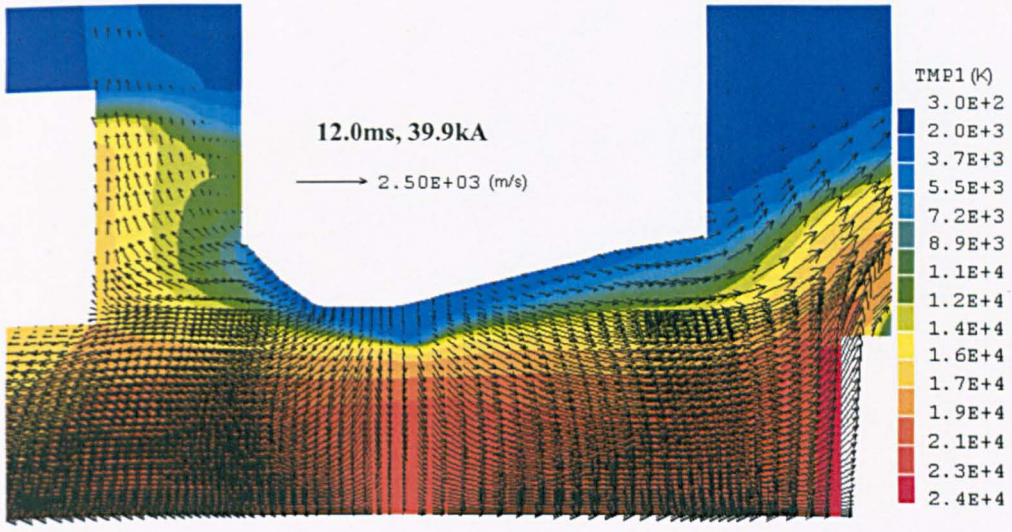


**Figure 5.37** Ablation takes place along the whole length of the nozzle. The position of the stagnation point is not sensitive to the current.

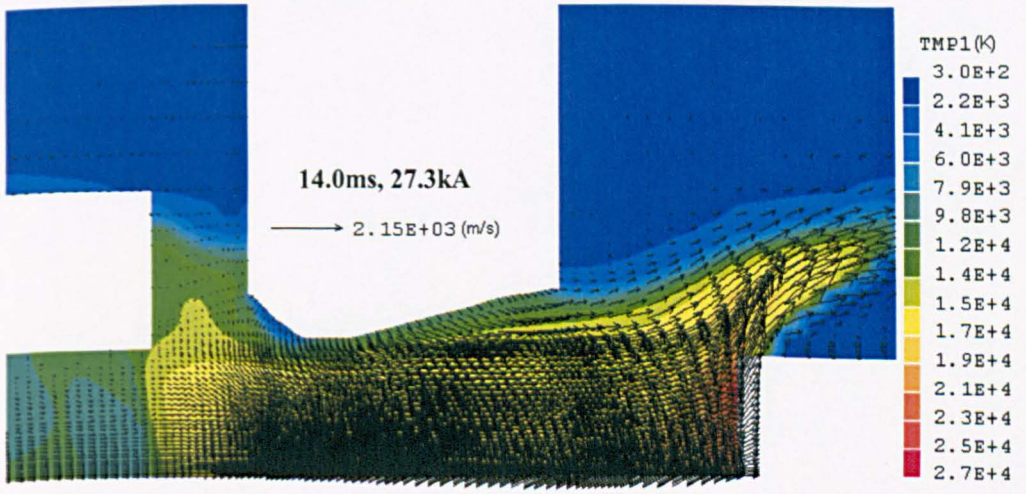


**Figure 5.38** The temperature and velocity distribution at 14.0ms. Flow is reversed although ablation continues at the nozzle wall.

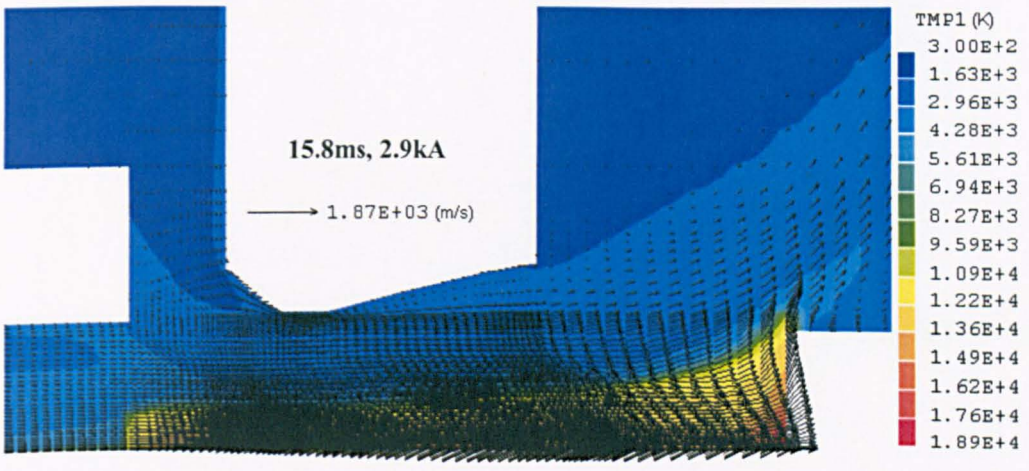


**Figure 5.39** The temperature and velocity distribution at 15.8ms. The gas surrounding the arc is at a temperature of 2000K.

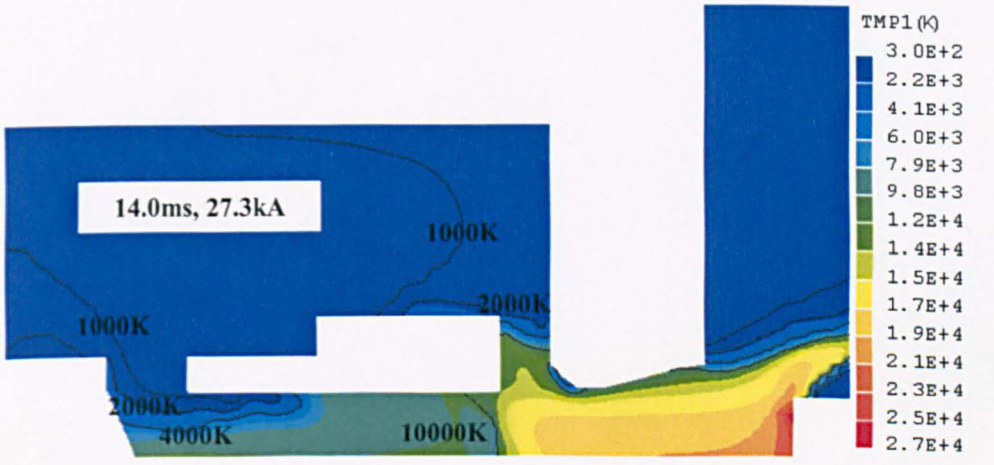


**Figure 5.40** Temperature in the interrupter at 14.0ms and 27.3kA.

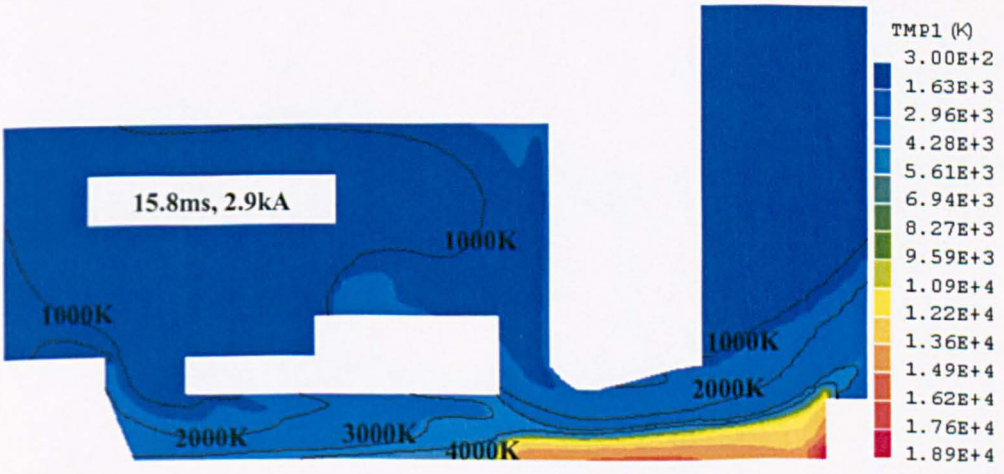


**Figure 5.41** Temperature in the interrupter at 15.8ms and 2.9kA. $SF_6$ temperature in the expansion volume is between 300K to 1000K.

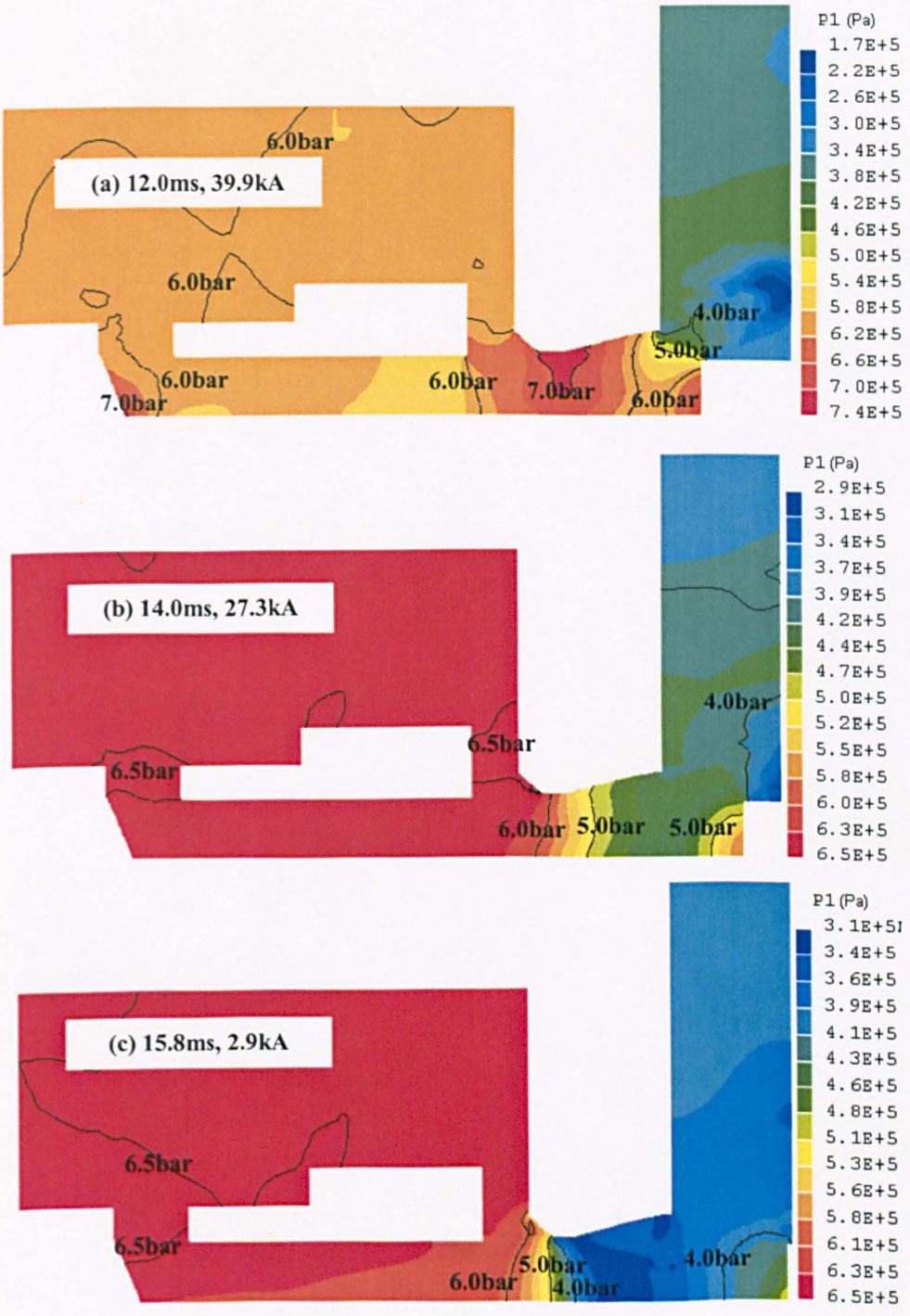


**Figure 5.42** Pressure distribution inside the interrupter, which is consistent with the flow in the nozzle. (a) The pressure in the nozzle is the highest. (b) The flow in the nozzle is reversed since the pressure in the expansion volume is the highest. (c) Pressure approaching current zero. There is substantial pressure drop in the nozzle.

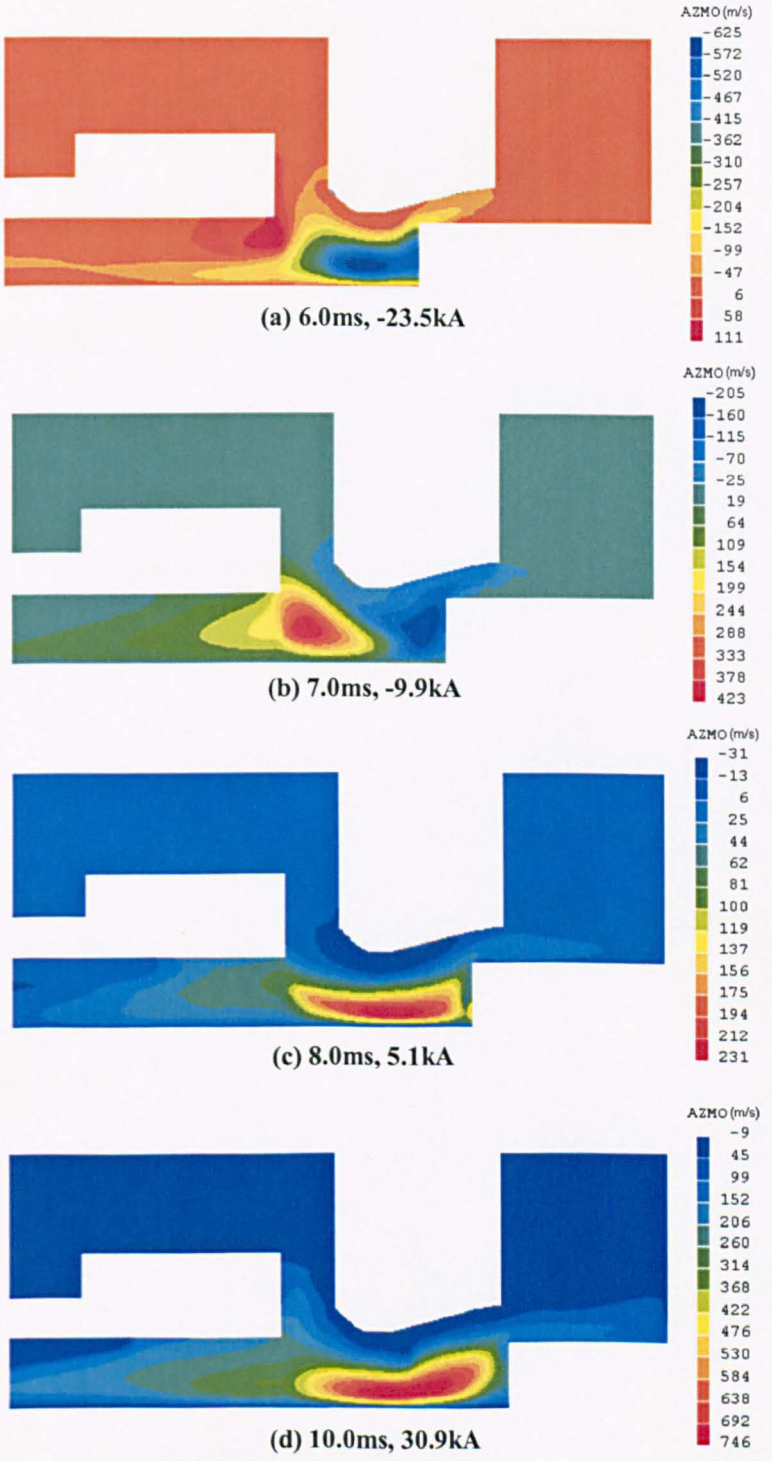


**Figure 5.43** Distribution of the azimuthal velocity (AZMO) at four instantaneous currents.

***E. Comparison between some results of with and without swirling flow.***

As previously stated in Chapter 4, the effect of the swirling flow would result in a substantial improving of interruption performance in this kind of circuit breaker. It is, therefore, important to compare the computed arc voltage, temperature, flow field and pressure with those calculated considering the absence of swirling flow, which means without attaching the permanent magnet in the arcing chamber. In addition, we carried out a sensitivity study by varying the percentage of radiation absorbed at the arc edge.

The comparison is given in Figure 5.44 and Figure 5.45. Results show that a change of 10% in the radiation absorption results in a maximum pressure difference of 0.5bar around second current zero. It is obvious that the pressure difference starts to occur shortly after ablation takes place (contact tip moves into the PTFE nozzle after 1.6ms) as shown in Figure 5.44 (case 1 and case 2). The predicted arc voltages do not change much during the first half cycle because the arc size and temperature is only weakly affected by the change in the radiation absorption percentage. However, the results show that the difference in the predicted arc voltage between case1 and case 2 in the second half cycle is responsible for the difference in the predicted pressure rise in the expansion volume. The predicted arc voltage of without swirling flow case is more or less the same up to 14.0ms. As previously discussed, the pressure rise in the expansion volume is mainly due to the nozzle ablation and heating by the high temperature. It is, therefore, interesting to see the effect of swirling flow in pressure rise in the expansion volume, and then it results in arc voltage difference before the second current zero.

The azimuthal movement of the arc tends to change flow fields and physical processes inside arc column, thus resulting in more enthalpy flux to expansion volume. Figure 5.46 shows that the enthalpy flux per unit area and time $\rho vh$ is plotted against axis at the location denoted by line $\overline{HH'}$ in Figure 5.1 at the three instantaneous times. The enthalpy flux enters from both sides of hollow contact to the expansion volume. The enthalpy flux of with the swirling flow case is in general higher than that of without the swirling flow case. This results in a higher-

pressure rise in the expansion volume, which explains the difference of arc voltage before the current zero in Figure 5.46.

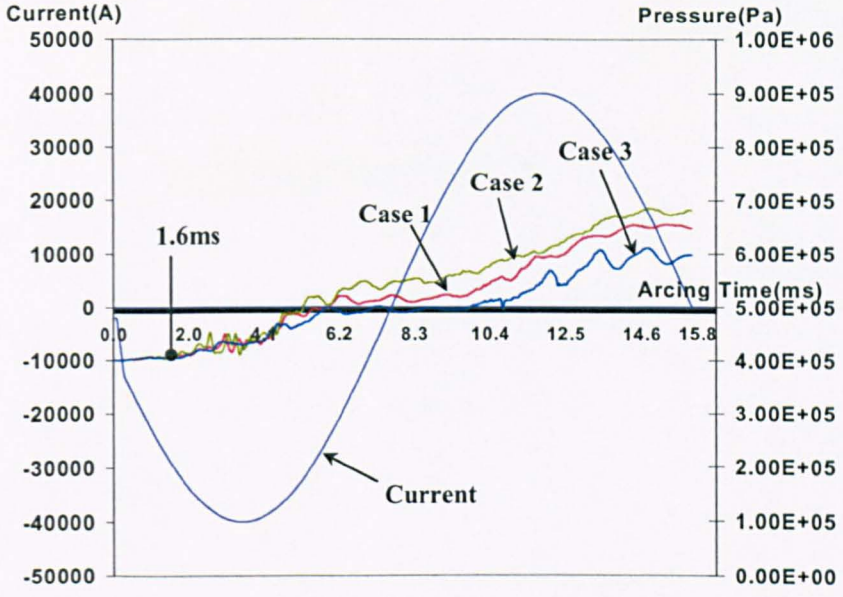


**Figure 5.44** Comparison of predicted pressure variation at the position indicated in Fig. 1. Case 1(red): 60% of radiation re-absorption with swirling flow. Case 2(green): 50% of radiation re-absorption with swirling flow. Case 3(blue): 60% of radiation re-absorption without swirling flow

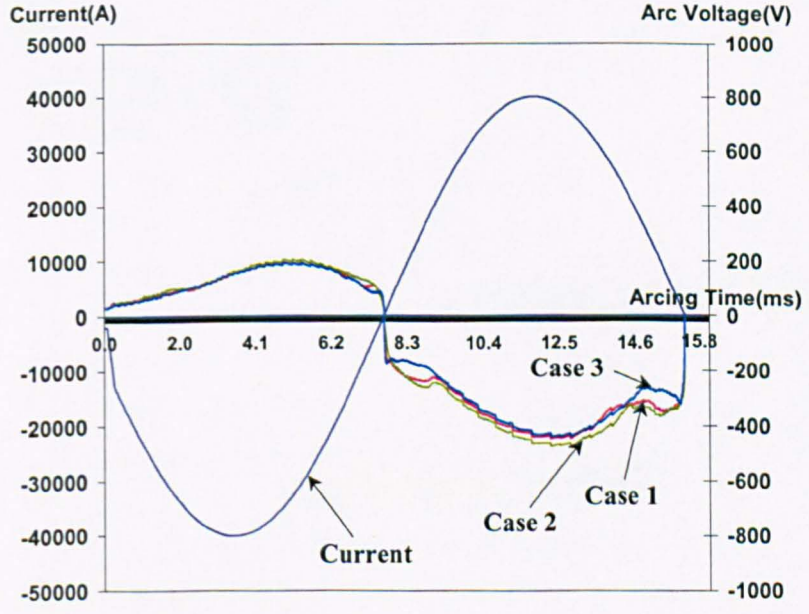


**Figure 5.45** Comparison of predicted arc voltage.
Case 1(red): 60% of radiation re-absorption with swirling flow. Case 2(green): 50% of radiation re-absorption with swirling flow. Case 3(blue): 60% of radiation re-absorption without swirling flow

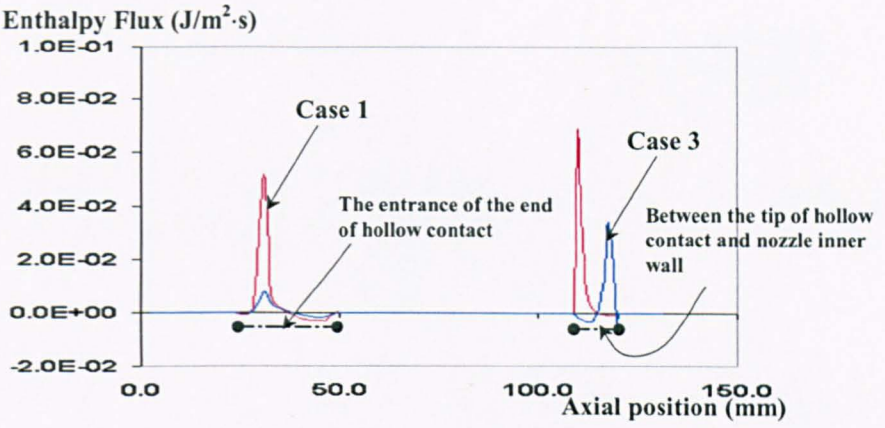


(a) 1.6ms with arcing current –30.2kA in phase 2.

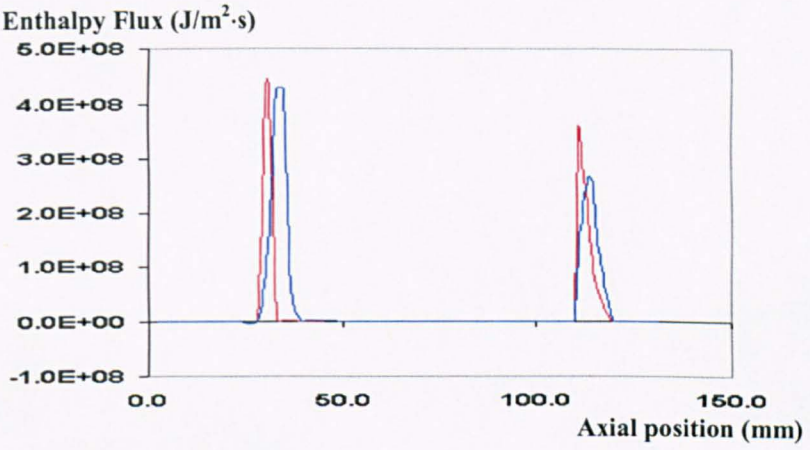


(b) 4.0ms with arcing current –39.3kA in phase 3.

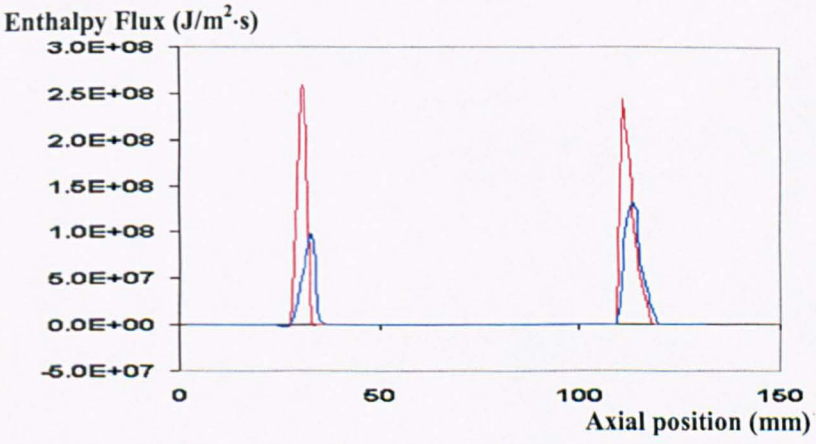


(c) 10.0ms with arcing current 30.9kA in phase 4.

**Figure 5.46** Enthalpy flux per unit area and time, $\rho vh$,, as a function of axial position at the cross section $\overline{HH'}$ in Figure 5.1 at three instants in high current phase. Case 1(red): 60% of radiation re-absorption with swirling flow. Case 3(blue): 60% of radiation re-absorption without swirling flow

## 5.6 Conclusions

Computer simulation of a 25.8kV hybrid circuit breaker (permanent magnet-assisted auto-expansion interrupter) for an arcing time of 15.8ms has been carried out. Typical results for flow fields, temperature and pressure were given and discussed.

Results show that nozzle ablation by arc radiation is the main factor of pressurization in the expansion volume in the high current phase. With the current waveform investigated, the pressure rise starts rapidly due to PTFE vapour at above 30kA, which is 1.6ms after arc initiation. Pressure waves are generated in the expansion volume when the hot PTFE vapour heats up and compresses the gas in the expansion volume. The propagation and reflection of the pressure waves are responsible for the pressure fluctuation. The proportion of re-absorption of arc radiation is an important factor determining the pressure rise prediction in the arc model from the sensitivity study. The effects of the swirling on arc have been investigated comparing the results of with and without swirling flow. The swirling flow results in a substantial role to increase the pressure in the expansion volume, and then affects interruption performance during current zero period.

# Chapter 6
# Conclusions and Future Work

## 6.1 Summary and conclusions

Computer simulation has been carried out for two types of $SF_6$ hybrid circuit breakers. For such breakers the arc energy is utilised to create the conditions for arc interruption at current zero and an externally imposed magnetic field to produce the arc rotation. In one type of the hybrid breakers, the magnetic field is produced by the arcing current flowing in an azimuthal coil and in the other it is produced by a permanent magnet. An arc model, which includes the turbulence enhanced momentum and energy transport, radiation transport and swirling flow, has been used to simulate the operation of the two types of the hybrid breakers. It is assumed that, when the current is sufficiently high, the behaviour of the arc can be approximated by an axisymmetric arc model. PHOENICS, a commercial CFD package, has been used to obtain the computational results. Electrical field, magnetic field, the velocity filed and temperature distribution are computed simultaneously. Computational results are compared with available experimental results, which are extremely scarce.

Computational results given in Chapter 3 have shown the effects of swirling flow on DC arc behaviour in a hybrid interrupter. The interaction of the arcing current with the externally produced magnetic field in a coil results in a Lorentz force in the azimuthal direction, which produces swirling of the arc. Strong swirling flow occurs in regions where radial current density is high. In comparison

with the arc without swirling, the axis pressure is lowered by the presence of swirling flow and the shape of the arc column is changed as a result of modified pressure and flow fields. The arc voltage is only slightly reduced in comparison with a similar arc without swirling flow.

The temperature and velocity fields for a 5kA DC arc with and without swirling are compared. The azimuthal movement of the arc tends to counteract the radial thermal conduction and radiation transport, thus resulting in a better thermal confinement of the arc. The azimuthal Lorentz force tends to generate very high swirling velocity. The direction of radial current density depends on the sign of the local gradient of arc cross section. For arcs with swirling flow, the arc cross section attains a maximum at a location nearly midway between two electrodes. Thus, the direction of rotation changes after passing the maximum arc cross section.

The arcing process following a sinusoidal current in a hybrid circuit breaker, the magnetic field is produced by the arcing current flowing in a coil has been simulated and the results are given in Chapter 4. The effects of the swirling flow on the behaviour of an ac transient $SF_6$ arc are discussed in detail. The thermal arc interruption capability is established in terms of the critical rate of rise of recovery voltage after current zero. Typical results at various instants are presented and discussed. The results show that the generation of swirling flow by the strong magnetic field interacting with the current density inside the arc column is closely coupled with the shape of the arc column. In association with contact movement, complex flow situations are developed during the high current phase under the accumulative effect of swirling flow and significantly affect the shape of arc column, the arc voltage and more importantly the pressure rise in the expansion volume. By combining the magnetic control of arc motion with "auto-expansion blowing" due to the Lorentz force and arc induced pressure gradient, circuit breaker performance can be considerably enhanced. The values of the parameters describing radiation transport and the choice of the turbulence length scale and the value of turbulence parameter may require further investigation when more test results are available for the verification of computer simulation.

In chapter 5, computer simulation of a 25.8kV hybrid circuit breaker (permanent magnet-assisted auto-expansion interrupter) for an arcing time of 15.8ms has been carried out. Typical results for flow fields, temperature and pressure are given and discussed. Results show that nozzle ablation by arc radiation is the main factor of pressurization in the expansion volume in the high current phase. With the current waveform investigated, the pressure rise starts rapidly due to nozzle ablation when current is approximately 30kA, which is 1.6ms after arc initiation. Pressure waves are generated in the expansion volume when the hot PTFE vapour enters and compresses the gas in the expansion volume. The propagation and reflection of the pressure waves are responsible for the pressure fluctuation. The rate of re-absorption of arc radiation is an important factor determining the pressure rise predicted by the arc model. The effects of the swirling on arc have been investigated by comparing the arcs with and without swirling flow. The swirling flow substantially increases the pressure in the expansion volume, which in turn is expected to and then affect interruption performance during current zero period.

It has been clearly demonstrated that the arcing processes inside a hybrid circuit breaker can be simulated, which take account of the swirling flow. The range of applicability of the values of some parameters describing radiation transport and turbulence need to be verified as soon as further test results are available.

## 6.2 Future work

One weakness of the present investigation is the assumption of axisymmetry. In the high current phase during which the arc fills the hole of the hollow contact, this assumption holds reasonably well. However, when the current decays towards current zero, the arc root on the hollow cathode will upset the axisymmetry. With further advancement in computer technology, the implementation of arc rooting

mechanisms into the arc model should be on the agenda. This will result in 3-dimensional arc modelling.

Certain physical processes are still modelled approximately with empirically determined parameters. These parameters are concerned with radiation transport and the turbulence enhanced momentum and energy transport. The radiation transport model is designed to cater for arcs in mainly axial flow, for which the radial temperature profile monotonically decays to ambient temperature. For the circuit breakers investigated in this thesis, this is not always the case. Work is needed to devise an approximate radiation transport model for non-monotonic varying radial temperature profiles. The partial characteristic method for radiation transport [88] should be employed to study in detail the radiation transport for such arcing situation. An approximate radiation transport model may be derived from such studies.

A very simple model, the ablation dominated model, has been used to calculate the rate of ablation. The amount of radiated power from the arc core available for ablation is expected to be dependent on the current and the arc cross section (Yan et al. [9]). Further refinement of ablation model along the lines of Zhang et al. [10] should be adopted to improve the prediction.

As regards the parameters required by the turbulence model, the values used in the thesis have given reasonable results when compared with experiments. These values should be optimised when more experimental results are available for the verification of computer simulation results.

Further investigation is required to examine the plasma state under a fast rising recovery voltage. The effects of departure from local thermal equilibrium on interruption capability need to be investigated.

# References


[1] G R Jones and M T C Fang, "The physics of high-power arcs", Rep. Prog. Phys., Vol. 43, pp. 1415-1465, 1980

[2] V. Aubrecht and J. J. Lowke, "Calculations of Radiation Transfer in $SF_6$ Plasmas using the Method of Partial Characteristics", J. Phys. D, Appl. Phys., Vol. 27, pp. 2066-2073, 1994

[3] J F Zhang, M T C Fang and D B Newland, "Theoretical investigation of a 2kA arc in supersonc nozzle", J Phys D: Apply Phys, 20, pp. 368-379, 1987

[4] R W Libermann and J J Lowke, "Radiation emission coefficients for sulphur hexafluoride arc plasmas", JQSRT, Vol. 16, pp. 253-264, 1975

[5] A M Cassie, "Arc rupture and circuit severity: a new theory", CIGRE paper 102, pp. 1-14, 1939

[6] O Mayr, "Beitrage zur theorie des statischen und des dynamischen lichtbogens (Contribution to the theory of static and dynamic arcs)", Arch. Elect., 37, pp. 588-608, 1943

[7] B E Launder and D B Spalding, "Mathematical models for turbulences", Academic Press, London and New York, 1972

[8] CHAM, PHOENICS, Phoenics is the name of a commercial CFD package supplied by CHAM which is based at Bakery House, 40 High Street, Wimbledon Village, London, SW19 5AU, UK

[9] J D Yan, M T C Fang and W Hall, "The development of PC based CAD tools for auto-expansion circuit breaker design", IEEE Trans. on Power Delivery, Vol. 14, No. 1, pp. 176-181, 1999

[10] J L Zhang, J D Yan, A B Murphy, W Hall and M T C Fang, "Computational Investigation of Arc Behaviour in an Auto-expansion Circuit Breaker Contaminated by Ablated Nozzle Vapour", IEEE Trans. On Plasma Science, Vol. 30, No 2, pp.706-719, 2002

[11] M Claessens, K Moller and H G Thiel, "A computational fluid dynamics simulation of high- and low-current arcs in self-blast circuit breakers", J. Phys. D, Appl. Phys., Vol. 30, pp. 1899-1907, 1997

[12] J Slepian, "Extinction of a long a.c. arc". AIEE Trans., Vol. 47, pp. 1398, 1928

[13] D C Prince and E J Poitras, "Oil-blast breaker theory proved experimentally", Electrical World, 97:400, 1931

[14] T E Browne, "A study of AC arc behaviour near current zero by means of mathematical models" AIEE Trans., Vol. 67 pp. 141, 1948

[15] W Elenbaas, Phillips Research Rep., Vol. 1, No. 5, 1946

[16] W Hermann, "Practical application of arc physics in circuit breakers-surveyof calculation methods and application guide", Technical report, CIGRE, Report of Working Group 13-01, 1987

[17] Working Group 13-01, "Applications of black box modelling to circuit breakers", Technical report, CIGRE, Final Report, 1992

[18] T E Browne, "Jr. Practical modelling of the circuit breaker arc as a short-line fault interrupter", IEEE Trans. Power Apparatus and Systems, 97, pp. 838-847, 1978

[19] T E Browne, "Jr. Simplified estimation of critical quantities for short-line fault interruption", IEEE Trans. Plasma Science, 8(4), pp. 400-405, 1980

[20] M Haupt and K Moller, "Contribution on the application of two pole arc models on $SF_6$ blast circuit breakers, ETZ Archiv, 9, pp. 255-260, 1987

[21] B W Swanson and R M Roidt, "Boundary layer analysis of an $SF_6$ circuit breaker arc", IEEE Trans., PAS-90, pp.1086-1903, 1970

[22] B W Swanson, R M Roidt and T E Browne, "Arc cooling and short line fault interruption", IEEE Trans., PAS-90, pp.1094-1102, 1970

[23] B W Swanson and R M Roidt, "Thermal analysis of an $SF_6$ circuit breaker arc", IEEE Trans., PAS-91, pp. 381-389, 1972

[24] B W Swanson and R M Roidt, "Some numerical solutions of the boundary layer equations for an $SF_6$ arc", Proc. IEEE Trans., Vol 59, pp. 493-501, 1971

[25] B W Swanson, R M Roidt and T E Browne, "A thermal arc model for short line fault interruption", ET-Z-A, Bd. 93, pp. 375-380, 1972

[26] B W Swanson, "A thermal analysis of short line fault interruption", IEE Winter Power Meeting, Paper C-47, 1974

[27] B W Swanson, "Nozzle arc interruption in supersonic flow", IEEE Trans., PAS-96, pp. 679, 1977

[28] D T Tuma and J J Lowke, "Prediction of properties of arcs stabilised by forced convection", J. Appl. Phys., Vol. 46, pp. 3361-67, 1975

[29] D T Tuma , "A comparison of the behaviour of $SF_6$ and $N_2$ blast arcs around current zero", IEEE Trans., Vol. PAS-99, No. 6, pp. 976, 1980

[30] D T Tuma and H Fong, "Current zero deformation by interaction of gas-blast arc with test circuit", IEEE Trans., Vol. PAS-99, pp. 976, 1980

[31] E Richley and D T Tuma, "Mechanisms for the temperature decay in the freely recovering gas blast arc", IEEE Trans., Vol. PAS-10, No. 1, pp. 2, 1982

[32] J J Lowke and H C Ludwig, "A simple model for high-current arcs stabilised by forced convection", J. Appl. Phys., Vol. 46, pp. 3352, 1975

[33] F R El-Akkari and D T Tuma, "Simulation of transient and zero current behaviour of arcs stabilised by forced convection", IEEE Trans., PAS-96, pp. 1784, 1977

[34] W Hermann, U Kogelschatz, L Niemeyer, D Ragaller and E Schade, "Experimental and theoretical study of a stationary high-current arc in a supersonic nozzle flow", J. Phys. D., Vol. 7, pp. 1703-22, 1974

[35] W Hermann, U Kogelschatz, L Niemeyer, D Ragaller and E Schade, "Investigation on the physical phenomena around current zero in HV gas-blast breakers", IEEE Trans., Vol. PAS-95, No. 4, pp. 1165-76, 1976

[36] W Hermann and E Schade, "Radiation energy balance in cylindrical nitrogen arc", JQSRT, Vol. 12, pp. 1257, 1972

[37] J D Yan, K I Nuttall and M T C Fang, "A comparative study of turbulence models for $SF_6$ arcs in a supersonic nozzle", J. Phys. D, Appl. Phys., Vol. 32, pp. 1401-1406, 1999

[38] M D Cowley, "Integral method of arc analysis: Pt. 1", J. Phys. D: Appl. Phys., Vol. 7, pp. 2218-2231, 1974

[39] M T C Fang and W H Bu, "Investigation of ablation-dominated AC nozzle arcs", IEE Proc.-A, Vol. 138, No. 1, pp. 71-77, 1991

[40] M T C Fang and D B Newland, "DC nozzle arcs with mild wall ablation", J. Phys. D: Appl. Phys., Vol. 16, pp. 793-810, 1983

[41] M D Cowley, S K Chan and M T C Fang, "Integral method of analysing electric arcs: Iii shape factor correlation for low radiation and laminar flow", J. Phys. D, Appl. Phys., Vol. 9, pp. 1085-1099, 1976

[42] M T C Fang, S K Chan and M D Cowley, "Dynamic behaviour of an a.c. arc column in a steady laminar accelerating flow", Proc. IEE, Vol. 122, pp580-590, 1975

[43] M T C Fang and D Brannen, "A current-zero arc model based on forced convection", IEEE Trans., Vol. PS-7, No. 4, pp. 217-229, 1979

[44] S K Chan, M T C Fang and M D Cowley, "The DC arc in a supersonic nozzle flow", IEEE Trans., PS-6, pp. 394-405, 1978

[45] W H Bu, M T C Fang and Z Y Guo, "The behaviour of ablation dominated DC arc", J. Phys. D: Appl. Phys., Vol. 23, pp. 175-183, 1990

[46] W Hermann and K Ragaller, "Theoretical description of the current interruption in HV gas blast breakers", IEEE Trans., Vol. PAS-96, No. 5, pp. 1546, 1977

[47] S K Chan, M T C Fang and M D Cowley, "Transient behaviour of interrupted arcs in laminar flow", J. Phys. D, Appl. Phys., Vol. 9, pp. 1757-1770, 1976

[48] M T C Fang, V R Malghan and G R Jones, "Investigation of quasi-steady state high current arcs in an orifice air flow", J. Appl. Phys., Vol. 48, pp. 2331-2337, 1977

[49] R E Blundell and M T C Fang, "A simplified turbulent arc model foe the current-zero period of a $SF_6$ gas-blast circuit breaker", J. Phys. D, Appl. Phys., Vol. 31, pp. 561-568, 1998

[50] M T C Fang and W Y Lin, "Current zero behaviour of a gas-blast arc Part 1: Nitrogen", Proc. IEE, Vol. 137, pt A, No. 4, pp. 175, 1990

[51] J F Zhang and M T C Fang, "A comparative study of $SF_6$ and $N_2$ arcs in accelerating flow", J. Phys. D, Appl. Phys., Vol. 21, pp. 730, 1988

[52] K Ragaller, W Egli and K P Brand, "Dielectric recovery of an axially blown $SF_6$ arc after current zero: Part 2 Theoretical investigation", IEEE Trans., Vol. PAS-10, No. 3, pp. 154, 1982

[53] R R Mitchell, D T Tuma and J F Osterle, "Transient two-dimentional calculation of properties of forced convection stabilized electric arcs", IEEE Trans., Vol. PAS-13, No. 4, pp. 207, 1985

[54] J J Lowke and H E Lee, "A numerical study of a two-dimensional circuit-breaker arc during current interruption", Int. Conf. On Gas Discharges and Their Applications, Oxford, 1985

[55] K Ragaller, W R Schneider and W Hermann, "A special transformation of the differential equations describing blown arcs", ZAMP, Vol. 22, pp92, 1971

[56] E Schade and K Ragaller, "Dielectric recovery of an axially blown $SF_6$-arc after current zero: Part 1 Experimental investigation", IEEE Trans., Vol. PAS-10, No. 3, pp. 141, 1982

[57] P J Shayler and M T C Fang, "Radiation transport in wall-stabilised nitrogen arcs", J. Phys. D, Appl. Phys., Vol. 11, pp. 1743-56, 1978

[58] Q Zhuang and M T C Fang, "Current zero behaviour of an $SF_6$ gas blast arc. Part I: laminar flow", J. Phys. D, Appl. Phys., Vol. 25, pp. 1197-1204, 1992

[59] M T C Fang, Q Zhuang and X J Guo, "Current zero behaviour of an $SF_6$ gas blast arc. Part II: turbulent flow", J. Phys. D, Appl. Phys., Vol. 27, pp. 74-83, 1994

[60] D Leseberg and G Pietsch, " Interferometrische undterschungen von schaltichtbogen in stromendem $SF_6$", Proc. 4$^{th}$ Int. Symp. On switching arc phenomena, Lodz, Poland, pp. 236-240, 1981

[61] D Leseberg, Ph.D. thesis, RWTH Aachen, Germany, 1982

[62] J J Lowke, "Recent progress in arc theory", Bulletin of the Technical University of Brno, 1992/2-4:11, 1992

[63] M T C Fang, "Mathematical modelling of basic processes in axial blown switching arcs", Bulletin of the Technical University of Brno, 1992/2-4:11, 1992

[64] S D Eby, J Y Trepanier and X D Zhang, "Modelling radiative transfer in $SF_6$ circuit-breaker arcs with the p-1 approximation", J. Phys. D, Appl. Phys., Vol. 31, pp. 1578-1588, 1998

[65] J Y Trepanier, X D Zhang and R Camarero, "Numerical simulation of a 2kA convection-stabilized arc using CFD tools", J. Phys. D, Appl. Phys., Vol. 30, pp. 3240-3252, 1997

[66] R Camarero, X D Zhang, H Pellegrin and J Y Trepanier, "Computation of self induced magnetic field in circuit breaker arcs", IEEE Trans. Plasma Sci., Vol. 25, pp. 974-981, 1997

[67] U Rutten, Proc. Gas Discharge and their Applications, pp 140-143, 1992

[68] C Fievet, J Maftoul, P Chevrier, M Barrault and J Millon Fremillon, "Industrial applications of high- medium- and low-voltage arc modelling", J. Phys. D, Appl. Phys., Vol. 30, pp. 1346-1355, 1997

[69] S V Patankar, "Numerical Heat Transfer and Fluid Flow", New York, Hemisphere, 1980

[70] S Kwan, Ph.D. thesis, University of Liverpool, United Kingdom, 1996

[71] H J Lingal, A P Strom and T E Browne, "An investigation of the arc-quenching behaviour of sulfur hexafluoride", AIEE Trans. Vol. PAS-72, pp. 242-246, 1963

[72] G J Easley and J M Telford, "A new design 34.5 to 69kV intermediate capacity $SF_6$ circuit breakers", IEEE Trans., Vol. PAS-83, pp. 1172-1173, 1964

[73] K Suzuki, T Toda, A Aoyagi, H Ikeda, A Kobayashi, I Ohshima and S Yanabu, "Development of 550kV 1-break GCB (Part I): investigation of interrupting chamber performance", IEEE Trans. on Power Delivery, Vol. 8, pp. 1184-1191, 1993

[74] T H Lee, Physics and Engineering of High Power Switching Devices, The MIT Press, 1975

[75] R T Lythall, The J&P Switchgear Book (7th Edition), Newnes-Butterworths, London, 1972

[76] P Chevrier, C Fievet, S S Ciobanu, C Fleurier and P Scarpa, "Study of the arc-electrode interaction in a $SF_6$ self-blast circuit breaker", J. Phys. D, Appl. Phys., Vol. 32, pp. 1494-1502, 1999

[77] C M Dixon, B-W Lee, J-M Seo and M T C Fang, "Numerical simulation of a hybrid rotating arc/auto-expansion interrupter", Proc. Of the XIII Int. Conf. on Gas Discharges and Their Applications, Glasgow, UK Vol. 1, pp. 206-209, 2000

[78] G R Jones, "High pressure arcs in industrial devices", Cambridge University Press, 1988

[79] H Schichting, "Boundary layer theory", McGraw-Hill, New York, 1968

[80] J D Anderson, J C Tannehill and R H Pletcher, "Computational fluid mechanics and heat transfer", McGraw-Hill, 1984

[81] G R Jones and M T C Fang, "The physics of high-power arcs", Rep. Prog. Phys., Vol. 43, pp. 1415-1465, 1980

[82] E Schade, "Recovery of switching arcs", Proc. XVIIth Int. Conf. On Phenomena Ionised Gases, pp. 277-297, 1985

[83] D Lesberg and G Pietsch, Interferometrische Unterschungen von Schaltischtbogen in stromendem $SF_6$ (Westdetscher), 1982

[84] L Niemyer and K Ragaller, " Development of turbulence by the interaction of gas flow with plasma", Z. Naturf. Vol. A28, pp. 1281-1289, 1973

[85] D Lesberg and G Pietsch, "Optical investigation on a $SF_6$ switching arc inside a glass nozzle", Int. Conf. on Gas Discharges and their Applications (London), pp. 9-12, 1982

[86] M Mitchnner and C H Kruger, "Partially Ionized Gases", John Wiley & Sons, New York, 1973

[87] R E Blundell, M T C Fang and A Vourdas, "Stability of a DC $SF_6$ Arc in an Axially Accelerating Flow", IEEE Trans. on Plasma Science, Vol. 25, No. 5, pp. 852-859, 1997

[88] C M Dixon, "Modelling and simulationnof physical processes occurring in high voltage interrupters", PhD thesis, 2001

[89] J D Yan and M T C Fang, "Visualisation of arcing process in an auto-expansion circuit breaker", IEEE Trans. Plasma Sci., Vol. 27, pp. 40-41, 1999

[90] V G Sevast'yanenko, "Radiation transfer in a real spectrum integration over frequency", J. Eng. Phys., vol. 36, pp. 138-148, 1979

[91] V G Sevast'yanenko, "Radiation transfer in a real spectrum integration with respect to the frequency and angles", J. Eng. Phys., vol. 38, pp. 173-179, 1980

[92] P Cheng, "Dynamics of a radiating gas with applications to flow over a wavy wall", AIAA Journal, vol. 4, no. 2, pp. 238-245, 1966

[93] H A Becker, F Liu and Y Bindar, "A comparative study of radiative heat transfer modelling in gas-fired furnaces using the simple grey gas and the weighted sum of grey gasses models", Int. J. Heat Mass Transfer, vol. 42, no. 10, pp. 3357-3371, 1998

[94] A Gleizes, Private communication, 1999

[95] G Bernard, P Malkin and W Legros, "An $SF_6$ circuit breaker using the auto-expansion principle", IEEE Trans. on Power Delivery, Vol. 3, No 4, pp. 1739-1744, 1988

[96] H Sasao, S Hamano, Y Wada, H Hasegawa and Kobayashi, "Development of a magnet-assisted autopuffer GCB", IEEE Trans. on Power Delivery, Vol. 5, No 3, pp. 1355-1361, 1990

[97] K Y Kweon, J D Yan and M T C Fang, "Computer simulation of $SF_6$ arcs in a duo-flow hybrid circuit breaker", Proc. of the XV Symposium on Physics of switching arc, Brno, Czech Republic, pp. 122-125, 2003

[98] J D Yan, M T C Fang and Q S Liu, "Dielectric breakdown of a residual $SF_6$ plasma at 3000K under diatomic equilibrium", IEEE Trans. Dielect. Elect. Insulation, Vol. 4, pp. 114-119, 1997

[99] C B Ruchti and L Niemeyer, "Ablation controlled arcs", IEEE Trans. on Plasma Science, Vol. PS-14, pp. 423-434, 1986

[100] J L Zhang, J D Yan and M T C Fang, "Investigation of the Effects of Pressure Ratios on Arc Behaviour in a Supersonic Nozzle", IEEE Trans. On Plasma Science, Vol. 28, No 5, pp. 1725-1734, 2000

[101] D G Lilley, "Prediction of Inert Turbulent Swirl Flows", AIAA Journal, vol. 11, pp. 950-960, 1973

[102] M R Barrault and G Bernard, "A study of a rotating arc $SF_6$ circuit-breaker under the action of a radial magnetic field", Int. Conf. On Gas Discharges and Their Applications, Oxford, pp. 130-133, 1985

[103] MAGSOFT, FLUX2D, Flux2d is a Finite Element Method based CAD program for the analysis and design of electromagnetic and thermal devices and processes, MAGSOFT Cor., 1223 Peoples Ave., Troy, NY 12180, USA

[104] A K Gupta, D G Lilley and N Syred, "Swirl Flows", Abacus Press, Tunbridge Wells, Kent and Cambridge, Mass., 1984

[105] L S Frost and R W Liebermann, "Composition and transport properties of SF6 and their use in a simplified enthalpy flow arc model", Proc. IEEE, vol. 59, pp.474-485, 1971

[106] D Chen and D R Turner, The transient magnetic field analysis of a rotating arc device, University of Liverpool internal report

[107] R B Leighton, R P Feynman and M Sands, The Feynman Lectures on Physics, Volume II, Addison-Wesley, 1964